# Growth and advanced characterization of solution-derived nanoscale $La_{0.7}Sr_{0.3}MnO_3$ heteroepitaxial systems

Jone Zabaleta Llorens

Departament de Materials Superconductors i Nanoestructuració a Gran Escala, ICMAB-CSIC
Supervisors: Prof. T. Puig Molina and Dr. N. Mestres Andreu
Tutor: Prof. A. Sánchez Moreno

Departament de Física
Programa de Ciència de Materials
Universitat Autònoma de Barcelona

Bellaterra, December 2011




# Growth and advanced characterization of solution-derived nanoscale $La_{0.7}Sr_{0.3}MnO_3$ heteroepitaxial systems

Dissertation presented in candidacy for the degree of
Doctorate of Philosophy in Materials Science by

**Jone Zabaleta Llorens**

Departament de Física
Programa de Ciència de Materials
**Universitat Autònoma de Barcelona**

*Departament de Materials Superconductors i Nanoestructuració a Gran Escala*, ICMAB-CSIC

Supervisors: Prof. T. PUIG MOLINA and Dr. N. MESTRES ANDREU

Tutor: Prof. A. SÁNCHEZ MORENO

Bellaterra, December 2011

*Para Santi y Lourdes*

# Contents

# Acknowledgments

I would like to thank the people and institutions that have made this thesis possible.

In the first place, I give thanks to my supervisors Prof. Teresa Puig and Dr. Narcís Mestres for the opportunity given to me to realize this work, the shared discussions, and their trust in my judgment. To Prof. Teresa Puig and Prof. Xavier Obradors for inviting me to come to ICMAB and for letting me be part of the *Superconducting Materials and Large Scale Nanostructures* group.

I want to acknowledge the Spanish *Ministerio de Educación* for the FPU fellowship, as well as the Spanish Government through the CONSOLIDER program for the financial support of the last six months. I also acknowledge the EU (HIPERCHEM, NESPA, European Light Sources Activities-ELiSA), to CSIC (CANAMUS), the Spanish Government (NANOARTIS, MAT2008-01022, NANOFUNCIONA), and the Generalitat de Catalunya (XARMAE, Pla de Recerca).

I give thanks to Prof. J. Mannhart, Prof. X. Obradors, Dr. A. Asenjo, Prof. C. Ocal, and Dr. J. Santiso for accepting being part of the jury of this thesis.

This work would have not been possible without the collaboration and interaction with a good number of scientific experts in various fields:

Special thanks go to Dr. A. Asenjo and Dr. M. Jaafar, from ICMM-CSIC, who started the Magnetic Force Microscopy investigations on my systems, which I later undertook in the context of a short stay in their laboratory. Thank you very much for your willingness to teach me how to use your equipment, your care in the investigation, and for all the discussions. Thanks also to O. Iglesias-Freire for his simulations on the behavior of the magnetic nanoislands.

I am also very grateful to Prof. M. Salmeron from LBNL in Berkeley, California, for having me in his group during a short 3 month stay, and for giving me full access to the equipment for Kelvin Probe Force Microscopy measurements. I am deeply indebted to Dr. A. J. Katan, who dedicated a great amount of his time teaching me how to be autonomous in the use of the equipment. I want to acknowledge his expertise, his detailed and rigorous explanations, and his disposition to answer my (many) questions.

The TEM experts in our group, Dr. P. Abellán, Dr. F. Sandiumenge, Dr. J. Gázquez, and F. Belarre are deeply acknowledged. Prof. J. Arbiol is acknowledged for his *Rhodius* simulations. Special thanks go to P. Abellán, for the time dedicated to my samples, her enthusiasm and know-how.

To Dr. S. Valencia, Dr. F. Kronast, and Dr. J. Herrero-Albillos, I would like to give thanks for the time I spent with them in BESSY II synchrotron, Berlin, making measurements on the manganite nanoislands. Thank you very much Sergio for your feedback concerning the preparation of the experiments and the data treatment and interpretation.

I also want to acknowledge Dr. J. A. Martín Gago, and the whole group of *Structure of Nanoscopic Systems* in ICMM-CSIC for having me during a short stay at their laboratories,

and for the time devoted to XPS and STM measurements of my samples. Special thanks go to Dr. L. Martínez who later undertook the measurements and the data treatment.

Thank you Dr. C. A. Ramos and Dr. R. Zysler from the Centro Atómico-Instituto Balseiro, in Bariloche, for the ferromagnetic resonance measurements, and thanks to Dr. C. Montón, from our group, who took the initiative and leaded these experiments.

I want to deeply thank Dr. M. Stengel for his fundamental contribution in the interpretation of the KPFM results and his enlightening explanations.

I want to thank Prof. A. Sánchez and Dr. C. Navau from the UAB for coming to the rescue in the understanding of the micromagnetic behavior of the LSMO nanoislands. I hope that their theoretical efforts will be fruitful and will shed light into the experimental evidence.

Prof. C. Ocal, M. Paradinas, and C. Munuera, thanks so much for your expert advices in the use of Scanning Probe Microscopies and for your help.

Dr. J. Santiso and Dr. X. Marti are also acknowledged for the efforts done in X-rays measurements on my difficult samples.

I would like to thank all the members, former and present, of the SUMAN group, for their help and support. I thank N. Romà for teaching me, when I arrived, how the laboratories worked, and both her and Dr. S. Ricart, for their willingness to answer my chemical doubts. To M. Gibert and C. Moreno, for their great support during our AFM experiments. To Dr. A. Palau for her transport measurements and for her readiness to try new experiments. A very special thanks go to A. Crespi for the time spent with my samples trying to get as much as we could from X-rays, as well as to N. Dix, whose expertise and creativity are awe-inspiring. Thanks to C. Montón for his patient explanations on how the SQUID worked, to R. Vlad for the cerium oxide buffer layer synthesis, to V. Rodríguez for the precursor solution preparation, to B. Bozzo, and A. Pérez and N. Alonso for the magnetometry and AFM measurements, respectively; special thanks go to M. Simón from the AFM laboratory for her reliability and patience.

A special mention goes for the group secretary, P. Alvarez, for her efficiency and organizational skills.

Thank you very much, Max, for your fine comments and suggestions, and for the time devoted to them. You made me realize there is always room for improvement, and, most importantly, you made me want to pursue it.

El apoyo moral que he recibido de tanta gente del ICMAB, miembros antiguos y presentes del grupo, podría llenar muchos párrafos. Mis compañeros de despacho, César, Patricia Ab., Anna Ll., y más tarde Jaume; ha sido un verdadero placer compartir despacho con vosotros, así como tantos momentos fuera del mismo. Neus, cómo puedo agradecer tu calidez y tu sentido común, en la acepción más pura de la palabra, que es tan poco común. Mariona C., voy a echar de menos las charlas contigo y tu empuje. Todo el tiempo compartido amb la Marta G., Roberto, Markos, Mariona de P., Josh, y con mi equipo de 'spinning'; muchísimas gracias Marta V., Anna P. y Patricia Al., por tantísimas risas.

No puedo olvidar a toda la gente de fuera de la ciencia, de Bilbao y de Barcelona, que me ha apoyado tantísimo, muchas gracias a todos. Los jueves de risas con las chicas; Mai e Isa, gracias por vuestra complicidad y apoyo incondicional, ha sido una suerte teneros cerca. And you too, Bene, a breath of fresh air and a flawless, solid support.

Y por supuesto, gracias a toda mi familia, siempre tan pendiente. Sois mi mayor fortaleza. Gracias Santi, gracias aita, gracias ama.

# Motivation

The boost of nanoscience and nanotechnology witnessed by this last decade has brought the discovery of new physical phenomena and the promise of a wide range of new devices and applications with real impact in fields such as medicine, industry, communications, or energy production and storage. On one hand, the downscaling of materials to nanometer sizes, while maintaining or even enhancing their performance, is imperative in the present context of, among others, energy efficiency and data storage: ultra-strong permanent magnets generated from nanosize features could, for instance, be used in lighter motors, while, the call for ultra-high density data recording can be met by effectively reducing the size of the magnetic bits. These examples belong to the field of nanomagnetism, which holds the promise to meet some of the many current worldwide scientific and technological challenges [1, 2]. The trend towards materials miniaturization is motivated, on the other hand, by the novel properties arising from geometries confined in the $10^{-7}$ m-$10^{-9}$ m length, which impose new relationships between the atomic and molecular constituents. Unraveling the behavior of these small building blocks, and, ultimately, predicting new phenomena, is the essential goal of nanoscience. Nanotechnology, in turn, aims at exploiting such phenomena in real applications, which demands mastering the fabrication of nanosize materials with tuned properties, and, furthermore, it requires to do so in a controlled way, scalable and cost effective, for a real social impact to be produced.

In the context of scalability and high-throughput required for application purposes, *bottom-up* fabrication approaches offer a great potential. They are based on the spontaneous gathering of atoms and molecules, under specific growth conditions, to form more complex architectures. Ranging from organic self-assembled monolayers and supramolecular arrangements, to self-assembled metal and semiconductor nanostructures, the fabrication of many functional materials relies on this principle of 'let nature do it' [3]. Moreover, self- assembly can yield narrow size distributions of highly uniform nanostructures. This is particularly desirable in heteroepitaxial semiconductor and oxide systems, where nanostructuring is classically attained by lithography-based techniques [4, 5]. Although highly precise, these *top-down* approaches, including optical lithography and the more recent X-ray, electron-beam or Focused Ion Beam lithographies, are typically serial procedures, with costly vacuum requirements, and, often, high energies that may damage the material. A step forward towards scalability and low cost within the bottom-up strategy for nanostructure fabrication is typified by solution-based methods, still scarcely explored but with demonstrated potential [6–9].

Among the large amount of materials and combinations of materials that can be manipulated, miniaturized, or assembled to form nanoscale entities with potential functionalities, metal oxides constitute a vast and interesting family, exhibiting a myriad of properties already in the bulk state. Ferroelectric, ferromagnetic, multiferroic or superconducting

are some of the behaviors found among the large variety of metal oxides, which range from rather simple binary oxides such as $Fe_3O_4$, $ZrO_2$, TiO or ZnO, to more complex materials like ternary perovskites or spinels ($SrTiO_3$, $La_{0.7}Sr_{0.3}MnO_3$, $BiFeO_3$, $CoFe_2O_4$...), and compounds like the high-critical temperature superconductors $YBa_2Cu_3O_7$ (YBCO) or $Bi_2Sr_2Ca_2Cu_3O_{10}$ (BSCCO). The downscaling of these oxides in the form of nanometric thin films, 3D nanodots and 1D nanowires, nanocomposites, or superlattices, has shown that new and fascinating phenomena may emerge [10–15]. This fact highlights the impact of lattice strains, surface to volume ratios, interfaces, and chemical and structural defects on the physical properties of nanoscale oxide systems.

The complex mixed-valence manganese oxides (manganites) $(RE_{1-x}AE_x)MnO_3$, with $RE$ a trivalent Rare-Earth ion and $AE$ a divalent Alkaline Earth ion, are paradigmatic examples of how the properties of a nanostructured oxide material may differ from those of its bulk compound. In the bulk state, manganites constitute one the most fascinating families within the complex oxides, where the interrelated electric, magnetic, and structural properties give rise to intriguing phenomena such as Colossal Magneto Resistance (CMR) [16, 17], and a high degree of spin polarization [18, 19]. These properties make them especially appealing for nanoscale applications in electron-spin based electronics (spintronics), among others [20, 21]. Regarding the influence of size decrease, it has been shown that thickness reduction down to a few nanometers of coherently strained lanthanum mixed-valence manganite thin films may decrease its Curie temperature [22–24] and suppress its characteristic metal-insulator transition [24–26]. The same compound was shown to change its easy magnetization axis, from in-plane to out-of-plane, in nanometer thick films subject to compressive strain, reflecting the competing shape and magnetoelastic anisotropy contributions in nanometric epitaxial systems [27–30].

In the present thesis we undertake the challenge of realizing and exploring different oxide heteroepitaxial systems with nanoscale $La_{0.7}Sr_{0.3}MnO_3$ (LSMO) mixed-valence manganite as the common ingredient, either in ultra-thin film or in 3D nanoisland configuration. We have optimized a solution-derived bottom-up approach, scalable and cost-effective, which will be demonstrated to yield room temperature ferromagnetic nanostructures. In particular, the election of the single crystal substrate onto which the LSMO is grown will determine whether the LSMO arranges into atomically flat films with thickness below $\sim$10 nm ($SrTiO_3$ (STO) and $LaAlO_3$ (LAO) substrates) or 3D self-assembled nanostructures with lateral sizes below the 200 nm (YSZ and MgO substrates). In addition to the effort done in controlling the growth of these ferromagnetic nanoscale systems, we have also explored them in depth, performing a comprehensive characterization of their morphology, crystallography, microstructure, and magnetic properties. In the specific case of self-assembled LSMO nanoislands we present a detailed investigation of their local magnetic and electrostatic properties by using advanced characterization tools. These techniques include Magnetic Force Microscopy, Photoemission electron microscopy, and Kelvin Probe Force Microscopy, all of them applied for the first time in nanometer-size LSMO features with the characteristics of the nanoislands shown in this work.

# Chapter 1

# Introduction

This brief introduction is intended to give a very general perspective on the applications, recent trends, and properties of nanoscale ferromagnetic systems, with emphasis in the components that, from an energetic point of view, will rule the magnetic domain structure at the nanoscale. We also shortly describe the general properties of mixed-valence lanthanum manganites, in particular $La_{1-x}Sr_xMnO_3$, in order to provide the reader with the general view of the physical phenomena that have made manganites one of the condensed matter physics hot topics of the last few decades. The chapters following this Introduction deal with largely different topics and techniques which will be there conveniently introduced. Because of the diversity of topics treated, an effort has been made to make each chapter self-consistent, although the report in the actual form follows a logical thread. A guide through the contents of the thesis is given at the end of this Introduction.

## 1.1 General trends in ferromagnetic nanostructures

The vast range of **applications** of nanoscale magnets covers disciplines as diverse as biomedicine, energy conservation, or the broad field of information technology and communications. In the diagnosis of diseases (e.g. magnetic biosensors), in therapeutic applications (nanomagnets for drug delivery), or in the quest for ultra-strong permanent magnets, the common ingredient appears in the form of nanometer size magnetic nanoparticles and nanoparticle ensembles [1, 31]. In the context of communication technologies, magnetic nanoscale materials offer a great potential for non-volatile magnetic random access memories (MRAMs), the building blocks of instant boot-up computers. MRAMs are based on magnetic tunnel junctions of magnetoresistive materials integrated in silicon-based microelectronics, and, contrary to charge-based RAMs, they maintain the stored information after the power is switched off [32]. Our information-based society also requires enhanced data storage capabilities. Going beyond the recently reached $1Tb/in^2$ density has prompted the size reduction and the nanometer resolution positioning of the magnetic bits. Magnetic storage devices are commonly based on *longitudinal recording systems*, where the bits consist of a number of in-plane magnetized grains ($\sim$10 nm diameter) within a Co-alloy granular medium such as CoCrPtB [33, 34]. However, the reduction of the nanoparticle size finds its limit the moment thermal fluctuations spontaneously reverse the grain magnetization (i.e. when $k_BT \gtrsim KV$), where $k_B$ is the Boltzmann constant, $T$ is the temperature,

$K$ is the anisotropy constant, and $V$ is the particle volume. At this so-called 'superparamagnetic limit', therefore, the stored information is thermally unstable and the device no longer fulfills its function [35]. *Perpendicular recording* is one of the current strategies for increasing the storage capacity while avoiding the superparamagnetic limit: the recording medium now exhibits out-of-plane anisotropy and the bits are stored perpendicular to the film surface. This configuration allows for thicker bits more closely packed to each other [33, 34]. Beyond these two approaches, recent advances head towards magnetic recording based on *lithographically patterned* or *self-organized individual magnetic nanoparticles*, where each nano-object equals one bit of information. Effective nanofabrication approaches are thus crucial for the control of nanomagnet size, shape, and positioning [33, 34].

The technological impact of size miniaturization in magnetic materials is intimately related to the **new and interesting phenomena** that arise when the size of magnetic materials approaches that of characteristic magnetic lengths (e.g. the ferromagnetic (FM) exchange length or the domain wall width of materials, both in the nanometer range). The magnetic configuration of nanosize objects greatly depends on their geometric restrictions, i.e. on their shape (including geometry and aspect-ratio) and size. In isotropic FM systems subject to no strain fields, the general picture is that of competing exchange energy and magnetostatic energy terms, which attempt to reach their corresponding minima in opposite ways: the minimum exchange energy is attained by parallel aligned spins, in a single domain or giant spin configuration. Meanwhile, the magnetostatic term seeks to minimize the magnetic energy within the free space surrounding the object, causing the single domain to divide into multiple domains [36]. The distance where the atomic exchange interactions prevail over the magnetostatic fields is given by the exchange length $l_{ex} = \sqrt{\frac{A}{\mu_0 M_S^2}}$, with $A$ the exchange stiffness constant of the material, $M_S$ its saturation magnetization value, and $\mu_0$ the vacuum permeability. For iron and cobalt, for instance, $l_{ex}$ takes the values $l_{ex}$(Fe)=1.5 nm and $l_{ex}$(Co)=2 nm, respectively. On the other hand, the existence of a domain wall within the nanomagnet depends on both the energy required to form such wall, as calculated from the global energy balance, and on the domain wall thickness $\delta$. The former gives a minimum size at which the presence of the domain wall is favorable, known as the *critical single domain radius*, $R_{SD}$, while the latter reflects the competition between the exchange energy (favoring wide walls) and the anisotropy energy (favoring narrow walls), i.e. $\delta \propto \sqrt{\frac{A}{K}}$, with $K$ the anisotropy constant of the material. Interestingly, while the $R_{SD}$ for a spherical Fe single crystal is $R_{SD}$=6 nm, the domain wall thickness is close to an order of magnitude higher, $\delta$=40 nm. From here it follows that Fe spherical particles below 40 nm won't exhibit multidomain structure, despite being well above the $R_{SD}$ value. However, this fact does not imply the nano-object to exhibit a uniform magnetization. Indeed, in between the tendency of small objects to exhibit single domain configuration and of larger particles to split into domains, there may exist, for nanostructures of particular geometries and aspect-ratios, an intermediate ground state known as the vortex state [37–39]. The vortex configuration appears when the reduction of the size below the submicron range forces complex multidomain structures into a magnetic flux closure state, rather than into a uniform magnetization state.

Recent **advances in characterization techniques** have greatly improved our understanding of nanoscale magnetic structures. In addition to 'averaging' macroscopic techniques like superconducting quantum interference device (SQUID), ferromagnetic resonance (FMR), or magneto-optical Kerr effect (MOKE), local techniques with sub-micron resolution are essential in order to gain insight into the physical phenomena taking place

within the nanostructures. The progress in Scanning Probe Microscopies such as Magnetic Force and Spin-polarized scanning tunneling microscopies (MFM and SP-STM) [40–42], as well as the enhanced spatial resolutions of synchrotron radiation sources making use of X-ray magnetic circular dichroism (XMCD) have allowed, among other achievements, the observation of the magnetic vortex core [10, 43], and have made its internal structure accessible [44–46]. The magnetic vortex configuration displays a continuous variation of the magnetization direction in the plane of the dot (which reduces the magnetostatic energy) and an out-of-plane perpendicular magnetization in the core [38, 47]. In fact, the vortex core has become an appealing memory unit candidate for data storage [48, 49]. Also, recently, various types of emerging devices such as microwave oscillators [50, 51] and amplifiers [52, 53] based on the properties of magnetic vortices were proposed.

The vast majority of the work done up to date in the context of ferromagnetic nanosize objects, however, has focused on nanostructures of simple ferromagnetic metals. Both experimental and theoretical investigations have thus aimed at understanding the behavior of nanomagnets made out of iron, permalloy ($Fe_{20}Ni_{80}$), cobalt, nickel, or their alloys, and, most commonly, in polycrystalline form. In their review of 2003, Martín and co-workers gather substantial bibliography on the fabrication and properties of magnetic metal nanostructures based on the above soft ferromagnets [54]. Nevertheless, the models valid for these materials, based mainly on the above picture of competing exchange and magnetostatic energies, are insufficient for the case of strained materials featuring single crystal or preferential textures, i.e. the case precisely inherent to epitaxially grown materials. This new context requires taking into account the magnetoelastic and magnetocrystalline anisotropy terms, with the corresponding added complexity.

Certainly, magnetoelastic and magnetocrystalline anisotropies, together with the exchange and magnetostatic contributions mentioned before, also decide on the magnetization processes of bulk materials. The fundamental difference is that, within confined geometries, their individual and collective influences are subject to new boundary conditions and, consequently, they give rise to novel effects. One example of the key role of anisotropies in the nanometer length concerns spin-reorientation transitions (SRT) in monolayer-thick Fe and Co films grown on Ag, Cu and Au. Theoretical and experimental studies have shown that a strong perpendicular surface anisotropy pulls the spins of the FM layer out of the film plane, overcoming the large demagnetizing field. The latter, however, pulls the magnetization back in-plane when the film thickness exceeds a certain limit, in the few monolayers range [55–58]. The geometric shape of 3D nanoparticles, whether triangular, square, circular...etc., is also a crucial parameter which gives rise to new anisotropies. For instance, the fact that only ellipsoids have uniform demagnetizing fields results in inhomogeneous magnetizations within nano-objects with sharp edges (like squares, rectangles, triangles...). Such *configurational anisotropy*, as named by Cowburn and co-workers, produces diverse magnetization patterns that slightly deviate from uniform magnetizations [59–61].

Although less studied, the striking properties of complex oxides such as the ferromagnetic mixed-valence lanthanum manganites make them especially appealing in a nanotructured configuration, as they are strong candidates for the aforementioned technological applications in magnetic sensors, data storage, and spin-based devices. In the next section we will briefly review the main properties of the strontium-doped lanthanum manganites. The multicomponent character of these oxides, in addition to the high sensitivity of their properties to the precise stoichiometry (chemical doping, oxygen content), make them of-

ten challenging to process from a materials point of view, especially in the sub-micrometer length. The last decades' advances in the field of heteroepitaxial growth permits nowadays optimal control of stoichiometries and crystalline quality of oxide thin films. A considerable amount of work thus exists concerning colossal magneto-resistive manganite thin-films [22, 25, 29, 62–65]. We will have the opportunity to go through some of this work when discussing the ultra-thin manganite films in Chapter 3. Conversely, the studies devoted to nanoislands and nanowires are much more scarce [66, 67], if not practically non-existent, as it is the case of the bottom-up fabrication approach followed in this thesis. As most transition metal oxides, these materials are notably harder than the classic metal ferromagnets and they are also chemically stable, which makes them especially challenging to process by wet and dry etching procedures [68, 69].

## 1.2 Main properties of mixed-valence manganites

Mixed-valence manganese oxides with a perovskite structure, which we shall in the following simply call *manganites*, are given by the general formula $A_{1-x}B_xMnO_3$; here $A$ is a trivalent rare earth cation (La, Nd, Pr...) or bismuth, and $B$ is a divalent alkaline earth cation (Ca, Sr, Ba...) or Pb. Manganites belong to the family of strongly correlated materials, in which diverse and complex phenomena arise from the subtle balance of many competing effects [70]. These competing mechanisms typically concern charge, orbit, spin, and lattice degrees of freedom, which, in turn, are governed by the electron-electron and electron-lattice interactions taking place in these compounds.

The field of manganites has been one of the most active within condensed-matter physics in the last few decades, and therefore the amount of literature concerning their growth, properties, and fundamental physics is vast. Here we attempt to give a very brief and general overview of the fundamental properties of manganites, with particular emphasis in the strontium-doped lanthanum manganite $La_{1-x}Sr_xMnO_3$, the relevant compound for this thesis. For a more in-depth treatment the reader is directed to the many excellent reviews that comprehensively cover the state of the art in the field [17, 68, 71–74].

#### Main features of manganites: colossal magnetoresistance and half metallicity

The striking discovery of a simultaneous ferromagnetic and metallic behavior in the mixed compounds $LaMnO_3$- $BMnO_3$, with $B$=Ca, Sr and Ba, by Jonker and Van Santen, dates back to 1950 [75]. Such a behavior was soon explained in the context of the Double Exchange Model (DE) by Zener [76], Anderson and Hasegawa [77], and de Gennes [78]. A renewed interest in manganites, however, arose decades later, in the 1990s, with the discovery that the application of a magnetic field induces a large change in the electrical resistance of $La_{0.67}Ca_{0.33}MnO_3$ thin films, in the vicinity of their Curie temperature $T_C$ [79]. Furthermore, this effect is accompanied by an intriguing metal-insulator transition occurring at $T_C$. Such negative magnetoresistance (MR) (the resistance decreases with the applied field) is three orders of magnitude larger than the Giant magnetoresistance (GMR) characteristic of multilayer and granular metals. For this reason this new effect became known as Colossal magnetoresistance (CMR). The GMR effect is based on the spin-dependent tunneling of electrons from one ferromagnet to another across a thin insulating barrier (e.g. two ferromagnetic grains separated by a grain boundary) [20, 80]. This tunneling can occur at low

fields ($\lesssim$0.1 T) and is largest when the alignment of ferromagnetic (FM) domains is parallel. It also increases with decreasing temperature and particle size [81]. Conversely, the CMR effect occurs in perfect manganite single-crystals, requires rather large fields, and is maximum at $T_C$, i.e. at the metal-insulator transition. Fig. 1.1 shows the temperature-dependent resistivity of a $La_{1-x}Sr_xMnO_3$ crystal ($x$=0.175) for different applied fields. The magnitude of the magnetoresistance is given by the expression $\Delta\omega/\omega=[\omega(H=0)-\omega(H=0)]\ \omega(H=0)$ (in $\%$). Open circles in Fig. 1.1 correspond to the negative MR for the case of $H$=15 T [82]. CMR is a phenomenon intrinsic to manganites, and the physics behind have raised, and still do, many fundamental questions [71]. On the other hand, the exploitation of these large resistance changes opens a wide range of technological opportunities in spin-based electronics.

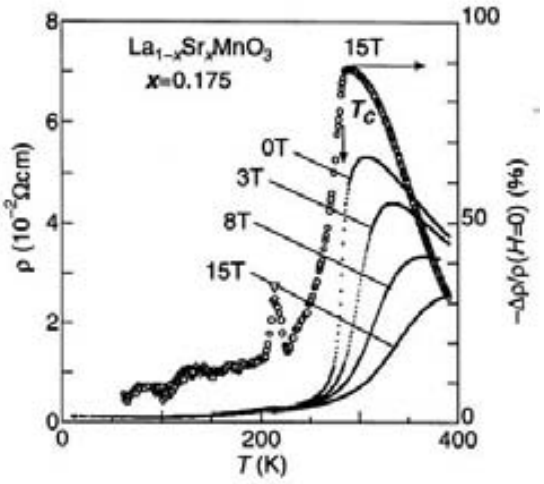


**Fig. 1.1:** *Temperature dependent resistivity of a $La_{1-x}Sr_xMnO_3$ (x=0.175) crystal for different applied magnetic fields. The curves show a metallic character ($d\rho/dT>0$) below $T_C$ and an insulator ($d\rho/dT<0$) behavior above $T_C$. The negative magnetoresistance -$\Delta\rho/\rho$ (in $\%$) for a 15 T applied field is given with open circles. Reproduced from [82].*

Another essential characteristic of manganites is their high degree of spin polarization. Together with some exotic compounds like Mn-based Heusler alloys [83] or chromium (IV) oxide [84], manganites are among the few compounds that exhibit half-metallic character, as first demonstrated by Park and co-workers [18]. In particular, while in most ferromagnetic metals (like Fe or Ni) both up and down spin sub-bands are partially occupied, in manganites the Fermi Energy level $E_F$ falls into the gap of one of the sub-bands (see Fig. 1.2). As a consequence, the spin polarization, given by the imbalance of up and down spin-dependent density of states $n$ at the Fermi level, $P=(n\ -n\ )\ (n\ +n\ )$, is in principle equal to one in half metals. Polarization values of $\sim$30-50$\%$ have been measured for Fe, Ni, Co, and their alloys [85], while reaching the ideal value of $\sim$100$\%$ for the case of $La_{0.7}Sr_{0.3}MnO_3$ [18]. This result is directly related to the predominant $d$-orbital character at the Fermi level characteristic of transition metal oxides, which enhances the on-site exchange interaction. The half metallicity makes manganites especially appealing for spin-based devices like magnetic tunnel juntions [86–88].

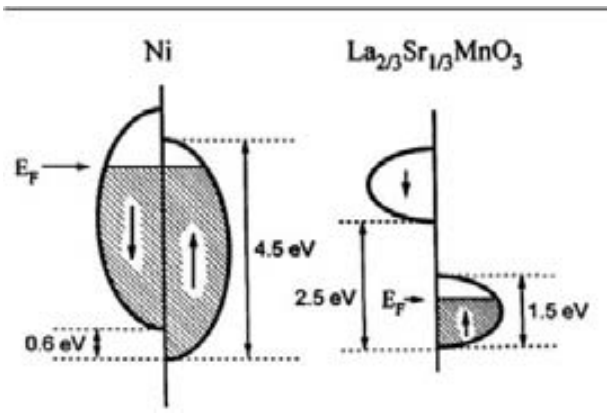


**Fig. 1.2:** *Sketch comparing the energy bands of a ferromagnetic metal (Ni) and of a fully polarized ferromagnetic half metal ($La_{1-x}Sr_xMnO_3$ with x=1/3). Reproduced from [81].*

### Crystal structure of perovskite manganites

Despite exhibiting phenomena such as CMR and half-metallicity, the building blocks of these complex oxides are remarkably simple. Fig. 1.3 illustrates the perovskite unit-cell, $ABO_3$, where $A$ is the trivalent La ion or the divalent Sr ion, in a ratio determined by the doping $x$, $B$ is the manganese ion, with average valence $3+x$, and $O$ is the oxygen anion. Manganese ions sit at the centers of oxygen octahedra, in a 6-fold coordination. Although the ideal perovskite holds a $Pm\bar{3}m$ cubic symmetry, many of the compounds with the perovskite-type structure show lower symmetries. This is the case of manganites, which generally adopt either rhombohedral or orthorhombic structures. For $La_{0.7}Sr_{0.3}MnO_3$ it is a common procedure, both in magnetic and structural studies, to describe its rhombohedral $R\bar{3}c$ structure in terms of the pseudo-cubic notation, which greatly simplifies the indexing and treatment of the structure [17, 22, 89, 90]. In such pseudo-cubic notation $La_{0.7}Sr_{0.3}MnO_3$ exhibits a lattice parameter $a$∼3.873 Å and an angle ∼90.26° [64], which implies a very slight deviation from a perfect cube. We will use this notation throughout the whole report.

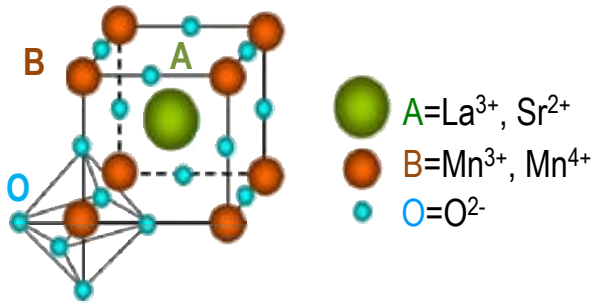


**Fig. 1.3:** *Unit cell of the LSMO perovskite structure.*

The tendency to distort from the ideal cubic perovskite may be understood via the relationship between the ionic radii of its constituents. According to Goldschmidt [91], we can define the *tolerance factor* $f$:

$$f = \frac{(R_A + R_O)}{\bar{2}(R_B + R_O)} \tag{1.1}$$

where $R_A$ and $R_B$ are the ionic radii of $A$ and $B$, respectively, and $R_O$ is the ionic radius of oxygen in an idealized model of rigid spheres. For an undistorted cubic perovskite structure, $f$ takes a value close to the unity, whereas materials where $f$ deviates from 1 tend to adopt lower symmetries. In most stable perovskites $f$ ranges from $\sim$0.8 to 1.1. The average cation radius $R_A$ critically influences the tilting and rotations of the oxygen octahedra, with a consequent impact on the Mn-O-Mn bond angle. Such bond angle, in turn, will determine the transport and magnetic properties of the manganite, as we shall mention later.

### Electronic structure of manganites

The crystal field due to the octahedral oxygen cage surrounding the Mn ion partially lifts the degeneracy of the $3d$ Mn multiplet, splitting it into a triply-degenerate $t_{2g}$ level and a doubly-degenerate higher energy $e_g$ state. Fig. 1.4 shows the schematic diagram of the energy levels of Mn, and how the electrons fill the levels in $Mn^{3+}$ ($3d^4$ configuration). A spontaneous distortion of the octahedron (elongation or compression along the axial direction), known as the Jahn-Teller (J-T) distortion, further lifts the degeneracy of the $t_{2g}$ and $e_g$ levels in the $Mn^{3+}$ (see Fig. 1.4). This phenomenon, of electronic origin, does not occur in the $Mn^{4+}$, where the $e_g$ level is empty. The alignment of the electrons is always parallel, following Hund's rules, and gives a total spin state $S$=2 and $S$=3/2 for $Mn^{3+}$ and $Mn^{4+}$, respectively. The lower energy $t_{2g}$ electrons, less hybridized with the oxygen $2p$ orbitals, are localized even in the metallic state of manganites. Conversely, the $e_g$ electrons can be itinerant, and are responsible for electric conduction when there are empty $e_g$ states available in the crystal. Those 'empty states' are achieved by hole-doping the parent compound ($LaMnO_3$, for instance, in the case of $La_{1-x}Sr_xMnO_3$): the substitution of the trivalent La by the divalent alkaline earth produces $Mn^{4+}$ ions with empty $e_g$ states. When there is no such hole-doping, strong correlation effects tend to localize the $e_g$ electrons, which is the reason why $LaMnO_3$ is an insulator.

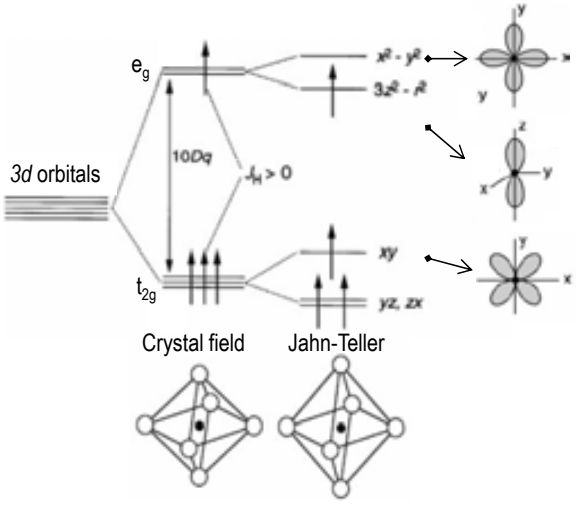


**Fig. 1.4:** *3d atomic levels of the Mn ion. The octahedral crystal field splits the five-fold 3d degeneracy into a triply-degenerate $t_{2g}$ low energy and a doubly-degenerate $e_g$ high energy level. For the case of $Mn^{3+}$, the spontaneous distortion of the octahedra (plotted in the form of an axial elongation) further lifts the degeneracy and stabilizes its electronic configuration. Adapted from [17].*

The reason why ferromagnetism and metallic behavior go hand in hand in these compounds is based on the electronic features outlined above, i.e. in the large exchange energy (large $J_H$∼2-3 eV) [17] or large on-site Hund coupling between the Mn $3d$ electrons. The *Double Exchange* (DE) mechanism consists in the jump of one $e_g$ electron to a neighboring empty $e_g$ state, mediated by the oxygen in between. In particular, the electron leaving $Mn^{3+}$ jumps to the oxygen orbital while the electron in the oxygen with the parallel spin simultaneously jumps to the $Mn^{4+}$ (see Fig. 1.5). In the strong coupling limit (i.e. $J_H$ is much greater than the intersite hopping interaction $t_{ij}^0$) the effective hopping interaction $t_{ij}$ depends on the relative orientation $\theta_{ij}$ of the spins of the neighbor $i$ and $j$ atoms in the following way [77]: $t_{ij} = t_{ij}^0 \cos\theta_{ij}$. Thus, the electron itineracy is largest when spins are

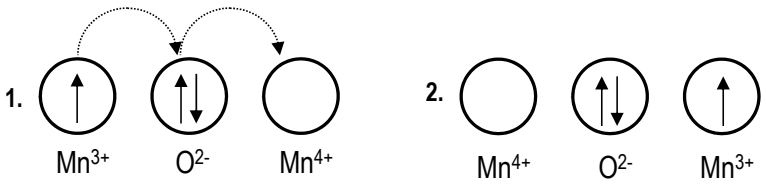


**Fig. 1.5:** *Double exchange model. Adapted from [71].*

parallel (ferromagnetic configuration), and zero if they are anti-parallel.

### Complexity in manganite systems

Although intuitive and useful, the DE model briefly outlined above is insufficient to explain all the phenomena shown by manganites, like, for instance, the particularities of the insulator state above $T_C$ [17]. In general, the more weight the insulating states acquire in the manganite, the greater the limitations of the DE model [71]. Other interactions like the electron-lattice interactions (such as collective Jahn-Teller distortions), charge/orbital ordering, or the antiferromagnetic superexchange, are all crucial for the understanding of the physics of manganites. Indeed, these interactions and their mutual competition are responsible for the rich phase diagrams characteristic of these compounds.

The fundamental parameters that characterize correlated systems like manganites are the electron hopping amplitude $t$ (or one-electron bandwidth $w$) and the band-filling $n$ (the density of carriers). Both parameters are changed in manganites by acting upon the chemistry of the compound: the change in the average cation radius leads to a change in the Mn-O-Mn bond angle of the perovskite structure (a change in the degree of lattice distortion), which affects the hopping amplitude of the itinerant electrons. On the other hand, by changing the doping $x$ we vary the band filling $n$ ($n = 1 - x$). Therefore, the greater the divalent ion doping, the more holes we are injecting into the structure. Fig. 1.6 shows the phase diagram of $La_{1-x}Sr_xMnO_3$, the prototypical large bandwidth manganite, where the DE model works best. It shows a stable ferromagnetic-metallic state, ranging from Sr dopings between $x$∼0.2 to $x$∼0.45, with a high $T_C$, maximum (∼360 K) for $x$=0.3. Decreasing the cation radius, by, for instance, doping the $LaMnO_3$ parent compound with Ca instead of with Sr, the Mn-O-Mn bond angle changes in a way that reduces the hopping amplitude. Upon bandwidth reduction, charge and orbital-ordered insulating phases become more dominant. Indeed, for further smaller cationic radius as in $Pr_{1-x}Ca_xMnO_3$, represen-

tative of 'small' bandwidth manganite*, there exists no stable ferromagnetic-metallic state at zero applied field [see Fig. 1.6 (b)].

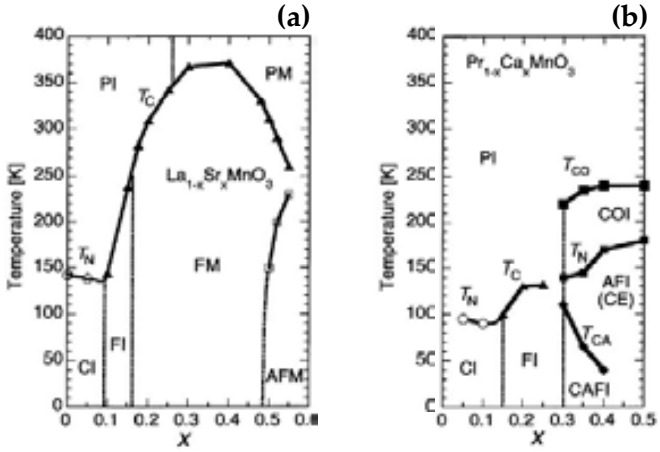


**Fig. 1.6:** *Magnetic and electronic phase diagrams for (a) $La_{1-x}Sr_xMnO_3$ and (b) $Pr_{1-x}Ca_xMnO_3$. FM, PM, PI, FI, CI, and AFM stand for ferromagnetic metallic, paramagnetic metallic, paramagnetic insulating, ferromagnetic insulating, spin-canted insulating and antiferromagnetic (A-type) metallic, respectively. In the $Pr_{1-x}Ca_xMnO_3$ phase diagram, COI denotes charge-ordered insulating state, and AFI (CE) and CAFI are an antiferromagnetic and canted antiferromagnetic insulating states, respectively, within the more general COI charge-ordered state. $T_C$ and $T_N$ are the Curie and Néel temperatures, respectively. Reproduced from [17].*

## 1.3 Outline of the thesis

Manganites exhibit a large number of interesting physical phenomena due to their interrelated structural, electronic, and magnetic properties. A flavor of this complexity was given in the above brief overview. The present thesis deals with the synthesis and characterization of chemically-derived nanoscale $La_{0.7}Sr_{0.3}MnO_3$ (LSMO) systems grown onto different single crystal substrates. The understanding of how the physics of correlated electron systems works in such nanoscale heteroepitaxys is thus beyond the scope of the present thesis, and, hence, left for future studies. We here set the basis for the fabrication of ultrathin films and 3D self-assembled nanoislands of ferromagnetic LSMO, using a scalable and versatile bottom-up approach, and provide a comprehensive characterization of the synthesized systems by means of both macroscopic and nanoscale experimental techniques. The manuscript is organized as follows:

*Chapter 2* presents the experimental procedure followed to grow the nanoscale LSMO heteroepitaxys object of this work. We give an overview of the different oxide substrate materials we have used, and we discuss the effect of heat treatments on the surface conditioning of these substrates. The necessary steps for the growth of nanoscale LSMO onto such substrates, by means of the chemical solution deposition method (CSD), are also described.

*Note that the average cation radii are <r>$_{(La,Sr)}$~1.4 Å and <r>$_{(Pr,Ca)}$~1.32 Å for $La_{1-x}Sr_xMnO_3$ and $Pr_{1-x}Ca_xMnO_3$, respectively [71].

The results of applying the procedure previously explained in Chapter 2 are extensively analyzed in *Chapter 3*. We show how the same methodology gives two distinct system configurations depending on the substrate underneath: ultra-thin LSMO films, below 10 nm thick, grow on top of perovskite-type $SrTiO_3$ and $LaAlO_3$ substrates, and are discussed in Part I. In contrast, LSMO arranges into a homogeneous dispersion of self-assembled LSMO nanoislands when grown onto fluorite-type and rocksalt-type structures, as shown in Part II. For each case we have accomplished the study of the system morphology, its crystal orientation and epitaxy, its microstructure, and the macroscopic magnetic and transport properties. Our results highlight the capability of this solution approach to generate epitaxial ultra-thin films and sub-200 nm lateral size nanostructures with Curie temperatures around $\sim$350 K.

Given the interest of nanoscale 3D structures, highlighted in this Introduction, and considering the scarce studies regarding 3D manganite nanostructures, we have devoted *Chapter 4* and *Chapter 5* to the local analysis of self-assembled ferromagnetic LSMO nanoislands grown on fluorite-type insulating substrates.

*Chapter 4* describes the magnetic force microscopy (MFM) investigation of the aforementioned system. We first discuss the experimental concerns linked to measuring fairly small (sub-200 nm wide) LSMO nanoislands, and we describe the optimization of the magnetic signal by choosing the adequate magnetic tip. Subsequently, we focus on the study of the variety of magnetic structures displayed by nanoislands, among which we identify the geometric parameters that promote the vortex state in these LSMO nanostructures. The effect on the magnetic nanoislands of an external in-plane magnetic field is also discussed.

Two advanced characterization techniques, novel in their application to a system of these characteristics, are used in *Chapter 5* to further investigate the local properties of the LSMO nanoislands. The first part of the chapter concerns a local chemical and magnetic study of the nanoislands using photoemission electron microscopy (PEEM) at synchtrotron facilities. We discuss the crucial role of the metal capping of the insulating substrates and explain the results that give simultaneous access to the nanoisland surface and bulk chemistry. We also describe the results and limitations of the X-ray magnetic circular dichroism experiments on our system of self-assembled LSMO nanoislands. The second part changes the topic to the electrostatic properties of the LSMO nanoislands, addressed by means of Kelvin Probe Force microscopy (KPFM). Here again, the insulating character of the substrate adds complexity to the experiment as well as to the interpretation of the results. We demonstrate that KPFM is sensitive to a change in contrast between different LSMO crystallographic planes. We argue that this contrast variation is directly related to a difference in the work function between those planes.

The main conclusions of the work are collected in the *General Conclusions*. An appendix at the end of the manuscript gathers the main specifications on the techniques used to characterize the samples. MFM, PEEM, and KPFM are not included there, since they are introduced in the corresponding chapters.

# Chapter 2

# Experimental procedure

This chapter describes the substrate materials and the methodology followed to generate the $La_{0.7}Sr_{0.3}MnO_3$ (LSMO) heteroepitaxial systems that are the object of this thesis. Far from being passive components that only provide mechanical support, oxide substrates play a key role in heteroepitaxial growth, especially at the nanoscale, where interfacial effects are important. We will first review their main crystallographic properties and then describe the protocols that we followed to treat their surfaces. The growth of nanostructured manganite oxides through the chemical solution deposition (CSD) route will be described afterwards. We will briefly present the growth procedure, postponing the detailed analysis and discussion of the results to Chapter 3.

## 2.1 Single crystal oxide substrates

Single crystal oxide substrates are one of the two ingredients that constitute the heteroepitaxial systems described in this thesis. Nucleation and growth of the oxide nanostructures is determined by the presence of the solid oxide substrate underneath and hence, its crystal structure and surface properties are crucially important. Oxide substrates are widely used for the heteroepitaxial growth of high temperature cuprate superconductors, multiferroic and magnetoresistive thin films (for a review on these topics see [92, 93] and references therein). The relevance of the substrates in relation with the grown species, is, in fact, one of the main points of this thesis as it will become evident throughout the manuscript. We have used four different oxide substrates, perovskite-type $LaAlO_3$ (LAO) and $SrTiO_3$ (STO), rock-salt structure MgO, and the fluorite-type yttria-stabilized zirconia ($Y_2O_3$:$ZrO_2$). This section is intended to give a general overview on such materials.

### 2.1.1 Perovskite-type substrates: $SrTiO_3$ and $LaAlO_3$

The perovskite structure was already introduced in the previous chapter, as it constitutes the building blocks of the manganites described in there. However, this structure is far from restricted to complex manganese oxides. Many inorganic crystalline solids adopt the $ABX_3$ perovskite structure, with two inequivalent A and B metal cations and X an anion that bonds to both. In particular, oxide perovskites, with $ABO_3$ general formula, in addition

to colossal magnetoresistance, can also exhibit superconductivity [94] and ferroelectricity [95]. In the ideal cubic perovskite, the larger A cation has 12-fold coordination to oxygen, while the smaller B cation sits at the centers of the octahedra formed by oxygens, in a 6-fold coordination (see Fig. 2.1). The structure may be also visualized as an alternate sequence of A-O and B-$O_2$ planes [Fig. 2.1(c)], stacked along each of its three orthogonal axes. The crystallographic parameters of the cubic ideal perovskite are written in Tab. 2.1. As we mentioned in Chapter 1, many of the compounds with the perovskite-type structure do not adopt cubic symmetry at room temperature. Instead, they commonly suffer cation displacements and tilting of the oxygen octahedra that give rise to lower symmetry structures such as tetragonal (e.g. $BaTiO_3$[96]), orthorrombic (e.g. the original Perovskite mineral $CaTiO_3$[97]) or rhombohedral (e.g. $LaAlO_3$[98]). The degree of deviation from the ideal cubic perovskite is quantified by the tolerance factor, the unity being the value of the undistorted cubic perovskite structure such as $SrTiO_3$ (STO). The value for $LaAlO_3$ (LAO) is $\sim$1.02.

| Space Group | Atom | Wyckoff Pos. | (x y z) coordinates |
|---|---|---|---|
| $Pm3m$ | A cation | 1b | $(\frac{1}{2}\ \frac{1}{2}\ \frac{1}{2})$ |
| | B cation | 1a | $(0\ \ 0\ \ 0)$ |
| | O anion | 3d | $(\frac{1}{2}\ \ 0\ \ 0)$ |

**Tab. 2.1:** *Crystallographic parameters of the ideal cubic perovskite structure.*

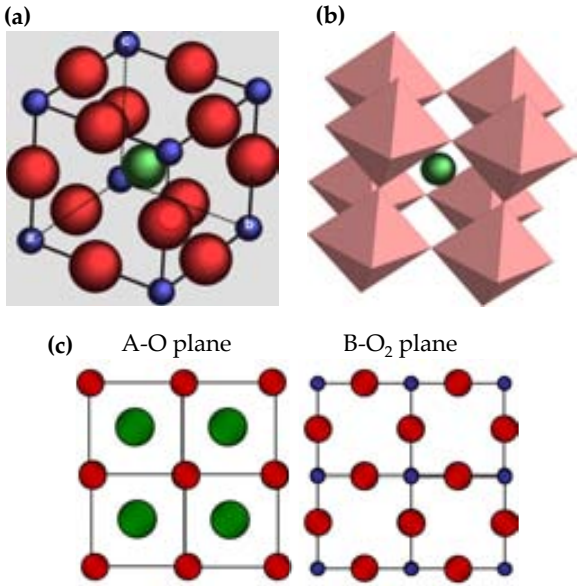


**Fig. 2.1:** *(a) 3D view of the ideal cubic perovskite unit cell with the A cation (green) at the center, B (blue) at the corners, and the oxygens (red) at half the edge length. (b) View of the perovskite illustrating the oxygen octahedra. In the idealized structure they remain untilted. (c) Top-view of the A-O and B-$O_2$ planes.*

### $SrTiO_3$

The ideal cubic perovskite structure (space group $Pm\bar{3}m$) is the one adopted by $SrTiO_3$ (STO) (read *strontium titanate*) at room temperature. At around 110 K, however, it undergoes an antiferrodistortive phase transition to a tetragonal phase (space group $I4\ mcm$) [99, 100], which is caused by the antiphase tilting of the oxygen octahedra. STO is widely used as substrate for the epitaxial growth of high $T_c$ superconducting layers and other functional perovskite oxides like the magnetoresistive manganite. This is mainly due to the low lattice mismatch between STO and these isostructural materials.

The STO substrates used in this work are 5 mm x 5 mm x 0.5 mm single crystals commercially available from Crystec. They are one side polished, have a nominal (001) orientation, and a lattice parameter $a_{STO} = 3\ 905$ Å given by the supplier. We measured the out-of-plane lattice parameter by X-Ray diffraction $\theta$-$2\theta$ scans (see Appendix A), which gave $a_{STO} = 3\ 90(7)$ Å, in good agreement with the value of the supplier and also with reported values in the literature [101].

### $LaAlO_3$

*Lanthanum aluminate*, $LaAlO_3$ (LAO), displays a cubic ideal perovskite structure at high temperatures, but undergoes a well established second order phase transition to the rhombohedral $R\bar{3}c$ structure close to 800 K, with parameters $a = b = c = 5\ 3547(3)$ Å and $\alpha = \beta = \gamma = 60\ 113(4)°$ [98, 102–104]. More conveniently, this rhombohedral distorsion is described in terms of the pseudocubic cell with $a_{LAO} = 3\ 79$ Å and $\alpha = 90\ 096°$ [104]. As in most phase transitions to lower symmetry structures, the cubic to rhombohedral transition is accompanied by twin plane formation, which relieves the strain caused by the lattice distorsion. {110} and {100} twin planes have been both reported, although the latter is more frequently observed [105, 106]. Such twin domains can be seen with optical microscopy and scanning probe techniques [Fig. 2.2 (a) and (b)]; sometimes even with the naked eye. A thorough description of twinning in LAO is given in the work by Bueble and co-workers [104]: a surface cooled through its transition temperature $T_C$ (∼800 K) down to room temperature, exhibits a *sawtooth* morphology, characteristic of the presence of such twin domains and caused by the relaxation of the macroscopic stress. Afterwards, this crystal is cut and polished into a flat surface. Under a subsequent annealing at $T>T_C$ the structure reorganizes and the footprints of the twinning emerge. When cooled down again at $T<T_C$, the phase transition triggers a new twinning so that the final surface topography is an superposition of footprints of previous domains and actual domains [Fig. 2.2 (c)].

The LAO substrates used in the present work are 5 mm x 5 mm x 0.5 mm single crystals commercially available from Crystec. They are one side polished, have a nominal (001) orientation and a given lattice parameter $a_{LAO} = 3\ 821$ Å. Literature values are closer to $a_{LAO} = 3\ 789$ Å [102, 104], in agreement with our X-Ray Diffraction measurements ($a_{LAO} = 3\ 79(2)$ Å ).

## 2.1.2 Rocksalt-type substrates: MgO

Oxides with rocksalt structure (also called NaCl-type structure) are among the most widely studied oxides. They are simple insulators that can be described in terms of mixed ionocovalent bonds, as opposed to complex oxides with strongly correlated electrons. *Mag-*

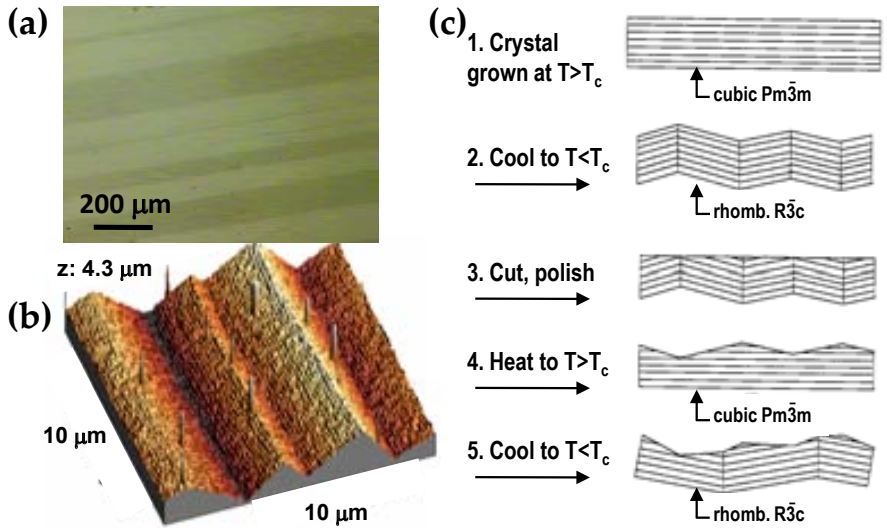


**Fig. 2.2:** *(a) Optical micrograph of a LAO substrate showing distinct contrast due to twin domains. (b) Atomic force microscopy 3D image of the characteristic sawtooth surface corrugation caused by twinning. (c) Schematic illustration of the process leading to overlaid twin domain 'footprints' and actual twin domains caused by consecutive cooling and annealing. Adapted from [104].*

*nesium Oxide* (MgO) is the paradigmatic example of this materials class and there are extensive literature studies concerning its structural and electronic properties from diverse theoretical perspectives [107–109]. MgO is used as support for metal catalysts [110] and also as substrate for high $T_C$ superconductor films where its low dielectric constant makes it suitable for high-frequency applications [111, 112].

Rocksalt structure may be described as two interpenetrated facecentered-cubic (FCC) lattices of opposite charge. It contains one formula unit per primitive cell and belongs to the $Fm3m$ spatial group. Fig. 2.3 below shows the atom coordinates that build up the MgO conventional unit cell, illustrated in the right panel.

| Space Group | Atom | Wyckoff Pos. | (x y z) |
|---|---|---|---|
| $Fm3m$ | Mg cations | 4a | (000) |
| | O anions | 4b | $(\frac{1}{2}\frac{1}{2}\frac{1}{2})$ |

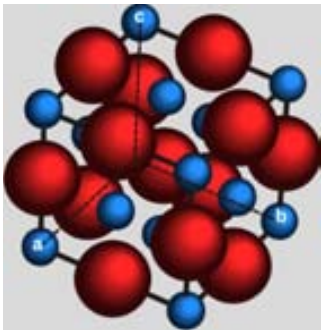

**Fig. 2.3:** *MgO crystal structure and its cubic unit cell displayed on the right. Blue spheres represent Mg cations and red spheres represent the oxygens.*

The MgO substrates used in thist work are 5 mm x 5 mm x 0.5 mm single crystals commercially available from Crystec. They are one side polished, have a nominal (001) orientation and a given lattice parameter $a_{MgO} = 4.21$ Å in agreement with literature [113]

and with our X-Ray Diffraction results ($a_{MgO} = 4.21(4)$ Å).

### 2.1.3 Fluorite-type substrates: $Y_2O_3$:$ZrO_2$ (YSZ)

Pure Zirconia, $ZrO_2$, displays a monoclinic structure at ambient conditions (room temperature and atmospheric pressure) and only reaches the cubic phase at very high temperatures (∼2650 K), after going through an intermediate temperature transition to tetragonal symmetry [114]. However, the doping of zirconia with a considerable amount of yttria (between 8-40 mol % $Y_2O_3$) stabilizes the cubic fluorite structure, space group $Fm3m$, at ambient conditions [115]. In addition to an increased resistivity against thermal stresses, such a doping introduces oxygen vacancies that make *yttria-stabilized zirconia* (YSZ) a remarkable ionic conductor, very commonly used as electrolyte in Solid Oxide Fuel Cells (SOFC) [116]. Fig. 2.4 displays the crystal structure parameters and the illustration of the conventional unit cell.

| Space Group | Atom | Wyckoff Pos. | (x y z) |
|---|---|---|---|
| $Fm3m$ | Zr cations | 4a | (000) Occ.0.81 |
| | Y cations | 4a | (000) Occ.0.19 |
| | O anions | 8c | $(\frac{1}{4}\frac{1}{4}\frac{1}{4})$ |

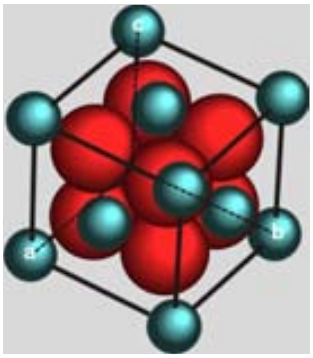

**Fig. 2.4:** *Crystallographic parameters of the YSZ structure (left panel) and the illustration of the unit cell containing 4 cations (blue) and 8 oxygens (red). The occupancy (Occ.) of the cations corresponds to an $Y_2O_3$ doping of 9.5 mol %.*

The YSZ substrates used in the present work are 5 mm x 5 mm x 0.5 mm one side polished single crystals from Crystec. The data sheet available from the provider sets the $Y_2O_3$ doping at 9.5 mol %, which means we have the cubic compound $Y_{0.19}Zr_{0.81}O_{1.9}$. They give a lattice parameter of 5.12 Å. However, from literature, a larger lattice parameter would be expected for such doping concentrations: values from $a_{YSZ} = 5.13$ Å to $a_{YSZ} = 5.14728$ Å are reported for 9.4 mol % [117] and 10 mol % [118], respectively. Indeed, our X-Ray Diffraction measurements for the 9.5 mol % doping gave a value $a_{YSZ} = 5.14(7)$ Å, which is in reasonable agreement with the literature values.

## 2.2 Substrate surface conditioning

The surface of the substrate, in contact with the phase grown on top, is decisive in heteroepitaxial growth. A clean surface free of contaminants, with roughness in the atomic scale and high crystallinity is required. A single-terminated surface in complex oxides such as perovskites is often also desirable, as in the case of superlattices, where an atomic-scale control of the alternating planes is necessary for tailoring their physical properties [11, 119].

There are extensive works on thermal and chemical treatments of substrates for the generation of surfaces with the above characteristics. We will review a few here, focusing on their application to our own substrates. These methodologies improve along with the advances in the techniques that enable substrate surface characterization: scanning probe microscopies, surface-sensitive spectroscopies, and surface diffraction techniques are among those used to characterize the structure and chemistry of surfaces. It is also worth noting the large amount of theoretical studies of oxide substrate surfaces. These works discuss the surface atomic and electronic structure and can predict energetically favored terminations and facets, among other characteristics. A substantial amount of experimental and theoretical studies are reviewed in the 1996 book by Noguera [120]. The number of works in the field has, from then on, remarkably increased.

Single crystals are cut through rational crystallographic planes such as (001), (011), and (111) for the cubic case. However, an unavoidable misorientation in the cutting process results in the well-known step-terrace morphology, where atoms reorganize into the nominal low-energy surface planes (Fig. 2.5). Specific thermal and chemical treatments provide atomic diffusion towards a well defined terrace-step structure and also trigger the desorption of contaminant adatoms. After such treatments, surfaces exhibit atomically flat terraces and steps that are integer or half-integer multiples of the crystal unit cell height $a$ [i.e. $na$ or $(n+\frac{1}{2})a$]. The smaller the miscut, the wider the terrace will be, as it follows from Eq. 2.1, where $\lambda$ is the width of the terrace. In most as-received substrates both $na$ and $(n+\frac{1}{2})a$ types of steps are typically present, which, for perovskites, implies that both A-O and B-$O_2$ terminations coexist.

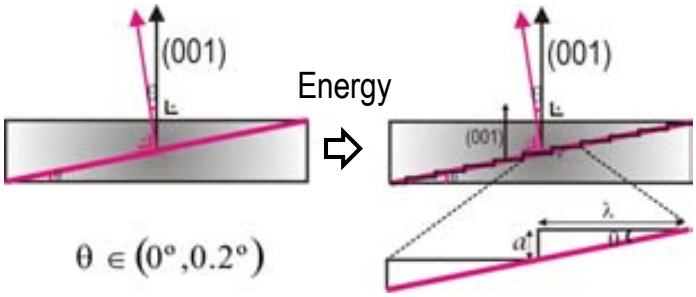


**Fig. 2.5:** *The real cut and polished surface differs typically in $\theta$ ∼0-0.2° from the rational crystallographic (001) plane. Under the effect of heat, surface atoms are able to diffuse to form (001) oriented terraces.*

$$\tan\theta = \frac{a}{\lambda} \tag{2.1}$$

### 2.2.1 (001)-oriented $SrTiO_3$ and $LaAlO_3$ surfaces

In the case of the widely studied STO surface, Kawasaki and co-workers were the first to develop a method, based on variable pH acid solutions, that attacks the most basic Sr-O termination and yields a single Ti-$O_2$ terminated surface [121]. Koster and colleagues proposed a similar method, although less dependent on the pH of the etching solution [122]. Here, the Sr-O termination reacts with $CO_2$ and water to give $SrCO_3$ and $Sr(OH)_2$, respectively. The latter hydroxide dissolves in acid solutions and leaves the more stable Ti-$O_2$ termination. These works have boosted many efforts in the development of procedures

to achieve the ultimate control of the surface structure and chemistry. Recent advances in this context include the nanopatterning of STO substrates with a controlled coexistence of the two terminations, achieved using simple high temperature annealing [123].

Fig. 2.6 shows two Atomic Force Microscopy (AFM) images of (001)-oriented as-received STO and LAO substrates after cleaning with acetone and methanol in an ultrasonic bath to eliminate non-polar and polar impurities, respectively. The terraces due to the miscut angle $\theta$ are observable, but they are not well defined. To improve the quality and achieve well defined step-terraces, after the cleaning, the substrates are put in a covered alumina crucible. This is then placed in a quartz tube that goes inside a high-temperature tubular furnace. Substrates are annealed at 900°C for 5 h under flowing oxygen (0.5 $l \cdot$ $min^{-1}$, regulated with a mass-flow controller). Heating and cooling rates are 15°C $\cdot$ $min^{-1}$ and 10°C $\cdot$ $min^{-1}$, respectively. Such process is reported in the literature to generate atomically flat terraces with a majority of Sr-O termination [124]. We will hereafter refer to it as *standard treatment*.

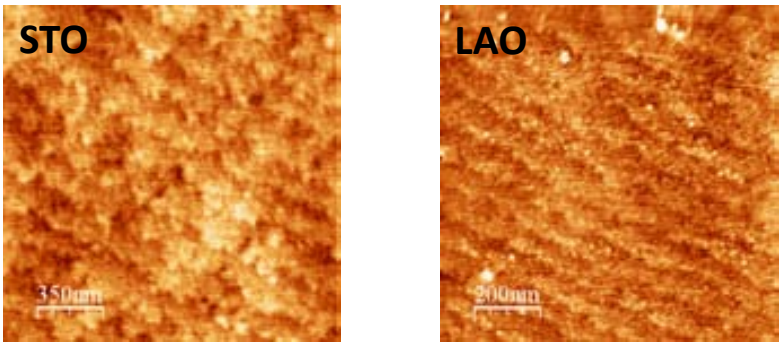


**Fig. 2.6:** *AFM topography images of as-received (001)-STO and (001)-LAO surfaces. The measurements were done after cleaning the impurities with acetone and methanol in an ultrasonic bath. The scale in* ***z*** *is 1.5 nm (STO) and 2.5 nm (LAO).*

The result of the described annealing process is shown in Fig. 2.7, which displays 1 µm $\times$ 1 µm AFM images of three different STO substrates, identically treated. In every case the presence of terraces is clearer than in the as-received substrates. However, the morphologies show an increasing step-edge roughness with increasing terrace width. These terraces appear very poorly defined in the $\lambda\sim$500 nm-wide case. Note also the presence of holes on the terraces. This is an evidence that atomic diffusion on the wide terraces was not enough to fully reconstruct them. In other words, for substrates with smaller miscut more energy is required to obtain smooth and well defined morphologies (higher temperature or longer annealing times). Nevertheless, even for the highest quality terrace structures, step heights of $na$ and $(n + \frac{1}{2})a$ were identified, indicative of coexisting Sr-O and Ti-$O_2$ terminations.

In order to obtain single Ti-$O_2$-terminated substrates, we chemically attacked the surface, following the procedure described by Koster et al. [122]: substrates were first ultrasonically cleaned in a Milli-Q purified water bath for 3 min, and then attacked with a buffer ammonium fluoride-hydrofluoric acid mixture solution for 30 s ($NH_4 \cdot HF$, pH 6.5, Sigma Aldrich). The acid was rinsed with more Milli-Q water and the substrate was finally put in the furnace and heat-treated at 900°C for 5 h. As we said above, such acid attacks the $Sr(OH)_2$ formed at the Sr-O termination in contact with water, leaving the more stable

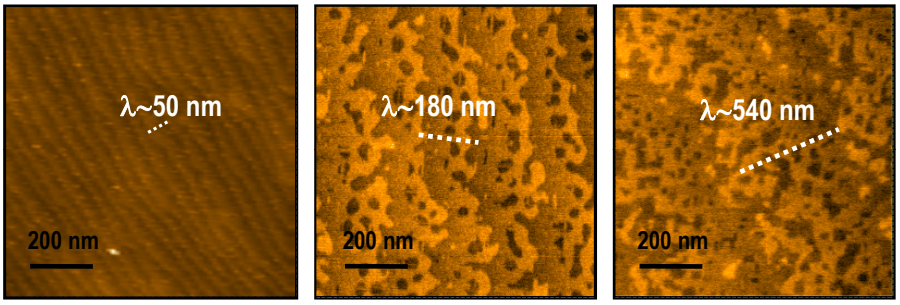


**Fig. 2.7:** *$1\mu m \times 1\mu m$ AFM topography images of three different STO substrates after the same thermal treatment. The scale in* **z** *is ∼2 nm.*

Ti-$O_2$ termination intact. The latter will be reconstructed into smooth terraces during the annealing. The comparison between a simply annealed and an etched and annealed STO surface is illustrated in Fig. 2.8.

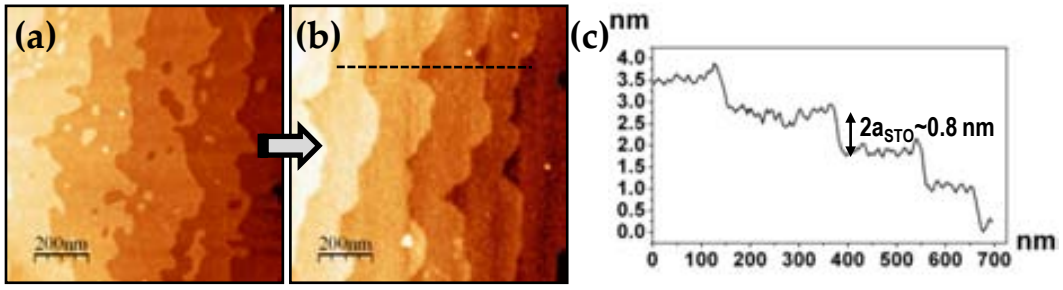


**Fig. 2.8:** *$1\mu m \times 1\mu m$ AFM topography images of the same STO substrate after the annealing process (a) and after the surface etching and final annealing (b). Note how the holes disappear and the edges straighten. (c) The line profile on the right shows the step height for the edged substrate is twice the STO lattice constant. The scale in* **z** *is ∼4 nm in the two AFM figures.*

Although this method seemed to be most effective to obtain smooth and single-terminated STO surfaces, it proved occasionally to be too aggressive for our STO crystals: Fig. 2.9 shows a wider ($4\ 7\ \mu m \times 4\ 7\ \mu m$) AFM image displaying very smooth terraces accompanied by a high density of etch pits. Such pits are holes of significant width (∼200 nm) and depth (∼4-20 nm). Representative length scales may be observed in the profile corresponding to the dashed line on the image. In some cases, the sum of many of them results in holes of large size, which propagate along the crystallographic [100] and [010] directions. Such features were reported in reference [122] to occur for more acidic etching solutions (pH 4.5) but not for the actual solutions and the etching time (30 s) used in our samples. The use of shorter times did not eliminate the etch pits. Note that most holes, although rounded from the high-temperature diffusion processes, appear faceted, consistent with the cubic structure of STO. From these results it seems that our STO substrates are characterized by defects that react to the acid attack: substantial chemical inhomogeneities (large amounts of Sr-O) or large numbers of structural defects like dislocations are likely to produce such etch pits. Indeed, identical treatments on different substrates such as the one from Fig. 2.10 showed a remarkably smooth surface with very few etch pits and holes, thus confirming our hypothesis. The critical point here, therefore, is the starting quality of the substrate.

We conclude from the above study that both the *standard treatment* and the *chemical etching plus annealing* process are capable of producing clean STO surfaces with well defined step-terrace morphologies. The latter also yields a single termination. However, the original miscut of the sample and its quality (e.g. the presence or absence of dislocations and other defects) will eventually determine the roughness and the presence of etch pits. In general, the standard treatment appears sufficient for having smooth and atomically flat STO surfaces, appropriate for the subsequent growth of LSMO.

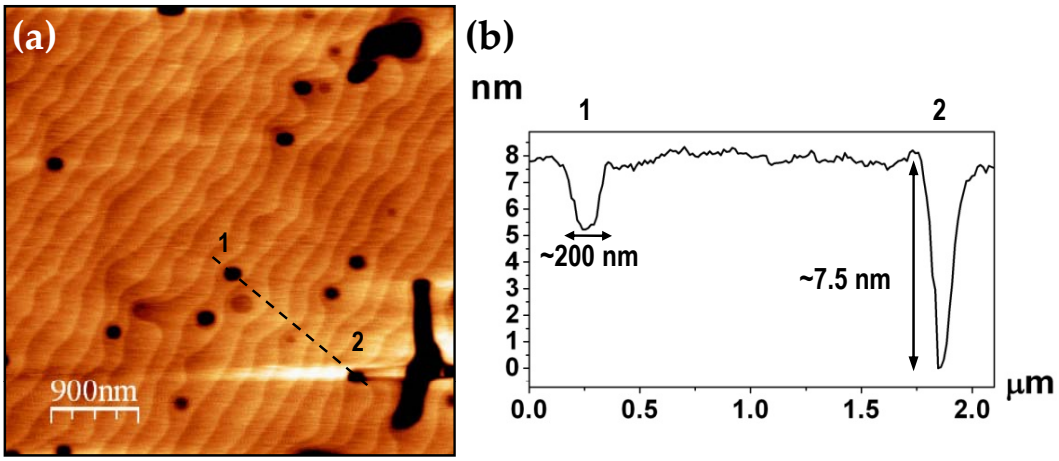


**Fig. 2.9:** *(a) 4.7$\mu m \times 4.7\mu m$ AFM topography image of an etched and annealed STO substrate displaying smooth steps along with holes from the acid attack. The image is thresholded in order to better distinguish the step-terrace morphology, the scale in z is ∼10 nm. (b) Line profile along the dashed line in (a) showing typical dimensions of the etch pits. Such holes can go as far as ∼20 nm into the crystal.*

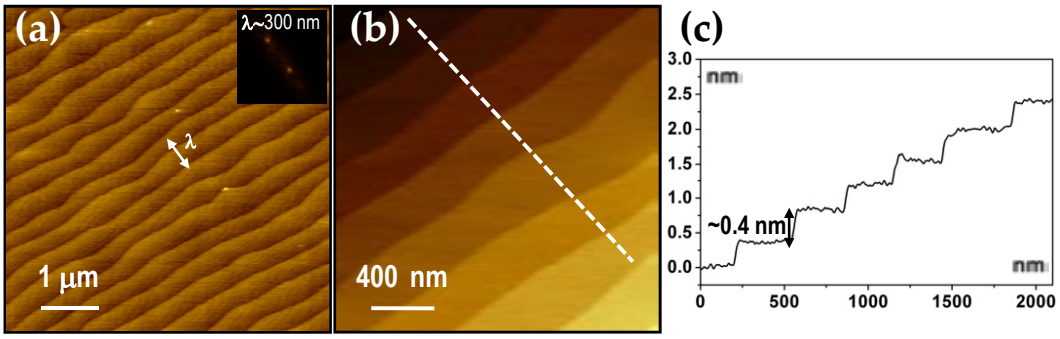


**Fig. 2.10:** *(a) 5.5$\mu m \times 5.5\mu m$ AFM topography image of an etched and annealed STO substrate displaying smooth steps and no visible holes from the acid attack. The Fourier Transform of the image shows the periodicity of the terraces, ∼300 nm wide. Scale in z is ∼3 nm. (b) 2$\mu m \times 2\mu m$ topography image of the same STO substrate. (c) Line profile along the dashed line in (b). The step corresponds to a single unit cell in height indicating single termination.*

The standard treatment described for STO was analogously applied to LAO substrates, for which no specific step-terrace forming procedure was available in the literature. We applied such a treatment in a great number of substrates, with very reproducible and satisfactory results. Contrary to STO, LAO substrates nearly always presented smooth and well

defined step edges, with unit-cell high steps. Fig. 2.11 presents the corresponding AFM image of a LAO substrate after the *standard treatment* and a line profile showing one unit-cell high steps. The etching procedure designed for STO was also tried on LAO substrates. Expectedly, neither an improvement nor a damage in the form of etch pits were observed, as such procedure specifically attacks the Sr-O termination.

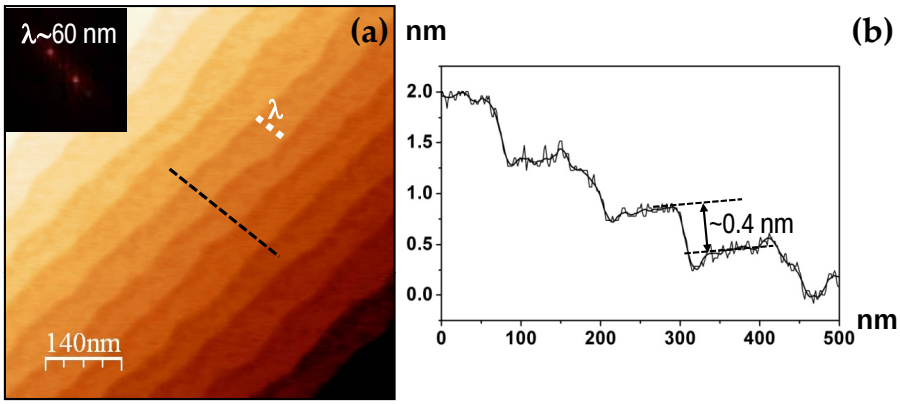


**Fig. 2.11:** *(a) 700 nm × 700 nm AFM topography image showing the λ ∼60 nm wide LAO terraces of a substrate after the standard treatment. (b) Line profile along the dashed line in (a) showing the unit cell step height.*

In (001)-LAO, the alternatively stacked La-O and Al-$O_2$ planes are positively and negatively charged, respectively. Several works point to the tuning of surface termination with temperature and atmosphere [11, 125–127]. In most cases, the annealings are performed in ultra-high vacuum chambers which is believed to favor La-O termination (poorer in oxygen) [125]. In contrast, in the X-Ray Photoelectron Spectroscopy (XPS) studies done in collaboration with Dr. J. A. Martín-Gago and Dr. Lidia Martínez (ICMM-CSIC Madrid), our air-treated LAO substrates showed a surface rich in Al, independent on whether the treatment atmosphere was oxidizing or reducing (Fig. 2.12). Specifically, the *La/Al* ratio decreased from ∼0.7 in the *as-received* substrates, to ∼0.3 in the substrates treated in $O_2$, Ar-$H_2$, or by successive oxidizing and reducing treatments. It is also worth noting that the oxidizing treatment promotes carbide formation, and how the carbide proportion has significantly decreased after the reducing treatments. The contamination carbon (C-C), on the other hand, remains constant, possibly because the surface was always measured after exposure to air. Besides, the morphology images in Fig. 2.13 show that no remarkable differences arise in the LAO substrates when heat-treated under different atmospheres, i.e. thermal energy appears to be the principal source of surface smoothening and step-terrace formation.

### 2.2.2 (001)-MgO surfaces

Regarding MgO substrates, abundant literature exists on their surface preparation and characterization, prompted by their wide use in film epitaxy and as support for metal particle growth. Already in 1990, Duriez and co-workers refer to many previous studies of UHV-cleaved and air-cleaved MgO crystals [128]. They also provide a comprehensive structural characterization using He diffraction, Auger electron spectroscopy, and Pd decoration to assess the crystallographic order, cleanliness and micro-topography of MgO sur-

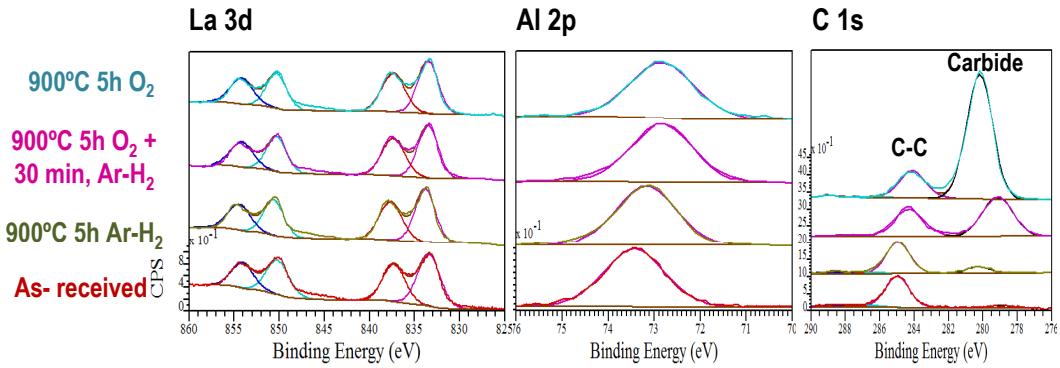


**Fig. 2.12:** *La 3d, Al 2p, and C 1s core level spectra as measured from XPS for heat-treated LAO surfaces (900°C) under different atmospheres. The area-calculation gives a* La Al *ratio of ∼0.7 for the as-received and of ∼0.3 for the heat-treated surfaces. Note how the carbide content is maximum in the oxidized LAO and gradually decreases for reducing atmospheres.*

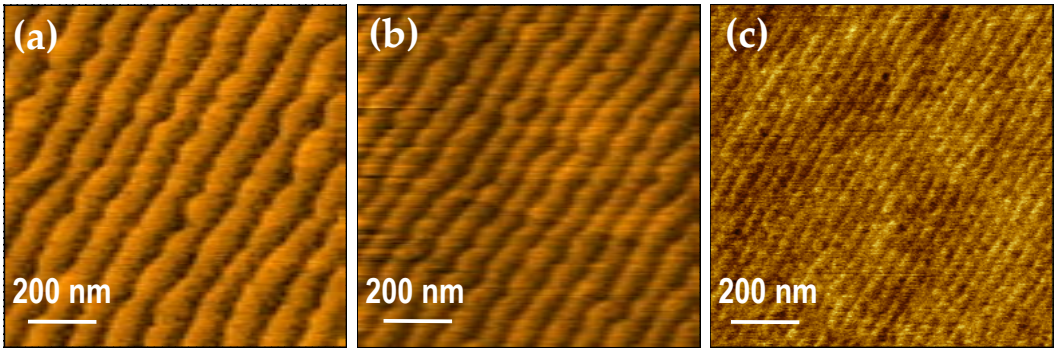


**Fig. 2.13:** *(a) 1$\mu m \times 1\mu m$ AFM topography images of heat-treated (900°C) LAO surfaces after (a) 5 h in $O_2$ atmosphere, (b) 5 h in Ar-$H_2$ atmosphere, (c) 5 h in $O_2$ plus 30 min in Ar-$H_2$ atmosphere.*

faces. A strong tendency from such surface towards water chemisorption and reaction, as well as towards ambient $CO_2$ adsorption are also described, in agreement with more recent theoretical and experimental works [129–132].

Fig. 2.14 shows AFM topography images of two different MgO substrates processed using the *standard treatment*. Little change is observed on their flat and step-free surfaces, although the presence of small pits (a representative pair is marked with green circles) seems larger before the annealing. Nevertheless, the root mean square (RMS) roughness actually increases a bit, from 0.2 nm to 0.3 nm, after annealing is performed. This is also the reason why the pits are less visible in the latter case, although their depth does not change (∼1.5 nm). Fig. 2.14 (b) displays a different substrate, which was not annealed, and that presents a very flat surface with neither terraces nor pits (RMS roughness 0.16 nm).

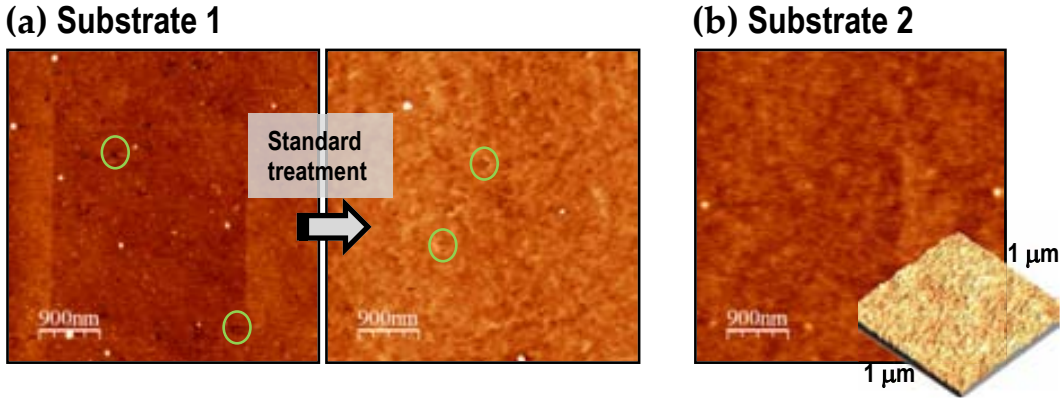


**Fig. 2.14:** *4.5µm × 4.5µm AFM topography images of two MgO surfaces. (a) Surface morphology of an organic-solvent cleaned MgO without thermal annealing (left) and after the 5 h treatment at 900°C in oxidizing atmosphere (right). (b) A different MgO substrate after just the acetone and methanol cleaning. z scale is ∼3 nm, ∼4.3 nm, and ∼2.4 nm (left to right).*

A large variety of surface morphologies have been described in the literature concerning the evolution of MgO with annealing temperature, time and atmosphere. Step-terrace morphologies, smoothening, or, conversely, considerable roughening (with microcrystal diffusion from the bulk) are among the features that have been reported [133, 134]. For instance, a diffusion-driven increase of terrace width has been observed after longer annealing times, while the terraces tend to narrow at higher temperatures due to evaporation processes [134]. These works also give a threshold temperature of 1000°C for the onset of step-terrace morphology formation, which is consistent with our findings at a lower temperature (900°C). However, the spread in the treatment parameters that were used in various literature works to achieve particular morphologies highlights the importance of the substrate quality. This includes the manufacturing conditions (whether it is air or UHV-cleaved), the presence of defects and impurities, and surface contaminants.

### 2.2.3 (001)-YSZ surfaces

A representative example of the effect of different treatments on YSZ substrate surfaces is shown in Fig. 2.15. Similar to MgO, YSZ substrates show no changes after the standard heat treatment [Fig. 2.15 (a)]: very flat and clean surfaces of RMS roughness ∼0.14 nm

are observed in both cases. Surface steps of width $\lambda$ can also be inferred (their orientation is marked in green dashed lines in the image). This is further confirmed by the Fourier transform, from which an average terrace width $\lambda$ $\sim$60 nm is deduced. A different as-received YSZ substrate shows identical characteristics (Substrate 2, cleaned with acetone and methanol just like Substrate 1), although steps here are very narrow and the image too large to be able to find the exact terrace size. In contrast, two other substrates (3 and 4), subject to a 1000°C annealing in oxygen for half of the time (0.5 l$\cdot$ min$^{-1}$, 2.5 h), display a clearer step-terrace morphology with very narrow terraces ($\lambda\sim$44 nm). Notice also how some of the steps, instead of being straight, meet at one point (some of these features are evidenced by green circles). Such coalescence has already been reported, although it was only observed at higher temperatures [135]. Substrate 3 appears homogeneously covered by similar round particles ($\sim$8 nm and $\sim$50 nm in height and diameter, respectively). Conversely, Substrate 4, from a different batch, did not exhibit such particles after undergoing an identical treatment as Substrate 3. On the contrary, it showed a remarkable cleanliness, hence ruling out the possibility that such treatment would produce segregation from the bulk.

In short, the cut and polished YSZ substrates used in this work came with little defects and showed highly planar surfaces. They can be either cleaned or cleaned and heat-treated (if further contaminant removal is desired), and they tend to form very narrow and smooth terraces, better reconstructed at 1000°C. A greater variety of morphologies, from planar surfaces to surfaces with holes or self-organized nanostructures was reported in the literature [136]. This again emphasizes the critical role of the quality of the substrate, determined by the growth and polishing methods used by the supplier.

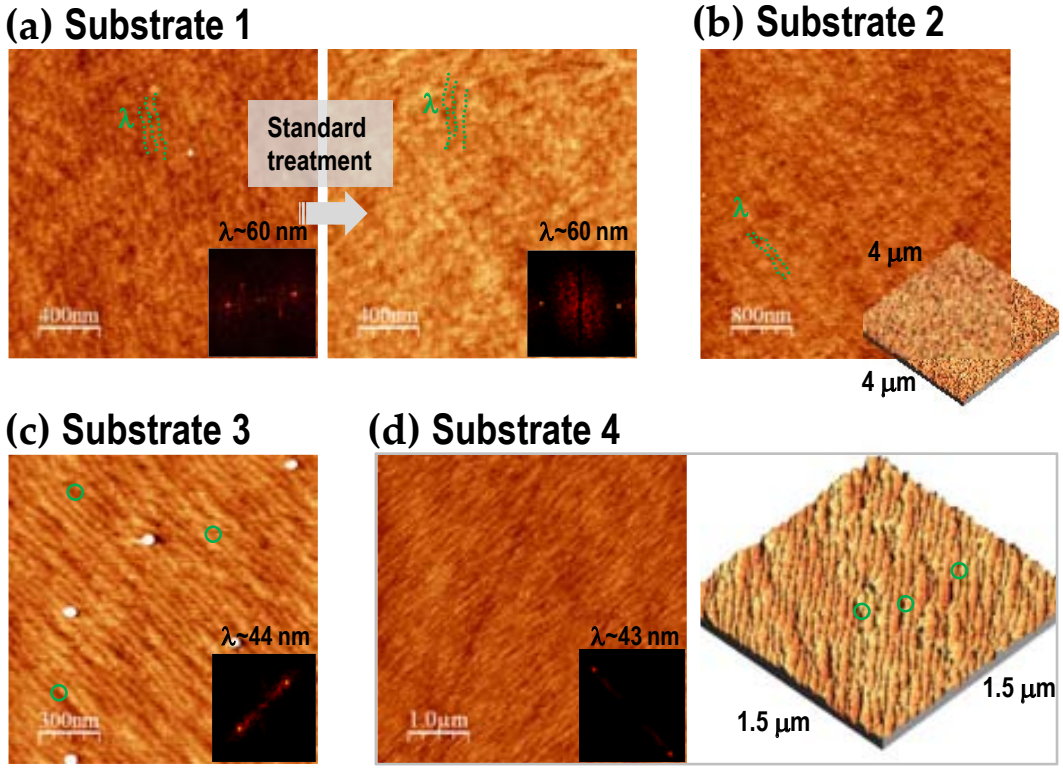


**Fig. 2.15:** *(a) 2μm × 2μm AFM images of an acetone and methanol-cleaned YSZ substrate before (left) and after (right) 5 h annealing at 900°C in $O_2$. The surfaces look identical except for a slightly greater presence of dirt particles in the non-annealed substrate (not shown). The step periodicity is observed, with indicative dashed green lines marking the terrace limits and the Fourier transforms of the images giving the spacing between them (∼60 nm). Scale in z is ∼1.4 nm in both. (b) 4μm × 4μm image of a different substrate just after the acetone and methanol bath, which shows little difference with respect to Substrate 1. RMS values are ∼0.13 nm and ∼0.16 nm (Subs. 1 and 2, respectively). (c) and (d) correspond to a 2.5 h 1000°C annealing in $O_2$ of two more YSZ substrates. Step-terrace morphology is more clearly discerned here than in (a) and (b), though terraces appear narrower (∼44 nm). Note also the coalescence of steps, some of them marked with green circles in (c) and in the 3D detail of (d). RMS values are very low, around 0.13 nm, z scale is ∼1.4 nm.*

## 2.3 Chemical Solution Deposition growth of $La_{0\ 7}Sr_{0\ 3}MnO_3$ films and nanostructures

In this section we describe the chemical solution deposition (CSD) method applied to the growth of $La_{0.7}Sr_{0.3}MnO_3$ nanoscale films and 3D nanostructures.

Our $La_{0.7}Sr_{0.3}MnO_3$ (LSMO) precursor solutions were prepared following the 'all-propionate' route described by Hasenkox et al. [137]. Briefly, stoichiometric amounts of metal propionates are mixed and dissolved in propionic acid under ambient conditions, stirred up for 30 min at room temperature and filtered with a $0\ 2$ μm diameter filter. The initial solution concentration, 0.3 M with respect to the Mn, is diluted down to concentrations in the 0.006 M to 0.1 M range. The metal propionates used, i.e. $La(OOCC_2H_5)_3$, $Sr(OOCC_2H_5)_2$ and $Mn(OOCC_2H_5)_2$, are synthesized from commercially available acetates (Aldrich) in a large excess of propionic acid (Aldrich). The solution chemistry, hence, is kept simple and the main goals of the CSD route are achieved: inexpensive starting compounds, adjustability of concentration and stoichiometry, as well as solution handling at ambient atmosphere [137]. The solution at 0.3 M concentration has a viscosity of 2.5 mPa · s which falls down to 1 mPa · s for 0.03 M concentration (precisely the viscosity of the propionic acid solvent). Contact angle measurements of the 0.03 M solution on the STO, LAO, YSZ and MgO substrates, both as-received, and after the *standard treatment* gave values below 15°, i.e. the solution perfectly wets all of the substrates, also independent of the treatment.*

After the synthesis, $14$ μl of precursor solution are deposited onto a clean and atomically flat substrate (see section 2.2), positioned at the center of the rotatory plate of a commercial spin-coater. The substrate attains 6000 rpm rotational speed in 1 s, which is kept constant for 2 min. At the end of the process the solvent has evaporated and the substrate appears covered with a homogeneous gel layer. Under identical deposited volume, angular velocity, acceleration, and spinning time, we expect the amount of deposited material to be the same, since the wettability is the same for all substrates. The main source of differences regarding the material quantity are rather small variations in the deposited volume. This is easily expected because the deposit is done by hand, approximately aiming for the center of the substrate.

The spin-coated sample is placed in an alumina covered crucible which is put inside a quartz tube, previously cleaned with water, soap and acetone. The tube is introduced in a high temperature furnace where metalorganic precursors decompose (∼300°C-400°C [138]) and the subsequent LSMO crystallization occurs (high temperatures $\gtrsim$ 700°C). The experimental conditions are tuned by modifying the growth temperature, the heating ramp and the dwell duration [see Fig. 2.16 (a)]. Rather slow heating and cooling ramps were used, $3°C \cdot min^{-1}$. Annealing was done in air and oxygen atmosphere (the latter typically at a flowing rate of $0.6\ l \cdot min^{-1}$, regulated with a mass-flow controller). Oxygen flow was introduced at around 800 °C and removed again at the same temperature during the cooling ramp. Both the slow ramp and the atmosphere settings were taken from previous works done in the group. Such studies optimized the parameters for the growth of magnetoresistive LSMO thin films [139, 140].

*Meaningful differences among contact angle values are only considered above ∼15°. We cannot resolve differences for smaller values, in practice saying that the solution *completely wets the substrate*.

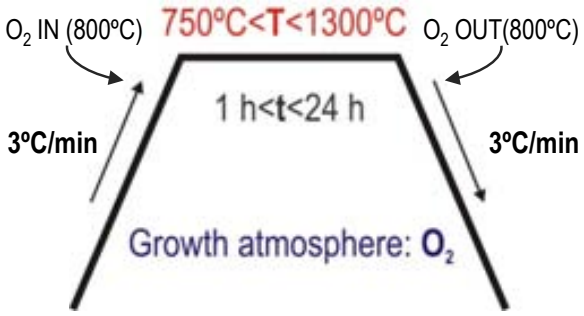


**Fig. 2.16:** *Typical heat treatment parameters for the generation of epitaxial* LSMO *on single crystal substrates. The $O_2$ flux was 0.6 $l \cdot min^{-1}$.*

## 2.4 Conclusions

In summary, we have introduced the principal characteristics of the oxide single crystal substrates used in this work. Along with a state-of-the-art on oxide surface conditioning, we have described our own strategy, mainly based on heat treatments performed at high temperature (900°C), ambient pressure, and under flowing oxygen. Such treatment succeeds in generating well-defined step-terrace morphologies in both STO and LAO substrates. In the case of LAO, it produces Al-rich surfaces with a considerable amount of carbides. The carbide content was seen to decrease when the treatment was performed under Ar-$H_2$ reducing conditions, with no observable change in topography or in the surface chemistry, as seen by XPS. Performed after an acid etching, the so-called *standard treatment* further selects a single termination in STO. On the other hand, the flat and clean surfaces of MgO and YSZ did not undergo appreciable variations after the *standard treatment*, although YSZ demonstrated a clearer tendency towards step-terrace morphology. Such terraces, very narrow, appear slightly better formed when the heat treatment is done at a higher temperature (1000°C). In the following, all of the STO and LAO substrates will be heat-treated following the *standard treatment*, while for MgO and YSZ we will use one or the other, as-received or heat-treated substrates indistinctly. Regardless of whether the thermal treatment is performed or not, the sonication with acetone and methanol is invariably done to clean the substrates from contaminants. An important point to keep in mind is that substrate variations should be expected from batch to batch, and hence AFM inspections of their topography will be carried out as often as possible.

# Chapter 3

# Nanoscale $La_{0.7}Sr_{0.3}MnO_3$ on single crystal oxide substrates

As outlined in the Motivation of this thesis, we establish the framework of our study in the context of nanoscale oxide heteroepitaxys, where the atomic arrangement of the substrate crystal determines the growth of the crystalline film on top. The procedure to chemically grow $La_{0.7}Sr_{0.3}MnO_3$ (LSMO) on top of single crystal oxide substrates was just described in Chapter 2. Whether this LSMO grows in a 2D film or in a 3D nanoisland form, epitaxial or random, strained or relaxed etc., will define the functional properties of the system. In the present chapter we give the general description in terms of morphology, epitaxy, microstructure, and macroscopic magnetic performance of solution-derived LSMO nanoscale systems grown onto a variety of (001)-oriented single crystal substrates. Such oxide substrates, recently explained, include the perovskite-type $SrTiO_3$ (STO) and $LaAlO_3$ (LAO), the fluorite-type YSZ, and the rock-salt MgO. The influence of the substrate in the final heteroepitaxy, or, more specifically, the key role of the film-substrate interaction, is evidenced soon enough: the same ultra-diluted precursor solutions, under identical heat treatments, yield two disparate landscapes: atomically flat <10 nm thick LSMO films are obtained on STO and LAO single crystals while onto YSZ and MgO, the result is an homogeneous dispersion of self-assembled LSMO nanoislands. We have divided the chapter into these two naturally differentiated blocks: we start by addressing the main characteristics of ultrathin LSMO films grown on STO and LAO and devote the second part of the chapter to the analysis and description of self-assembled LSMO nanoislands.

## 3.1 Heteroepitaxial growth basics

The word *epitaxy* comes from the Greek, where *epi* means 'located on' and *taxis* means 'arrangement'. We understand epitaxial growth as the growth of a crystal (the film material) on top of another crystal (the substrate material) in such a way that the atomic arrangement within the substrate continues within the film on top. An epitaxial film-substrate interface thus implies that atoms of the film material will occupy lattice positions of the substrate and vice versa [141]. If film and substrate are the same material we talk of *homoepitaxy*, while the opposite case is known as *heteroepitaxy*. From a thermodynamic perspective, het-

eroepitaxial growth is commonly described in terms of the free surface/interface energies of substrate and film, and of their elastic strain energy.

The generation of a free surface involves the breaking of chemical bonds, with the consequent net increase of energy of the system. ***Surface free energy*** $\gamma$ is hence directly related to the reversible work $dW$ done on a material when its surface area is increased by $dA$, i.e. $dW{=}\gamma dA$ [141, 142]. Similarly, the chemical bonding between the atoms in the film and in the substrate also has an energy associated, the interface energy, which is less than the sum of their individual surface energies. Young's equation, $\gamma_s{=}\gamma_{fs}{+}\gamma_f\cos\theta$, is derived from minimizing the surface energy required to generate a spherical cap island (like the one sketched in Fig. 3.1) with respect to the wetting angle $\theta$ [141]. The relative values of the surface free energy provide a first classification of the *growth modes* in heteroepitaxial systems [143]: the film will grow layer by layer if $\gamma_s{>}\gamma_{fs}+\gamma_f$ (also known as Frank-van der Merwe or 2D growth) [144], or it will start by generating 3D islands if $\gamma_s{<}\gamma_{fs}+\gamma_f$, following the so-called Volmer-Weber growth [145]. A combination of 2D and 3D growths can also occur, known as Stranski-Krastanov growth mode [146], which typically implies the presence of lattice mismatch between the film and the substrate.

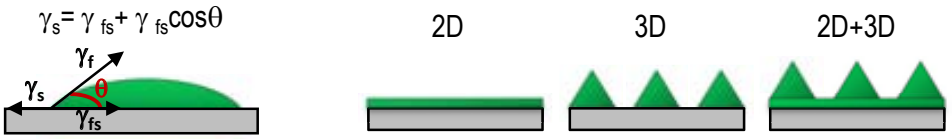


**Fig. 3.1:** *Liquid nucleus in equilibrium model. Young's equation represents the balance among the different components of the surface free energy $\gamma$. The growth mode can be 2D, 3D, or a combination of both, depending on the relative values of the substrate ($\gamma_s$), film ($\gamma_f$), and interface ($\gamma_{fs}$) surface energies.*

Lattice mismatch $\epsilon$ (Eq. 3.1) refers to the difference in lattice parameter between the film and the substrate, i.e.

$$\epsilon = \frac{a_s - a_f}{a_f} \tag{3.1}$$

where $a_s$ and $a_f$ are the equilibrium parameters of the substrate and film, respectively. $\epsilon$ is directly related to the other essential component in heteroepitaxial growth, the ***elastic strain energy*** $E_{elastic}$, which scales like $E_{elastic}{\sim}\epsilon^2$ with the lattice mismatch [141, 147]. In a 2D + 3D-like growth as the aforementioned, the film will initially grow adapting its in-plane lattice constant to the bulk substrate lattice constant. As the film grows thicker the elastic strain energy associated to the film deformation also increases. The formation of 3D islands provides a way for relaxing the built-up elastic energy: the upper lattice planes within the island can relax towards their intrinsic lattice constant because they are no longer constrained in the direction parallel to the interface [see Fig. 3.2 (a)]. The greater the island volume, the greater will be the relaxation provided with respect to a film of equal volume. And, for the same island, its volume strain relaxation is larger for the case of smaller lateral size to thickness ratio $D/t$ [Fig. 3.2 (b)]. On the other hand, the generation of 3D structures implies an additional cost in surface energy, which scales with the area of the island. The trade-off between the energy gain due to island relaxation and the energy cost due to the new surface formation will determine whether the 2D to 3D transition occurs or not. This simplistic model neglects the kinetics of the process, such as material transport issues from one state to the other (which will, in turn, depend on the temperature, pressure, etc.) [148].

In addition to 3D island formation, a typical strain-relieving mechanism is the generation of misfit dislocations, i.e. the dislocations formed at the interface between substrate and film. It has been shown that the barrier to generate dislocations is proportional to $\epsilon^{-1}$, while it scales with $\epsilon^{-4}$ for the generation of 3D islands [149]. In other words, the generation of islands is enhanced in large lattice-mismatched systems.

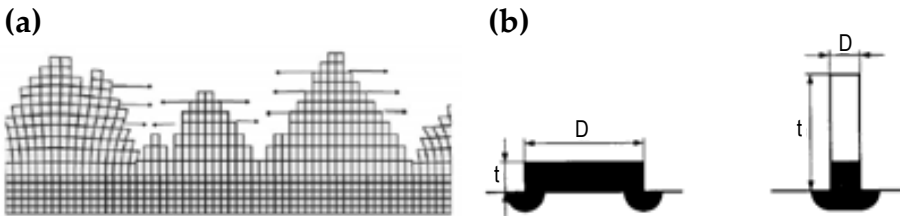


**Fig. 3.2:** *(a) Volume strain relaxation is achieved by 3D coherent (non-dislocated) nanoislands. Arrows indicate the direction of the elastic strain relaxation. Reproduced from [150]. (b) For a fixed nanoisland volume, coherent 3D nanoislands are capable of larger elastic relaxation in the case of low* D t *values. Reproduced from [147].*

The driving force for the spontaneous ordering of nanostructures on a crystal surface is the long range elastic interaction. Such elastic interaction is caused by the strain fields that a 3D island exerts on the substrate due to island/substrate lattice mismatch. For instance, a compressively strained island on a substrate ($a_f$<$a_s$) will tend to expand along the direction parallel to the interface. The substrate will react against this tendency by compressing itself along the free surfaces adjacent to the edges of the island (see Fig. 3.3) [151]. The substrate strain fields cause islands to interact repulsively with each other, thus limiting coarsening processes. In this context of strain-driven structure formation we refer to *self-assembly* when the spontaneous features exhibit a narrow size distribution and we talk of *self-organization* when the structures show an additional tendency to form ordered arrays [150]. The substrate-mediated interaction between islands is sometimes neglected in self-assembled diluted nanoisland systems (nanoisland size $\ll$ nanoisland separation), but it cannot be ignored for denser arrays of nanostructures. This term includes, among others, the isotropic/anisotropic nature of the medium, the lattice mismatch, or the island to island distance [152]. Theoretical studies have demonstrated its effect on coarsening processes of nanoislands, while experimental results point at its influence on the shape transition of semiconductor heteroepitaxys [153].

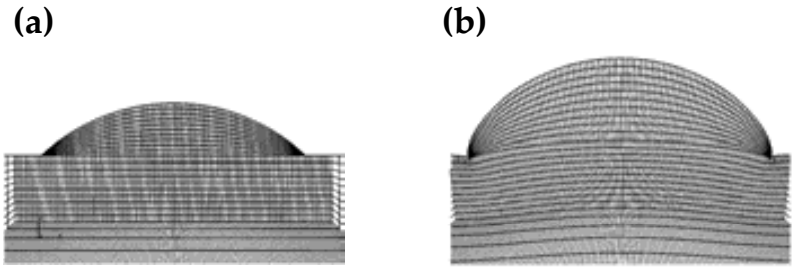


**Fig. 3.3:** *Finite element simulations of island and substrate. (a) Undeformed mesh showing the spatial island and substrate discretization. (b) The mesh deforms as a result of the mismatch strain between the island and the substrate. Reproduced from [151].*

At the beginning of the chapter we have anticipated that, under equal processing parameters, LSMO grows into a 2D film on STO and LAO substrates, whereas it arranges spontaneously into self-assembled nanoislands in the case of YSZ and MgO substrates. Equal processing conditions include the use of identical solution concentration, spin-coating parameters, growth ramps and temperature, annealing times, and atmosphere. The solution wettability of the different substrates was also tested to be the same. Equilibrium theories of heteroepitaxial growth based on the energetic concepts of surface and elastic strain energies depicted above provide the tools for evaluating whether the equilibrium state of the system is, effectively, 2D or 3D. Kinetic effects will then make the real observed system deviate more or less from the one predicted by thermodynamics [150]. Surface energy contributions can be calculated from analytical expressions, given a specific island shape [149, 154, 155]. Analytical expressions for the elastic strain energy of islands have also been derived [154–156]. The total energy of a system of islands is also influenced by other terms such as the interaction between islands explained above (more important the closer the islands are), and the contribution of island edges, which is short-range and positive. The latter, for simplicity, can be sometimes neglected [154], but it has also been explicitly taken into account, as in the work by Shchukin and Bimberg [147]. The application of the existing energetic models has been successfully used in our group for predicting shape selection and thermodynamic stability of strain-driven cerium oxide nanoislands grown on LAO [157]. There are no data, however, concerning the surface energy of LSMO, a multicomponent oxide with the additional complexity of having different possible surface terminations. The $(001)_{\mathrm{LSMO}}$ surface, for instance, could in principle have the Mn-O or the (La,Sr)-$O_2$ termination. Even if we could base the analysis on the scarce surface free energy data for other manganite systems like $La_{1-x}Ca_xMnO_3$ [158], there remains the generalized lack of knowledge regarding interface energies. The distinct nature of perovskite-perovskite, perovskite-fluorite, and perovskite-rocksalt interfaces suggests that the interface energy plays a substantial role in deciding the final heteroepitaxial configuration of each of our systems.

# Part I

# $La_{0.7}Sr_{0.3}MnO_3$ on perovskite-type substrates

The present section is concerned with the results of the growth of LSMO, by means of chemical solution deposition (CSD), onto STO and LAO perovskite-type substrates. As seen in the previous chapters, both LSMO and the chosen single crystal substrates have perovskite structure. The difference in lattice parameters between LSMO ($a_{LSMO} = 3\ 873$ Å) and STO ($a_{STO} = 3\ 90(7)$ Å) is very small, yielding a nominal tensile lattice mismatch of $\epsilon$=($a_{STO}$-$a_{LSMO}$)/($a_{LSMO}$) ∼0.9%. For LAO ($a_{LAO} = 3\ 79(2)$ Å), the lattice mismatch changes sign to compressive, with a larger magnitude of $\epsilon$=($a_{LAO}$-$a_{LSMO}$)/($a_{LSMO}$) ∼-2%. As anticipated in the introduction to this chapter, we find that CSD growth of ultradiluted LSMO solutions on STO and LAO yields ultra-thin films. We will describe these two systems in parallel, starting by the morphological and structural characteristics of the ultra-thin LSMO films and ending up by giving the main points regarding their magnetic and electrical properties.

## 3.2 Morphology and microstructure of ultra-thin LSMO films on STO and LAO

### 3.2.1 Morphological characteristics

For the growth of LSMO on top of perovskite-type STO and LAO substrates we followed the steps described in section 2.3 of Chapter 2. In brief, we used precursor solution concentrations in the 0.015 M-0.1 M range (in Mn) and spin-coated them onto STO and LAO single crystals. The subsequent annealing step was performed in a high temperature furnace under flowing oxygen, at 900°C for 1 h. Before the LSMO growth, the substrates were heat-treated according to the *standard treatment* procedure described in Chapter 2. We may recall that such treatment cleans the substrate surface from organic contamination and reconstructs the miscut surface into a step-terrace architecture.

#### LSMO on STO

The morphology of a LSMO film grown in such a way is shown in Fig. 3.4. The precursor concentration used was 0.03 M. Remarkably, the film entirely reproduces the underlying STO substrate step-terrace morphology, with atomically flat terraces and steps a LSMO unit cell (u.c.) high $a$∼4 Å. The root mean square (RMS) of the film is as low as half a unit cell (∼0.2 nm); this is comparable to the highest quality LSMO on STO films reported in the literature, e.g. grown layer-by-layer by pulsed laser deposition (PLD) [159]. The periodicity of the steps gives a terrace width $\lambda$ of ∼110 nm, calculated from the Fourier transform of large atomic force microscopy (AFM) images [see Fig. 3.4 (b)].

It follows from Fig. 3.4 that the morphological features of the LSMO film are determined by the underlying substrate surface. Such influence is further confirmed by Fig. 3.5, where we show the AFM study of a bare STO substrate after the *standard treatment*. As remarked in Chapter 2, the wider the substrate terraces, the less effective is the thermal treatment in producing smooth, well-reconstructed terraces. This is the case of the STO surface in Fig. 3.5 (a), which exhibits rough edges and a great amount of small holes within the terraces. Expectedly, subsequent growth of LSMO [Fig. 3.5 (b)] results in a considerably rougher thin film than the one in Fig. 3.4, despite using identical processing conditions.

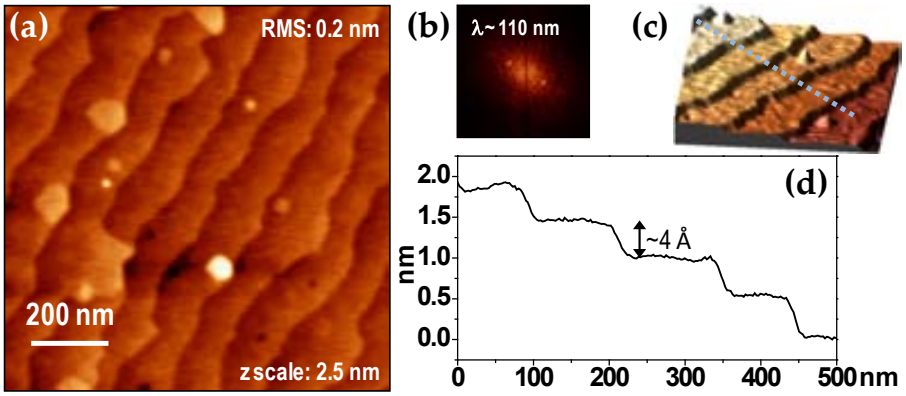


**Fig. 3.4:** *AFM topography analysis of a LSMO thin film grown onto a STO substrate (solution concentration 0.03 M and heat treatment at 900°C for 1 h.) (a) 1$\mu m \times 1\mu m$ AFM image showing the step-terrace morphology of the film, inherited from the underlying substrate surface. RMS roughness is ∼0.2 nm. (b) An average terrace width of λ∼110 nm is deduced from the Fourier transform of the AFM images. (c) 3D AFM image highlighting the staircase morphology of the LSMO thin film. (d) A line profile across the image in (c) reveals the height of the step is 1 unit cell.*

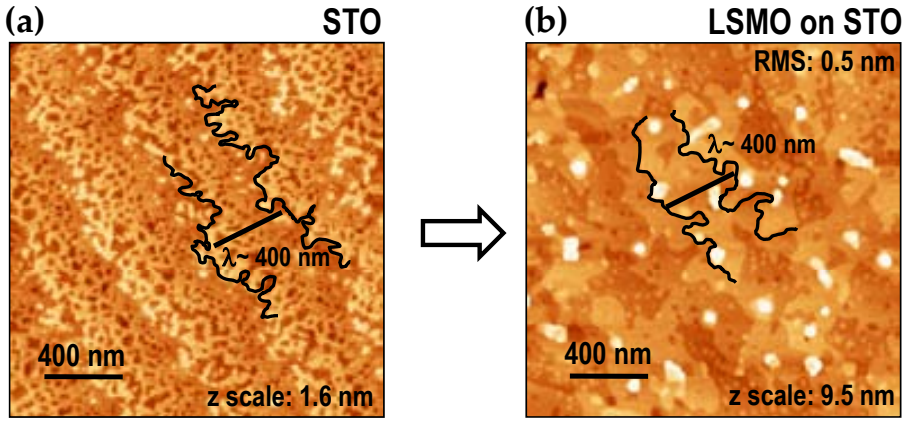


**Fig. 3.5:** *2$\mu m \times 2\mu m$ AFM image of a bare STO substrate after the thermal 'standard treatment' (a), and after the growth of LSMO on top of it (0.03 M, 900°C 1 h) (b). The rough edges and the presence of holes in the terrace give out a rougher LSMO film, compared to the film in Fig. 3.4.*

A natural question regarding these films, which reflect the architecture of the underlying substrate , is 'how thick they are'. We act upon the *film thickness* $t$ by modifying the precursor solution concentration: the more concentrated the solution, the larger amount of material will crystallize, i.e. the thicker the film will be (provided that such material homogeneously covers the whole substrate surface). Previous works in the group have shown that LSMO precursor solutions from propionates with concentrations ∼0.3 M, (i.e. one order of magnitude above the actual solutions) result in LSMO films of $t$∼25-30 nm [140]. Our thin films, on the other hand, are too thin to be able to measure the step resulting from attacking part of the film. Nevertheless, the studies performed on self-assembled LSMO nanoislands grown from identical solution concentrations onto YSZ substrates, enable a rough calculation of the thickness values at these low concentrations. Such estimation is further supported by the extrapolation of the existing data for thicker films [140], and with the local measurements from transmission electron microscopy cross-sections (next section). Overall, we find that the average expected film thickness $t$ for 0.015 M, 0.03 M, and 0.1 M precursor solution concentrations is around ∼1.5 (±0.5) nm, ∼3.5 (±0.5) nm, and ∼10 (±5) nm, respectively. The procedure for estimating these numbers in nanostructured LSMO on YSZ samples will be discussed later in section 3.4.1 of this chapter.

More examples of the various LSMO thin-film morphologies that we obtained depending on the underlying substrate surface, are displayed on Fig. 3.6. Note that we have included a film grown from a 0.015 M solution. We see that it also exhibits well-defined atomically flat terraces, as the films with twice the amount of material. All these films were treated at 900°C for 1 h, after evidence that higher temperatures and longer annealing times resulted in a de-wetting process, where bare substrate spots coexisted with film-covered spots.

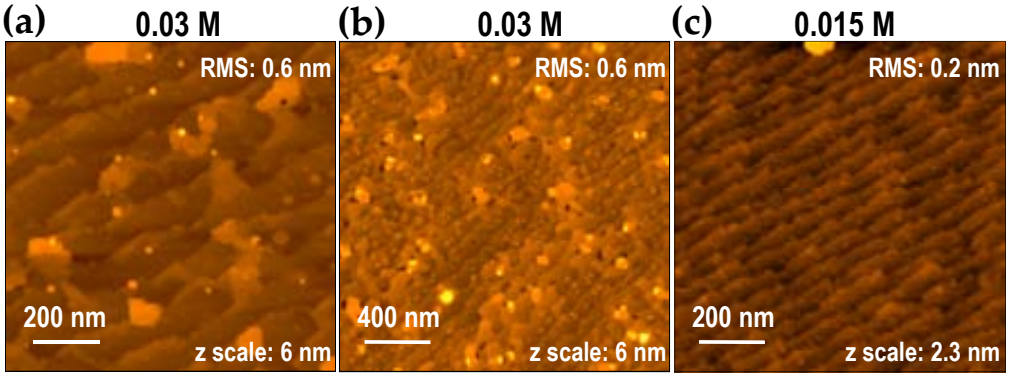


**Fig. 3.6:** *AFM topography analysis of three LSMO thin films grown onto three different STO substrates. The heat-treatment was 900°C 1 h for all.*

We have thus seen that the LSMO on STO ultra-thin film morphology is fully determined by the STO substrate surface underneath. The differences from one film to another simply reflect the substrate condition, from wider to narrower terraces, or from rougher to smoother films, depending on the quality of the substrate step-terrace structure. These results underline the high mobility of the LSMO/STO system at 900°C, with atoms finding their preferred positions, i.e. those which match the substrate crystalline structure. Furthermore, it would appear that the interface energy between LSMO and STO is very low: the lower the interface energy, the more 2D-like is the film growth, i.e. the smoother the

film tends to grow. The latter will be better understood in comparison with the 3D nanostructure results obtained on non-perovskite substrates, discussed in Part 2 of this chapter.

### LSMO on LAO

Identical processing conditions were applied to the growth of LSMO thin films on LAO substrates, previously heat-treated as in the case of STO. Recall that the *standard treatment* of LAO substrates almost invariably led to well-defined stepped surfaces, displaying smooth terraces with well reconstructed edges, at variance with the less predictable STO surfaces (see Chapter 2). Remarkably, the resulting thin films were found to exhibit less reproducible morphologies than those obtained from LSMO on STO: not all of the films, although grown identically, reflected the underlying LAO step-terrace architecture. Fig. 3.7 shows three LSMO/LAO films (0.03 M) after 900°C 1 h heat-treatment. Narrow terraces can be easily distinguished in Fig. 3.7 (a) but not in Figs. 3.7 (b) or (c); in the latter samples the film surface shows either small islands (b), or holes (c), also evidenced in the line profiles below. We also observed that the films reproducing the underlying LAO surface have a tendency to segregate nanoislands as the ones, ∼20 nm high, seen in Fig. 3.7 (a). Such islands greatly increase the RMS roughness [∼2.4 nm for Fig. 3.7 (a)]. Although less pronounced, we also observed this same trend toward nanoisland segregation in LSMO on STO, where nanoislands had a typical height below ∼5 nm. Previous results in our group have reported the spontaneous outcropping of La-Sr oxide islands in the case of thicker LSMO films ($t$∼25-60 nm) grown on STO and LAO also by chemical methods [6, 140, 160]. Nevertheless, at this point, the specific composition of the nanoislands segregated in the present $t \lesssim 10$ nm ultra-thin films remains unclear.

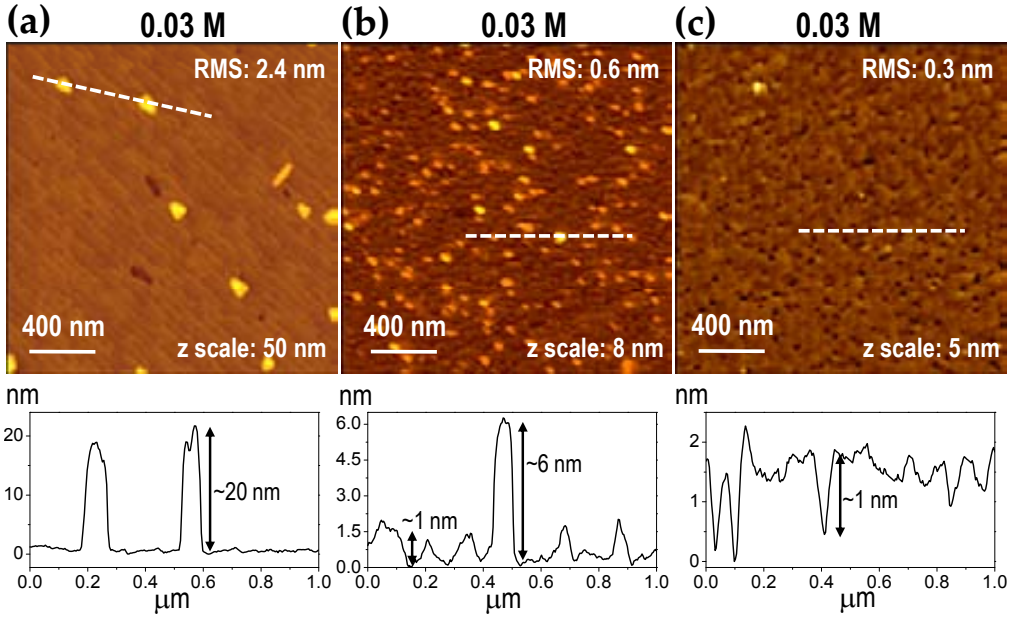


**Fig. 3.7:** *AFM topography analysis of three LSMO thin films grown onto three different LAO substrates, using 0.03 M solution concentrations and identical heat treatment of 900°C for 1 h. While (a) displays the underlying substrate step-terrace morphology, (b) and (c) exhibit rougher films with either little islands (b) or little holes (c). The outcropped islands in (a) are around ∼20 nm in height.*

Fig. 3.8 shows a magnified image of the step-terrace morphology exhibited by the sample of Fig. 3.7 (a). Note that an area featuring no outcropped nanoislands shows a very smooth surface, with RMS roughness of ∼0.2 nm and a low $z$ height scale. Nevertheless, we also identify the presence of holes, with typical depths of around ∼1.5 nm, which correspond to around 4 LSMO unit cells. Besides, the heights of the LSMO film steps are not uniform, but combine instead integer and half-integer multiples of the LSMO unit cell, as observed in the line scan of Fig. 3.8 (b).

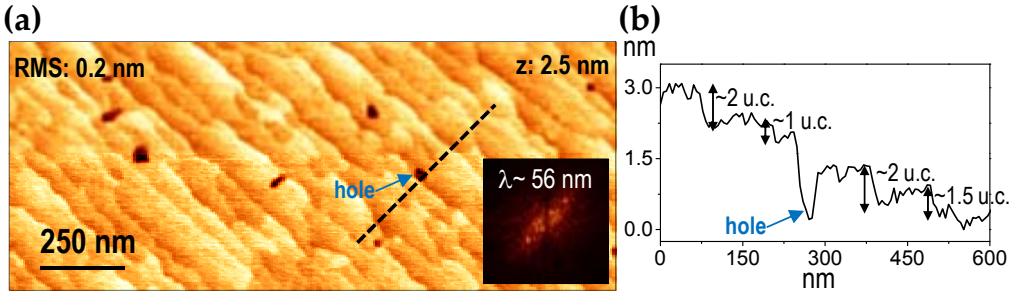


**Fig. 3.8:** *(a) AFM image of the sample in Fig. 3.7 (a) showing the detailed step-terrace morphology of the LSMO film. The terrace average width is λ∼56 nm. (b) Line scan along the dashed line in (a). The steps in the LSMO layer exhibit integer and half-integer multiples of the LSMO unit cell.*

We may conclude that, at variance with LSMO/STO ultra-thin films, LSMO/LAO films show a less predictable morphology, alternating step-terrace architecture with other rougher configurations that display small islands or even holes. The nominal lattice misfit for LSMO on LAO is notably larger than for STO ($\epsilon$∼-2% against $\epsilon$∼0.9%), in addition to changing sign from tensile to compressive. A tendency of the film towards relaxation caused by this larger strain energy could explain our observations of a greater surface disorder in LSMO/LAO systems. In other words, as a consequence of a partial or total relaxation, the film could exhibit a larger freedom with respect to the epitaxy imposed by the substrate, and, thus, a greater surface disorder. The main characteristics of the strain state of these ultra-thin films are examined in the following section.

### 3.2.2 Epitaxial relationship, strain, and microstructure

To be able to identify the LSMO structure we conducted X-ray diffraction (XRD) experiments (Theta-2Theta, phi-scans, and reciprocal space maps) and scanning transmission electron microscopy (STEM) cross-section analysis. The former, either using a X-ray diffraction standard diffractometer (Bragg-Brentano geometry) or a diffractometer with a 2D detector (GADDS D8, Advance System, Bruker) (see Appendix A), were unable to resolve the LSMO peaks in samples with 0.015 M and 0.03 M concentrations. The main difficulties stem from the small amount of material (which yields a low signal) and from the fact that the substrate peaks, very intense, fall next to the LSMO peaks. Nevertheless, we were able, in the case of LAO, to identify the LSMO peak in thin films grown from 0.1 M solution concentrations, which are expected to display a layer nominal thickness of around ∼10 (±5) nm. Fig. 3.9 shows the XRD intensity profile obtained from a phi-scan around the $(110)_{\mathrm{LAO}}$ reflection ($2\theta$∼33.4°), for three different samples: a bare LAO substrate, heat treated at 900°C for 5 h following the *standard treatment* (named $\mathrm{LAO}_{s.t.}$), and two LSMO thin films grown on $\mathrm{LAO}_{s.t.}$ substrates from 0.05 M and 0.1 M LSMO solutions, heat-treated at 900°C

for 1 h. A shoulder is detected in the 0.1 M sample at a $2\theta$ that coincides with the value expected for the $(110)_{\mathrm{LSMO}}$ reflection in bulk LSMO ($2\theta$~32.7°). Since Theta-2Theta scans of the same film (not shown) give no peaks other than the (00l), (which are unidentified due to the proximity with the substrate) we can deduce that the LSMO grows epitaxially, i.e. $(001)_{\mathrm{LSMO}}$ $(001)_{\mathrm{STO}}$. A hint of a shoulder is also detected in the more diluted 0.05 M sample (red curve), but its resemblance with the tail from the substrate reflection (black curve) makes it difficult to unambiguously ascribe it to LSMO. We thus conclude that for 0.1 M concentrations [thickness $t$~10 (±5) nm] our XRD equipment is close to the limit of resolving the LSMO structure on LAO.

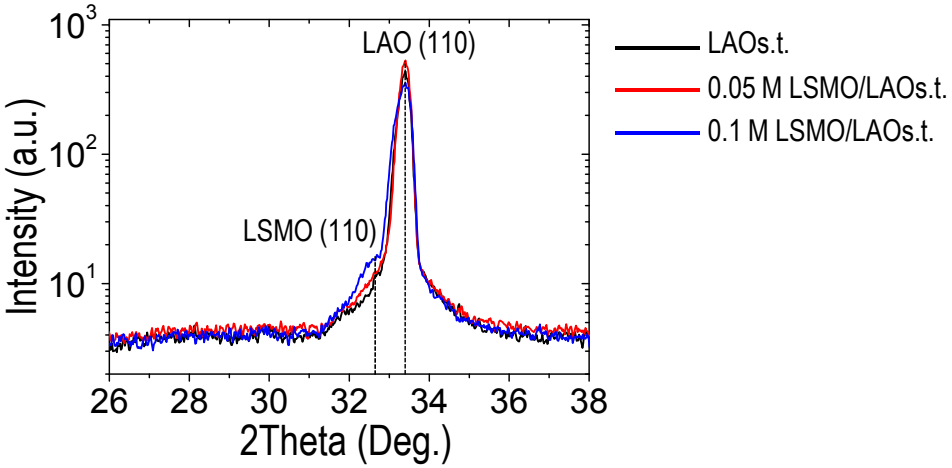


**Fig. 3.9:** *Comparison of the XRD measurements done around the $(110)_{LAO}$ reflection for three different samples: a bare LAO substrate after the standard heat treatment ($LAO_{s.t.}$), and two LSMO thin films grown out of 0.05 M and 0.1 M precursor solutions.*

The LSMO phase in samples from 0.03 M concentrations [nominal thickness $t$~3.5 (±0.5) nm] was identified by cross-section $Z$-contrast STEM studies*. $Z$-contrast imaging is indeed optimal for addressing the crystalline quality, the epitaxial relationship, as well as the strain state of nanostructures. Note that the contrast in a $Z$ contrast image is roughly proportional to $Z^2$, $Z$ being the atomic number of the imaged element. Consequently, heavy atom columns will appear brighter than those featuring light atoms. Fig. 3.10 shows two STEM images of a LSMO thin film (0.03 M) grown onto a STO substrate. The local thickness of the film derived from the image is $t$~2.4 nm (~6 u.c.). The film is highly crystalline and grows cube-on-cube on top of the STO substrate, i.e. $(001)_{\mathrm{LSMO}}$[100] $(001)_{\mathrm{STO}}$[100], which is precisely the configuration that yields the minimum lattice mismatch, $\epsilon$~0.9%. The interface is abrupt and shows no structural disorder, i.e. no misfit dislocations are observed in scanned lengths as large as ~16 nm. These results indicate a fully strained film, where the LSMO has its bulk lattice value ($a_{LSMO}$~3.873 Å) slightly expanded in-plane in order to match the STO lattice parameter ($a_{STO}$~3.905 Å). In turn, such in-plane expansion results in the shrinking of the out-of-plane lattice parameter in an overall tetragonal distortion of the lattice.

It is expected that such ultra-thin LSMO films should be fully strained given their small thickness. Additionally, reciprocal space maps in CSD-grown ~25 nm thick LSMO

* $Z$-contrast imaging, high angular annular dark field (HAADF)-$Z$-contrast, or simply STEM will be indistinctly used throughout this chapter in reference to Scanning Transmission Electron Microscopy.

films on STO, done previously in the group, showed fully strained films [6, 140]. The Poisson ratio $\nu$ of a material relates its in-plane extension (compression) with the consequent out-of-plane compression (extension), by means of the expression $\nu$=$\epsilon_{zz}/(\epsilon_{zz}$-$2\epsilon_{xx})$, where $\epsilon_{xx}$=$(a_{xx}$-$a_{bulk})/a_{bulk}$ and $\epsilon_{zz}$=$(a_{zz}$-$a_{bulk})/a_{bulk}$ are, respectively, the in-plane and out-of-plane deformations relative to the film bulk lattice parameter, ($a_{bulk}$=$a_{LSMO}$). Typical values for LSMO span from $\nu$=0.34 [64] to $\nu$=0.37 [65], which imply an out-of-plane lattice parameter between 3.840 Å and 3.835 Å (considering a fully strained LSMO film, i.e. $a_{xx}$=$a_{STO}$=3.905 Å). In addition to the strain state of the films, further data on the chemical composition of film and interface (for instance, on possible interdiffusion) can be obtained in principle from STEM measurements combined with EELS (electron energy loss spectroscopy). Such measurements are currently underway.

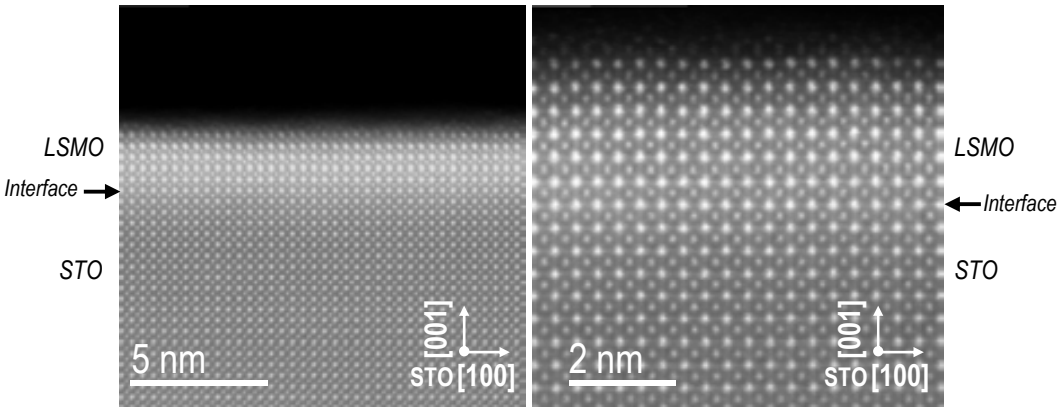


**Fig. 3.10:** *Z-contrast cross-section images of a LSMO thin film (t∼2.4 nm) on a STO substrate. The film grows coherently with a cube-on-cube epitaxy. Courtesy of M. Roldán and J.Gázquez.*

Analogously to LSMO on STO, LSMO films grown on LAO are also highly crystalline and show no secondary phases within the film matrix. Fig. 3.11 shows a $Z$-contrast image corresponding to the sample of Fig. 3.7 (a) and Fig. 3.8. Fig. 3.11 (a) reveals that the film has some discontinuities (recall the holes pointed out in Fig. 3.8), and that it is constituted of flat terraces of various thickness, with values mainly between 2-7 nm. A closer inspection of one of the terraces [Fig. 3.11 (b)] shows the transition from a region with bare substrate (a hole) to a LSMO terrace, which appears faceted in the $(101)_{\mathrm{LSMO}}$ lateral and the $(001)_{\mathrm{LSMO}}$ top planes. Remarkably, all of the steps present in the film exhibit lateral facets oriented along the $(101)_{\mathrm{LSMO}}$ crystallographic plane, suggesting that their surface energy is comparable to the surface energy of the $(001)_{\mathrm{LSMO}}$ planes. This is surprising as the {100} planes are commonly assumed to be the least energetic in other perovskite structures such as STO [161]. Concerning the epitaxial orientation, LSMO grows on LAO with a cube-on-cube epitaxy, i.e. $(001)_{\mathrm{LSMO}}$[100] $(001)_{\mathrm{LAO}}$[100], as on STO. At variance with STO, however, films on LAO exhibit misfit dislocations with Burgers vector $b$=a$_{LAO}$[100], spaced at distances ∼17 nm, in good agreement with the theoretical $|b|/\epsilon$∼18 nm distance expected for a complete misfit relaxation of the film. Fig. 3.12 shows a high magnification STEM image of the LSMO film on LAO, featuring two misfit dislocations at the interface. Note that the presence of the dislocations produces a bending of the film surface. Such dislocations are easily detectable after Fourier filtering the image. As for LSMO on STO, EELS chemical analysis is currently underway for LSMO on LAO.

In summary, CSD-grown LSMO ultra-thin films on STO and LAO substrates ($t$∼2-5

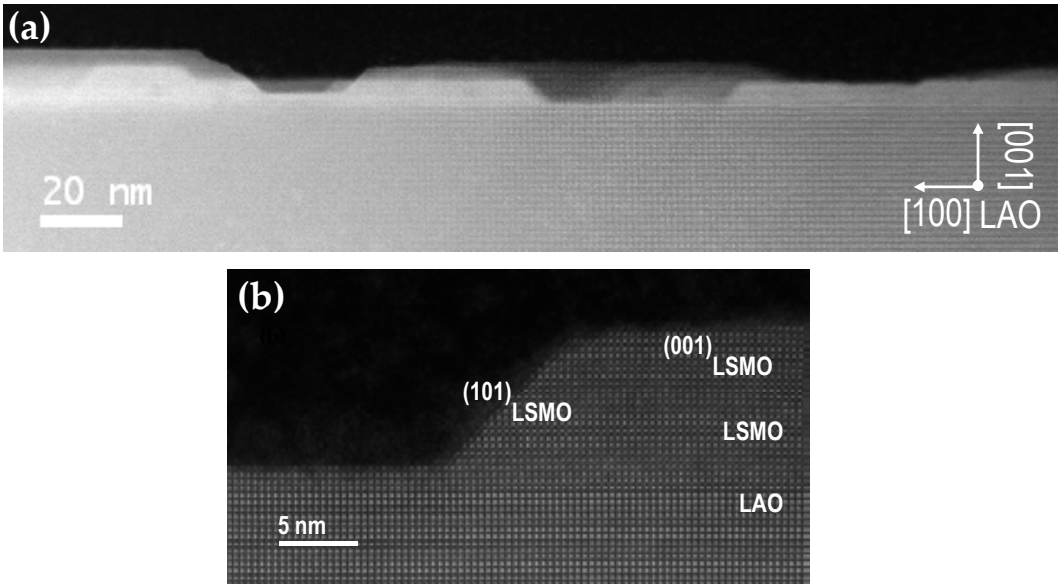


**Fig. 3.11:** *Z-contrast cross-section images of a LSMO thin film on a LAO substrate. (a) The film grows with a cube-on-cube epitaxy and features various thicknesses in the 2-7 nm range. (b) The LSMO terraces are faceted in the $(101)_{LSMO}$ lateral and $(001)_{LSMO}$ top planes. Courtesy of M. Roldán and J.Gázquez.*

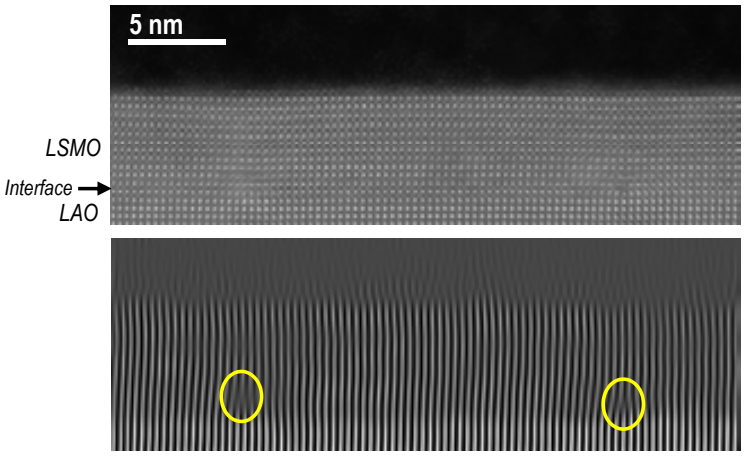


**Fig. 3.12:** *Z-contrast cross-section image (top-row) and its corresponding Fourier transform filtering image (bottom-row) of the LSMO ultra-thin film on LAO, which displays two misfit dislocations, ∼17 nm apart. Note the bending on the film surface produced by the dislocations at the interface. Courtesy of M. Roldán and J.Gázquez.*

nm) exhibit high crystallinity and no spurious phases within the matrix. They grow epitaxially with a cube-on-cube orientation. While on STO the LSMO films grow fully strained, they exhibit a completely relaxed structure when grown, after identical processing, onto LAO. We have also observed that LSMO terraces of different thickness coexist in the case of LSMO on LAO; these appear faceted in oblique $(101)_{\mathrm{LSMO}}$ and top $(001)_{\mathrm{LSMO}}$ crystal planes.

## 3.3 Macroscopic magnetic and transport properties of ultra-thin LSMO films on STO and LAO

We now move to the study of the magnetic and transport properties of the ultra-thin LSMO films described above. **Macroscopic magnetic measurements** were done using a superconducting quantum interference device (SQUID) at temperatures between 10 to 300 K and varying magnetic fields from 0 to 7 T. Both 0.03 M LSMO films grown on STO and on LAO (nominal average thickness $t$∼3.5±0.5 nm), annealed at 900°C for 1 h, showed ferromagnetic hysteresis in the whole temperature range up to room temperature (RT). Fig. 3.13 shows the resulting magnetization loops at 35 K. Both films exhibit very similar behavior, with a saturation magnetic moment $m_S$∼2×10$^{-5}$ emu for LSMO/LAO and $m_S$∼1.8×10$^{-5}$ emu for LSMO/STO. We can calculate the total volume of material from the estimated film thickness ($t$∼3.5 nm), which is assumed to be homogeneously distributed throughout the 5 ×5 mm$^2$ substrate surface. The corresponding saturation magnetization (for $m_S$∼2×10$^{-5}$ emu) is then $M_S$=230±40 kA/m. The large error stems from the substantial uncertainty in the thickness value (±0.5 nm) . Bulk LSMO (with 3.7$\mu_B$ per Mn atom) [64, 82] exhibits a magnetization of ∼590 kA/m, which is around 2.5 times higher than the value we measure in these ultra-thin films. In other words, only around $t$∼1.36 nm from the nominal average thickness $t$∼3.5 nm would contribute to the measured magnetic signal, if we should consider these 1.36 nm to contribute with a bulk-like 590 kA/m magnetization. The detailed inspection of the center of the hysteresis loops reveals some differences between the LSMO thin film grown on STO and on LAO: the latter exhibits higher remanence values (∼9×10$^{-6}$ emu against ∼5×10$^{-6}$ emu) and coercive fields ($\mu_0 H_c$ ∼140 Gauss against $\mu_0 H_c$ ∼115 Gauss). High coercive field values have been related to the presence of misfit dislocations at the film-substrate interface [22], which is in agreement with the dislocation-relaxed LSMO/LAO interface displayed by our solution-derived LSMO thin films.

The temperature dependence of the magnetic moment is given in Fig. 3.14. We have normalized both curves to the magnetic moment value at low temperature ($T$=16 K) to better compare them. We show, however, the high $T$ range to avoid the paramagnetic slope present at low temperatures, which is most probably caused by impurities within the substrate . Note that the applied in-plane magnetic field was 100 Gauss for LSMO/LAO films and 500 Gauss for LSMO/STO films. The magnetic moment, deduced from each of the loops in Fig. 3.13, is $m$∼1.1×10$^{-5}$ emu for these two field values, which constitutes a reasonable compromise between low applied magnetic field and a measurable magnetic signal. Both curves in Fig. 3.14 give similar Curie temperature $T_C$∼350 K, although LSMO on STO exhibits slightly lower magnetic moment values.

More details on the uncertainty of the thickness are given in Part II of this chapter.
This issue will be further discussed in Part II of this chapter.

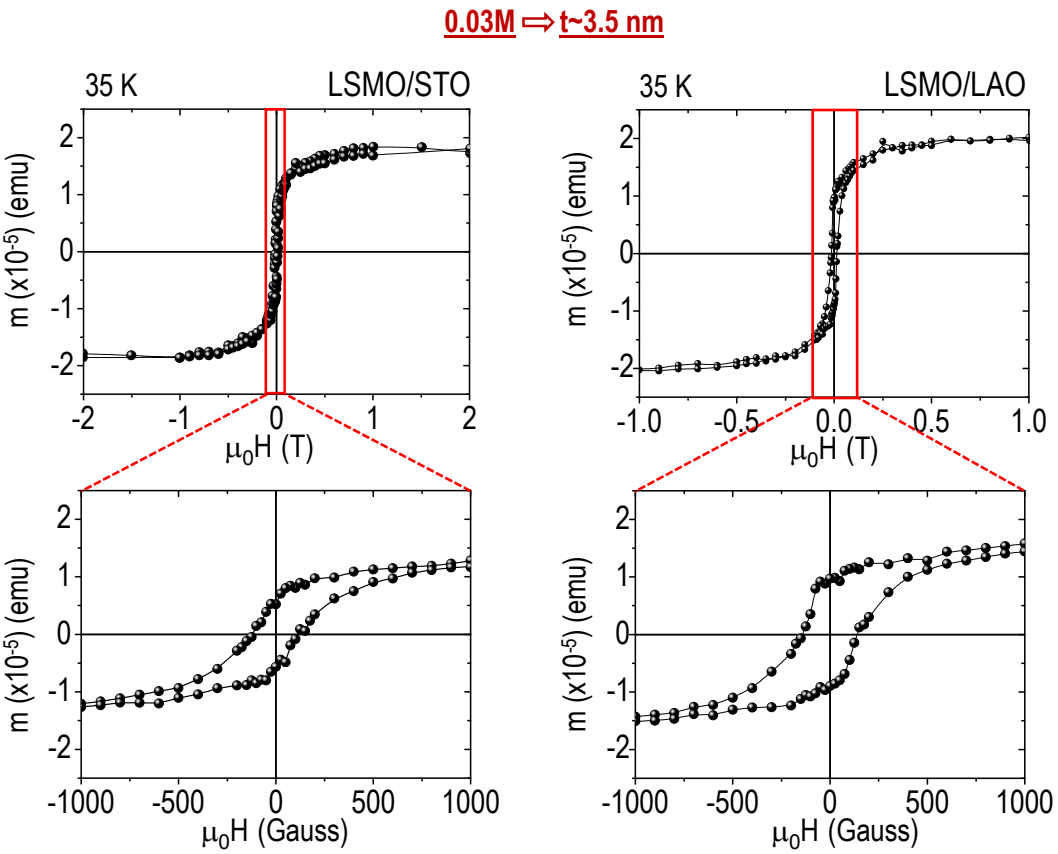


**Fig. 3.13:** *Magnetization loops (35 K) for 0.03 M LSMO thin films on STO and on LAO. Films display a saturation magnetization $m_S \sim 2\times10^{-5}$ emu, which corresponds to a volume magnetization $M_S$=230±40 kA/m, as deduced from the film thickness t=3.5±0.5 nm value.*

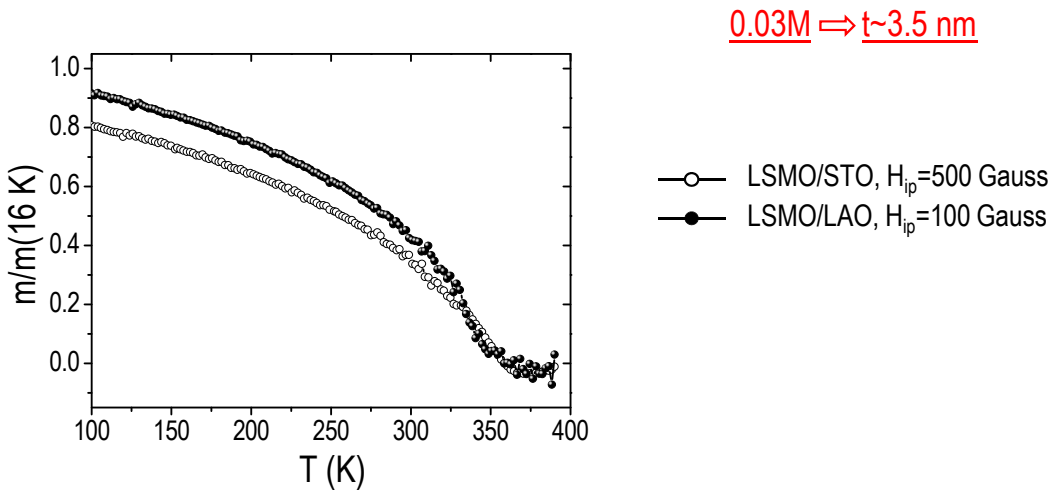


**Fig. 3.14:** *Normalized temperature dependent magnetic moment for LSMO ultra-thin films on STO (open dots) and LAO (full dots). The magnetic field (500 Oe and 100 Oe) was applied in-plane.*

There is large amount of work done concerning the study of the magnetotransport properties of LSMO thin films. Among these, many works have focused on the effect of epitaxial strain [22–25, 65, 162–165]. These works mainly examine the influence of strain by decreasing the film thickness and/or by growing the film onto different single crystal substrates. It is widely accepted that strain is accommodated by the tilt and/or distortion of the $MnO_6$ octahedra, hence influencing the $Mn^{3+}$-$O^{2-}$-$Mn^{4+}$ bond angle and, in consequence, the hopping of the electrons responsible for the (ferro)magnetic and metallic behavior of manganites [17, 71]. The general trend observed is a decrease of $T_C$ and of the magnetization with increasing strain and decreasing thickness. For instance, recently published data show that increasing tetragonal tensile distortions ($\epsilon\sim$-0.13% to $\epsilon\sim$2.5%) on the structure of PLD-derived $La_{0.67}Sr_{0.33}MnO_3$ thin films (thickness ∼10-40 nm) yield progressively lower magnetization and $T_C$ values [22]. Previously, in their work of 2009, Adamo et al. gave evidence of how commensurately strained $La_{0.7}Sr_{0.3}MnO_3$ ∼22 nm films, grown by molecular beam epitaxy (MBE) over a large number of different oxide substrates, display $T_C$ values in agreement with the theoretical predictions by Millis and co-workers [166]. According to their experimental results, fully commensurate compressively strained LSMO on LAO ($\epsilon\sim$-2.3%) shows a highly depressed $T_C$ value around ∼290 K, while when grown on STO, i.e. under a tensile and substantially lower mismatch ($\epsilon\sim$+0.6%), $T_C$ is ∼350 K, i.e. close to the bulk LSMO value.

Our STEM data for ultra-thin ($\lesssim$10 nm) LSMO films pointed at fully strained 0.03 M films (i.e. $t\sim$3.5 nm) on STO, while presenting a relaxed microstructure for the case of 0.03 M LSMO on LAO. The latter is certainly a remarkable result if we consider that for PLD films it is generally reported that full LSMO relaxation occurs at $t\sim$30 nm (see e.g. the work of Angeloni et al. [163]). Angeloni and co-workers also give evidence of fully strained films of $t\sim$8 nm thickness [163]. These results highlight that different growth techniques (i.e. CSD or PLD) have a different impact on the microstructure of the films. In line with the PLD films by Angeloni et al., Tsui and co-workers also report fully coherent $t\sim$25 nm thick LSMO films on LAO grown by sputtering [162]. On the other hand, regarding LSMO on STO, it is equally noteworthy that the solution-derived films here discussed (estimated average thickness ∼3.5±0.5 nm) show a clear ferromagnetic behavior, with $T_C$ above 350 K. Although the theoretical model by Millis et al. (verified by Adamo et al. in ∼22 nm MBE LSMO films [65]), would not predict a substantial decrease in $T_C$, the actual majority of experimental results on ultra-thin LSMO films report highly suppressed $T_C$ values. Fig. 3.15 reproduces the temperature dependent magnetization measurements on ultra-thin LSMO films on STO (PLD grown) of two state-of-the-art works in the literature. They both show the gradual suppression of $T_C$ for decreasing film thickness values. At ∼8 u.c. (∼3.2 nm) either the fading of the ferromagnetic curve (Kim et al. [23]) or a clear reduction of $T_C$ below 300 K (Huijben et al. [165]) are measured.

In addition to macroscopic magnetic properties, **electric transport properties** of the CSD-derived thin LSMO films were also investigated. The temperature dependence of resistivity, $\omega(T)$, was measured in the standard four-probe geometry, using a physical properties measurement system (PPMS, Quantum Design). Fig. 3.16 shows the $\omega$ vs. $T$ behavior of eight solution-derived LSMO films grown on LAO and STO from various precursor solution concentrations ranging from 0.03 M (nominal average thickness $t\sim$3.5 nm) to 0.1 M (nominal average thickness $t\sim$9 nm). The thinnest films (0.03 M), both on STO and on LAO, are insulating in the whole measurable $T$ range, with LSMO/STO showing the most resistive behavior. This result suggests that the misfit dislocations present at the

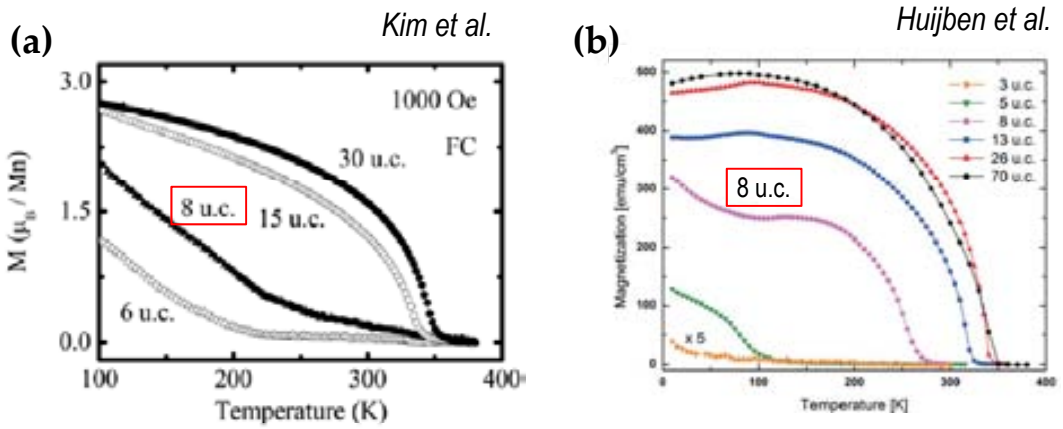


**Fig. 3.15:** *Temperature dependent magnetization measurements for PLD-grown LSMO ultra-thin films on STO. In-plane external magnetic fields of (a) 1000 Gauss [23] and (b) 100 Gauss [165] were used. At 8 u.c. (3.2 nm thick films) the FM behavior is highly depressed.*

LSMO/LAO interface, while increasing the $H_C$ values, do not affect the transport properties of the film. Similar conclusions were reached for PLD-grown manganite films by Yang et al. [22]. Conversely, for films grown from $\geq$0.06 M concentrations a metal-insulator transition is measured, and the resistivity values of LSMO/STO systems appear below those obtained for LSMO/LAO films. Note also that the resistivity of the LSMO films decreases with increasing the concentration (i.e. with larger average film thicknesses). The estimated or nominal average thicknesses for 0.03 M, 0.06 M, 0.07 M, and 0.1 M are 3.5 nm, 5.5 nm, 6.3 nm, and 9 nm, respectively Thus, summarizing, we observe that $\sim$5.5 nm sets a limit above which CSD-derived LSMO thin films show a metallic behavior for low temperature range, while for $\sim$3.5 nm and below we expect insulator behavior with no associated metal-insulator transition. In LSMO/STO multilayers grown by PLD, Kourkotis et al. recently measured metallic behavior in LSMO films as thin as $\sim$2 nm, provided that there is no disorder caused by chemical intermixing. With increasing disorder, however, identified by means of HAADF STEM, they observe that films with the same thickness become insulator [167]. The presence of a similar kind of disorder in our CSD-derived films cannot be ruled out at present. Indeed, further STEM measurements to identify oxygen vacancies, cationic intermixing...etc. are underway.

Concerning the values of the metal-insulator transition temperature, $T_{MI}$, Fig. 3.16 shows that for 0.06 M films ($\sim$5.5 nm) on LAO and STO $T_{MI}$ is around 200-250 K, and that it takes higher temperature values for increasing concentrations. This tendency is further highlighted in Fig. 3.17, which shows explicitly the $T_{MI}$ values for LSMO films grown from different solution concentrations. From Figs. 3.16 and 3.17, thus, it follows that $T_{MI}$ varies with the thickness of the LSMO film and that it shows values below 350 K. Remarkably, all of these LSMO thin films, regardless of the solution concentration and of the substrate underneath (whether STO or LAO), showed a Curie temperature $T_C\sim$350 K. In other words, the metal-insulator transition and the ferromagnetic-paramagnetic transition appear decoupled in these thin manganite films.

Such striking result indicates that a mechanism different from the intrinsic physics re-

The estimated thickness values are deduced from the LSMO on YSZ self-assembled nanoisland systems, as explained in section 3.4.1 of Part II of this chapter.

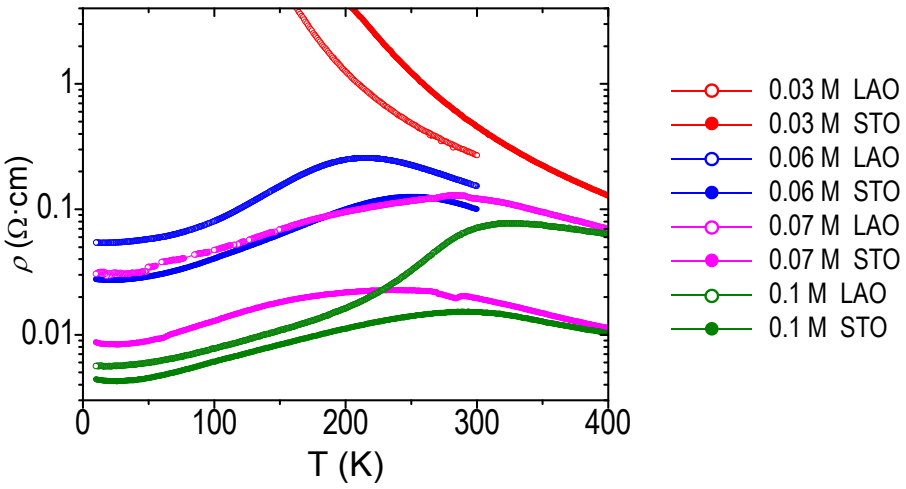


**Fig. 3.16:** *Temperature dependence of the resistivity for LSMO thin films grown on STO and LAO from precursor solution concentrations between 0.03 M and 0.1 M. Courtesy of A. Palau.*

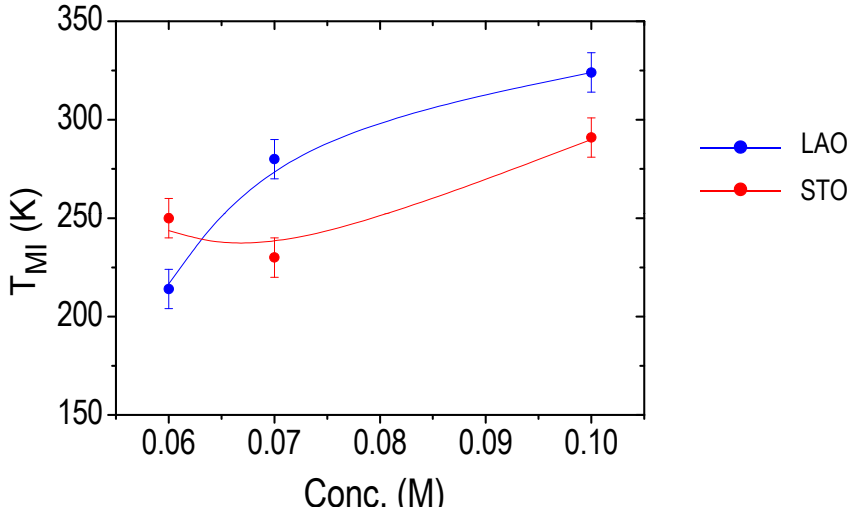


**Fig. 3.17:** *Metal-insulator transition temperatures for the different LSMO films grown on LAO and STO from different precursor solution concentrations. Courtesy of A. Palau.*

lated to manganites must be at play in our scenario of solution-derived LSMO films with nominal thickness below ∼10 nm. An Anderson type of localization in 2D films, where electrons are immobilized due to their multiple scattering with random defects in the potential of the solid [168], could, for instance, explain a metal to insulator transition in our very thin films, where the magnetic ordering is not necessarily affected. These interesting results, however, remain preliminary and thus future work is necessary to ascertain the physics behind them. Fig. 3.17 also reveals that $T_{MI}$ increases with increasing solution concentration (e.g. for 0.1 M $T_{MI}$ reaches room temperature). This suggests a good agreement with previous findings in our group concerning thicker ($t$∼25 nm) CSD-derived LSMO films (grown from 0.3 M solutions) [6, 140]: for such $t$ values LSMO shows bulk-like properties with $T_{MI}$=$T_C$∼360 K, as expected in manganites. Although in our present case the decoupling of $T_{MI}$ and $T_C$ is clear for low concentration films, we must note that for very thin films below $t$∼10 nm the uncertainty in the value of $t$ is large (recall, for instance, the thickness oscillations in LSMO/LAO films discussed previously). Thus, more statistics will be needed in order to ascribe exact $T_{MI}$ values to different $t$ values.

The magnetoresistance MR, defined as -$\Delta\omega$=[$\omega$(H=5)-$\omega$(H=0)]/$\omega$(H=0) (in %), of two LSMO thin films (0.06 M, $t$∼5.5 nm) grown on LAO and STO is plotted in Fig. 3.18. The top panels show the temperature dependence of the resistivity (as already shown in Fig. 3.16) from where the MR curve is calculated (bottom panel). For zero applied field, these 0.06 M LSMO/LAO and LSMO/STO films exhibit maximum resistivity values of $\omega$∼2.56×$10^{-1}\Omega\cdot$cm and $\omega$∼1.26×$10^{-1}\Omega\cdot$cm, respectively. These numbers are around two orders of magnitude larger than the maximum resistivity value $\omega$∼1.4×$10^{-3}\Omega\cdot$cm obtained for CSD-derived 'standard' 0.3 M LSMO films [6]. By 'standard' we refer to the aforementioned LSMO 0.3 M films ($t$∼25 nm) that exhibit magnetotransport properties comparable to bulk LSMO [6]. Regarding magnetoresistance values, 0.06 M thin films show a maximum MR of ∼24% both on LAO and STO, which doubles the usual MR values registered for the aformentioned bulk-like LSMO thin films (MR∼11%) [6]. Nevertheless, further work in our group has recently shown that nanocomposite LSMO films, where canonical LSMO coexists with inclusions from other phases, show enhanced values of magnetoresistance and broadening of the MR peaks. These are there argued to stem from chemical and/or structural disorder [169, 170]. Our current results in ultra-thin LSMO films bring new data to this discussion and are worth a much deeper investigation, beyond the scope of this thesis work.

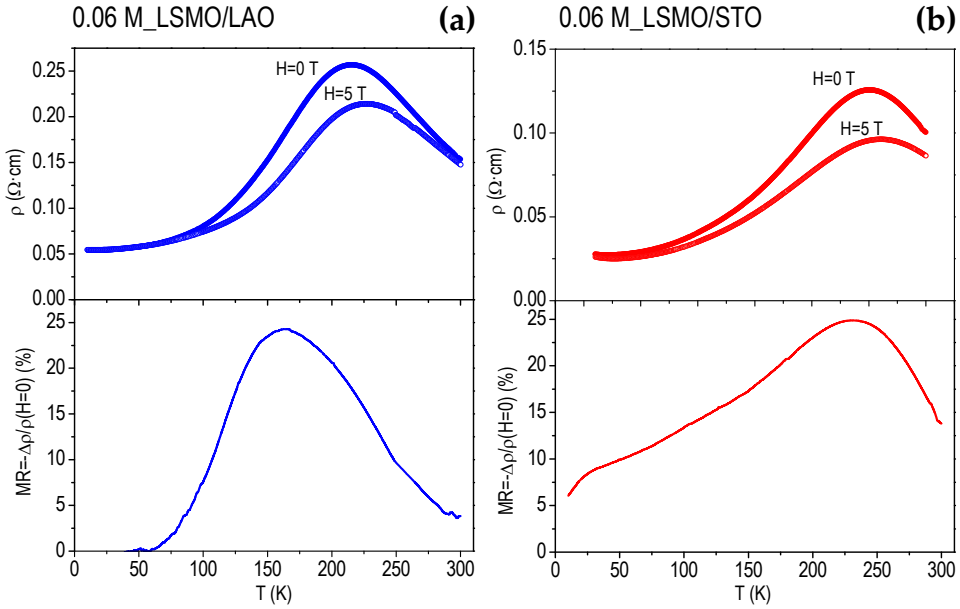


**Fig. 3.18:** *Magnetoresistance of chemically grown LSMO thin films (0.06 M, i.e. ∼5.5 nm average thickness) on (a) LAO and (b) STO substrates. Top panels show the resistivity dependence with temperature at zero applied field and at H=5 T, applied perpendicular to the film. Bottom panels show the magnetoresistance, MR, defined as -Δρ=[ρ(H=5)-ρ(H=0)]/ρ(H=0) (in %). Courtesy of A. Palau.*

# Part II

# $La_{0.7}Sr_{0.3}MnO_3$ on highly dissimilar substrates

We now turn to examine the main characteristics of CSD-grown LSMO onto non-perovskite substrates, namely YSZ and MgO. As described in Chapter 2, and also at the beginning of the present chapter, YSZ and MgO crystallize in a fluorite and a rocksalt structure, respectively. The nominal lattice mismatch with respect to LSMO ($a_{LSMO} = 3\,873$ Å) is $\epsilon$=($a_{YSZ}$- $\overline{2}a_{LSMO}$)/( $\overline{2}a_{LSMO}$)∼-6% for YSZ ($a_{YSZ} = 5\,14(7)$ Å), and $\epsilon$=($a_{MgO}$-$a_{LSMO}$)/($a_{LSMO}$) ∼+8.8% for MgO ($a_{MgO} = 4\,21(4)$ Å). Note that the minimum mismatch occurs when the LSMO crystallographic axes are rotated by 45° with respect to those of YSZ. Still, the values are high, especially when compared to the mismatch in the LSMO/STO and LSMO/LAO systems. The difference in crystal structure and the high mismatches imply that the growth scenario is now very different from that for LSMO grown on STO and LAO. Indeed, the deposition and subsequent growth of ultradiluted LSMO solutions onto YSZ and MgO results in a homogeneous dispersion of self-assembled nanoislands, in striking contrast with the previously described ultra-thin LSMO films on STO and LAO. The following sections deal with the morphological, crystallographic, microstructural, and macroscopic magnetic study of these LSMO nanoislands.

## 3.4 LSMO on YSZ

### 3.4.1 Main features of solution-derived self-assembled LSMO nanoislands on YSZ

LSMO on (001)-YSZ was grown following the guidelines of the Chemical Solution Deposition (CSD) methodology explained in section 2.3 of Chapter 2, i.e. in an identical manner as in the case of the STO and LAO substrates. Unlike solution-derived LSMO thin films on STO and LAO, the study of which was already initiated within our group, the LSMO/YSZ system was unexplored at the time we undertook this work. Previous works in our group involving the growth of $CeO_2$ nanostructures proved helpful at the beginning, pointing at the use of very diluted solution concentrations (in the 0.005 M-0.05 M range), as a strategy for obtaining highly uniform self-assembled nanoisland dispersions [157, 171–173]. Nevertheless, the particularities of the LSMO/YSZ system required that the growth parameters be optimized in the present work, essentially starting from scratch. The present section is devoted to the description of solution-derived self-assembled LSMO nanoislands on YSZ, in terms of solution concentration, growth thermal treatments, and crystallographic structure.

#### In uence of precursor solution concentration

Our first goal was to analyze the role of the material quantity in the obtained heteroepitaxy and to determine the conditions for nanoisland growth. A straightforward way of influencing the amount of deposited material is to modify the precursor solution concentration, as we commented briefly for the case of LSMO on STO and LAO. For LSMO on YSZ we studied different solution concentrations in a diluted range, from 0.006 M to 0.09 M (in Mn), on the basis, aforementioned, that we sought nanoisland formation. The spin coating parameters (velocity, acceleration, time) were kept invariant for all the samples in the manuscript. Fig. 3.19 displays AFM topography images of representative samples grown from different starting solution concentrations. The growth temperature was 900°C for all samples and the annealing times varied from 1 h to 3 h.

Fig. 3.19 (a) shows a bimodal island distribution with a majority of small islands (thickness $t$∼8 nm, lateral size $D$∼50 nm) and a minority of larger ones (a total of six in the image, $t$∼25 nm, $D$∼200 nm). Note that the latter appear surrounded by a clean stepped substrate. This strongly suggests an Ostwald ripening type of coalescence at this specific evolution stage, in which large islands grow at expenses of smaller islands, which shrink and finally disappear, their atoms having diffused towards the large structure [174].

More uniform nanoisland dispersions, with no agglomerated nanostructures, are found for the 0.015 M-0.06 M concentration range. Figs. 3.19 (b), (c) and (d) show well-defined individual nanoislands, with increasing lateral size for increasing concentration, and a reasonably narrow size distribution, especially in the 0.015 M and 0.03 M case. Increasing the solution concentration to 0.09 M, the $z$ scale drops to 20 nm and we no longer have nanoislands. Instead, we obtain a continuous granular film with RMS roughness of around 2 nm. This was further confirmed by testing for LSMO conductance with a standard two-probe multimeter, which gave a value in the order of hundreds of kOhms. Hence, the film not only is continuous, but also conducting, as expected for LSMO.

From these results we deduce that concentration ranges between 0.015 M and 0.06 M are required to obtain a self-assembled nanoisland system, i.e. a system in which the spontaneous gathering of atoms and molecules under the specific growth conditions leads to nanoislands with a narrow size distribution. After nucleation has taken place, the driving force for the particular nanoisland arrangement is the energy minimization, which, in our oxide heteroepitaxy case, involves surface and interface energies, and the elastic strain energy due to the lattice mismatch between LSMO and YSZ. In other words, we have a strain-induced nanoisland self-assembly in which the island interaction is substrate-mediated. This is the reason why the dispersion we see in the $5\ \mu m \times 5\ \mu m$ images extends uniformly all over the 5 mm $\times$ 5 mm substrate. We checked this by performing large AFM scans ($50\ \mu m \times 50\ \mu m$) at multiple different substrate spots.

Through the volume analysis of a large number of AFM images we are able to roughly deduce what amount of material we have in each sample. The equivalent thickness $t_{eq}$ parameter represents the thickness of a hypothetical film made from uniformly distributing the totality of the island volume throughout the 5 mm $\times$ 5 mm substrate surface. The results of such measurements for samples grown from different precursor concentrations are plotted in Fig. 3.20. Data corresponding to 0.09 M, 0.2 M, and 0.5 M are from a different work, reporting the AFM profilometry measurements of acid-attacked LSMO films grown on LAO and STO, also by CSD [140]. The amount of material, represented by $t_{eq}$, increases linearly with increasing concentration. Equivalent thickness data $t_{eq}$ and their associated errors, as well as the number of samples averaged, are listed in Tab. 3.1. It is worth noting that the estimated amount of thickness for the more diluted case, 0.006 M, is in the order of the monolayer. Such small amount of material implies that the first formed nuclei are likely to be inhomogeneously distributed, which may explain the subsequent non-uniform nanoisland distribution, with agglomerations, observed in Fig. 3.19 (a).

#### In uence of annealing time

In a closed system as the one we have, where the whole amount of material is present from the initial deposition stage, it is expected that kinetic events such as atomic diffusion should lead the system towards its thermodynamic equilibrium. By increasing the annealing time

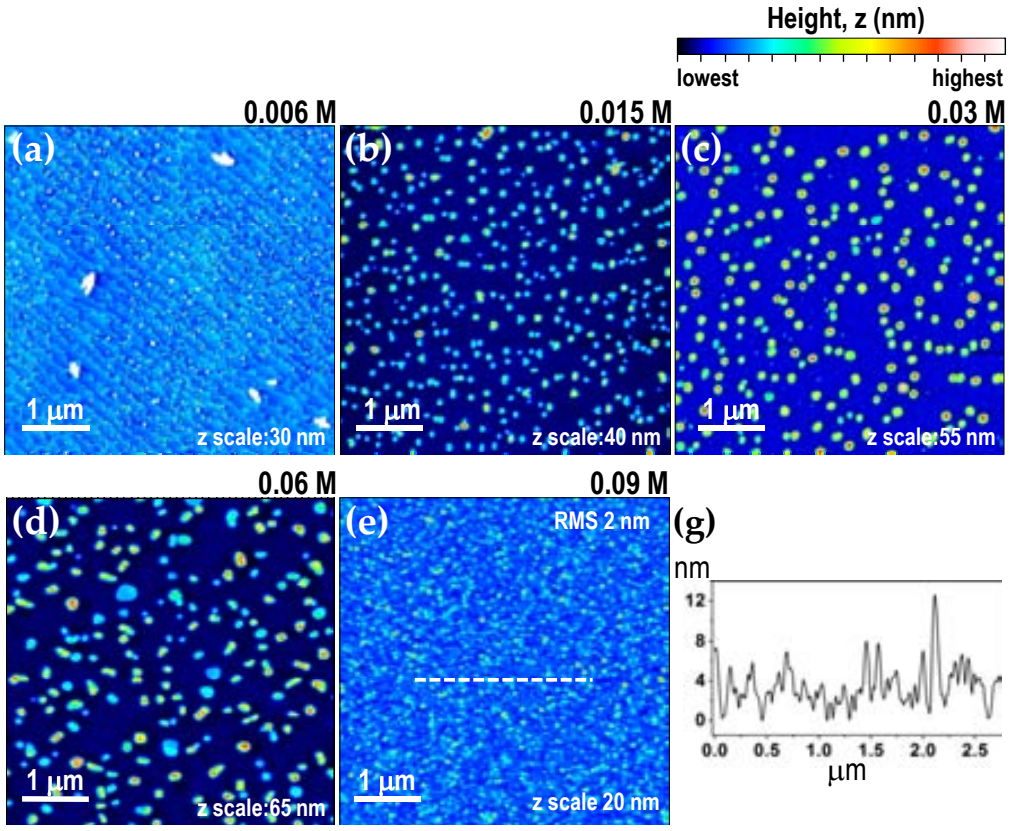


**Fig. 3.19:** *5µm × 5µm AFM topography images of the nanoscale LSMO systems resulting from deposition and growth of different solution concentrations. Growth T was 900°C and annealing times varied between 1 h to 3 h. (a) At 0.006 M, the little amount of material may lead to nucleation inhomogeneities, reflected in the bimodal nanoisland distribution. (b),(c)&(d) For concentrations in the 0.015 M to 0.06 M range we observe a homogeneous dispersion of well-defined nanometric islands, with narrower size distribution. (e) For 0.09 M, islands no longer develop and the resulting system is a continuous film with a ∼2 nm RMS roughness. (g) Line scan corresponding to the dashed line in (e), showing the roughness profile of the film.*

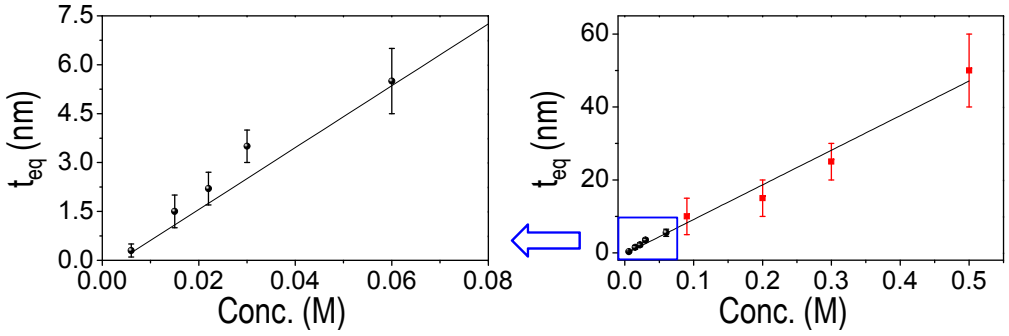


**Fig. 3.20:** *LSMO precursor solution concentration plotted against the equivalent LSMO layer thickness. Black dots are all from measurements on LSMO/YSZ systems of the present work.* $t_{eq}$ *values are deduced from AFM volume estimations. Red squares at 0.09 M, 0.2 M, 0.3 M, and 0.5 M are from LSMO layers grown by CSD on STO and LAO substrates, obtained from measuring the step of a chemically attacked layer [140].*

| Conc. (M) | $t_{eq}$ (nm) | $\Delta t_{eq}$ (nm) | No.Samples |
|---|---|---|---|
| 0 .006 | 0.3 | 0.2 | 2 |
| 0 .015 | 1.5 | 0.5 | 5 |
| 0 .022 | 2.2 | 0.5 | 3 |
| 0 .03 | 3.5 | 0.5 | 11 |
| 0 .06 | 5.5 | 1 | 2 |
| *0.09 | 10 | 5 | _ |
| *0.2 | 15 | 5 | _ |
| *0.3 | 25 | 5 | _ |
| *0.5 | 50 | 10 | _ |

**Tab. 3.1:** *LSMO precursor solution concentration with its corresponding LSMO equivalent layer thickness.*Data taken from the thesis work of C. Moreno [140].*

and stopping regularly to analyze the system, we can follow its spontaneous evolution, study the coarsening processes that take place, or evaluate the system mobility.

Fig. 3.21 reproduces the result of the growth of a 0.03 M precursor solution at 900°C for 2 h, 3 h and 12 h. At first sight, the three images of Fig. 3.21 (a) look very much alike. A dispersion of well-defined nanoislands homogeneously covers the $5\ \mu m \times 5\ \mu m$ AFM topography images, with an area coverage below the 20%. The magnified views in Fig. 3.21 (b) reveal a tendency towards substrate surface cleaning for increasing annealing times: small particles will eventually diffuse and join the larger well-defined nanoislands. In addition to the square-shape islands of the 2 h sample, the 3 h sample exhibits some triangular nanostructures, although these were found not to be characteristic of the 3 h treatment (we sometimes observed them after shorter treatments). We will see later in the chapter that they exhibit a different crystal orientation. Additionally, both in the 3 h and 12 h treated samples, a few islands show polygonal shapes different from squares or triangles. Some of them appear highlighted with white squares in Fig. 3.21 (a). It is well known that, upon annealing, nanostructure facets tend to vary due to the adsorption of adatoms. These adatoms can come from material resting on the surface. This appears to be the case in here, given the progressive cleaning of the substrate surface that accompanies nanoisland evolution towards polygonal shapes.

Ostwald ripening processes refer precisely to the above-mentioned dissolution of small islands into larger islands [174]. Other coarsening processes may coexist together with Ostwald ripening. An example is static coalescence, in which two nearby islands grow towards their equilibrium shape, meet, and subsequently merge into a larger island [157, 175]. Fig. 3.22 (a) shows a zoomed image of what at first sight resembles a uniform hexagonal island. The 3D topography and amplitude images below reveal, however, that such large island is formed by two colliding triangles. Some of the large polygonal islands inside white squares in Fig. 3.21 (a) could be the result of such processes. Fig. 3.22 (b) displays two pairs of merging islands, taken from the 12 h sample of Fig. 3.21 (a).

Let's now examine the evolution of the system from a more general point of view, i.e. considering the statistical thickness $t$ and lateral size $D$ data for a collection of nanoislands. The histograms in Fig. 3.23 evidence that heat-treated samples at 900°C for 2 h and 12 h show very similar values: in the 2 h sample we have mean thickness and lateral size values around $t\sim$30 nm and $D\sim$120 nm, respectively. At 12 h, the system evolves to island

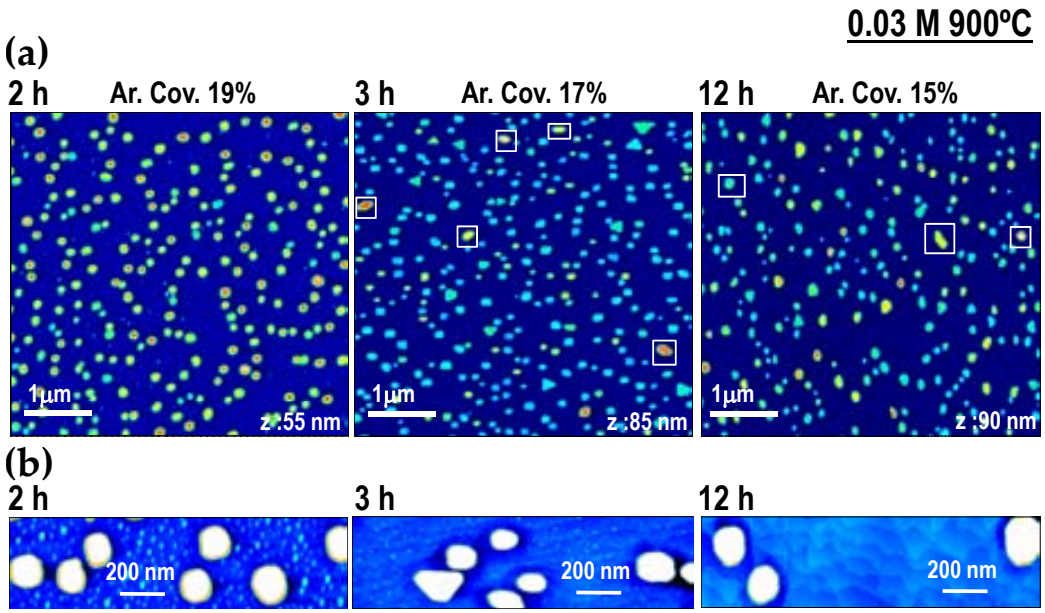


**Fig. 3.21:** *(a) 5µm × 5µm AFM topography images of self-assembled LSMO nanoislands grown at 900°C on YSZ for 2 h, 3 h, and 12 h. 0.03 M precursor solutions were used in each case. The majority of islands show square shape. Triangular islands are also observed, as well as a few polygonal structures, marked within white squares. (b) Zoomed-in images of (a) showing the progressive cleaning of the substrate upon sample annealing.*

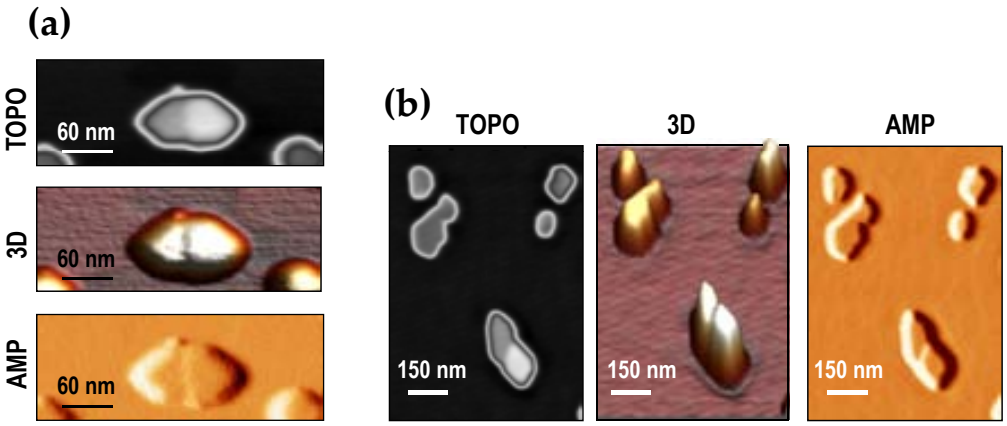


**Fig. 3.22:** *(a)&(b) 2D topography, 3D, and amplitude images of merging LSMO nanoislands. The presence of what originally were two islands is best seen in the 3D and amplitude images. It is expected that, let the system to evolve, atoms will diffuse and finally yield a fully reconstructed single structure.*

thicknesses of around $t$∼40 nm and lateral sizes $D$∼130 nm. This is also accompanied by a slight decrease in area coverage, as expected, since the same amount of material (corresponding to a 0.03 M solution) was deposited. Note that the lateral size values of islands are always much larger than their thickness values, with mean $D$ $t$ aspect ratios of around 4. This is a general trend of LSMO nanoislands, as we will confirm throughout the thesis. Interestingly, it appears that at 2 h the system was already near its thermodynamic equilibrium, showing small size variations upon subsequent annealings, even after several hours. In other words, it seems that the kinetic events which push the system towards its equilibrium have already taken place by the time we looked at the system after 2 h of annealing. This indicates a high atomic mobility of LSMO on YSZ at 900°C. It is worth noting that the heating ramp used is very slow ($3°C \cdot min^{-1}$), so the system may be already near its equilibrium at the moment of reaching the annealing plateau.

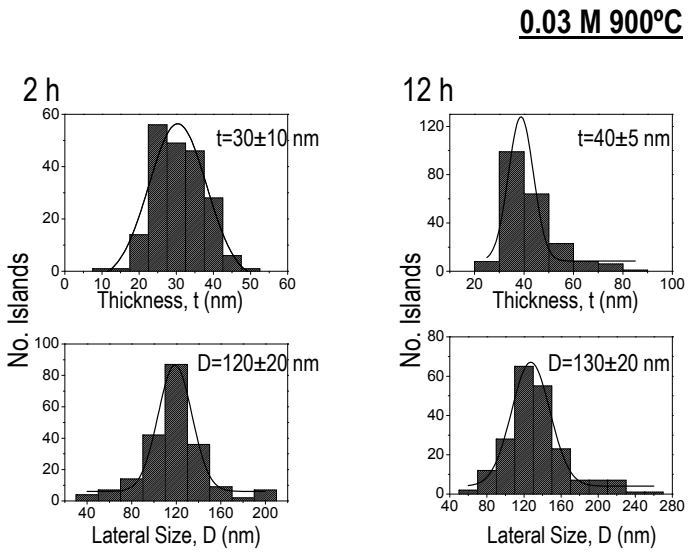


**Fig. 3.23:** *Thickness* t *and Lateral size* D *histograms extracted from 0.03 M 900°C heat-treated samples at 2 h and 12 h.* D *values were deduced from measuring the whole perimeter of each island and then assuming a perfect square. No triangles were taken in the measurement.* t *shows values in the 20-40 nm range, while* D *values are in the hundreds of nm range. The error is the standard deviation of the Gaussian fit.*

In summary, the above analysis illustrates the evolution of the self-assembled nanoisland system. This is showcased by small variations in the size range ($t$∼30 nm $D$∼120 nm) of the LSMO nanoislands on YSZ, when heat-treated at 900°C. A slight increase of the island volume in times as long as 12 h is accompanied by the substrate surface cleaning. In addition to Ostwald ripening processes (small islands coalescing into larger islands) other coalescence mechanisms have been identified, such as the static coalescence of already formed faceted islands. Overall, the slow evolution shown by the system at this temperature, along with the fact that nanoislands are well formed and faceted already in the 2 h annealing stage, suggest that, by that time, the system has already undergone the main kinetic events leading to its equilibrium state. A study of what happens at higher temperatures, where a new equilibrium might take place, results thus of great interest. Prior to this we will investigate the crystal structure of nanoislands and their epitaxial relationship with respect to (001)-YSZ.

### LSMO nanoisland crystallographic orientation

#### $(001)_{\mathrm{LSMO}}$-ORIENTED NANOISLANDS

For the sake of simplicity, in the previous sections we have referred to the self-assembled nanoislands as LSMO nanoislands. However, XRD analysis is necessary to be able to determine whether the crystal structure of our islands corresponds indeed to LSMO. We also expect to ascertain the epitaxial growth imposed by the YSZ single crystal substrate underneath. Fig. 3.24 displays a $\theta$-$2\theta$ scan corresponding to a system of self-assembled nanoislands grown from a 0.03 M solution on YSZ, processed at 900°C for 1 h. Along with the (001) intense substrate peaks we clearly identify the $(002)_{\mathrm{LSMO}}$ reflection peak at $2\theta$=46.9°. Weakly emerging from the background noise, the $(001)_{\mathrm{LSMO}}$ peak, expected less intense than the $(002)_{\mathrm{LSMO}}$, can also be observed at $2\theta$=23°. We have indexed the LSMO reflections in terms of the pseudocubic notation, as we already did for LSMO on STO and LAO ($a_{LSMO} = 3\ 873$ Å). This result already indicates epitaxial growth of the nanoislands, with their (001) planes parallel to the substrate (001) planes. The rocking curve in Fig. 3.24 (b) shows the out-of-plane texture of the nanoisland ensemble, with a large full width at half maximum (FWHM) value of$\sim$3.3°. If it were a continuous film, such broad peak would indicate a rather poor epitaxy. Nevertheless, for nanometric structures, a general peak broadening is not unexpected. Indeed, the nanoisland out-of-plane orientation is highly sensitive to the substrate structure such as surface roughness or the presence of steps and kinks on which islands nucleate and grow. This may induce the formation of tilted domains and other misorientations [176]. Also, it is well known that the accommodation of misfit strains through dislocations at the interfaces can trigger nanoisland rotations. In summary, a large number of slightly misoriented islands appears consistent with the observed rocking curve.

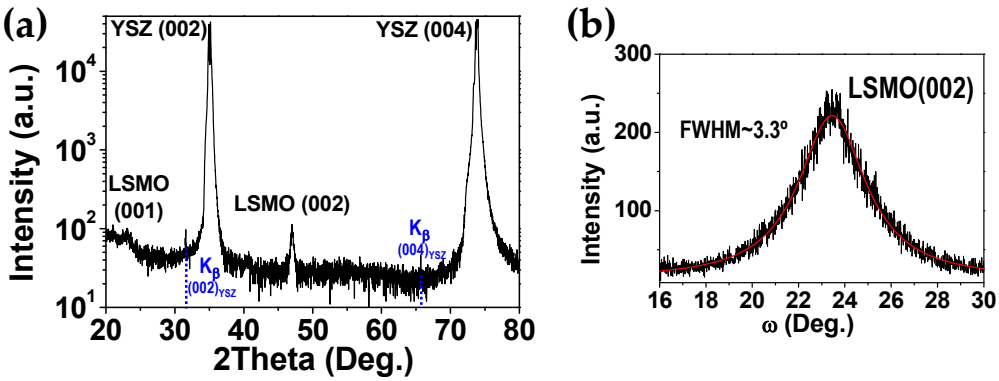


**Fig. 3.24:** *(a) $\theta$-$2\theta$ scan showing the out-of plane epitaxial growth of a self-assembled LSMO nanoisland system grown onto YSZ from a 0.03 M solution at 900°C for 1 h. (b) Rocking-curve of the $(002)_{LSMO}$ reflection exhibiting a FWHM of 3.3°.*

In order to study the in-plane epitaxial relationship between the LSMO nanoislands and the YSZ substrate we conducted phi-scan measurements with a XRD diffractometer equipped with a 2D detector (XRD$^2$ measurements, see Appendix A). Integration in $2\theta$ of the collected $2\theta$-$\gamma$ frames (with $\Delta\theta = 2°$, 180 frames in total), leads to the pole figures shown in Fig. 3.25. Both the $(011)_{\mathrm{LSMO}}$ and the $(022)_{\mathrm{YSZ}}$ poles appear at $\gamma$=45° [consistent with the out-of-plane (001) orientation], but are rotated in-plane $\theta$=45° with respect to each other, indicating that nanoislands adopt the epitaxial relationship $(001)_{\mathrm{LSMO}}[110]$ $(001)_{\mathrm{YSZ}}[010]$.

The interface arrangement $[110]_{\mathrm{LSMO}}$ $[010]_{\mathrm{YSZ}}$ of our heteroepitaxy would therefore correspond to a nominal misfit $\epsilon\sim$-6% between the [110] direction of LSMO ( $\overline{2}a_{\mathrm{LSMO}}$= 5.477 Å) and the [100] direction of YSZ ($a_{\mathrm{YSZ}}$=5.14(7) Å). This significant difference in lattice mismatch at first sight suggests a highly strained heteroepitaxy. This, however, would entail an unfavourably large building up of strain energy. Thus, it is natural to expect the relaxation of the nanostructure via misfit dislocation formation. As a matter of fact, although very roughly estimated, the LSMO lattice parameter deduced from the $\theta$-$2\theta$ scans corresponds to the bulk LSMO value, already indicating a relaxed structure.

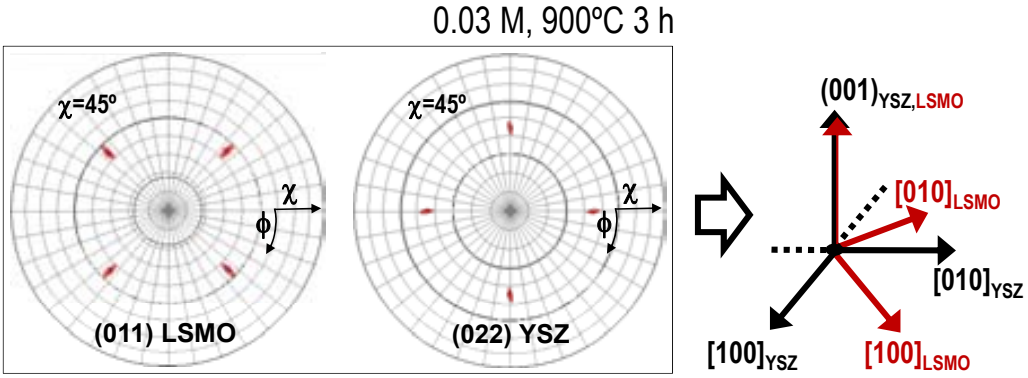


**Fig. 3.25:** *Pole figures of the $(011)_{LSMO}$ and $(022)_{YSZ}$ reflections indicating $(001)_{LSMO}$[110]//$(001)_{YSZ}$[010] oriented nanoislands. The epitaxial relationship is sketched on the right panel. The sample was 0.03 M, heat-treated at 900°C for 3 h.*

Further evidence of the nanoisland strain state and of the epitaxial arrangement was obtained using high resolution transmission electron microscopy (HRTEM) and electron diffraction (ED) measurements. Fig. 3.26 (a) shows an ED pattern of a selected area, containing both the YSZ substrate and a single LSMO nanoisland. The epitaxial relationship of the individual island with respect to the YSZ substrate agrees with the $(001)_{\mathrm{LSMO}}$[110] $(001)_{\mathrm{YSZ}}$[010] epitaxy, obtained from XRD measurements, for the whole nanoisland ensemble. Note also that the sublattices of the substrate and the nanoisland can be easily distinguished with the naked eye. Moreover, a measure of the lattice spacing separation is consistent with a complete relaxation of the lattice parameters for LSMO. A HRTEM image of an interfacial region is shown in Fig. 3.26 (b). Fourier filtering analyses reveal that the strain contrast observed at the interface corresponds to dislocations with Burgers vector $b$=($a_{\mathrm{YSZ}}$/2)[100] (evidenced with arrows in the image), with the extra half plane residing in the substrate in order to accommodate the compressive lattice mismatch in the island. The average distance between dislocations measured in the image, $\sim$4.0 nm, coincides with the theoretical value $b/\epsilon$ for a complete misfit relaxation. Our results thus confirm that the LSMO islands on YSZ are free of misfit strains. They also demonstrate the good crystalline quality within an individual island.

### $(111)_{\mathrm{LSMO}}$-ORIENTED NANOISLANDS

Despite constituting the vast majority of the nanoislands, the out-of-plane (001)-oriented nanostructures are not the only present in our LSMO/YSZ system. The triangular morphology observed in a number of samples, in fact, points at a different out-of-plane orientation. This was indeed proved in a sample exhibiting a notable amount of triangular features (around the 25% of the total island population). Fig. 3.27 shows the AFM topography im-

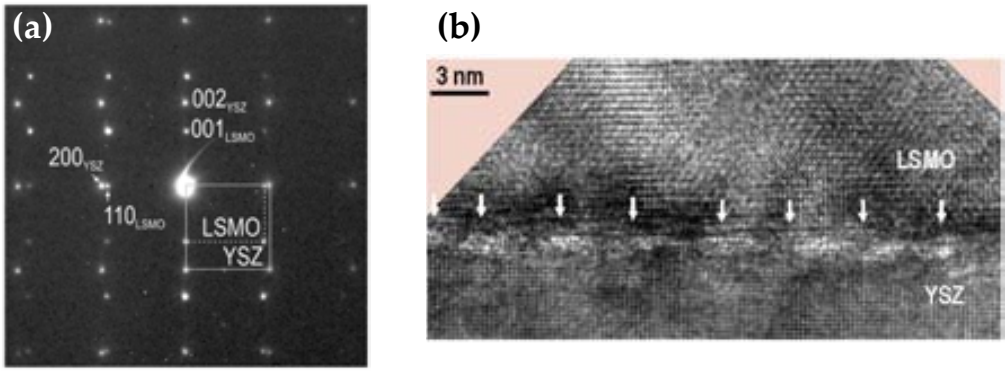


**Fig. 3.26:** *(a) ED pattern taken across the island-substrate interface. It shows the epitaxial relationship $(001)_{LSMO}[110]//(001)_{YSZ}[010]$. The LSMO and YSZ lattices are marked by dashed and continuous lines, respectively. (b) Cross-sectional HRTEM image of a (001)-oriented LSMO nanoisland, where the arrows indicate regularly spaced misfit dislocations at the island/substrate interface. The LSMO island and the YSZ substrate are viewed along the [110] and [010] zone axes, respectively. Courtesy of P. Abellán.*

age of the sample featuring both square and triangular nanoislands. The pole figure of the $(011)_{\mathrm{LSMO}}$ reflection, with poles falling at $\chi$=35.3°, indicates the presence of the $(111)_{\mathrm{LSMO}}$ out-of-plane orientation, which coexists with the previously described $(001)_{\mathrm{LSMO}}$ population. The multiplicity of a reflection displaying the (111) out-of-plane orientation is 3. The fact that we observe 12 poles in total accounts for the four different in-plane orientations that the triangle can choose on the substrate. The presence of four populations is proved through AFM images; we have highlighted an example of each in Fig. 3.27 (a). The poles encircled in Fig. 3.27 (b) correspond to one of the four populations, separated 120° in $\phi$.

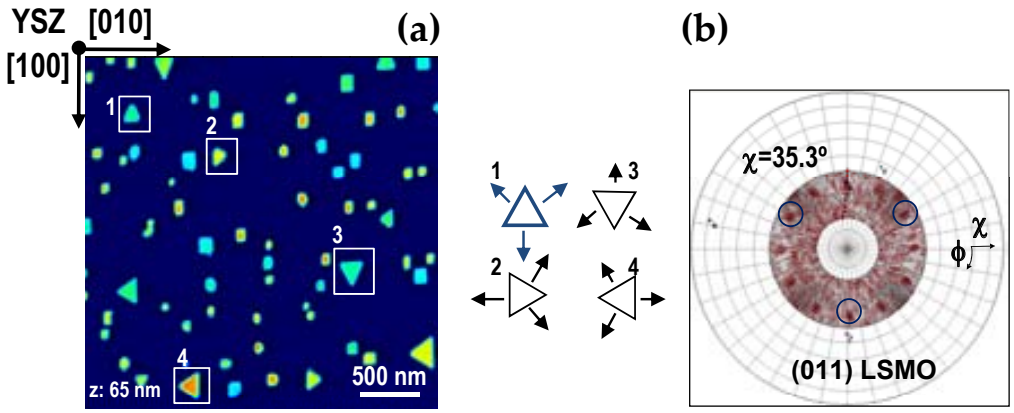


**Fig. 3.27:** *(a) 3$\mu$m × 3$\mu$m AFM topography image of a 0.03 M LSMO nanostructured sample, processed at 900°C for 1 h. In addition to the square shape islands we may observe a large number of triangular islands. Examples of the four possible in-plane orientations are marked within white squares. (b) Up to 12 poles, at $\chi$=35.3°, are detected in the $(011)_{LSMO}$ reflection pole figure due to the four possible in-plane orientations; each of them yields three 120° separated poles.*

The epitaxial relationship of the $(111)_{\mathrm{LSMO}}$ oriented islands is further supported by TEM and ED analysis. Fig. 3.28 (a) shows the ED pattern for one $(111)_{\mathrm{LSMO}}$-oriented nanoisland displaying the epitaxial arrangement $(111)_{\mathrm{LSMO}}$[11-2]||$(001)_{\mathrm{YSZ}}$[100]. Since there

are four possible ways for the island to orient on the substrate, the in-plane epitaxial relationship can also be $[1-10]_{\mathrm{LSMO}}$ $[100]_{\mathrm{YSZ}}$ for the 90° rotated triangle, and $[-1-12]_{\mathrm{LSMO}}$ $[100]_{\mathrm{YSZ}}$ and $[-110]_{\mathrm{LSMO}}$ $[100]_{\mathrm{YSZ}}$ for the corresponding mirror images. The four possible arrangements are sketched in Fig. 3.28 (b). It is also important to note that this epitaxial configuration imposes two different nominal misfit values on the in-plane matching directions. While the misfit for $[1-10]_{\mathrm{LSMO}} < 100 >_{\mathrm{YSZ}}$ is $\epsilon\sim$-6% (the same as for the in-plane directions of the $(001)_{\mathrm{LSMO}}$-oriented square pyramids), the nominal misfit value for $[-1-12]_{\mathrm{LSMO}} < 100 >_{\mathrm{YSZ}}$ is as large as $\epsilon\sim$-19%. These values are indicated in the sketch of Fig. 3.28 (b). Nonetheless, similarly to the case of the $(001)_{\mathrm{LSMO}}$-oriented nanoislands, the ED patterns indicate that these large strains are also relaxed in the case of $(111)_{\mathrm{LSMO}}$-oriented triangles.

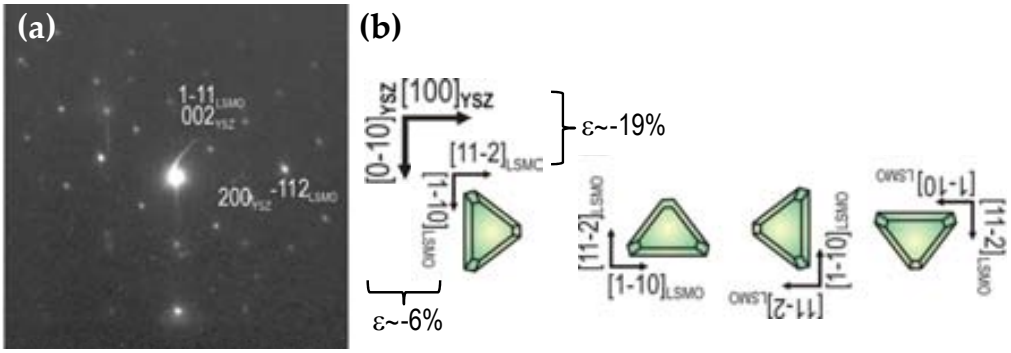


**Fig. 3.28:** *(a) ED measurement of a $(111)_{LSMO}$-oriented triangular nanoisland, zone axis $[110]_{LSMO}$, exhibiting a $(111)_{\mathrm{LSMO}}$[11-2] $(001)_{\mathrm{YSZ}}$[100] epitaxial relationship. (b) Sketched diagram of the four possible in-plane epitaxial arrangements of the $(111)_{LSMO}$ nanoislands. The nominal misfit values between nanoisland and substrate are ∼-6% and ∼-19% for the two orthogonal directions.*

In summary, we have found that the solution-derived self-assembled structures that we grow are LSMO nanoislands of high crystalline quality and relaxed strain state. The vast majority of them exhibit a $(001)_{\mathrm{LSMO}}$ out-of-plane orientation with respect to the (001)-YSZ substrate and are oriented at 45° with respect to the plane. We have also identified a minority population of $(111)_{\mathrm{LSMO}}$-oriented nanoislands, which exhibit triangular morphologies. The analysis done here concerns nanostructured samples grown at 900°C. The next section deals with the system characteristics at higher annealing temperatures.

### In uence of high annealing temperatures

In order to examine the effect of higher temperatures in the self-assembled LSMO nanoisland system we performed a series of experiments at 1000°C and 1300°C. Both LSMO and YSZ are reported to be thermodynamically stable at these temperatures and at the oxygen pressures that we use ($p_{O_2}\sim$1 bar) [177–180]. Fig. 3.29 shows 5 μm × 5 μm AFM topography images of two LSMO systems, both grown from 0.03 M solutions, and subject to $T\geq$1000°C annealings. The nanoisland *t* and *D* distributions are also shown. The first thing to note with respect to the 900°C examples of Fig. 3.21 is a clear decrease in area coverage together with a notable increase in both nanoisland *t* and *D*. At 1000°C islands easily attain lateral sizes around ∼180 nm and thicknesses in the ∼60 nm range. It appears that the atomic diffusivity at 1000°C is high enough to promote coarsening, i.e. the growth of large

islands at the expense of smaller islands. This yields a system in which 40 nm-thick and 100 nm-wide islands coexist with 100 nm-thick and 300 nm-wide structures. By increasing the temperature to 1300°C, islands attain even higher thickness and lateral sizes, i.e. $t\sim$80 nm and $D\sim$220 nm [see Fig. 3.29 (d)]. The inset in Fig. 3.29 (c) shows a thresholded image, where the color scale has been restricted (nanoislands appear saturated) to better see the substrate step morphology. We see that the high diffusivity at such high temperatures promotes the evolution of the terraces into curved and rounded-shape steps. These structures feature heights larger than one unit cell (what is known as *step bunching*).

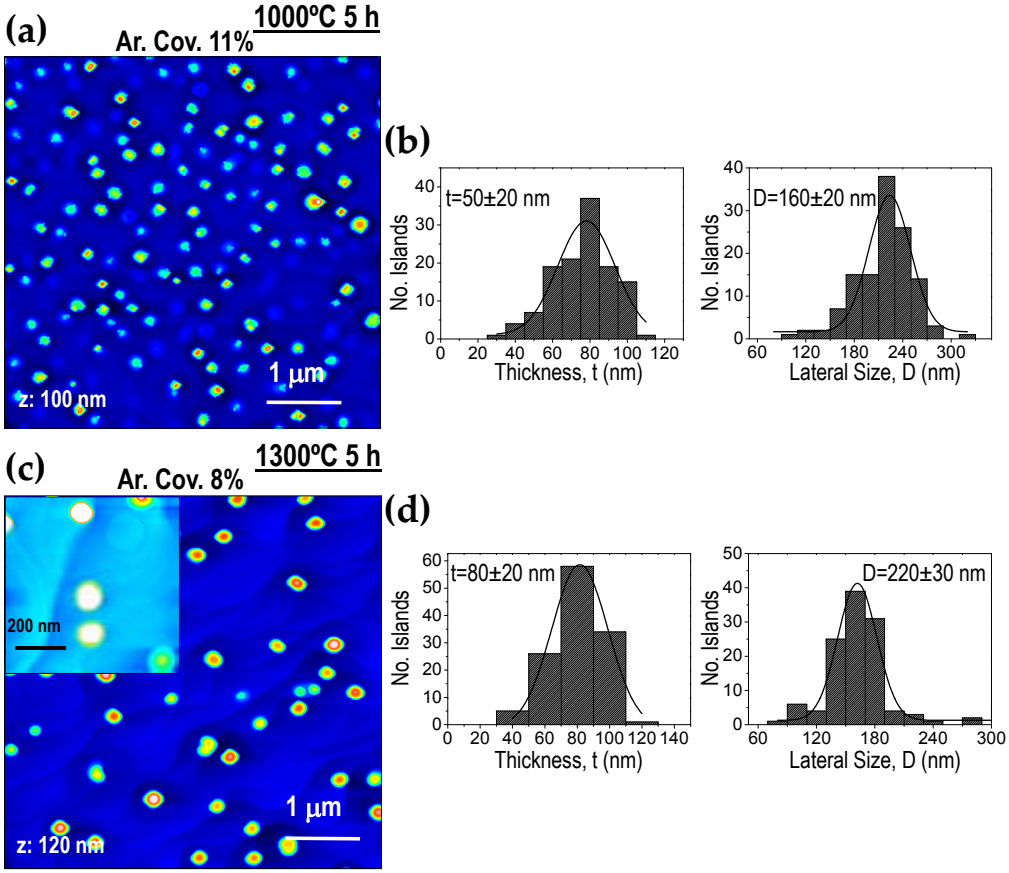


**Fig. 3.29:** *5$\mu$m × 5$\mu$m AFM topography images featuring self-assembled nanoislands after heat-treatments at (a) 1000°C for 5 h, and (c) 1300°C for 5 h. The solution concentration was 0.03 M. (b)&(d) Nanoisland thickness and lateral size histograms show larger and higher nanoislands with increasing annealing T.*

In order to examine the crystal structure of the systems annealed at high temperature we performed XRD measurements. Fig. 3.30 shows the $\theta$-$2\theta$ analysis of two self-assembled nanoisland systems on YSZ (0.03 M), annealed at (a) 1000°C for 24 h, or (b) 1300°C for 5 h. The sample treated at 1000°C for 24 h exhibits an intense and narrow $(002)_{\mathrm{LSMO}}$ peak in addition to a small yet clear $(001)_{\mathrm{LSMO}}$ peak, which was hardly detectable in the 900°C 1 h sample of Fig. 3.24 (a). Such increase in the intensity suggests an improvement in the crystallinity of the LSMO phase at high temperatures. In contrast, the intensity of the $(002)_{\mathrm{LSMO}}$ reflection decreases substantially in the $\theta$-$2\theta$ scan of the 1300°C sample, while two other peaks, marked with red arrows, appear. As a matter of fact, although less evi-

dent, there are also traces of these new peaks in the $\theta$-$2\theta$ scan of image (a), also indicated with red arrows. No evidence for such peaks was found in 900°C treated samples (see e.g. Fig. 3.24).

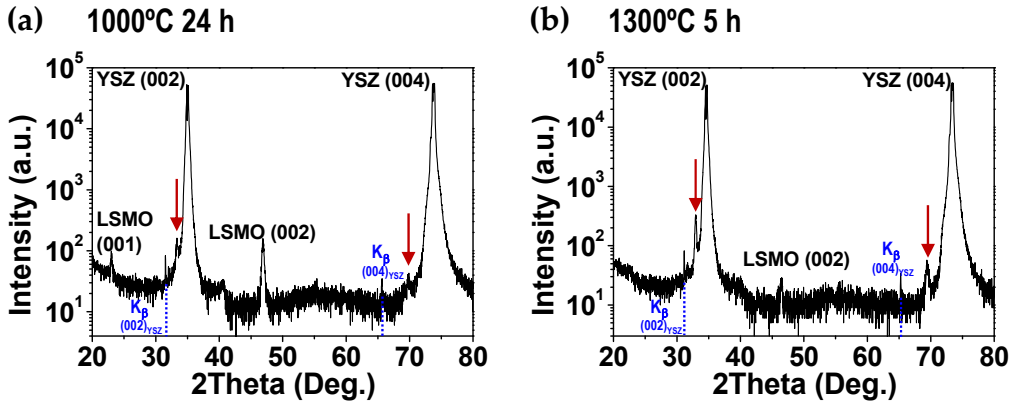


**Fig. 3.30:** *$\theta$-$2\theta$ scans of self-assembled LSMO nanoislands on YSZ, heat treated at (a) 1000°C 24 h, and (b) 1300°C 5 h. Note how the LSMO reflections are clear in (a) and, in contrast, barely noticeable in (b). Two new peaks (marked with red arrows), particularly obvious in (b), also develop.*

Fig. 3.31 shows the zoomed-in $\theta$-$2\theta$ scans from Fig. 3.30 (b), to better appreciate the two new peaks. Interestingly, the corresponding $2\theta$ values, i.e. $2\theta$=33.2° and $2\theta$=69.7°, accurately match the (004) and (008) reflections of the cubic pyrocholore $La_2Zr_2O_7$ (read *Lanthanum zirconate*, LZO) compound [181–183]. Moreover, the I(004)/I(008) ratio of our measurement, around 5.6, is in fair agreement with the reported ratios found in the literature [I(004)/I(008)=5.34 [181], I(004)/I(008)=4.8 [182]]. The insets in Fig. 3.31 display the rocking curves of the $(004)_{\mathrm{LZO}}$ and $(008)_{\mathrm{LZO}}$ reflections, with FWHM values of ∼2° and ∼1.4°, respectively. From these results it follows that LSMO chemically reacts with YSZ to form LZO. Pole figures from XRD[2] measurements were also recorded for the most intense $(222)_{\mathrm{LZO}}$ reflection, with $2\theta$=28.6° (not shown). Next to the substrate $(111)_{\mathrm{YSZ}}$ reflection at $2\theta$=30°, we detected, in the 1300°C heat-treated sample, a notable shoulder, absent in 900°C treated samples. Despite being difficult to resolve due to the nearby intense and wide substrate peak, it was already sufficient to prove that LZO grows cube on cube on top of YSZ, i.e. $(001)_{\mathrm{LZO}}[100]$ $(001)_{\mathrm{YSZ}}[100]$ . This epitaxial relation gives a lattice mismatch $\epsilon$=-4.45% (2 YSZ unit cells $2a_{YSZ}$=10.3 Å, are matched to one LZO unit cell $a_{LZO}$=10.78 Å).

In conclusion, our findings show the formation of epitaxial LZO grown from the interfacial reactivity of the YSZ substrate in contact with LSMO at 1300°C. In fact, a subtle indication of LZO formation, not yet at expenses of LSMO formation, is already detected at large annealings (24 h) at 1000°C. The reaction between YSZ and LSMO grown with different methods and subject to different heat treatments has produced a large body of work, mainly prompted by the great interest of the LSMO/YSZ cathode-solid electrolyte system for Solid Oxide Fuel Cells (SOFCs) [184–187]. It is generally accepted that long annealing times and high temperatures can yield an evaporation or diffusion of Mn into YSZ, along with the reaction of La with (Yttrium doped) zirconia [185, 188]. Insulating and with 1000 times less ionic conductivity than YSZ, LZO severely hampers the adequate operation of SOFCs. Consequently, in both the search for ferromagnetic self-assembled nanostructures,

[2] Alternatively, the fact that no peak appeared at any other $\phi$ value different from the substrate $\phi$ value yields the same conclusion.

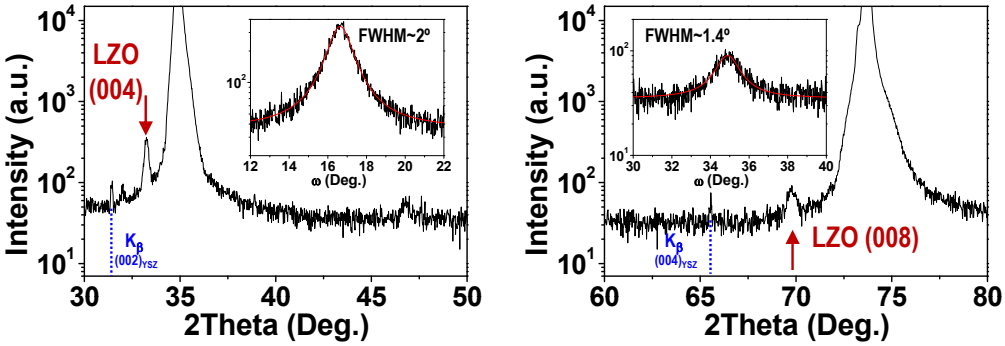


**Fig. 3.31:** *Zoomed-in θ-2θ scans from Fig. 3.30 (b). The peaks marked with red arrows indicate the* $(004)_{\mathrm{LZO}}$ *and* $(008)_{\mathrm{LZO}}$ *reflections. The rocking curves of those two peaks are displayed in the insets of the graphs.*

and for SOFC applications, it is of considerable relevance to determine the experimental conditions at which this reaction occurs.

### 3.4.2 Morphology of self-assembled LSMO nanoislands on YSZ

So far we have discussed the evolution of the LSMO self-assembled nanoisland system and illustrated the general trends in island thickness and lateral size distribution. The crystallographic orientations of two island populations, the predominant out-of-plane $(001)_{\mathrm{LSMO}}$ and the less abundant $(111)_{\mathrm{LSMO}}$ [in the following named $(001)_{\mathrm{LSMO}}$-oriented and $(111)_{\mathrm{LSMO}}$-oriented nanoislands], were also determined. In this section we will focus on the detailed individual morphology of the LSMO nanoislands. This knowledge will be necessary for later studies on the magnetic properties of the nanoislands.

#### Main morphologies of LSMO nanoislands on YSZ

Fig. 3.32 summarizes the general aspect of the standard system of self-assembled LSMO nanoislands grown from a 0.03 M solution at 900°C for 3 h. The $1\,5\ \mu\mathrm{m} \times\ 1\,5\ \mu\mathrm{m}$ AFM image in Fig. 3.32 (a) shows the nanoisland ensemble, which consists of a majority of square-base nanoislands and also includes one triangular structure. The truncated edges of the triangle are a common feature of these structures. The line profile in Fig. 3.32 (b) evidences typical nanoisland sizes with thickness $t\sim$20-35 nm and lateral size $D\sim$120 nm. These values are approximate due to the AFM tip-nanoisland convolution, which also precludes resolving the actual angle of the island facets.

The geometry and facets of the nanoislands may be derived from cross-section TEM images such as the low magnification TEM micrograph in Fig. 3.33 (top row). The high resolution (HR) low magnification images in the lower panel display two individual LSMO islands: Fig. 3.33 (a) shows the truncated pyramid morphology of a square-base $(001)_{\mathrm{LSMO}}$-oriented island and, next to it, Fig. 3.33 (b) displays a large flat $(111)_{\mathrm{LSMO}}$-oriented nanoisland, i.e. triangle-based. The inclined facets in (a) are found to be the $(111)_{\mathrm{LSMO}}$ crystallographic planes, as deduced from the projected $\sim$55° angle of the facet with respect to the [001]-substrate horizontal direction. The square-base $(001)_{\mathrm{LSMO}}$-oriented nanoislands are thus truncated pyramids limited by lateral $(111)_{\mathrm{LSMO}}$ facets and top and bottom

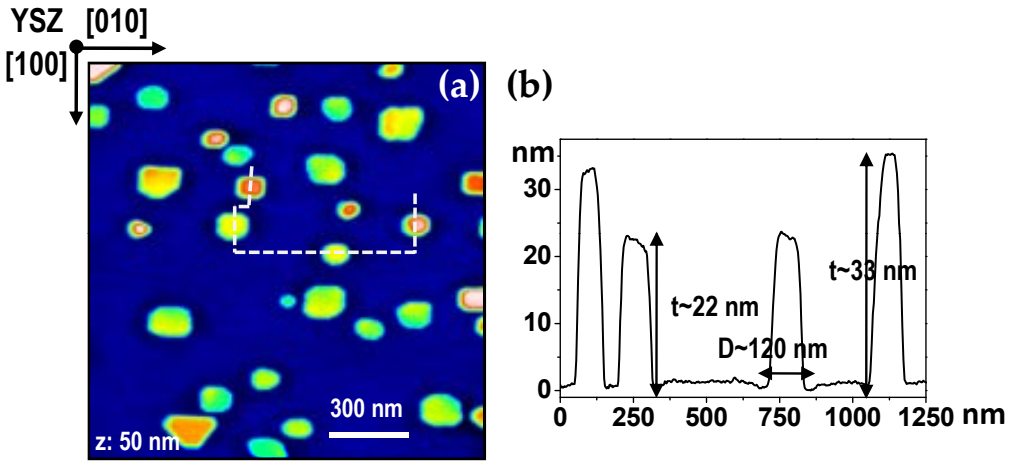


**Fig. 3.32:** *(a) 1.5$\mu$m $\times$ 1.5$\mu$m AFM topography image of a 0.03 M 900°C 3 h treated LSMO on YSZ self-assembled nanoisland system. (b) Line profile corresponding to the dashed line in (a), showing the typical nanoisland sizes.*

$(001)_{\mathrm{LSMO}}$ planes. Regarding the triangular islands, Fig. 3.34 (a) shows the TEM image of a $(111)_{\mathrm{LSMO}}$-oriented nanoisland, seen along the $[-110]_{\mathrm{LSMO}}$ direction. The projected lateral facets of the image are in agreement with $(1-1-1)_{\mathrm{LSMO}}$ and $(001)_{\mathrm{LSMO}}$ crystallographic planes, as indicated in the image. TEM image analysis are thus consistent with $(111)_{\mathrm{LSMO}}$ top facets laterally bounded by $1-11$ $_{\mathrm{LSMO}}$ planes at ~70.5° from the top plane, truncated at the edges by $(001)_{\mathrm{LSMO}}$ facets. A top-view drawing of the nanoisland orientation is sketched in the lower panel. Fig. 3.34 (b) shows a 3D model of the $(111)_{\mathrm{LSMO}}$-oriented LSMO nanoisland, displaying its facets and the epitaxial relationship with respect to YSZ.

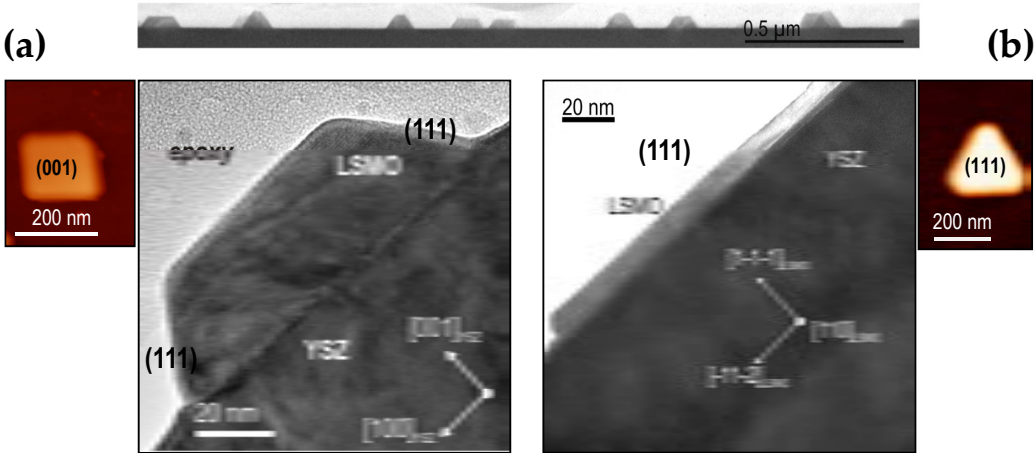


**Fig. 3.33:** *(Top-row) Low resolution TEM cross-section image of a collection of self-asssembled LSMO nanoislands on YSZ. (a)&(b) HR low magnification cross-section images of (a), a $(001)_{LSMO}$-oriented nanoisland, exhibiting a truncated pyramid geometry shaped by (111) lateral facets, and (b), a $(111)_{LSMO}$-oriented nanoisland. The YSZ substrate and the LSMO island are viewed along the [010] and [110] zone axes, respectively. The AFM images next to the TEM images indicate the in-plane morphology of each of the islands. TEM images courtesy of P. Abellán.*

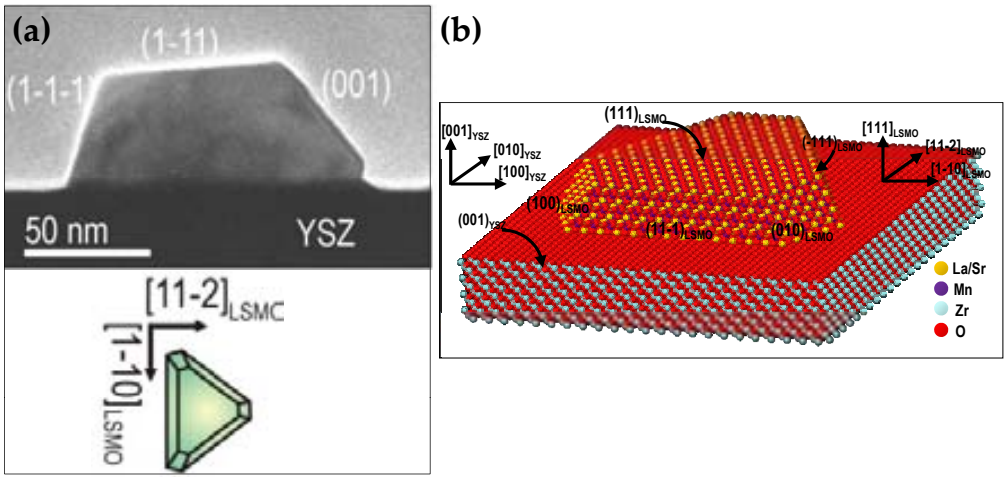


**Fig. 3.34:** *(a) TEM image of a* $(111)_{\mathrm{LSMO}}$*-oriented nanoisland showing its facets. The nanoisland is seen along the* $[-110]_{\mathrm{LSMO}}$ *direction. Courtesy of P. Abellán. A top-view drawing of the nanoisland is sketched below. (b) 3D model for the* $(111)_{LSMO}$*-oriented island showing its facets and its epitaxial relationship with respect to the substrate. Note that the truncated edges correspond to 100 planes. The simulation is done using the program 'Rhodius' from Universidad de Cádiz [189, 190] (courtesy of Prof. J. Arbiol).*

The above results concern the main structures observed in the LSMO/ YSZ system under standard treatment conditions, i.e. 900°C annealing for 1 to 3 h. However, the LSMO/YSZ system exhibits an alternative island morphology which can arise from identical processing conditions as the ones just mentioned. Fig. 3.35 illustrates this fact: it shows two $1\ 5\ \mu\mathrm{m} \times 1\ 5\ \mu\mathrm{m}$ AFM images, (a) and (b), of two samples grown from 0.03 M solutions processed at 900°C for 1 h. While in (a) we obtain the previously described arrangement of well separated triangular and square-base islands, Fig. 3.35 (b) displays a much denser assembly featuring square islands which appear rotated by 45° with respect to the square islands of Fig. 3.35 (a). Strictly speaking, the base of these new islands is not necessarily squared, but it shows a trend towards a rectangular shape. For the sake of simplicity, however, we are going to name the squares from sample (a) *regular-squares* and those in (b) *rotated-squares*. The difference in morphology is apparent in the amplitude images (a') and (b'). Interestingly, XRD pole figure measurements for the sample featuring rotated-squares gave exactly the same epitaxial relationship as the one discussed for regular-square $(001)_{\mathrm{LSMO}}$-oriented nanoislands, i.e.$(001)_{\mathrm{LSMO}}[110]$ $(001)_{\mathrm{YSZ}}[010]$. This is illustrated in the sketches of Figs. 3.35 (a") and (b"). As a result of having the same crystallographic orientation it follows that the oblique facets of the rotated-squares cannot be the $(111)_{\mathrm{LSMO}}$ facets, as in the case of the regular-square nanoislands. Simulations of the system were done in collaboration with Prof. J. Arbiol using the *Rhodius* simulation tool from UCA (Universidad de Cádiz) [189, 190]. A number of possibilities including the 101 and 201 family of planes were revealed as possible options for the inclined facets of the rotated-squares. However, TEM cross-section studies would be required for confirmation. In brief, in this alternative configuration, the crystallographic orientation of nanoislands remains the same and only the morphology of the islands changes, accompanied by a qualitative change in the self-assembly, which proceeds via formation of smaller and closely spaced nanoislands.

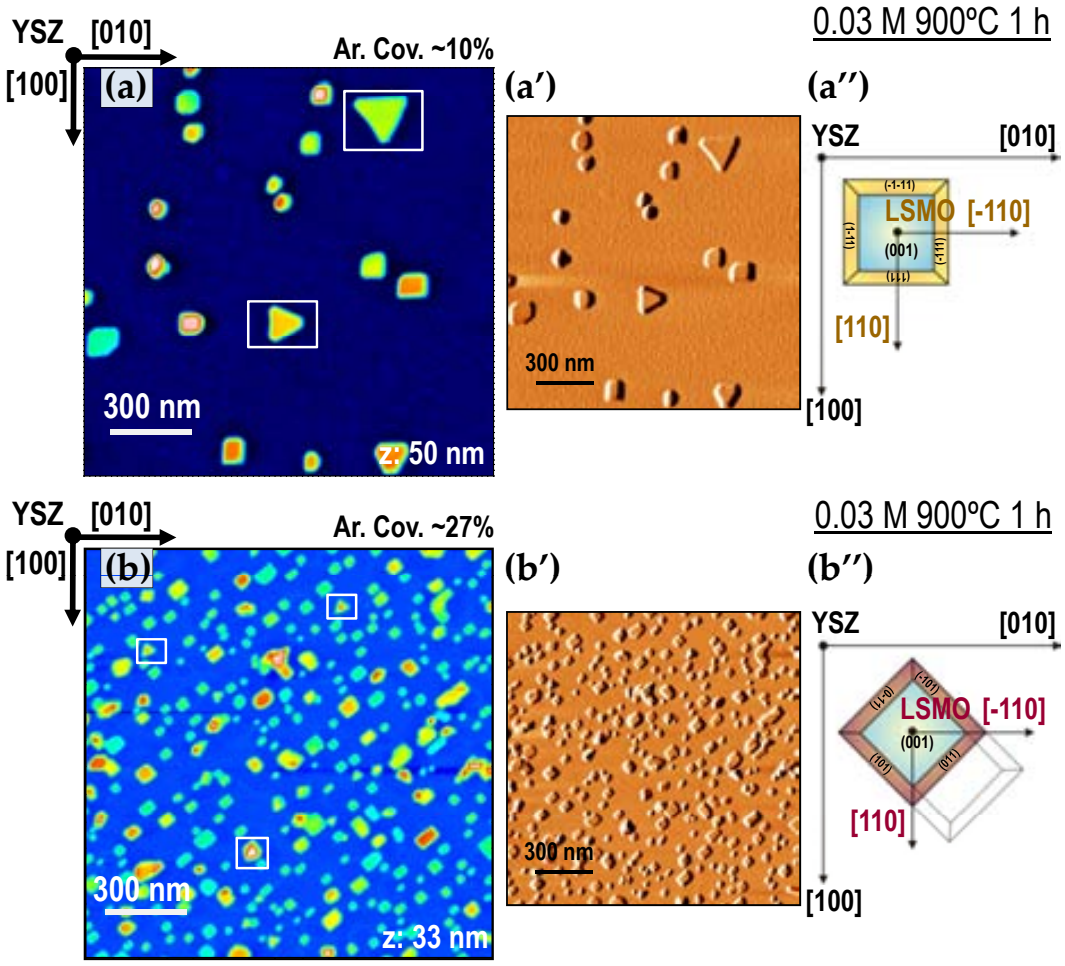


**Fig. 3.35:** *Morphological differences exhibited by LSMO nanoisland ensembles after identical growth processing. (a)&(a') 1.5$\mu$m × 1.5$\mu$m AFM topography and amplitude images, respectively, of the sample with $(001)_{LSMO}$-oriented regular-squares. It exhibits some $(111)_{LSMO}$-oriented islands (triangles) as well. The area coverage is in the 10-15% range. (b)&(b') 1.5$\mu$m × 1.5$\mu$m AFM topography and amplitude images, respectively, of the sample featuring closely packed rotated-square islands, 45° rotated with respect to the regular-square islands in (a). Some very few triangular islands may also be detected, far smaller than their (a) image counterparts (inside white squares). Area coverage ranges between 25-35%. The epitaxial arrangement of the square-base nanoislands in both samples is identical, as sketched in (a") and (b"). Nonetheless, the truncated square pyramids in (a") display $(111)_{LSMO}$ lateral facets, while the islands in (b") show different facets. One of the possibilities, the $\overline{1}01$ family of planes, is indicated in (b").*

**Study of the possible mechanisms driving the LSMO nanoisland morphologies on YSZ**

In order to examine the driving force responsible for the regular and rotated-square nanoisland shapes, we first considered the substrate surface. The critical role of the substrate surface in the self-assembly of epitaxial nanoislands is a widely accepted issue, yet not always well understood. Surface defects, step kinks and edges, typically provide preferential nucleation sites, and also may influence the growth kinetics of the first formed nuclei [191, 192]. The morphology of the substrate surface will also affect the stress distributions within a nanostructure and, consequently, its relaxation mechanisms. For instance, the formation of dislocations will vary for islands nucleated on a flat terrace or on a kink. These issues have been investigated by Hesse and co-workers, also in oxide heteroepitaxial systems. Their studies show the impact of substrate pits and steps on the morphology and domain distribution of oxide nanoislands, as compared to islands grown on perfectly flat YSZ substrates [176, 193, 194].

In an attempt to associate our observed LSMO morphologies to some underlying substrate pattern, we analyzed the YSZ substrate surface characteristics. Fig. 3.36 shows the AFM images of four LSMO/YSZ nanostructured samples. In them, either rotated-square [(a) and (b)] or regular-square [(c) and (d)] nanoisland are present, after identical growth processing. We can also identify a few triangles. AFM topography images ($1\ \mu m \times 1\ \mu m$, at the center of the figure) are thresholded, i.e. their $z$ scale is reduced in order to better see the height distribution within the substrate surface. This makes the island morphology blurry, and therefore we have included the phase images corresponding to each sample ($0\ 5\ \mu m \times 0\ 5\ \mu m$, in gray). The latter images clearly display the distinct island morphologies. The surface steps in the images exhibit one unit cell heights. An example is given for Fig. 3.36 (a).

An analysis of Fig. 3.36 (a), reveals remarkably large substrate terraces, $\lambda \sim 400$ nm wide, displaying plenty of kinks and holes. Note also that most of the nanoislands are located at the edges of substrate steps. A very different landscape emerges from Fig. 3.36 (b), where substrate terraces are very narrow and smooth, and hence the islands occupy more than one terrace. Although, again, island nucleation is likely to happen at the steps edges, the large size of the structure with respect to the terrace width makes this point difficult to confirm. Still, the interaction between island and substrate is clearly revealed in the curving of the substrate step at nanoislands locations, (some of this bending is signaled with arrows). Note that a similar influence of the island on the substrate terrace is apparent in Fig. 3.36 (c): the substrate steps near an island curve towards the high level side. Furthermore, $\sim 5$ u.c. high trenches develop around the islands, as revealed by the dark halos surrounding the structures, and by the line profile displayed at the left of the image. Previous works suggest that these trenches develop via diffusion of surface molecules from the immediate surroundings towards the nanostructures [193, 194]. In any case, it appears that both in Figs. 3.36 (b) and (c) the substrate surface morphology and the effect of the island presence on the substrate steps are comparable. Despite similar substrate-nanoisland interaction one sample features rotated-square islands and the other regular-square structures. An intermediate terrace width is found in Fig. 3.36 (d), where the bending of the substrate due to the presence of islands also occurs. Note how in this case, as the island size is slightly smaller than the terrace width, one can clearly see that the nanoisland sits on the step edge, which curves at the sides of the structure. It is not difficult to imagine, in a subsequent evolutionary stage, the complete receding of the step to yield a similar situation as that observed in Fig. 3.36 (c).

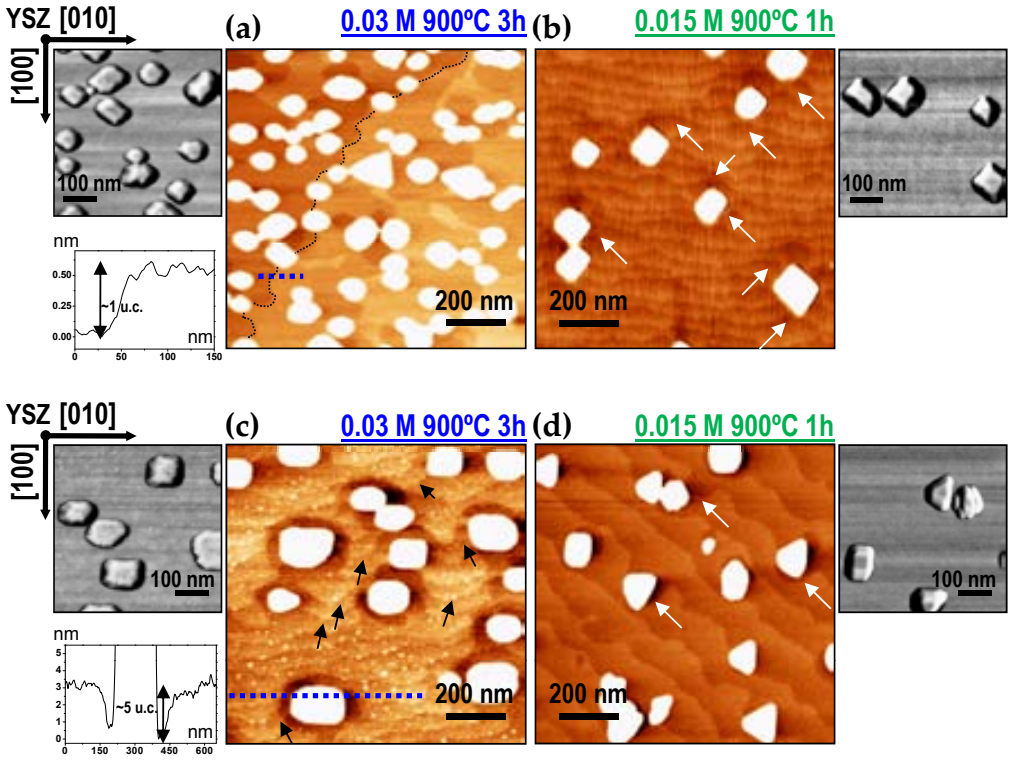


**Fig. 3.36:** *Two 0.03 M 900°C 3 h and other two 0.015 M 900°C 1 h samples featuring either rotated-square (top row) and regular-square island (bottom row) morphologies. The $1\mu m \times 1\mu m$ AFM topography images, in the center, are thresholded in order to emphasize the underlying substrates' step-terrace structure. Phase images at the sides of the topography images, $0.5\mu m \times 0.5\mu m$, in grey, show the different nanoisland shapes, either rotated or regular-square. Substrate terraces vary from wide in (a) to very narrow in (b) and (c). They display 1 u.c. of step height, exemplified by the line scan in (a) (blue dashed line marks the exact place of the profile). In sample (c) islands appear surrounded by ∼5 u.c. high trenches, depicted in the corresponding line profile. Little arrows throughout the images indicate some of the substrate step bending.*

From the above results we deduce that the specific substrate step-terrace morphology is not a determining factor deciding whether rotated-square or regular-square island morphologies will occur. This is suggested by the fact that nanoisland-substrate interactions appear to be independent of the nanoisland shape.

Once we have ruled out the substrate surface as the driving force for a specific nanoisland shape, we need now to consider the nanoislands by themselves. The fact that nanoislands from samples grown after the same treatment show either $111_{LSMO}$ or $101_{LSMO}$ crystallographic planes (supposing we have the latter family of planes in the rotated-square nanoislands) suggests that the surface energies of these facets might be of comparable magnitude. No surface free energy values for different $La_{0.7}Sr_{0.3}MnO_3$ crystal planes are reported in the literature. For similar compounds such as $La_{1-x}Ca_xMnO_3$, however, no strong differences are reported for the energies of low index crystal planes, with values that vary very slightly from one crystal plane to another and which further depend on the specific chemical termination [whether Mn-terminated or La/(Ca,Sr) terminated] [158].

Within the hypothesis of two energetically close scenarios one would in principle expect both nanoisland morphologies to coexist on the same sample. This situation, however, was very rarely observed in the more than three dozens of processed samples. This observation underlines the relevance of island-island interaction (in addition to the similarity in surface free energies of the LSMO facets): once the system has opted for a certain nanoisland morphology, either regular or rotated-square, this will be the shape of all of the nanoislands [1]. To corroborate this picture it is useful to verify whether one island morphology may be closer to the thermodynamic equilibrium than the other. For that purpose we studied early and advanced evolution stages of the system by moving away from the 900°C 1-3 h heat treatments presented so far, as we explain next.

Fig. 3.37 shows the experimental results of LSMO on YSZ self-assembled nanoisland systems at advanced stages [$T \geq 900$°C, (a) and (b)] and fairly initial stages [(c) and (d)] of its evolution. As also done in Fig. 3.36, we threshold the AFM topography images, and we also provide zoomed-in phase images that reveal the morphology of the nanoislands. The first thing we notice is that all samples, whether in the initial or in the advanced stage, exhibit the rotated-square nanoisland morphology. In fact, the examples shown in Fig. 3.29, annealed at $T \geq 1000$°C, already showed this rotated-square morphology. Therefore, we can dismiss the hypothesis that there is a gradual shape evolution from a less stable configuration towards a more stable equilibrium configuration. Nevertheless, further experiments are required to prove if regular-squares are never achieved at the extreme conditions, i.e. at high temperatures and long annealing times, and at low temperatures and short annealing times. At present, we do not have enough statistics to rule out such possibility. Concerning the substrate surface, note that the high $T$ and long annealing in Fig. 3.37 (a) results in a strong step meandering, with step heights as large as $\sim$5 u.c.; these again emphasize the redistribution of substrate material in this nanostructured system, as we already observed in Fig. 3.36 (c). Remarkably, although the substrate behavior was similar in Fig. 3.36 (c), the nanoisland shape was regular-square, while here it displays rotated-square shape. This once more confirms that the substrate morphology does not determine the nanoisland shape.

In summary, in this section we have presented the study of the LSMO nanoisland

[1] When talking about the different nanoisland morphologies we are only considering $(001)_{\mathrm{LSMO}}$-oriented islands, i.e. not the triangular islands. Triangles have a different crystallographic orientation, and thus their formation is decided at the nucleation stage.

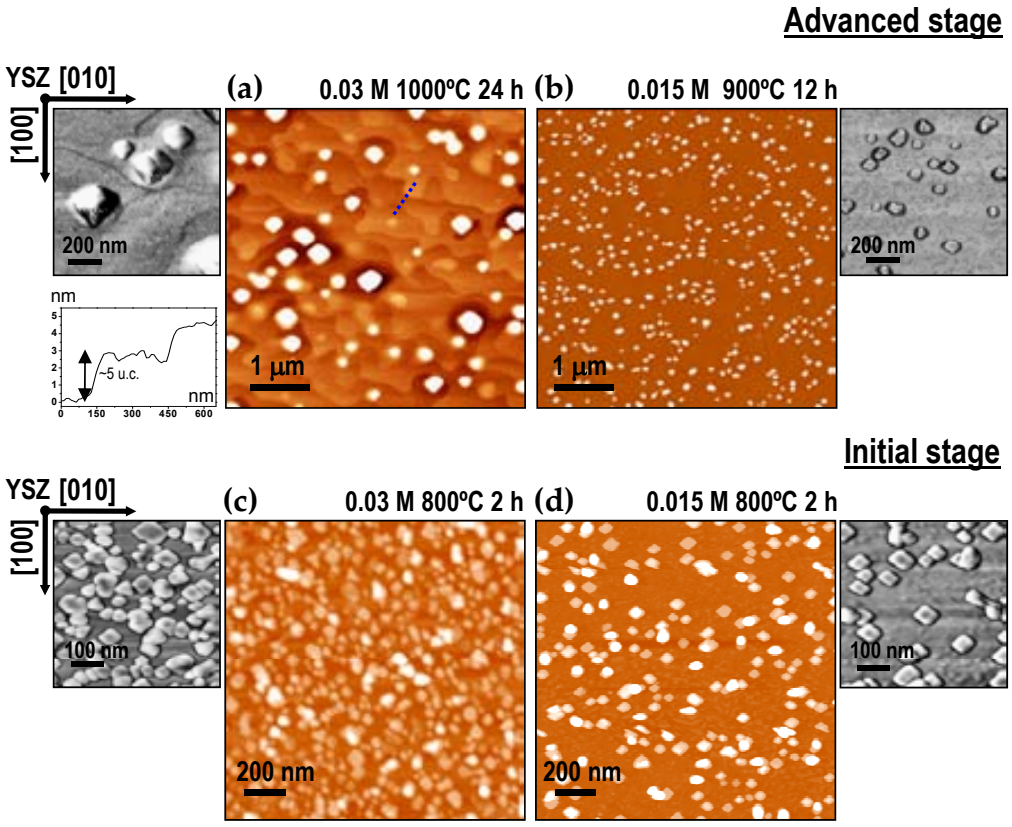


**Fig. 3.37:** *Comparison of the nanoisland morphologies obtained at advanced stages (top row) and initial stages of the system evolution (bottom row). All of the examples feature rotated-square nanoislands. AFM topography images (in the center of the figure) are thresholded in order to observe the underlying substrate morphology while, at their sides, phase images illustrate the nanoisland shape. High T and long annealing times in (a) result in the substrate terrace meandering and in the building of steps as high ∼5 u.c. In (b), although clean, the substrate does not form a clear step-terrace structure. Finally, the initial evolution stage and the density of the system imaged in (c) and (d) suggest that there may be considerable amount of material left on the substrate.*

morphology on YSZ. We have shown that $(001)_{\mathrm{LSMO}}$-oriented and $(111)_{\mathrm{LSMO}}$-oriented nanoislands display square-base truncated pyramid and triangular-base shapes, respectively, faceted along well-defined crystallographic planes. We have also demonstrated that $(001)_{\mathrm{LSMO}}$-oriented nanoislands exhibit two possible morphologies, either regular-square or rotated-square. The crystallographic orientation of both nanoislands is identical, which indicates that they are shaped by different LSMO lateral facets. Our results also show that both $(001)_{\mathrm{LSMO}}$ configurations appear under identical processing conditions, suggesting they are energetically close. These two morphologies do not appear to coexist, which suggests that island-island interaction may play a key role. Additionally, we have shown that the nanoisland morphology, whether regular or rotated-square, does not depend on the substrate morphology. Surface steps, when treated at high $T$ and/or for long times, undergo strong bending and meandering, attaining heights that are well above one unit cell. Finally, there appears not to be an 'initial stage' or 'advanced stage' morphology, although a more exhaustive study would be necessary to conclusively correlate the influence of the heat treatment on the final nanoisland configuration.

### 3.4.3 Magnetic Characterization of LSMO on YSZ self-assembled nanoislands

After having investigated the growth aspects of CSD-derived self-assembled LSMO nanoislands grown on YSZ, we now turn to the study of their macroscopic magnetic properties. The present section will focus on the macroscopic magnetic properties of the LSMO on YSZ nanoisland system, while the nanoscale magnetic behavior will be addressed in the following chapters.

#### Magnetization loops and Curie Temperature

Macroscopic magnetization measurements were carried out in a SQUID magnetometer (Quantum Design MPMS-XL7) at temperatures between 10 K to 300 K and varying magnetic fields from 0 T to 7 T. Fig. 3.38 shows the in-plane isothermal magnetization loops measured for a collection of epitaxial LSMO nanoislands grown on YSZ from a 0.015 M solution, heat treated at 900°C for 1 h [see the appearance of the system in Fig. 3.19 (b)]. We have plotted the SQUID measured signal, i.e. the magnetic moment $m$, against the in-plane applied field $H$. The substrate diamagnetic response ($M$ linear dependency against $H$) has been subtracted in order to extract the ferromagnetic (FM) behavior specific to the LSMO nanoislands. Note that we measure $m$ values below $2 \times 10^{-5}$ emu, near the effective resolution limit of our measurements, which we found to be in the $\sim 10^{-6}$ emu range. Recall that 0.015 M yields an ultra-thin FM layer with $t_{eq}\sim$1.5 ($\pm$0.5) nm (see Fig. 3.20). For higher concentrations, the signal to noise ratio improves (Fig. 3.40 shows a representative example of a 0.03 M sample). The bottom row of Fig. 3.38 displays the magnified view of the center of the loops, to better appreciate the $M$ vs $H$ dependency. Coercive fields $H_C$ decrease from $\sim$200 Oe at 35 K, down to $\sim$150 Oe at 110 K, and $\sim$20 Oe at 300 K. The saturation and remanence magnetic moment, as well as the coercive field inferred from Fig. 3.38, are summarized in Tab. 3.2.

In Fig. 3.39 we show the saturation magnetization values $M_S$ deduced from the hysteresis loops for a number of samples with nanoislands grown from distinct concentrations. Here $M_S = \frac{m_s}{V} = \frac{m_s}{St_{eq}}$, with $m_s$ the saturation magnetic moment, $S$ the substrate surface

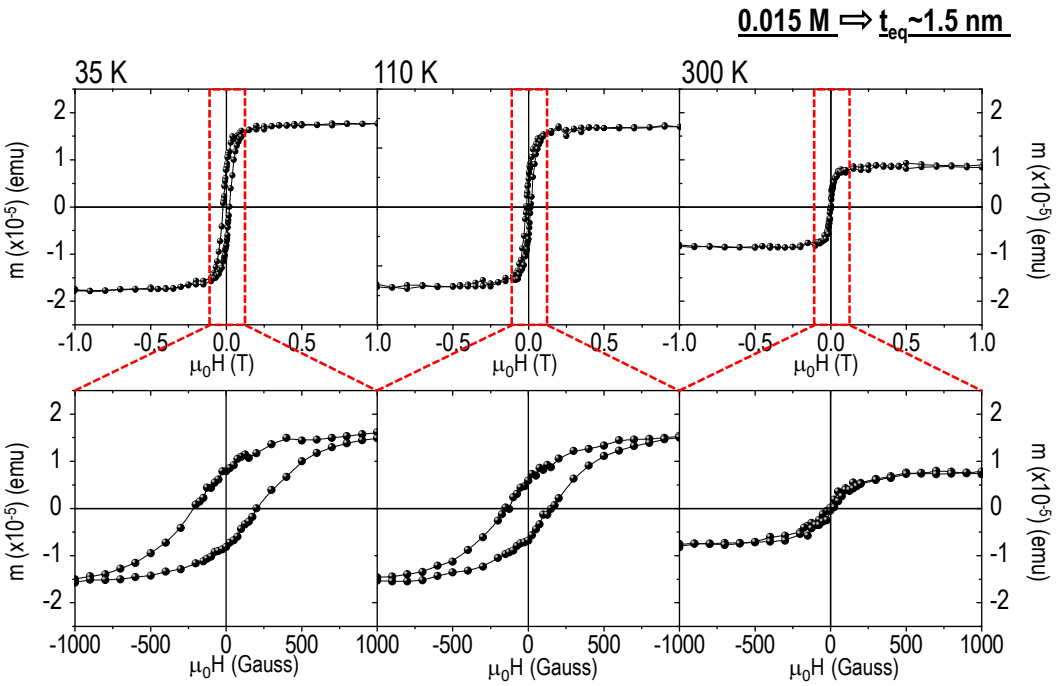


**Fig. 3.38:** *Isothermal magnetization loops for various temperatures measured with SQUID. The bottom row displays a magnified view of the center of each loop. The sample of self-assembled LSMO nanoislands was grown from a 0.015 M precursor solution, i.e. $t_{eq}$~1.5 nm, treated at 900°C for 1 h, see Fig. 3.19 (b).*

| T (K) | $\mathbf{m}_S(\times 10^{-5})$ (emu) | $\mathbf{m}_r(\times 10^{-5})$ (emu) | $\mathbf{H}_C$ (Oe) |
|---|---|---|---|
| **35** | 1.8 | 0.8 | 214 |
| **110** | 1.7 | 0.7 | 150 |
| **300** | 0.86 | 0.2 | 20 |

**Tab. 3.2:** *Magnetic moment and coercive field values inferred from Fig. 3.38.*

(5 mm $\times$ 5 mm) and $t_{eq}$ the equivalent film thickness. The large error bars in Fig. 3.39 associated to $M_S$, are given by the expression $\Delta M_S = \left|\frac{\partial M_S(t_{eq})}{\partial t_{eq}}\right| = \frac{m_s}{St_{eq}^2}\Delta t_{eq}$, i.e. they originate from the large uncertainty in the estimate of the $t_{eq}$ values (see Tab. 3.1). For comparison, we have plotted bulk LSMO $M_S$ values at different temperatures, taken from the work of Park et al. [19]. In addition to the expected decrease of $M_S$ with $T$, we observe that the saturation magnetization values of the LSMO nanoisland ensemble are not far from the reported values for bulk LSMO, which is a remarkable fact considering the island nanometric dimensions, typically below $t\sim$40 nm and $D\sim$200 nm in thickness and lateral size, respectively. Only for 300 K the measured magnetization seems to diverge more substantially from the values reported for bulk LSMO. It is also worth emphasizing the general trend of decreasing magnetic signal with decreasing solution concentration. We shall go back to discussing this point later in the section. Let's also remark that the 0.03 M LSMO ultra-thin films on STO and LAO studied at the beginning of this chapter exhibited saturation magnetizations in the order of $\sim$230 kA/m at 35 K, which is more than a factor 2 smaller than the $M_S$ values obtained for LSMO nanoislands on YSZ, grown from 0.015 M ($\sim$480 kA/m at 35 K) and 0.03 M ($\sim$465 kA/m at 110 K) solutions. Tab. 3.3 collects the data which yield the plot in Fig. 3.39.

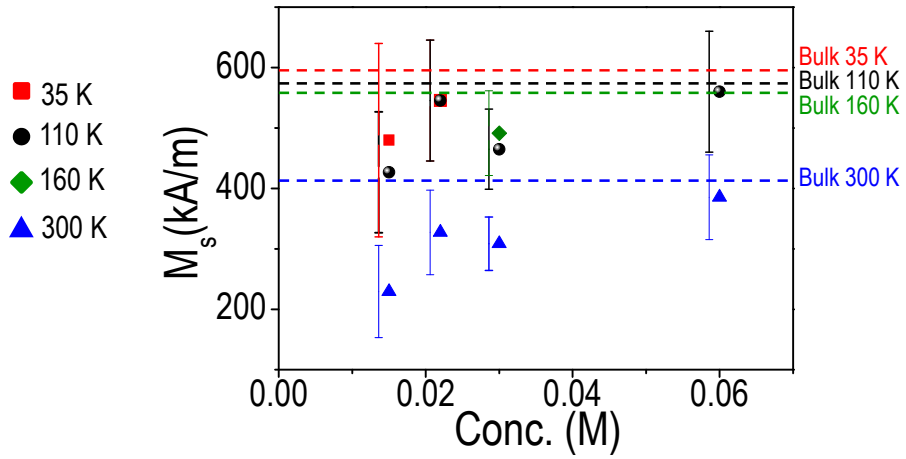


**Fig. 3.39:** *In-plane $M_S$ values for various temperatures, of different self-assembled LSMO nanoislands on YSZ. The horizontal axis indicates the precursor concentration. The plotted data are listed in Tab. 3.3. The dashed lines indicate the bulk LSMO $M_S$ values from the work of Park et al. [19].*

Fig. 3.40 shows the magnetization curves measured at 110 K for a 900°C 3 h sample grown from a 0.03 M solution [see Fig. 3.32 (a)], both with in-plane and out-of-plane applied field. The two hysteresis loops in Fig. 3.40 reveal that the easy magnetization axis of our system of self-assembled epitaxial LSMO nanoislands lies within the sample plane. An in-plane easy axis is expected in ferromagnetic thin films, due to the strong shape anisotropy [195]. Such a behavior is not straightforward in 3D objects, nor in compressively strained nanoscale systems. As a matter of fact, thin LSMO films grown under compressive strains have been reported to exhibit an out-of-plane easy magnetization axis as a consequence of the magnetoelastic contribution [27, 28, 196]. Nevertheless, in our LSMO nanoislands, the nominal $\epsilon\sim$-6% compressive strain is relaxed, and, on the other hand, although, strictly speaking, they are 3D objects, they are rather flat islands with typical $D$ $t$ values larger than 4. The overall behavior, in the end, is that it results easier to satu-

| **Conc.** (M) | $\mathbf{t}_{eq}$ (nm) | $\Delta\mathbf{t}_{eq}$ (nm) | **T** (K) | $\mathbf{m}_S(\times\mathbf{10}^{-5})$ (emu) | $\mathbf{M}_S$ $(\frac{\text{emu}}{\text{cm}^3})$ | $\Delta\mathbf{M}_S$ $(\frac{\text{emu}}{\text{cm}^3})$ | $\Delta\mathbf{M}_{S,rd.}$ $(\frac{\text{emu}}{\text{cm}^3})$ | $\mathbf{H}_C$ (Oe) | **No.Samp.** _ |
|---|---|---|---|---|---|---|---|---|---|
| 0.015 | 1.5 | 0.5 | 35 | 1.8 | 480 | 160 | 200 | 200 | 1 |
| | | | 110 | 1.6 | 427 | 142 | 100 | 130 | 2 |
| | | | 300 | 0.86 | 229.3 | 76 | 80 | 20 | 1 |
| 0.022 | 2.2 | 0.5 | 35 | 3.1 | 563 | 128 | 100 | 155 | 1 |
| | | | 110 | 2.9 | 527.3 | 120 | 100 | 115 | 1 |
| | | | 300 | 1.8 | 327 | 74 | 70 | 20 | 1 |
| 0.03 | 3.5 | 0.5 | 110 | 4.07 | 465 | 66 | 70 | 115 | 3 |
| | | | 160 | 4.3 | 491 | 70 | 70 | 90 | 1 |
| | | | 300 | 2.7 | 309 | 44 | 40 | 20 | 2 |
| 0.06 | 5.5 | 1 | 110 | 7.7 | 560 | 102 | 100 | 100 | 1 |
| | | | 300 | 5.3 | 386 | 70 | 70 | 30 | 1 |

**Tab. 3.3:** *In-plane saturation magnetic moment* $\mathrm{m_s}$ *and magnetization* $\mathrm{M_s}$ *values for a set of different solution concentrations, measured by SQUID.* $\Delta M_S$ *is the error associated to* $\mathrm{M_S}$*, due to the uncertainty in the* $\mathrm{t_{eq}}$ *equivalent thickness estimation.* $\Delta M_{S,rd.}$ *represents the error rounded up to a single significant figure. 1 emu/cm*$^3$*= 1 kA/m.*

rate the system with an in-plane applied magnetic field than with an out-of-plane field. In order to determine which in-plane direction is the easy magnetization axis, we conducted Ferromagnetic Resonance experiments, which we shall discuss in the next section.

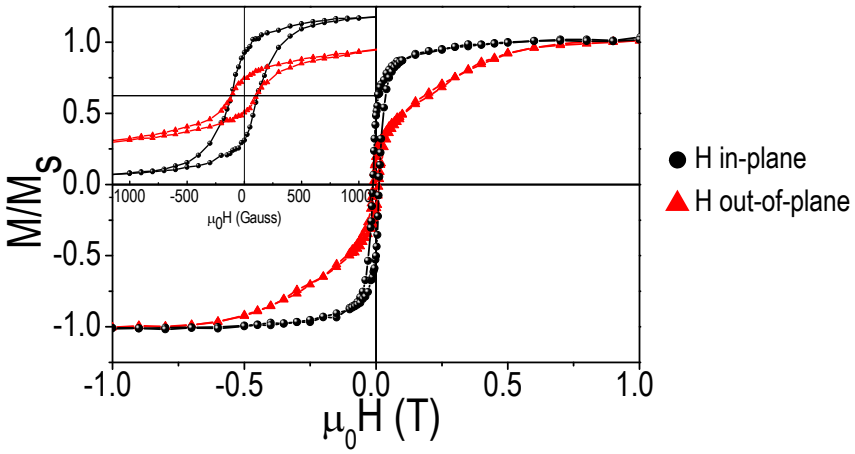


**Fig. 3.40:** *Normalized magnetization vs H loops at T=110 K for magnetic fields applied in-plane (black dots) and out-of-plane (red triangles), indicating that the easy axis of the self-assembled LSMO nanoisland system lies within the sample plane. The sample was grown from 0.03 M solution, heat-treated at 900°C 3 h. A magnified view of the center of the cycles is given in the inset.*

Fig. 3.41 shows the temperature dependence of the saturation magnetization of LSMO on YSZ nanoislands grown from 0.015 M and 0.03 M precursor solutions. The Curie temperature deduced from the plots, $T_c$∼350±5 K, is close to that of bulk LSMO ($T_C$∼360 K [82]), which is quite a remarkable result for sub-200 nm wide ∼20-30 nm thick nanostructures. This high $T_C$ value can be correlated to the absence of strain within the islands

-deduced from XRD and TEM investigations- and also to the non-invasive self-assembly growth process, which prevents the degradation of the magnetic properties caused by ion implantation or radiation damage induced by nanolithography processes [66]. A $T_C$ ∼350 K value was also measured for the 0.06 M nanostructured sample (not shown).

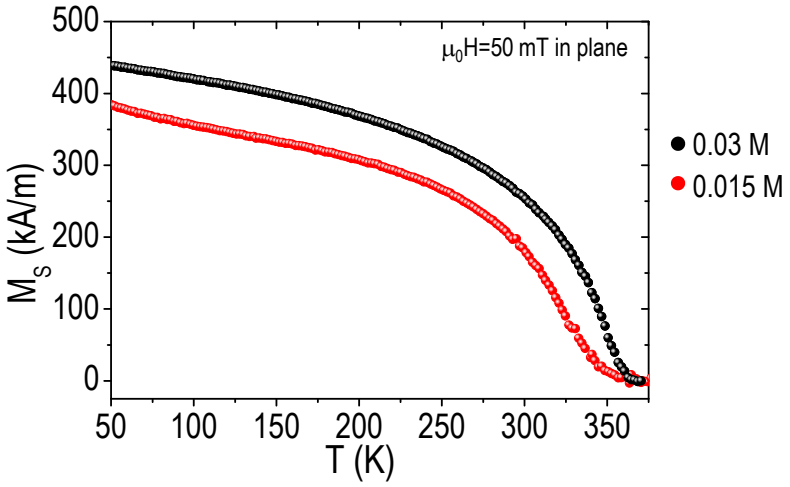


**Fig. 3.41:** *Saturation magnetization as a function of temperature for two LSMO on YSZ nanoisland samples grown from 0.015 M and 0.03 M precursor solutions. $T_C$ takes a value close to 350 K. A 50 mT in-plane magnetic field was applied.*

It is noteworthy that the magnetic signal plotted in Fig. 3.41 is larger in the case of the 0.03 M sample, consistent with the general trend that emerges from Fig. 3.39, which shows larger $M_S$ values for increasing concentration values. For smaller precursor solution concentrations, the general tendency is to have smaller self-assembled nanoislands, i.e. increased surface to bulk ratios. Lower magnetic signals could thus be related to the presence of a ferromagnetic dead layer. As already mentioned for LSMO on STO and LAO, the existence of ferromagnetic dead layers is associated to free surfaces and interfaces of manganite thin films and nanostructures. Such surface and interface layers are precisely the places where the lattice symmetry is broken, defects and non-stoichiometries may be important, and the $Mn^{3+}$-$O^{2-}$-$Mn^{4+}$ angles distort with respect to the bulk [25, 26, 197].

Fig. 3.42 shows the volume fraction within an individual LSMO nanoisland which would be non ferromagnetic, plotted as a function of $D$ for specific $t$ values. We have considered the last 1 nm or 2 nm of the nanoisland to be a ferromagnetic dead layer. The calculations are done for $(001)_{\mathrm{LSMO}}$-oriented regular-square islands (the island sketch is plotted next to the graph of Fig. 3.42). We have derived the non-FM volume by multiplying the dead layer thickness (assuming an homogeneously thick layer) to the area of the square-base truncated pyramid. As it follows from the plot, the larger the island (larger $t$ and $D$), the smaller is the non-ferromagnetic fraction. If we take, for instance, a common $D$ value of 120 nm, the percentage of non-FM volume can vary from an upper limit of ∼44% (if we consider a 2 nm dead layer in a $t$=10 nm thick island), to a lower limit of ∼11% (for a $t$=30 nm island and taking a 1 nm thick dead layer). These two limits are indicated in Fig. 3.42. The difference between the magnetization of a 0.03 M derived LSMO nanoisland system ($M_S$∼465 kA/m at T=110 K, see Fig. 3.39 and Tab. 3.3) and that of bulk LSMO from Park et al. (∼575.25 kA/m at T=110 K) [19] gives a non-FM volume of ∼20%, which is within the

range of our calculated non-FM volume fractions. We will further comment on the dead layer in the context of the LSMO nanoisland nanoscale analysis of Chapters 4 and 5.

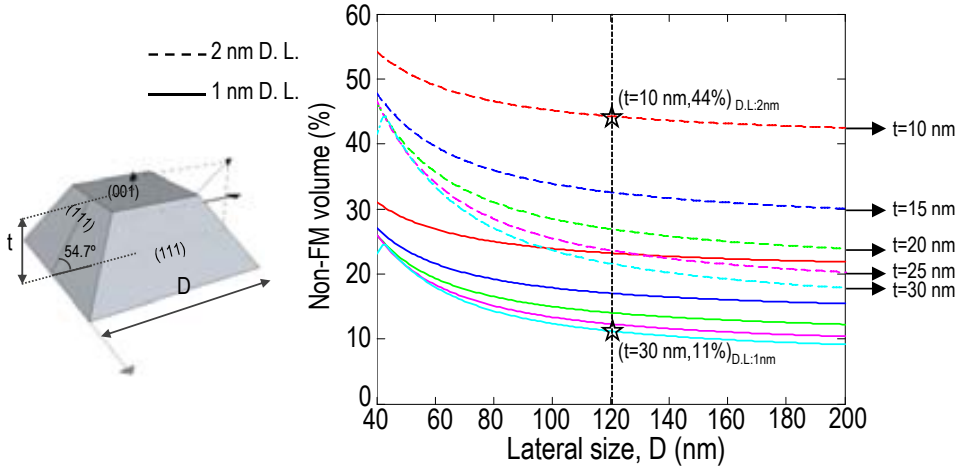


**Fig. 3.42:** *Non-FM volume percentage within a $(001)_{LSMO}$-oriented nanoisland, considering 1 nm (dashed lines) and 2 nm (solid lines) thick FM dead layers (D. L.). The different colors stand for different island thickness values, i.e. 'red'=10 nm, 'blue'=15 nm and so on. The sketch on the left hand side remarks the nanoisland geometry.*

### In-plane magnetic anisotropy and magnetocrystalline anisotropy constant measurement through FMR

Ferromagnetic Resonance (FMR) experiments were conducted to study the in-plane magnetic anisotropy of the system of self-assembled LSMO nanoislands on YSZ. These measurements were performed in a Bruker ESP 300 spectrometer operated at 9.5 GHz in a rectangular X-band cavity operating in the TE102 mode. The FMR spectra reported here were done at 150 K keeping the applied field, $H$, in the sample plane. A representative 0.03 M 900°C/ 2 h sample, like the one imaged in Fig. 3.21 (a) was measured. Hence, a sample consisting of regular-square pyramidal nanoislands. The results here presented are the outcome of the collaboration with Dr. C. A. Ramos and Dr. R. D. Zysler from *Centro Atómico* and *Instituto Balseiro* in Bariloche, Argentina. Fig. 3.43 shows the measured in-plane angular dependence of the resonant field $H_r$. This value is obtained at each angle by fitting the FMR spectra with a Lorentzian lineshape. Experimental data show a clear angular dependence of $H_r$ at 150 K. Note that a minimum in $H_r$ indicates an easy magnetization axis, in this case the [110] axis of the LSMO nanoislands.

To explain the origin of the observed anisotropy we followed a standard formalism [198]. The energy density function is defined as follows, developing up to the first order the magnetocrystalline anisotropy term:

$$E = -\mu_0 HM + \frac{\mu_0}{2} M^2 (N_x\alpha_x^2 + N_y\alpha_y^2 + N_z\alpha_z^2) + K_1(\alpha_x^2\alpha_y^2 + \alpha_x^2\alpha_z^2 + \alpha_y^2\alpha_z^2) \qquad (3.2)$$

where the first term represents the Zeeman energy, the second is the magnetostatic contribution ($N_x$ $N_y$ $N_z$ are the demagnetizing factors) and the third is the cubic crystalline anisotropy, with $\alpha_i$ the direction cosines of the magnetization $M$. In this in-plane configuration, no magnetoelastic contribution should be expected since the strain exerted by the

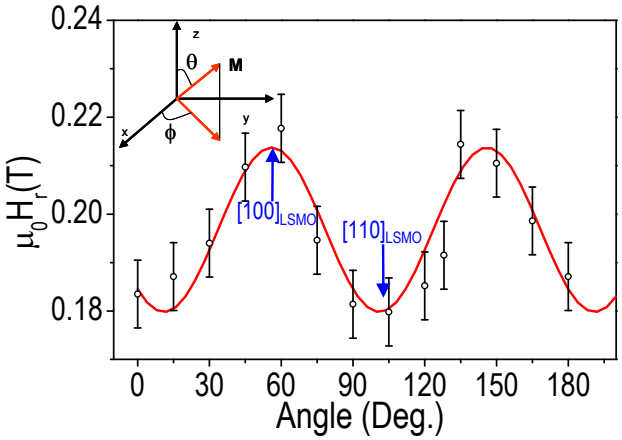


**Fig. 3.43:** *FMR results. Open symbols represent the measured in-plane dependence of the resonant field $H_r$ at 150 K. The solid line is the fitting to the experimental data according to Eq. 3.4. The inset shows the coordinate system used. The $H_r$ minima, when the field is applied parallel to the $[110]_{LSMO}$ direction, indicate an easy magnetization axis.*

substrate on the pseudocubic LSMO is isotropic [195]. Moreover, we can rule out any possible deviation from a truly isotropic in-plane strain because nanoislands are fully relaxed. Concerning the magnetostatic contribution, we estimated the demagnetizing field of a flat square-based pyramid magnetized perpendicularly to its base and found $N = 0\,70 \pm 0\,05$ for island aspect-ratio *D/t* in the range of 4±1, which are the typical values found for this kind of sample. Considering $N_x + N_y + N_z = 1$ ($N_x = N_y = N \sim 0\,15$) it turns out that the effective shape demagnetizing factor for the applied field, $H$, parallel to the pyramid base, depends only on the difference $N - N \equiv \Delta N$. We rewrite Eq. 3.2 using the coordinate systems sketched in the inset of Fig. 3.43:

$$E = \mu_0 M H[\sin\theta\cos(\theta - \theta_H)] + \frac{\mu_0}{2} M^2 \Delta N \cos^2\theta + \frac{K_1}{4}(\sin^4\theta \sin^2 2\theta + \sin^2 2\theta) \qquad (3.3)$$

where ($\theta$, $\theta$) define the position of $M$ (inset in Fig. 3.43), and $H$ is applied in the *xy* plane at an angle $\theta_H$ with respect to the [100] axis. From the conditions $\frac{dE}{d\theta} = 0$ and $\frac{dE}{d\phi} = 0$ we reach the corresponding equilibrium positions: $\theta = \frac{\pi}{2}$ and, by assuming $K_1\ M << \mu_0 H$, $\theta = \theta_H$, thus indicating that $M$ lies in the *xy* plane and that it is parallel to the applied field. Evaluating the second derivative of Eq. 3.3 at the equilibrium positions $\theta = \frac{\pi}{2}$ and $\theta = \theta_H$, and replacing the result in the Smit-Beljers equation [198], we obtain the FMR condition for our system of nanoislands:

$$\left(\frac{-}{\gamma}\right)^2 = \left[\mu_0 H + \mu_0 \Delta N\ M + \frac{2K_1}{M}\left(1 - \frac{1}{2}\sin^2 2\theta\right)\right]\left(\mu_0 H + \frac{2K_1}{M}\cos 4\theta\right) \qquad (3.4)$$

where $\gamma$=0.34 T, $= 2\bar{}\nu$ with $\nu$=9.5 GHz the X-band microwave frequency used, and $\gamma$ is the gyromagnetic factor for LSMO. The fitting of the experimental data to the Eq. 3.4 (solid line in Fig. 3.43) yields the values $\mu_0 \Delta N\ M(150\ K) = (0\,393 \pm 0\,004)$T and $2K_1\ M(150\ K) = -(0\,021 \pm 0\,002)$T. Our numerical estimation of the flat pyramids' effective demagnetizing field gives $\mu_0 \Delta N\ M(150\ K) = (0\,3 \pm 0\,1)$T, where we have introduced the measured saturation magnetization at 150 K $M = 0\,95 \times (465 \pm 70)$ kA/m, reduced a 5% from the 110 K value listed in Tab. 3.3 **. Thus both values compare well

**We did not take directly the $M_S$ value at 150 K from the *M(T)* curve in Fig. 3.41 because it corresponds to a

and prove the validity of the assumptions made in the treatment. On the other hand, the value for the magnetocrystalline anisotropy constant $K_1$ is deduced from $2K_1\ M$, giving $K_1(150K) = -(5\pm1)$ kJ/m$^3$. This result is in the order of what it is reported in literature for LSMO films grown along the (001) plane which show the [110] in-plane easy axis [90, 199]. To our knowledge, this is the first reported shape anisotropy study for LSMO nanoislands, along with the first measurement of $K_1$ in such nanoscale systems.

In conclusion, regarding the macroscopic magnetic properties of self-assembled LSMO nanoislands on YSZ, we have shown that the nanoisland ensemble exhibits clear ferromagnetic behavior, with in-plane anisotropy, saturation magnetizations not far from the reported LSMO bulk values (especially at low temperatures), and $T_C$∼350 K, i.e. well above room temperature, and close to the $T_C$∼360 K of bulk LSMO. Such values are not straightforward to obtain in sub-micrometer magnetic oxide nanostructures: on one hand, their processing relies typically on e-beam lithography and/or ion milling procedures, that were found to lower the $T_C$ due to radiation damage and ion implantation [66]. The spontaneous self-assembly process described in this work avoids these detrimental effects. On the other hand, the influence of strain on the magnetic properties, widely claimed to cause lower $T_C$ values, is also avoided: LSMO nanoislands show a highly crystalline strain-relaxed structure. We have also discussed the possible role of a ferromagnetic dead layer, which could account for the lowering of the magnetization signals measured in the nanoisland ensembles. Finally, we have analyzed the role of different magnetic anisotropy contributions in the overall anisotropy of the self-assembled LSMO system, which has been proved to display an in-plane $[110]_{\mathrm{LSMO}}$ magnetic anisotropy. This highlights the influence of the magnetocrystalline anisotropy (with $< 111 >_{\mathrm{LSMO}}$ easy axis), and that of the shape anisotropy, due to the platelet-like nanoisland shape. To the best of our knowledge, no LSMO nanoislands with lateral sizes below ∼200 nm and bearing the ferromagnetic properties presented in this work have been reported up to date.

## 3.5 LSMO on MgO

In the present section we investigate a different oxide heterostructure, again consisting of two very different compounds: perovskite type LSMO is now grown on MgO single crystal, a well known binary oxide with rocksalt structure. The difference in lattice parameter between LSMO and MgO results in a nominal tensile mismatch of +8.8%. Similarly to what we have seen concerning the LSMO/YSZ heteroepitaxy, a homogeneous dispersion of self-assembled nanoislands is also obtained for LSMO on MgO. However, and at variance with the previous case, the ferromagnetic nature of the LSMO nanodots appears now largely supressed. Also, the particular nanoisland self-assembly observed here, with nanoislands decorating MgO step edges, appears dominated by island-substrate interaction. In order to shed light into these facts, and further motivated by the intrinsic microstructural richness of this system, a detailed TEM characterization of the LSMO/MgO interface has been carried out in parallel to the present work, in the context of a recent PhD thesis within our group [160].

single sample. Rather than that, we used the *M(T)* curve to extrapolate the decrease of *M* with *T*, but taking the more realistic averaged value of $M_S$ at 110 K from Tab. 3.3

### 3.5.1 General view of the system

Our knowledge of CSD-grown LSMO on YSZ paved the way for the fabrication of self-assembled LSMO nanoislands on MgO substrates. By using LSMO precursor solution concentrations in the range of 0.015 M to 0.06 M (in Mn), we achieved a homogeneous self-assembly of LSMO nanoislands on MgO, covering the whole 5 mm $\times$ 5 mm substrate. Fig. 3.44 shows the result after processing a 0.03 M LSMO precursor solution deposited on a MgO substrate at 900°C for 3 h. The 1 µm $\times$ 1 µm AFM topography image, in Fig. 3.44 (a), displays a high concentration of square and rectangular-base nanoislands, with thickness $t$ typically below 10 nm and widths $D$ in the 40-60 nm range. The area coverage for this sample is $\sim$35%. The amount of material calculated from AFM volume analysis is comparable to what we obtained from growing 0.03 M solutions onto YSZ substrates. This was expected, since identical spin-coating conditions were used, and the same wettability of the solution with respect to the MgO was measured (recall the Experimental procedure description in Chapter 2). Hence, the *Concentration* vs *Equivalent thickness* relation plotted in Fig. 3.20 equally holds for this system.

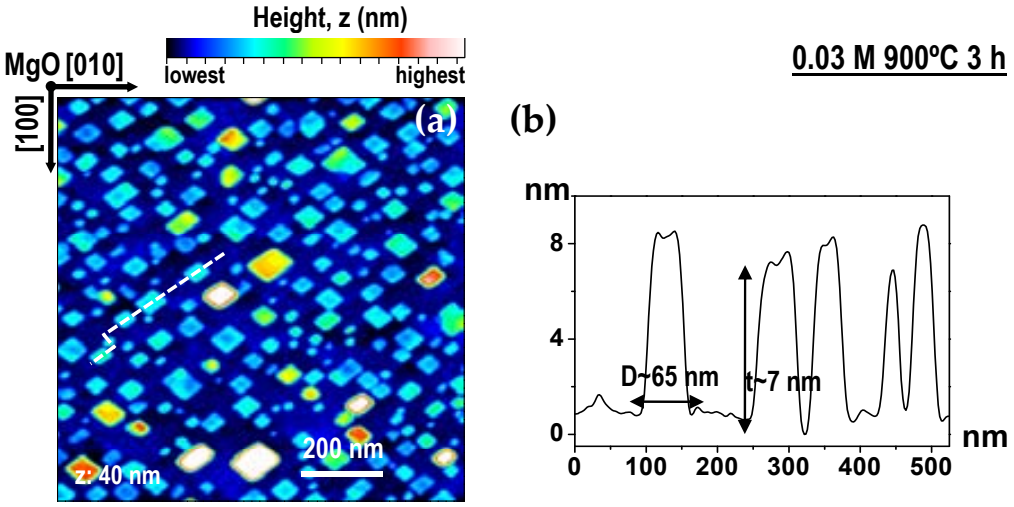


**Fig. 3.44:** *(a) 1$\mu$m $\times$ 1$\mu$m AFM topography image of self-assembled LSMO nanoislands grown on MgO from a 0.03 M solution, heat-treated at 900°C for 3 h. (b) Line profile corresponding to the dashed line in (a), showing the typical island sizes.*

A statistical study of nanoisland sizes gives the thickness $t$ and lateral size $D$ distributions plotted in Fig. 3.45 (a). Some very few islands ($\sim$3% in the AFM image of Fig. 3.44) exhibit $t$ values of $\sim$30-40 nm. If we neglect them, the thickness distribution appears centered in $t\sim$7 nm values, with a remarkably narrow dispersion (a standard deviation of $\sim$2 nm is measured). The lateral sizes are in the order of $D\sim$50 ($\pm$20) nm, which gives aspect ratios of around $D$ $t\sim$7. These high aspect ratio values underline, once more, the tendency of solution-derived heteroepitaxial systems to give nanoislands with widths larger than thicknesses, a trend already highlighted in the LSMO/YSZ case. The $Z$-contrast STEM image in Fig. 3.45 (b) further illustrates the lateral size vs thickness relation. Recall that the intensity in a STEM micrograph is proportional to the $Z$ atomic number of the imaged element (the higher the $Z$, the brighter the contrast). Nanoislands are thus seen as bright structures against the darker MgO substrate ($Z_{La}$:57, $Z_{Sr}$:38, $Z_{Mn}$:25 and $Z_{Mg}$:12).

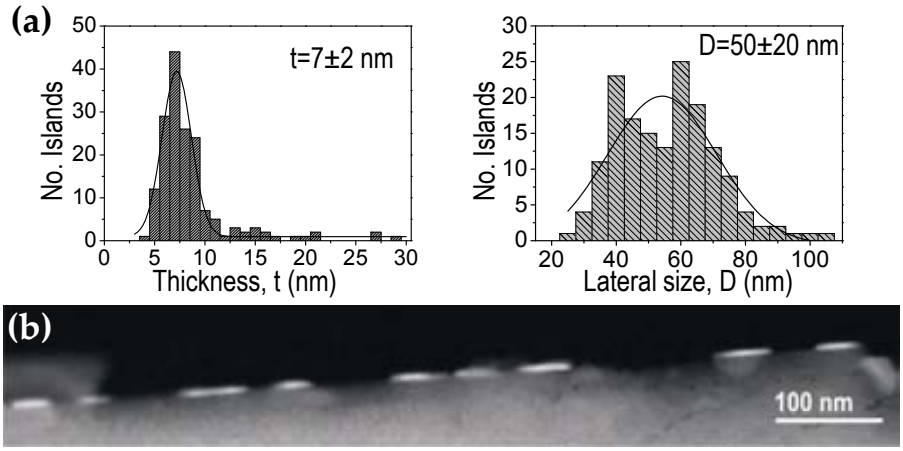


**Fig. 3.45:** *(a)* t *and* D *histograms showing the island size distribution. The values correspond to the sample shown in Fig. 3.44. (b) Low magnification STEM image showing 9 platelet-like LSMO nanoislands (in bright contrast). STEM image courtesy of P. Abellán.*

### Crystallographic orientation

We combined XRD $\theta$-$2\theta$ scans with pole figure measurements recorded with a 2D detector in order to assess the overall crystallographic orientation of the nanoislands. A $(001)_{LSMO}$ out-of-plane orientation emerges both from the $\theta$-$2\theta$ scan and from the pole figure of the $(011)_{LSMO}$ reflection, which appears at $\gamma$=45°. From the simultaneous measurement of the $(111)_{MgO}$ reflection, rotated 45° in $\theta$ with respect to the $(011)_{LSMO}$ spots, we deduce that nanoislands withstand a cube-on-cube epitaxy, i.e. $(001)_{\mathrm{LSMO}}[100]$ $(001)_{\mathrm{MgO}}[100]$. It is with such interface arrangement that the lattice mismatch between islands and substrate is minimum (although still considerably high, $\sim$8.8%). Note that this epitaxial relation is general, i.e. we measured it for all LSMO on MgO nanostructured templates with solution concentrations ranging from 0.015 M to 0.06 M, and annealings from 1 h to 24 h at temperatures between 900°C and 1000°C. It is also worth noting that the LSMO poles [see Fig. 3.46 (b)] exhibit a large spread in $\gamma$, suggesting a certain degree of misorientation among the nanostructures.

As a matter of fact, by tuning the contrast and the intensity of the pole figure we can actually distinguish the fine structure, which consists of five well-resolved spots [Fig. 3.47 (a)]. We further performed a more detailed $\theta$ scan around a single $(011)_{\mathrm{LSMO}}$ reflection using smaller steps ($\Delta\theta$=0.5° instead of the standard $\Delta\theta$=2°). The result, plotted in Fig. 3.47 (b), unambiguously shows a central spot (corresponding to perfect cube-on-cube epitaxy) surrounded by four satellite peaks. The latter appear displaced, both in $\gamma$ and $\theta$, by 2°-5°, with the maximum intensity at a value of 4($\pm$0.5)° both for in-plane and out-of-plane disorientation values. A detailed HRTEM investigation of the LSMO/MgO interface has evidenced the presence of dislocations with Burgers vectors $b$=$\frac{a}{2}$[100] and $b$=$\frac{a}{2}$[001], producing a rough and defective interface [160, 200]. While $b$=$\frac{a}{2}$[100] dislocations accommodate the high nominal tensile strain between LSMO and MgO, it is demonstrated that the $b$=$\frac{a}{2}$[001] dislocations account for rigid body rotations of the LSMO nanoislands. In particular, islands with out-of-plane tilts of $\sim$2°, $\sim$4°, and a maximum of $\sim$5°, along with nanoislands with perfect cube-on-cube epitaxy (no rotation), have been observed [160]. A magnified view of the LSMO/MgO interface, including three dislocations, is shown in the HRTEM

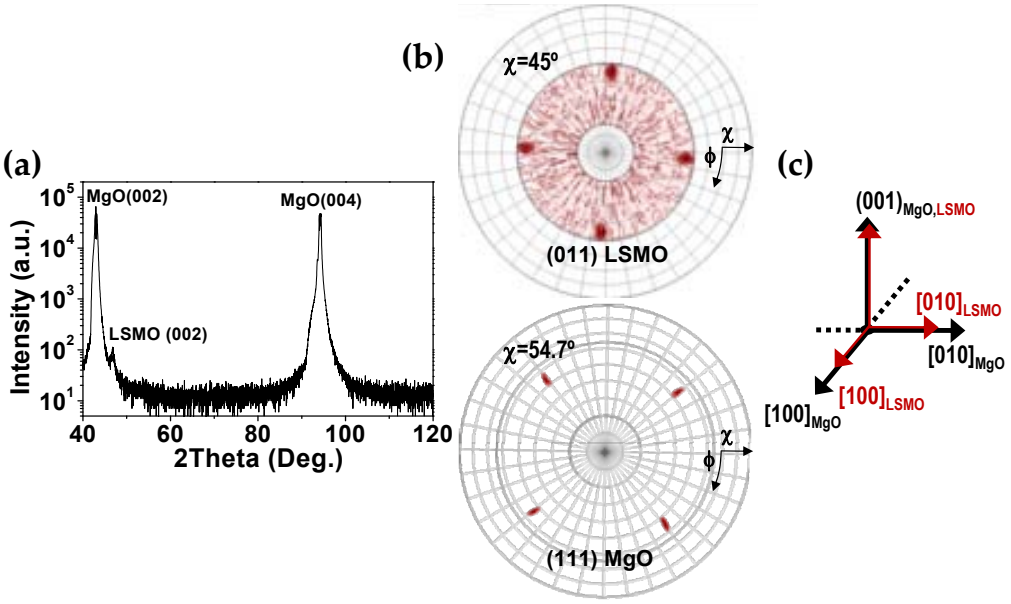


**Fig. 3.46:** *(a) $\theta - 2\theta$ scan of a LSMO nanoisland ensemble on MgO. The $(002)_{LSMO}$ reflection is observed at $2\theta$=46.9°. (b) Pole figure measurements of the same sample giving the in-plane cube-on-cube interfacial arrangement. (c) Schematic diagram of the LSMO on MgO heteroepitaxy. The sample measured in the figure was 0.03 M, heat-treated at 900°C for 1 h.*

micrograph of Fig. 3.47 (c). Note that No. 3 consists of two superimposed dislocations, i.e. $b$=$\frac{a}{2}$[100] and $b$=$\frac{a}{2}$[001], while each No. 4 and 5 only exhibit the strain-accommodating partial dislocation, $b$=$\frac{a}{2}$[100]. The dislocations responsible for the out-of-plane tilt result in a net rotation about the in-plane <110> directions. This explains, by taking into account the two possible tilt senses, the four satellite LSMO poles detected in the pole figure measurements [200].

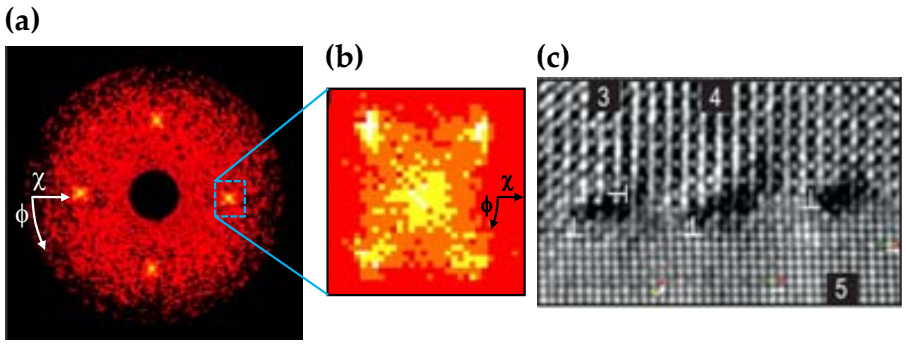


**Fig. 3.47:** *(a) $(011)_{\mathrm{LSMO}}$ pole figure. The step used was $\Delta\chi$=2°. (b) The phi-scan measurement of a single $(011)_{\mathrm{LSMO}}$ reflection, using a $\Delta\chi$=0.5° step, further reveals the fine structure of a single reflection, consisting of one central and four satellite peaks. The maximum intensity both in $\chi$ and in $\gamma$ is measured at 4°$\pm$ 0.5°. (c) Detailed HRTEM image of the LSMO/MgO interface, featuring misfit accommodating dislocations (symbol ) and a dislocation responsible for nanoisland rotation (symbol ). HRTEM image courtesy of P. Abellán and M.J. Casanove.*

### Nanoisland morphology

Fig. 3.48 (a) shows the *Z*-contrast STEM cross-section image of a LSMO nanoisland on MgO, seen along the $[100]_{\mathrm{MgO}}$ direction (which is also the $[100]_{\mathrm{LSMO}}$ direction). The good crystalline quality is evident from the clear arrangement of the atomic columns within the island. Note that the brighter central part of the island, indicating a thicker specimen, is a consequence of the in-plane rotated-square nanoisland morphology [see Fig. 3.44 (a)]. Arrowheads point at surface steps, which adopt half unit cell heights at the nanoisland/substrate interface [160]. The top facet is clearly a $(001)_{\mathrm{LSMO}}$ plane, as expected from AFM topography images and XRD results. The projection of the lateral facets into the observation plane falls at 90° with respect to the substrate horizontal line. Two possible nanoisland shapes would yield this projection: either a *boxed-shape* island with $\langle 110 \rangle_{\mathrm{LSMO}}$ lateral planes, or a *truncated pyramid* with $\langle 111 \rangle_{\mathrm{LSMO}}$ oblique planes, truncated at the corners by $\langle 100 \rangle_{\mathrm{LSMO}}$ facets. We have schematically illustrated both possibilities in Fig. 3.48 (b).

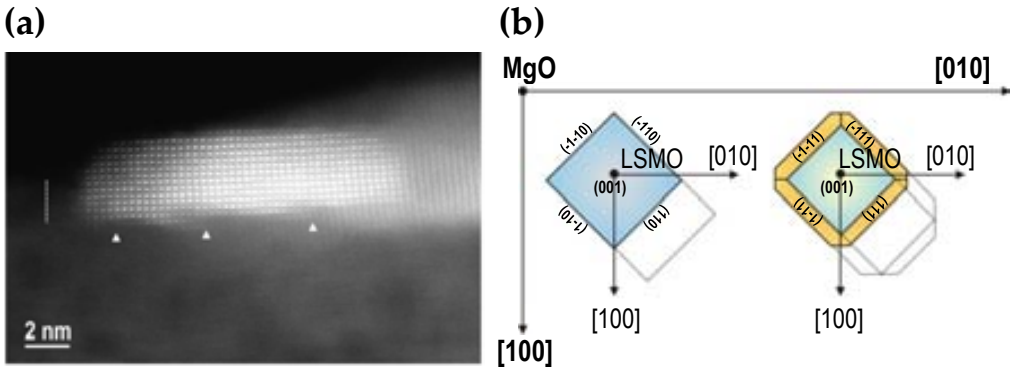


**Fig. 3.48:** *(a) HAADF-STEM image of a LSMO on MgO nanoisland viewed along the [100] direction. The arrowheads mark the substrate steps. (b) Sketch of the two possible island morphologies according to the STEM results. The epitaxial relationship and the nanoisland facets are indicated. STEM image courtesy of P. Abellán.*

### Evolution of the LSMO on MgO nanostructured system. The role of the substrate morphology in the nanoisland self-assembly

In Fig. 3.49 we compare $5\ \mu\mathrm{m} \times 5\ \mu\mathrm{m}$ AFM images of two samples: one heat-treated at 900°C for 1 h, the other at 1000°C for 24 h. The solution concentration was 0.03 M for both. Analogous conditions resulted in a substantial evolution of the LSMO/YSZ system [recall Fig. 3.21, Fig. 3.23, and Fig. 3.29] but do not trigger a notable change in the present case. The area coverage is very similar, as well as the thickness distribution (*z* scale is around 60 nm). Nanoislands may appear slightly more rounded in the high *T* sample, which is expected from the enhanced atomic diffusion. If we look at the substrate surface in Figs. 3.49 (a') and (b') (by saturating the island contrast), we can see the effect of the different thermal annealings. Well-defined substrate steps are apparent in the 3D image of both samples. In Fig. 3.49 (a) the terraces along the <110>$_{MgO}$ directions feature sharp edges and kinks. These terraces are still observable in the sample of Fig. 3.49 (b), although they appear more rounded by the effect of atomic diffusion at high temperatures (a few have

been marked with white dotted lines). Note also that small square holes have developed, and that islands sit at their rims and at the terrace edges.

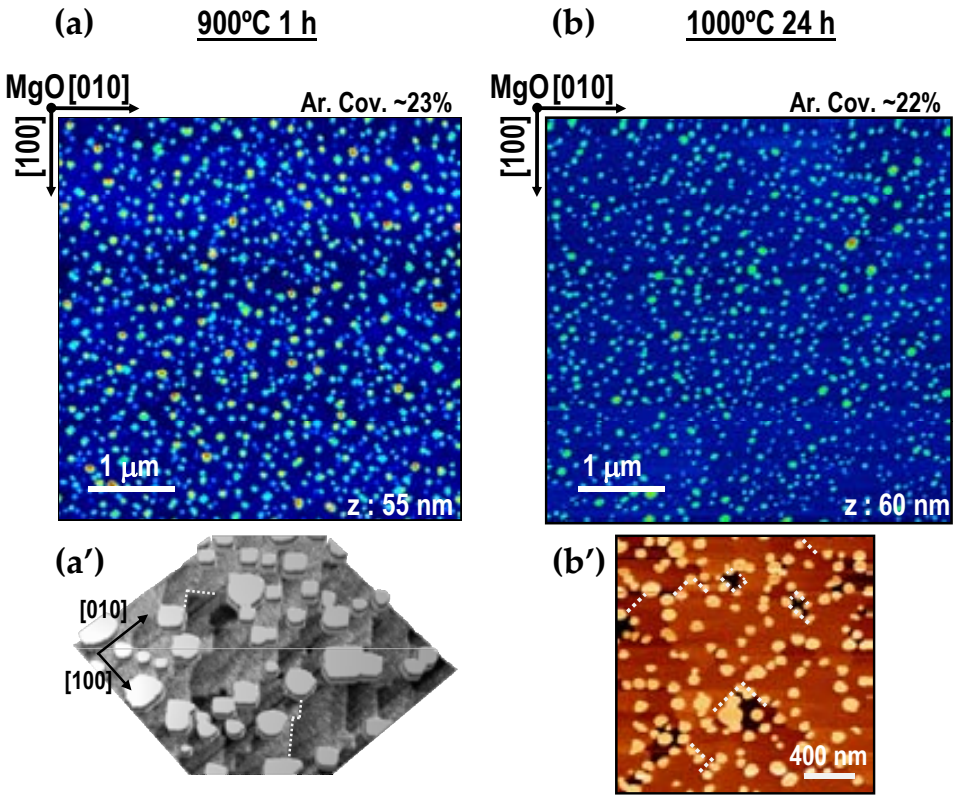


**Fig. 3.49:** *5$\mu m \times 5\mu m$ AFM topography images of LSMO on MgO self-assembled nanoislands resulting after (a) 900°C 1 h and (b) 1000°C 24 h heat treatments. Solution concentrations of 0.03 M were used. (a')&(b') 1$\mu m \times 1\mu m$ and 2$\mu m \times 2\mu m$ topography details of the step edges, aligned along the <110>$_{MgO}$ directions, showing the preferential location of nanoislands at step edges and rims.*

As we already stated in Chapter 2, upon thermal treatments at 900°C, MgO does not form well-defined steps. This is shown again in the AFM topography image of the bare substrate in Fig. 3.50 (a). After the deposition of 0.03 M LSMO precursor solution and the subsequent heat treatment (also at 900°C, but just for 1 h), however, a well defined step-terrace morphology develops, with the surface steps running along the <110>$_{MgO}$ directions. It is also worth emphasizing that samples featuring LSMO nanoislands grown at 900°C for 1 h on substrates with no previous heat treatment exhibit <110>$_{MgO}$ aligned steps in identical manner. At higher temperatures, as shown in Fig. 3.50 (b), terraces adopt a rounder shape at the kinks and edges but we may still detect the <110>$_{MgO}$ directions that they follow. In the 900°C 1 h sample we observe 0.5, 1, and 1.5 u.c. step heights which increase up to 5 and even 6 u.c. at high temperatures, due to step-bunching. Note how, in both cases, the observed step-terrace configuration is intimately linked to the distribution of the nanoislands, which preferentially locate at the kinks and terrace edges. See, for instance, in Fig. 3.50 (b), how the decoration pattern formed by nanoislands is determined by their positioning on top of substrate edges. Besides, in the totality of nanostructured LSMO on MgO samples processed at $T \leq 1000$°C (around 15), we always observed a rotated-square

island morphology, i.e. with its edges parallel to the substrate terrace edges. All of this is in remarkable contrast to what we discussed for the case of LSMO nanoislands on YSZ, where we saw the nanoisland disposition and morphology to be independent of the substrate step-terrace structure.

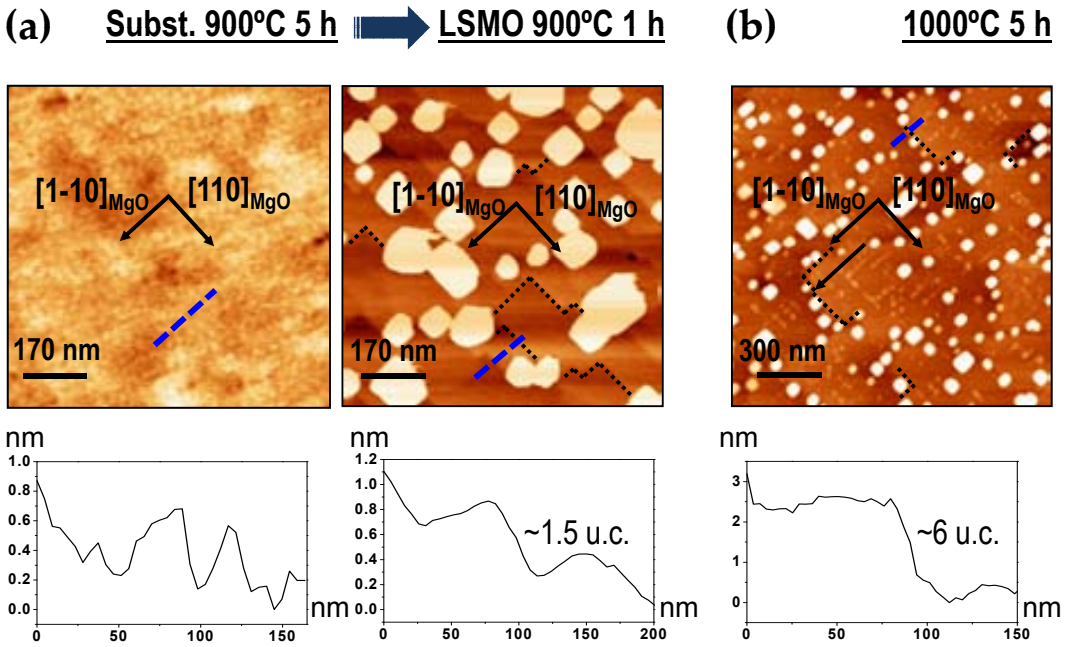


**Fig. 3.50:** *(a) MgO bare substrate after 900°C 5 h annealing under flowing oxygen (left), and after the subsequent deposition and growth of LSMO 0.03 M at 900°C for 1 h (right). The well-defined step-terrace morphology occurs only after the LSMO deposition. (b) Another sample after deposition of LSMO and annealing at 1000°C for 5 h. Square and rectangular-base nanoislands decorate the underlying step edges. Dotted black lines indicate some of the MgO terraces. The blue dashed lines correspond to the line profiles of the substrate steps below.*

The presence of sharp edges on the surface of substrates has been proved an efficient way of directing the self-assembly of nanostructures in heteroepitaxial systems. Nanoislands are seen to preferentially locate at those edges under specific conditions. These preferential location sites or *edges* can be found in naturally occurring surface steps [200], at the rims of holes...etc, or can be made deliberately by different lithography techniques [201], focused ion beam [202], or even using more exotic approaches like nanoindentation [172]. This provides for an effective strategy for the control of nanoisland positioning, as required in many nanotechnology applications. Lagally and co-workers explained these experimental facts by theoretically predicting the appearance of certain local energy minima at either concave or convex places of otherwise flat substrates [201]. A nanostructure may either relax or increase its elastic strain energy by locating at a curved site. The competition between this elastic strain relaxation and the interface energy of the nanostructure, both dependent upon the curvature of the underlying site, are at the origin of the appearance of the local energy minima, where nanoislands preferentially locate [201].

We now examine how the system behaves if we push it to temperatures as high as 1300°C for 5 h, as we did for the LSMO on YSZ self-assembled nanoislands in section 3.4.1. Fig. 3.51 reveals that for LSMO on MgO, the system undergoes a remarkable transforma-

tion. Note that the AFM image of Fig. 3.51 (a) is the same size as the images in Figs. 3.49 (a) and (b), 5 µm × 5 µm, but now it features very few and large triangular-base nanoislands ($t$∼60 nm, $D$∼380 nm) which stand on top of a leaf-like substrate surface pattern. This surface is far from atomically flat, featuring holes in the 5-15 nm range [see the line profile of Fig. 3.51 (b)]. Within the different 'terraces' perfectly squared holes develop, as expected from a cubic material, although these holes, remarkably, follow the <110>$_{MgO}$ directions. Note that, at lower temperatures, we have seen such orientations to be the ones adopted by terraces. Moreover, we have also identified the presence of small holes at 1000°C, which could be the precursors of the actual structures.

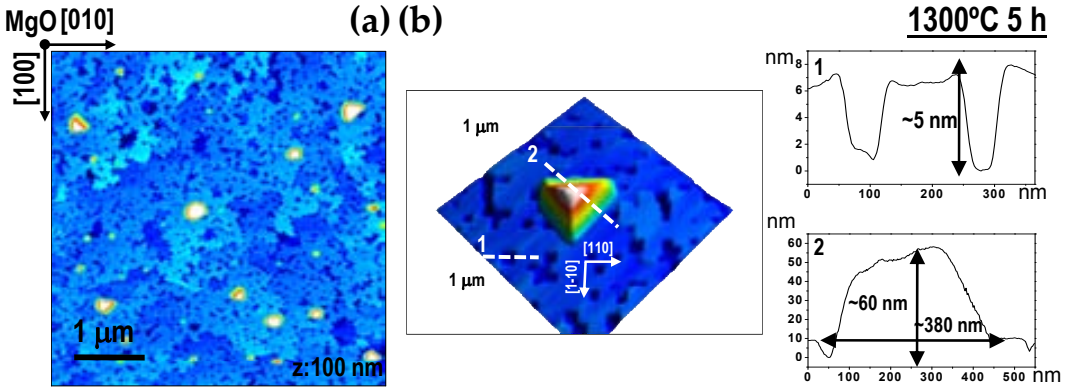


**Fig. 3.51:** *(a) 5µm × 5µm AFM topography image showing the transformation of substrate and LSMO nanoislands when the heat treatment (0.03 M solution) is performed at 1300°C for 5 h. (b) A 3D detail of a single island, as large as 380 nm in lateral size. The dashed lines numbered* 1 *and* 2 *correspond to the line scans on the right.*

The $\theta$-$2\theta$ and pole figure measurements of the 1300°C treated system, displayed in Fig. 3.52, reveal that, despite the striking morphological difference, nanoislands hold the same epitaxial relationship as the LSMO on MgO nanoislands heat-treated at $T\leq$1000°C: they grow epitaxially and cube-on-cube on top of MgO. Due to their different shape with respect to the square islands discussed before, it follows that their facets are also different, which should be verified by TEM cross-section studies. It is also worth mentioning that, for these high $T$ samples, the spread in $\gamma$ of the LSMO poles is far smaller, as it is deduced from comparing the pole figures in Fig. 3.46 and Fig. 3.52. This result suggests that, after the 1300°C annealing, these new islands do not exhibit the 2° to 5° tilts.

Further experiments are needed to shed light into the striking morphological transformation we observe in the LSMO/MgO heteroepitaxy upon 1300°C annealings. MgO is thermodynamically stable at 1300°C and ambient pressure [203] and so it is in principle not expected that it should undergo such a change. Also, 1300°C were not enough to produce a comparable evolution of the LSMO/YSZ heteroepitaxy, despite in this case a chemical reaction was also involved. It would be thus necessary to investigate the intermediate stages between 1000°C (where no transformation is observed) up to 1300°C. Also it would be interesting to study the effect of these high $T$ treatments on bare MgO substrates, in order to assess the role of the LSMO nanoislands on the observed transformation.

In summary, throughout this section we have shown the general features of self-assembled LSMO nanoislands on MgO. Compared to LSMO on YSZ, when grown onto MgO, nanoislands exhibit smaller sizes, with a majority of them displaying thicknesses below

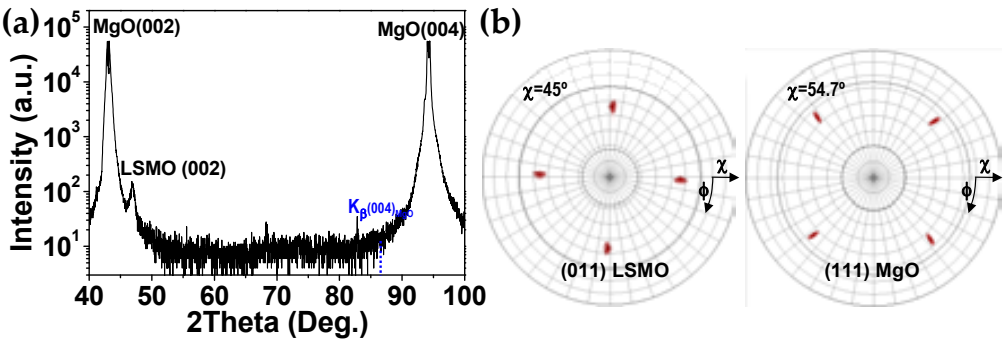


**Fig. 3.52:** *XRD study of self-assembled LSMO nanoislands on MgO, (0.03 M, 1300°C 5 h). (a) $\theta - 2\theta$ scan showing the out-of-plane $(002)_{LSMO}$ reflection. (b) Pole figures confirm the cube-on-cube epitaxial relationship.*

10 nm and lateral sizes in the ∼50 nm range. As already seen for LSMO/YSZ, LSMO on MgO nanoislands are also highly crystalline structures. They grow cube-on-cube, with a tendency towards out-of-plane tilting, as seen by X-ray pole figure analysis. In contrast to LSMO nanoislands on YSZ, which showed various morphologies, their shape when grown onto MgO is always the same, rotated squares with edges parallel to the substrate <110> step-edges. Moreover, nanoislands exhibit the tendency to locate on the these step edges. When subject to 1300°C the system undergoes a radical change, characterized by the morphological transformation of the substrate and of the islands, which exhibit very large sizes around $t$∼60 nm and $D$∼350 nm.

### 3.5.2 Magnetic properties

We have already anticipated that LSMO/MgO nanostructured templates exhibit highly supressed magnetic properties. This is in striking contrast with our findings concerning LSMO nanoislands on YSZ (see section 3.4.3). Fig. 3.53 displays the isothermal magnetization loops (field applied in-plane) for two identically grown nanostructured LSMO samples, one on YSZ (at 110 K), the other on MgO (at 77 K). The saturation magnetic moment, $m_S$, of the MgO sample is less than half the $m_S$ value for the YSZ sample (∼1.7 $\times 10^{-5}$ emu against ∼4 $\times 10^{-5}$ emu). In terms of magnetization, the value for LSMO nanoislands on MgO is around $M_S$∼194±30 kA/m. This means a decrease in magnetization close to ∼60% with respect to LSMO nanoislands on YSZ [taking the averaged $M_S$ value (0.03M, 110 K) in Tab. 3.3], and around ∼66% if we take bulk LSMO value at 110 K [19]. Note also that the MgO value in Fig. 3.53 was measured at 77 K, so it is expected to further decrease at 110 K, the temperature at which LSMO/YSZ was measured.

The temperature dependence of the magnetic moment for a system of LSMO nanoislands on MgO (0.03 M 900°C 3 h, full dots) is plotted in Fig. 3.54. For comparison, we also plot the temperature dependence of two bare substrates, a MgO and a YSZ single crystal, both heat treated at 900°C, the same as the LSMO/MgO nanostructured sample. The temperature dependence of the LSMO/MgO system shows no ferromagnetic behavior. On the contrary, it exhibits the same trend as the bare MgO substrate, with a paramagnetic to diamagnetic transition at around 50 K. The main difference between the two curves is a less negative (diamagnetic) signal in the case of the LSMO/MgO sample, which can be explained by the weak (and positive) ferromagnetic signal slightly shifting the magnetic

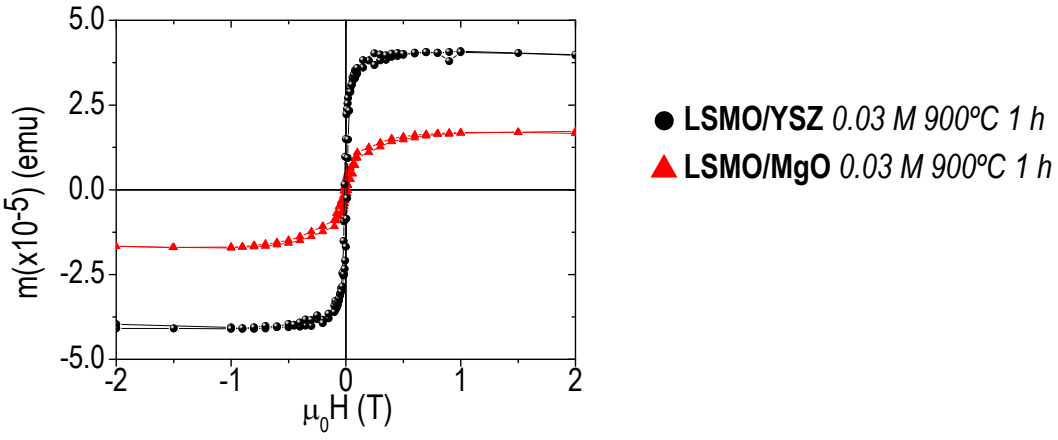


**Fig. 3.53:** *Isothermal magnetization loops for two identically grown LSMO self-assembled nanoisland samples, one on YSZ (at 110 K), the other on MgO (at 77 K). The latter shows a highly depressed magnetic behavior. Magnetic field was applied in-plane.*

moment with respect to the bare MgO substrate sample. Concerning the YSZ substrate, we measure a similar temperature dependence of the magnetic moment, although the diamagnetic signal at $T$∼250 K is around four times weaker than the diamagnetic signal of MgO (∼$0.25\times10^{-5}$ emu vs ∼$1\times10^{-5}$ emu, in absolute values). In conclusion, the low ferromagnetic signal exhibited by the LSMO islands on MgO, along with the large substrate diamagnetic signal, preclude measuring the collective FM behavior and thus the $T_C$ value of the LSMO nanoislands on MgO.

Regarding the paramagnetic to diamagnetic transition measured for MgO and YSZ, it is worth noting that these single crystal substrates are known to contain several impurities such as calcium, aluminum, silicon, chromium or iron [204–207]. A recent work by Khalid and co-workers analyzes the paramagnetic and ferromagnetic signals measured in nominally diamagnetic single crystals, finding that the various impurities within the substrates account for such signals. In particular, for the case of MgO, they ascribe the low $T$ paramagnetic signal of the temperature dependent magnetization to magnetic ions occupying lattice sites [208]. Whether the weak ferromagnetic signal measured in LSMO/MgO (Fig. 3.53) is solely the result of magnetic impurities within the MgO substrate is, however, unlikely. The $M$ vs $H$ behavior measured for bare substrates (not shown) did not give the ferromagnetic signal shown in Fig. 3.53. Also, the temperature dependence for LSMO/MgO of Fig. 3.54, although weak, shows a certain positive contribution not present in the bare MgO substrate.

### 3.5.3 Strain state of LSMO nanoislands on MgO

In section 3.3 of this chapter we already mentioned that the dependence of magnetic and electric properties with strain is a widely investigated issue, although still controversial in its application to the mixed-valence manganite compounds [22–25, 65, 162–165]. Therefore, the effects of accommodating a much higher lattice mismatch of ∼8.8%, which we have seen reflected in the highly defective LSMO on MgO interface, could be considered of relevance, regarding the supressed magnetic properties discussed in section 3.5.2. The XRD $\theta-2\theta$ scans of Fig. 3.46, with $(002)_{\mathrm{LSMO}}$ falling at $2\theta$∼46.9°, show that, overall, the

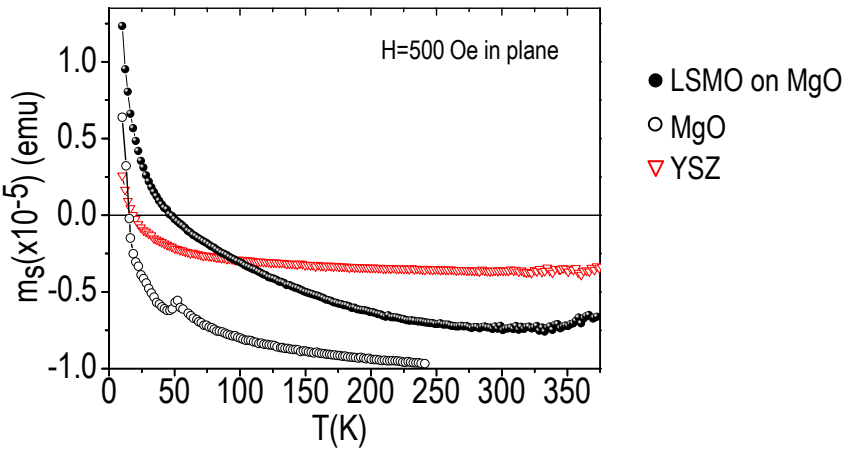


**Fig. 3.54:** *Magnetic moment as a function of T for: a system of self-assembled LSMO nanoislands on MgO (0.03 M, 900°C 3 h) (full dots); a bare MgO substrate (open dots); a bare YSZ substrate (open triangles). No ferromagnetic behavior is observed for the LSMO on MgO nanostructured system. Instead, we measure the substrates' dependence against T. A field of 500 Oe was applied in-plane in the three measurements.*

lattice parameter of the nanoislands is close to the bulk LSMO value, within the accuracy of our measurement (with error ∼0.2°, i.e. $\Delta a_{LSMO}$=±0.1 Å). This relaxation proceeds via a combination of mechanisms, the main being the introduction of misfit dislocations at the LSMO/MgO interface. For LSMO on YSZ we measured almost bulk-like magnetic properties in highly relaxed nanoislands. Nevertheless, nanoislands on MgO appear quite different from the previous case. They are very small and their defective interface therefore constitutes a higher fraction of the nanostructure volume. Detailed TEM investigations of the strain state, including the assessment of the strain fields around dislocation cores, were carried out in order to elucidate their possible impact on the suppressed ferromagnetic properties. We present here the main conclusions of these studies. The reader is directed to reference [160] for a more in-depth analysis concerning the TEM and STEM results.

Fig. 3.55 shows a HRTEM image of a LSMO nanoisland on MgO, and its corresponding $\epsilon_{xx}$ and $\epsilon_{yy}$ deformation maps, calculated using the Geometric Phase Analysis (GPA) method [209]; *x* stands for the direction parallel to the interface, and *y* for the normal direction. A mean variation of $\epsilon_{xx}$=(-8.1±0.7)% between the island (in green) and the substrate (in red) in Fig. 3.55 (b) accounts for a change in the in-plane lattice parameter of ∼-8.1% between island and substrate. The negative sign points at a decrease in lattice parameter as we go from the substrate (which is taken as reference) towards the island. Considering a fully-relaxed LSMO nanoisland, its parameter variation with respect to the MgO substrate would take the value $(a_{LSMO} - a_{MgO})\ a_{MgO}$=-8.1%, i.e. the same as experimentally measured. Similarly, the variation of the out-of-plane parameter displayed in Figs. 3.55 (c) and (e) also points at a complete relaxation within the measurement error [$\epsilon_{yy} = (-8\ 0 \pm 1\ 0)\%$]. In conclusion, our nanoisland is fully-relaxed. Additionally to the island relaxation, an island rigid body rotation (i.e. with no involved shear deformations) of 2.2° (±0.6°) was measured (also by GPA, not shown), a common feature of this system of nanoislands, as previously discussed. Finally, note the extreme color contrast variation (from blue to yellow) observed, regularly spaced, at the LSMO/MgO interface [Figs. 3.55 (b) and (c)]. These are the contrasts typically yielded by misfit dislocations.

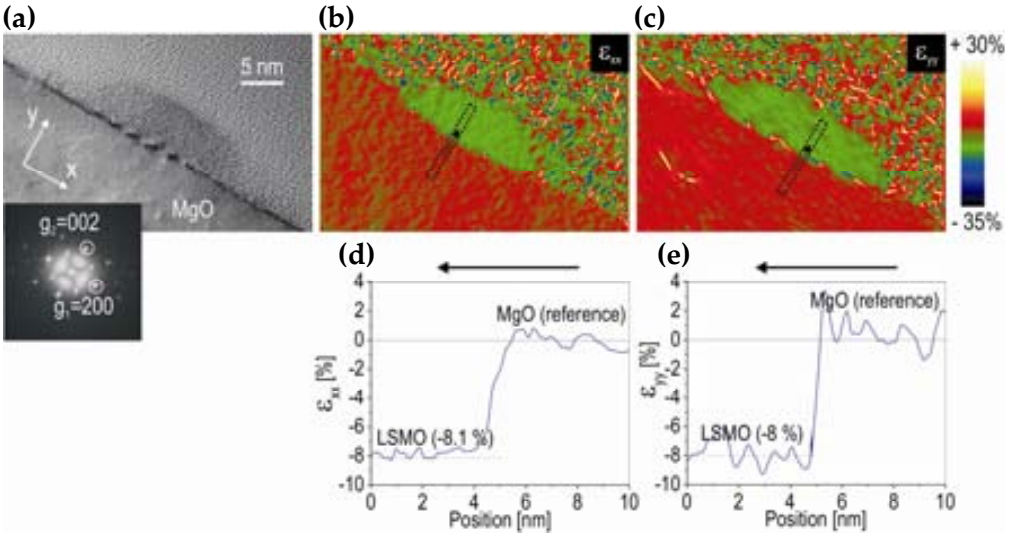


**Fig. 3.55:** *Strain state of a LSMO nanoisland on MgO assessed by the GPA method. (a) HRTEM image showing the source image for the strain maps calculation. The inset shows the Fourier transform of the image, indicating the (200) and (002) spots selected for the GPA analysis. (b)&(c)* $\epsilon_{xx}$ *and* $\epsilon_{yy}$ *deformation maps illustrating the in-plane and out-of-plane change in lattice parameter, respectively, by means of the abrupt color change from red to green. It is a negative variation, according to the scale bar, i.e. a compression. (d)&(e) The intensity profiles are calculated along the boxed regions marked in (b) and (c), and quantify the mean change in lattice parameters, in the order of* $\sim$*8%. Courtesy of P. Abellán.*

It is interesting to take a closer look at the strain field around the core of the misfit dislocations. By quantifying the extension of the deformation fields within the islands we can qualitatively evaluate their impact on the magnetization. It is known that the saturation magnetization $M_S$ depends on the product $\lambda_S\phi$, where $\lambda_S$ is the magnetostriction constant and $\phi$ refers to the stress associated to the strain $\epsilon$. In particular, $M_S$ will tend to decrease if $\lambda_S\phi$ is <0, and increase otherwise [210, 211]. Fig. 3.56 (a) shows a HRTEM image of a typical LSMO on MgO nanoisland with a number of dislocations at the interface. The relative deformation map (in %) of the in-plane lattice parameter with respect to the substrate associated to one of these dislocations (number 3), has been calculated by GPA [Fig. 3.56 (b)]. The unstrained MgO substrate, taken as reference, features a green color, meaning $\epsilon_{xx}\sim 0\%$. The green to dark red region defines an in-plane lattice variation towards smaller values (compressive, <0). The greatest compression (-10% with respect to MgO) is around the dislocation core, where the extra half-plane resides. At a height of $\sim$1.5 nm from the core, however, the change in relative deformation is -8%, meaning that the bulk LSMO lattice parameter is recovered (i.e. relaxed structure). In width (direction parallel to the interface), the deformation field extends up to $\sim$1 nm. Opposite to the compressed core, on the substrate side, the light green to purple variation defines a tensile strain ($\phi$>0). Contour lines indicate selected constant values.

Assuming that the measured deformation is purely mechanical (no chemical variations) the elastic stress $\phi$ can be inferred from Hooke's law, $\phi_i = C_{ij}\epsilon_j$ where $C_{ij}$ (i,j=1,...6) are the elastic stiffness coefficients and $\epsilon$ is the relative deformation of the LSMO lattice within the island with respect to the bulk LSMO lattice. Note that we have written $\epsilon$ to avoid confusion with the macroscopic $\epsilon$ handled up to this moment, which accounts for

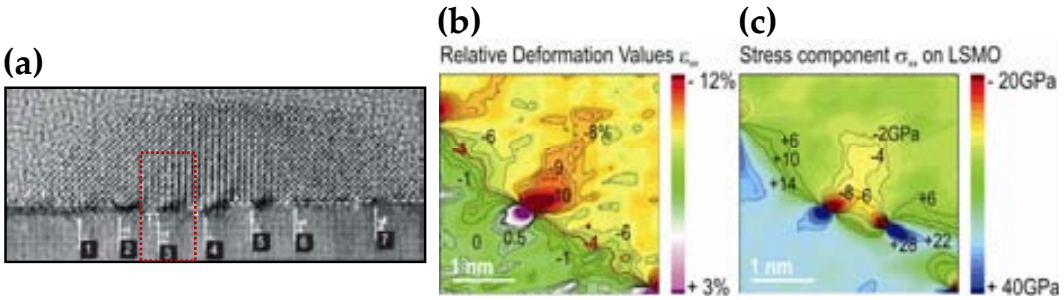


**Fig. 3.56:** *(a) HRTEM image of a LSMO nanoisland on MgO showing misfit dislocations (numbered) at the interface. (b) $\epsilon_{xx}$ deformation map around misfit dislocation number 3, boxed in (a) with dashed lines. Values are relative to the unstrained substrate. (c) $\sigma_{xx}$ stress distribution of the same area. Note the presence of a stress center, adjacent to the one derived from the dislocation in (b). The source of such stress is another dislocation, now with the extra half-plane parallel to the interface [its presence is indicated in (a)]. Recall the dependency of $\sigma_{xx}$ with the out-of-plane deformation , i.e. $\sigma_{xx}(\epsilon_{xx}\ \epsilon_{yy})$. Courtesy of P. Abellán.*

the deformation of the lattice with respect to the MgO substrate. With the assumption of plane conditions (zero strain along the zone axis $z$ direction) and taking into account that no shear strain was measured, the in-plane stress may be written as $\phi_{xx} = C_{11}\epsilon_{xx} + C_{12}\epsilon\ yy$, where $xx \equiv 1$ and $yy \equiv 2$. Elastic stiffness coefficient values were taken from the literature for a slightly different LSMO composition ($La_{0.83}Sr_{0.17}MnO_3$) [212]. Full details of the derivation are given in [160] and references therein. The resulting stress map is displayed in Fig. 3.56 (c).

The magnetostriction constant $\lambda_S$ for LSMO is positive for all temperatures until near $T_C$ with a value $\lambda_S \sim 10^{-4}$ at 90 K [213] (recall that the LSMO on MgO hysteresis cycle plotted in Fig. 3.53 was measured at 77 K). In consequence, a possible degradation of $M_S$ would be expected in the region featuring negative $\phi$ values of Fig. 3.56 (c) (where $\lambda_S\phi$<0). Such regions, assuming a similarly stressed behavior in the zone-axis direction (not measured) would amount to a volume of ∼1.5 nm$^3$ (1.5 nm×1 nm×1 nm). Considering the misfit dislocations present in a box-shaped LSMO nanoisland of the typically measured sizes, the total volume of the island which could be degraded would only account for the ∼4% of the total volume. This seems far too small to justify the 60% magnetization loss measured by SQUID. The strain-induced defective LSMO/MgO interface may contribute to the decrease of $M_S$, but, in any case, as a secondary effect.

Numbers closer to the measured magnetic signals are deduced from considering the effect of a magnetic dead layer of ∼1-2 nm of thickness, surrounding both the nanoisland free and interface surfaces. For a boxed-shape island of typical sizes $t$∼7 nm and $D$∼50 nm, the amount of volume which would not contribute to the magnetic signal would be between ∼32% and ∼55%, for 1 nm and 2 nm dead layer thicknesses, respectively . Moreover, the presence of such dead layer could be related to a possible Mn-Mg interdiffusion between the nanoislands and the substrate. Indeed, Nakamura and co-workers have reported such interdiffusion in sol-gel derived ∼200 nm thick LSMO films, which results in a detrimental effect on the resistivity and magnetization behavior of the films with temperature [214]. Manganese and magnesium have similar ionic radii in octahedral coordination

The dead layer (*d.l.*) volume was calculated by taking the whole area of the parallellepipedic island without the dead layer thickness, i.e. (*t*-2*d.l.*) and (*D*-2*d.l.*), and multiplying it by *d.l.*.

(around 0.8 Å) [215, 216], and, besides, it is well known that, within the LSMO lattice, manganese is the most mobile ion [217, 218]. From XRD and TEM studies we obtain that the LSMO nanoisland microstructure agrees with the expected lattice for LSMO, and, consenquently, in case of interdifussion, Mg should occupy the Mn sites as substitutional defects and viceversa [214]. To assess the hypothesis of interdiffusion in our LSMO nanoisland system and clarify its mechanisms, EELS local chemical measurements have been undertaken, in collaboration with J. Aguiar and Prof. N. D. Browning at UC Davis in California, USA. Preliminary results already indicate the presence of manganese within the substrate matrix, and hold promise for sheding light into the particular mechanisms responsible for the chemical interdiffusion and its subsequent impact on the magnetic properties.

## 3.6 Conclusions of Chapter 3

Throughout this chapter we have presented the main characteristics of the chemically grown LSMO nanoscale systems on perovskite type STO and LAO, on YSZ fluorite, and on MgO rock-salt substrates. Highly crystalline ultra-thin LSMO films below 10 nm of thickness grow onto the perovskite-type substrates, either strained (on STO) or relaxed (on LAO), but in both cases featuring high Curie temperature values $T_C$∼350 K. These values are very close to the reported bulk LSMO $T_C$, in contrast with the generally reported trend of depressed $T_C$ for films of such thickness. Transport measurements in a set of varying thickness LSMO samples have shown totally insulating behavior in films with average estimated thickness of $t$∼3.5 nm. Conversely, a metal-insulator transition was found for films with average thickness above ∼5.5 nm, with the remarkable fact that this transition appears decoupled from the ferromagnetic to paramagnetic transition; we saw that while $T_C$ is always around 350 K, the metal-insulator transition occurs at notably lower values, especially for thinner films. An Anderson type of 2D localization was mentioned as a possible mechanism leading to such behavior. Also, the thin LSMO films here reported showed increased MR values around ∼20%. Similar results have been reported in the literature for largely thicker LSMO nanocomposite films, and argued in those works in terms of structural and chemical disorder in such films. In our case, further investigations are required in order to shed light into the particular mechanisms behind these remarkable results.

The same growth procedure as in the perovskite case, but applied to YSZ and MgO substrates, results in highly uniform self-assembled nanoisland distributions. These nanoislands are crystalline, epitaxial, and present a highly relaxed microstructure attained through the introduction of misfit dislocations at the interface. LSMO on YSZ nanoislands show two main crystallographic orientations, a minority triangle-shaped $(111)_{\mathrm{LSMO}}$ and a majority $(001)_{\mathrm{LSMO}}$ population. The latter population shows two possible morphologies, regular or rotated-square, indicating the similarity of the LSMO facet energies. This is not the case for nanoislands on MgO, which invariably exhibit a rotated-square shape. The nanoisland shape on MgO substrates appears closely related to the substrate morphology, displaying edges parallel to the substrate step edges, along the <110>$_{MgO}$ directions. Nanoislands further show the interaction with the underlying MgO by preferentially locating at the rims of the substrate step terraces. Also, they tend to exhibit out-of-plane tiltings, which is the result of the dislocations found at the LSMO/MgO interface. The magnetic properties of nanoislands on YSZ are the best among the different systems analyzed, featuring the highest magnetic moments, and a $T_C$ comparable to bulk LSMO values. The magnetic anisotropy axis was calculated to be the $[110]_{\mathrm{LSMO}}$, with a magnetocrystalline anisotropy

constant value $K_1$(150 K)=(-5$\pm$1) kJ/m$^3$, as measured, for the first time, in LSMO nanoislands. Conversely, LSMO on MgO nanoislands show very faint magnetic signals. We discussed the possible impact of the strain around the misfit dislocation cores on the magnetic properties of the system, concluding that it cannot account for the registered magnetic signal loss. We then argued that a 1 nm to 2 nm thick dead magnetic layer can better explain the suppressed magnetization values. Furthermore, preliminary local chemical analysis indicate a Mg-Mn exchange between substrate and nanoislands, pointing at the potential key role of chemical interdiffusion on the depressed magnetic properties.

# Chapter 4

# Magnetic structure of LSMO nanoislands

As concluded from Chapter 3, $La_{0.7}Sr_{0.3}MnO_3$ (LSMO) nanoislands on YSZ single crystals exhibit magnetization values and Curie temperature close to the bulk LSMO values reported in the literature. However, the magnetic properties of individual islands are not accessible via macroscopic techniques like SQUID magnetometry. Not at least in the case of a system encompassing a broad variety of island size and morphologies, like the solution-derived LSMO nanostructures we have discussed. In the present chapter we explore the individual magnetic structure of the LSMO nanoislands grown on YSZ. For this purpose we exploit the capabilities of Magnetic Force Microscopy (MFM), performed in air and at room temperature.

Since in the late 80s Martin and Wickramasinghe [219] and separately Sáenz and coworkers [220] first adapted an Atomic Force Microscope to image magnetic fields and magnetic domains, MFM has become a routinely used technique for characterizing magnetic samples at the submicrometre scale. Domain walls, ferromagnetic domain patterns, and magnetic vortices are some of the phenomena that can be studied by means of MFM. Besides, this is a flexible technique that supports operation under tunable conditions like high vacuum and low temperature. Meanwhile, it can be easily operated in air and at room temperature, as we have done, taking advantage of the high $T_C$ value of our system of ferromagnetic (FM) nanoislands. An additional fact, essential for us, is that insulating samples can be imaged without difficulties. This is in clear contrast with other techniques such as Photoemission Electron Microscopy (PEEM), where the insulating substrate is a limiting factor, as we will discuss in Chapter 5. The main drawback of MFM is the lateral resolution, which in our conditions turned out to be around 50 nm. Also, it remains mainly a qualitative tool: the magnetic contrast we measure is proportional to the gradient of the force between tip and sample. Hence, to obtain a mapping of the field distribution, one would need to perform a double integration with well-defined boundary conditions, and know the exact characteristics of the tip. This is why imaging magnetic samples is not as difficult as interpreting the results, and also the reason why significant efforts are now directed towards correlating the MFM observations to possible magnetic landscapes via numerical simulations.

After a brief Introduction to the MFM technique, the present chapter describes the

tuning of the experimental parameters to our system of self-assembled LSMO nanoislands. The crucial role of the tip for successful MFM imaging is emphasized. Doing so permits unveiling aspects of the system that could otherwise be easily disregarded. In particular, we will see that different nanoisland size and morphologies exhibit different magnetic structures. We will be able to draw a complete magnetic phase diagram in which the vortex state occupies a central role. As this is the first time vortex states have been imaged by MFM in sub 200 nm wide LSMO islands, we have carried out a thorough analysis of our observations, trying to contextualize them in the framework of existing experimental results and analytical and micromagnetic models. Finally, we will conclude with a brief summary and point out the open questions that will likely motivate future work on this topic.

## 4.1 Basics on MFM

In Magnetic Force Microscopy (MFM), a sharp magnetized tip is scanned over the sample surface, while held a few tens of nm away from it. As a type of Scanning Probe Microscopy (SPM), in MFM the tip is the probe which senses the interaction due to tip-sample forces, in this case magnetic forces. A fundamental point here is to be able to discern magnetic interactions from the whole range of simultaneous forces interacting between the tip and the sample (attractive Van der Waals, repulsive Pauli interaction, electrostatic forces, capillary and adhesion forces...). Some forces are short range while others, like magnetic forces, are long range [see Fig.4.1 (a)]. Tuning the tip to sample distance may thus help disentangle the interactions at play. The *nm* range distance between the tip and the sample enables sensing very small forces in the $10^{-13}-10^{-5}$ N range [221]. To know the particular characteristics of the material under investigation will also be relevant to interpret the data. These issues are generally addressed using different measuring modes and tuning the particular electronics of the feedback system.

In the *Dynamic Operation* mode used in our measurements, the sharp tip is set to oscillate at the resonance frequency of the small cantilever, to the end of which the tip is attached. This free oscillation frequency is determined by the force constant of the cantilever $k$ (determined, in turn, by its geometrical and mechanical parameters). When the tip approaches the sample surface, however, the perturbation sensed by the oscillating tip will affect its motion: a shift in the amplitude $A$, frequency , and phase $\theta$ occurs [222]. Such displacements in $A$, and $\theta$ reflect the magnitude and the attractive/repulsive nature of the interaction between tip and sample. The variations of the tip oscillation are detected by the deviation of a laser beam focused on the tip (optical detection mode) and quantified using the appropriate lock-in techniques. In the case of small external forces, the $F^{ext}$ is treated as a perturbation that causes the cantilever to have an effective force constant $k_{eff} = k - F_z^{ext} z$, where we take only the direction of the tip-sample distance $z$, i.e. $F^{ext} = F_z^{ext}$. Eqs. 4.1, 4.2 and 4.3 below show the expressions of the shift in $A$, and $\theta$ caused by such external force.

$$\Delta A \quad \frac{Q}{2k}\frac{F_z^{ext}}{z} \tag{4.1}$$

$$\Delta = - _0 = -\frac{^0}{2k}\frac{F_z^{ext}}{z} \tag{4.2}$$

$$\tan\theta = \frac{^0}{Q(\ ^2 - \ ^2_0)} \tag{4.3}$$

where $Q$ is the Quality factor of the oscillation, $k$ is the force constant of the cantilever, $\omega_0$ its resonance frequency and $z$ the oscillation direction.

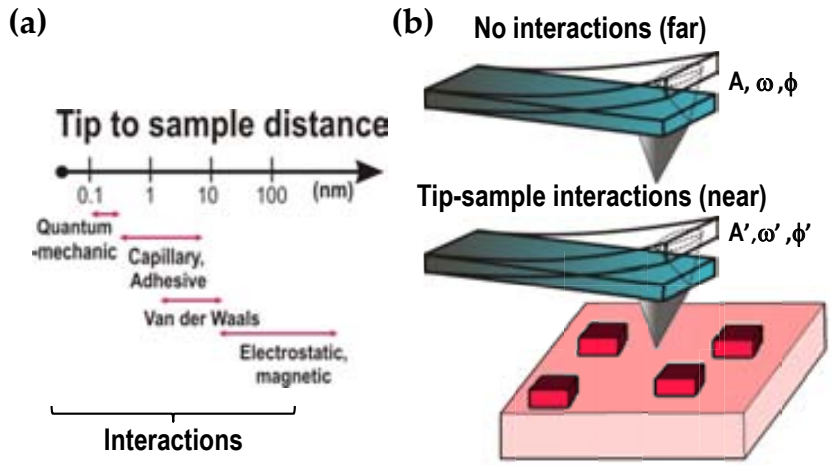


**Fig. 4.1:** *(a) Scheme of the distance range at which different tip-sample interactions are present. (b) Sketch of the oscillating cantilever with the tip at its end; far from the substrate (above) and near the substrate (below) where the tip-sample forces change the amplitude, frequency and phase of the oscillation.*

Using $A$, $\omega$ or $\phi$ as feedback parameters we can register the shifts with respect to a certain electronic set-point and react to make such shift equal to zero. Such 'reaction' is achieved by the expansion or contraction of the piezoelectric tubes that control the tip-sample distance. This way, if the amplitude $A$ is the selected feedback parameter for measuring the topography signal, our topography image will be a constant amplitude image where the expansion/contraction of the piezo is registered. The stronger the interaction, the stronger the shift in $A$ will be and the more the piezo will expand or contract. This is evidenced in an enhanced contrast in the topography image.

As commented before, it is not trivial to interpret the forces that produce the measured shifts because all kind of interactions are generally present. For the particular case of magnetic forces, the energy at a distance $\vec{r}$ between the magnetic tip and the sample may be written as [223]:

$$E(\vec{r}) = -\mu_0 \int_{tip} [\vec{M}_{tip}(\vec{r'})\ \vec{H}_{sample}(\vec{r}+\vec{r'})]\mathrm{d}^3\vec{r'} \tag{4.4}$$

where $\vec{M}_{tip}(\vec{r'})$ is the tip magnetization at the $\vec{r'}$ coordinate within the magnetic coating of the tip, $\mathrm{d}^3\vec{r'}$ is the coating unit volume, and $\vec{H}_{sample}(\vec{r}+\vec{r'})$ is the stray field produced by the magnetic sample at that point of the tip. In other words, the magnetic interaction between the tip and the sample is determined by the convolution of the tip magnetization and the stray field of the sample. Note that we would obtain an equivalent expression by swapping the subscripts in 4.4 and extend the integral for the sample volume elements. Such energy produces a force between the tip and the sample (Eq. 4.5) which gradient is proportional to the measured shift in our amplitude, frequency or phase parameters, following what we saw in Eqs. 4.1, 4.2 and 4.3.

$$\vec{F}^{ext}(\vec{r}) = -\vec{\nabla}E(\vec{r}) \tag{4.5}$$

The exact expression for the force will depend on the specific forms of $\vec{M}_{tip}$ and $\vec{H}_{sample}$

for different magnetic materials, geometries...etc and it is far from being trivial. A good number of models have been proposed in particular cases for the force between the magnetic sample and tip [224, 225, 225–229]. For the case of a tip modeled as a dipole with magnetic moment $m$, the expression 4.5 takes the form [226]:

$$F^{ext}(r) = \mu_0 \quad (m \cdot H) \tag{4.6}$$

and the force gradient, proportional to the $A$, and $\theta$ shifts, will thus be

$$\frac{F_z^{ext}}{z} = \mu_0 m \frac{^2H}{z^2} \tag{4.7}$$

in which we took the tip magnetic moment $m$ to be independent of $z$. Accordingly, the MFM contrast we measure, given by the shifts of the oscillating parameters of our cantilever (Eqs. 4.1, 4.2 and 4.3), is proportional to the stray field variation in the direction perpendicular to the sample surface. Note again that only the $z$ component of the force has been written. We are here assuming that our MFM signal comes only from the variation of the force component along the perpendicular direction, which is generally a reasonable approximation since the cantilever oscillation is along $z$. The nanometric tip radius is responsible for nanoscale lateral and vertical resolution [230].

Along with the variation of the stray field of the sample, the magnetic dipole $m$ representing the tip in Eq. 4.7, plays a role too in the origin of the measured magnetic contrast. Moreover, in real experiments, the choice of the magnetic tip is particularly important: we may or may not be able to measure the same sample depending on the magnetic characteristics of the selected tip. For instance, a tip with a strong magnetic moment may modify the domain structure of the measured sample, while one with a weak magnetic moment may be altered by the stray field of a strong magnetic sample. In either case, the contrast obtained from the measurement will not be representative of the specific sample, and data interpretation will hence require special care. The ideal situation for a *non-destructive MFM operation* was expressed by Hartmann in terms of the relative values of anisotropy fields $H_K$ and the saturation magnetization values $M_S$ of tip and sample [224]:

$$\frac{H_K^{samp}}{M_S^{tip}} \geq 1 \tag{4.8}$$

$$\frac{H_K^{tip}}{M_S^{samp}} \geq 1 \tag{4.9}$$

By meeting these conditions we expect the MFM data to reliably reflect the original sample magnetic structure. However, they also imply that on a soft magnetic sample we are constrained to the use of tips of rather low magnetic moment, which can make the obtained signal too weak to be measured. This is why the appropriate choice of the tip is essential.

The study here presented was carried out in collaboration with Dr. Agustina Asenjo and Dr. Miriam Jaafar from the *Group of magnetism and magnetization processes* at the Instituto de Ciencia de Materiales de Madrid (ICMM-CSIC). I also profited from their expertise while working under their supervision in the context of a short 1 month stay in the course of my PhD thesis.

## 4.2 Experimental procedure: tuning the MFM operation on self-assembled LSMO nanoislands

### 4.2.1 Experimental set-up and measuring conditions. Magnetic contrast

The measurements were done using a commercial ambient AFM/MFM system from Nanotec Electrónica S.L, working at room temperature. This microscope was appropriately modified by M. Jaafar as part of her PhD work to be able to apply constant in-plane and out-of-plane magnetic field while imaging the sample. A detailed description of the system is given in her thesis [231] and in the corresponding article [232]. Our main goal is to learn what the micromagnetic structure of individual islands is, and how their magnetic domain configuration varies under applied field. A great number of experiments were done in remanence, a few with out-of-plane applied magnetic field, and some with in-plane magnetic field. Details on the out-of-plane set-up can be found in the thesis by M. Jaafar [231]. The in-plane set-up, which we used more often, is sketched in Fig. 4.2. It consists of a copper electromagnet (0.5 mm diameter wire) connected to two iron bars that enclose the magnetic flux created by the coil and that are separated by an air gap. The sample is located between the ends of the iron pieces and the field intensity can be changed by changing their separation, with values from 4 to 8 mm. In our case, maximum fields of ∼45 mT were reached when applying a 2 A current flow through the coil. The *current* to *field* calibration is done systematically before a series of measurements, especially if the electromagnet is manipulated or the gap width changes. For such purpose we used a Hall probe (STB5X, 0.020”). A cooling system keeps the coil refrigerated. This is important because the current may flow for hours (every MFM image can take from 5 to 20 min to be completed). However, the large distance between the coil and the sample (∼13 cm) as well as the cooling system were proved to give very small temperature changes: a 3 K temperature rise was measured by the application of a 0.11 T field during 3 hr [231].

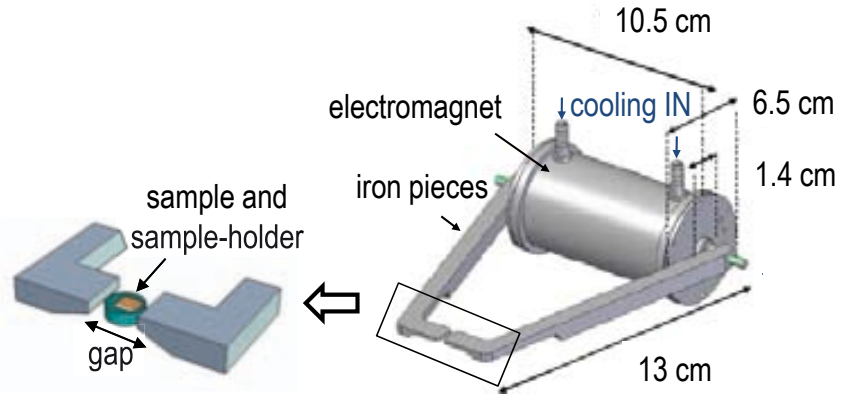


**Fig. 4.2:** *Schematic illustration of the coil system used for in-plane magnetic field application. Adapted from [231].*

MFM imaging was performed in the dynamic mode using the lift-mode operation, i.e. the oscillating cantilever was placed at two different distances from the sample surface for each scanned line: close to the surface (∼10 nm) first, for topography data acquisition, and far from the surface afterwards, for the magnetic signal collection, at typical retrace distances of 30-60 nm. In our particular case, after the topography measurement, the

piezoelectric tube, in charge of the tip-to-sample distance regulation, repeats the previous topography movements at the larger retrace distance. This way, the sample surface and the tip are maintained at a constant distance and we are able to exclude topography effects in the magnetic signal. Choosing the appropriate distance is essential in order to avoid topography crosstalk from the MFM image while keeping a good signal-to-noise ratio. We have used the oscillation amplitude $A$ to track the topography signal. The magnetic interaction, in turn, is detected in the contrast measured in the phase shift channel, during the retrace scan. This so-called Amplitude modulation-AFM is the usual operating mode in air: small quality factors $Q$ [50-1000] yield the feedback in $A$ while the functional properties of the materials are commonly mapped by recording the phase shift between the driving force and the tip oscillation [222].

In addition to the above, we have used a second feedback, known as the *Phase Locked Loop* (PLL), which is implemented in the Nanotec electronics and software. It works by changing the excitation frequency at which the cantilever is driven in order to keep the phase constant (at its resonance value $\frac{\pi}{2}$, usually). The phase shift being equal to zero, the information contained in the amplitude is solely due to its real part. In other words, we have no contribution from forces other than Van der Waals in the topography image (adhesion, capillary, and magnetic forces are left out). Since the phase shift is kept to zero, the magnetic interaction is recorded in terms of the frequency needed to make this phase shift zero. From Eq. 4.2 it follows that we will observe a positive shift in the frequency when repulsive forces are present, and, conversely, a negative shift when the attractive forces pull the cantilever closer to the surface.

Fig 4.3 shows the topography and the magnetic contrast images, (a) and (b) respectively, of an LSMO nanoisland ensemble grown on a (110)-oriented YSZ substrate. Since the feedback is done in amplitude ($A$), topography image is a constant $A$ image, and the Amplitude image thus records the feedback error in trying to keep $A$ constant. Similarly, we show the MFM image (recorded at a 30 nm retrace distance), shown as the excitation frequency given to the cantilever to keep the phase unchanged. The phase image is thus its corresponding error signal. The non-zero error signals are the typical obtained; we have enhanced the contrast in order to highlight them. At a first glance, the nanoisland ensemble appears as agglomerate bunches of poorly defined nanoislands. This is seen very clearly in the amplitude channel. In the MFM image, however, the magnetic contrast arises only from well-separated individual islands. By looking at the amplitude image more closely, we can correlate the original island to its corresponding magnetic contrast. The MFM image hence helps distinguishing magnetic islands and non-magnetic material attached to them.

Magnetic tips are saturated using a permanent magnet prior to imaging the sample. The tip is usually magnetized parallel to its axis, that is, perpendicular to the sample surface, which is done easily because of its large shape anisotropy. We may then take the magnetic moment of the tip to be $m \sim m_z$. Bearing in mind that the magnetic contrast is proportional to the force gradient in $z$, we will then see the largest contrast in the regions with out-of-plane magnetization. Two representative examples of the MFM contrast obtained with out-of-plane and in-plane magnetized samples are given in Fig. 4.4 (taken from [231]). They correspond to (a), magnetic Ni nanowires (magnetization along their long axis $\pm z$) embedded in a porous alumina non-magnetic matrix, where the magnetic contrast comes from each of the wires; and (b), in-plane magnetic domains within a commercial hard disk drive track. The magnetic contrast there arises from the domain walls.

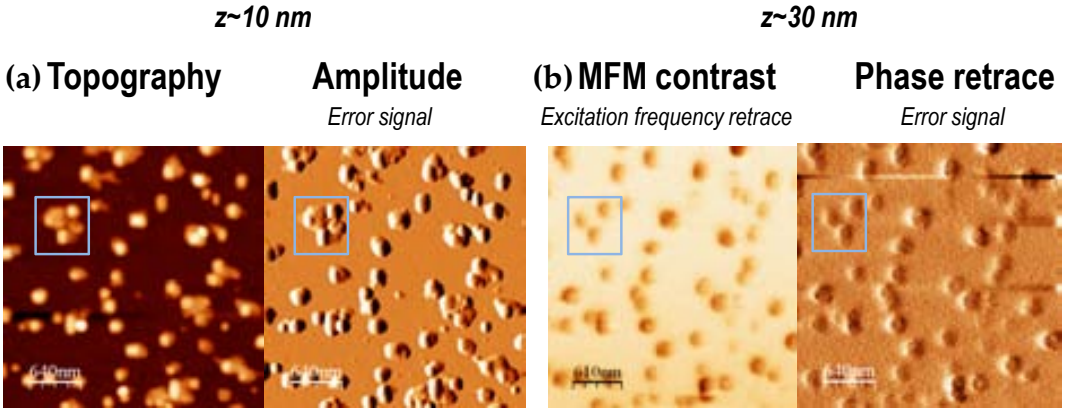


**Fig. 4.3:** *(a) Topography image (left) and the corresponding amplitude image (right) taken at z∼10 nm from the sample surface. The z bar comprehends 90 nm and 180 mV, respectively. (b) Excitation frequency image [magnetic contrast image (left)] and its corresponding phase image (right) taken at a retrace distance z∼30 nm from the sample surface. The z bar comprehends 4 Hz and 10 mV, respectively. The blue squares highlight that what seems agglomerated material in (a), are three distinct magnetic islands in reality, surrounded by non-magnetic dirt, as evidenced in (b).*

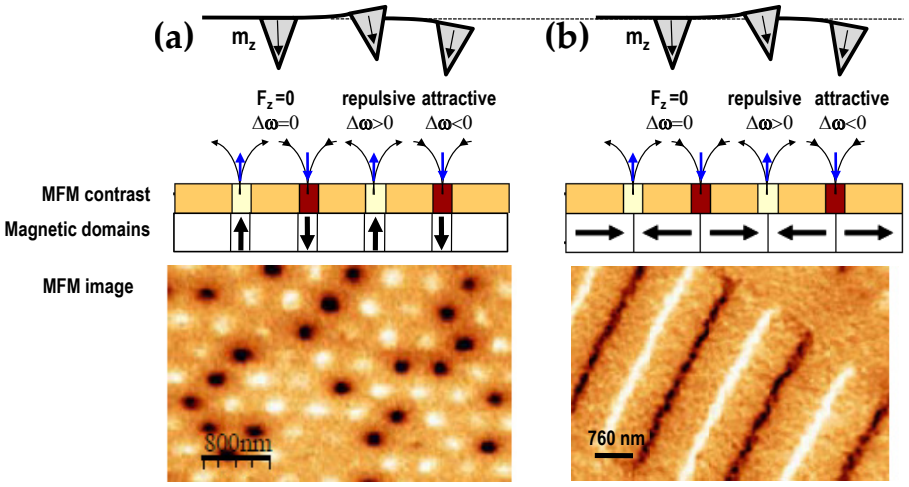


**Fig. 4.4:** *(a) Out-of-plane magnetized Ni nanowires embedded in a porous alumina matrix. (b) In-plane magnetized magnetic domains in a hard drive disk. The tip-sample attractive (repulsive) magnetic interaction reduces (enhances) the oscillation frequency, represented as a dark (bright) contrast against the non-magnetic background. Figure adapted from [231].*

### 4.2.2 Towards the optimal imaging of LSMO nanoislands: the role of the magnetic tip

**The critical role of the magnetic tip in MFM imaging**

Our CSD-derived LSMO nanoislands largely depart from the above paradigmatic examples of ferromagnetic in-plane and out-of-plane samples. From Chapter 3 we know that the magnetization of the nanoislands is comparable to the 590 emu/cm$^3$ of bulk LSMO at low temperature. We know as well that it falls down to 300$\pm$40 emu/cm$^3$ at 300 K. Besides, although we expect the nanoisland magnetization to lie in-plane, we cannot neglect the presence of non-zero out-of-plane component (recall the hysteresis cycles for LSMO on YSZ described in Chapter 3). In addition to a low magnetization, the small nanoisland volume implies a very small magnetic moment. While these averaged values do not account for the individual behavior of the nanoislands, they already point out that the tip-sample magnetic interaction will not be strong. As a soft ferromagnet with low coercive field, we may also expect the stray field of the magnetic tip to modify the nanoisland domain configuration. Keeping all this in mind, the first step in the MFM study was to check whether the magnetic signal could be measured at all, and whether this could be done without modifying the original magnetic structure of the nanoisland.

To this end, initially, experiments were performed by applying an out-of-plane magnetic field. Fig. 4.5 (a) displays the measured Amplitude image (i.e. the topography error) and Fig. 4.5 (b) the MFM image of the same area of a LSMO nanoisland ensemble grown on (001)-YSZ, which we shall call *Sample 1* hereafter. The MFM image was collected during the retrace scan under a magnetic field of 30 mT, applied perpendicular to the sample (parallel to the tip magnetization). We expect the 30 mT field to align many of the island magnetic moments parallel to the tip magnetic moment. This would then be reflected as a dark contrast at the island location. The amplitude image shows the faceted shape of the square-base nanoislands; also, the substrate is not completely clean, but covered with small islands. As we already remarked in Chapter 3, this may happen in some LSMO/YSZ nanostructured samples. However, their small volume prevents us from detecting any magnetic signal. We focus then on the well-defined 'large' LSMO nanoislands. Indeed, such nanoislands can be well discerned against the non-magnetic background, mainly because of their edge contrast. On one hand, the edges of abrupt features are the places where the feedbacks fail and thus they are also the places that most likely show the convolution of different interactions. On the other hand, we cannot completely rule out the magnetic nature of that intense contrast: first, the contrast remains identical under changes of the scanning direction, suggesting that it could be a real effect, not an artifact from the tip-island edge interaction (Fig. 4.6). Second, the geometry of the island, faceted in the (111) planes, also favors such contrast. As shown in the sketch of Fig. 4.5, the magnetization always tends to align with the structure edges, in order to minimize the magnetostatic energy. It may thus be reasonable to have such intense dark contrast in the nanoisland edges when the out-of-plane applied field is parallel to the tip magnetization. Finally, one may also notice the darkest spots in the center of some nanoislands (inside black squares in Fig. 4.6). Although hard to distinguish, they indicate an out-of-plane magnetization direction, parallel to the tip magnetization. This result could indicate the nanoislands show a vortex configuration, with in-plane magnetic moments except in the center or vortex core, where the magnetization points out-of-plane. We shall discuss this configuration later in the Chapter.

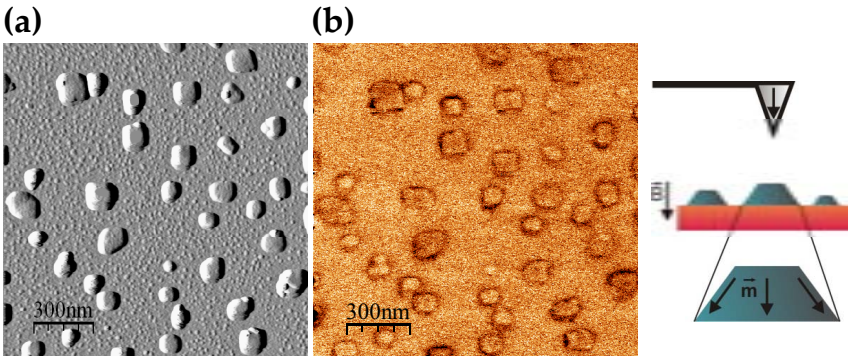


**Fig. 4.5:** *(a) Amplitude image of the LSMO nanoislands showing the faceted morphology of their truncated pyramid shape. (b) Corresponding MFM image acquired while applying 30 mT to the sample. The main dark contrast is located at the edges. A sketch of the tip and sample magnetic moments is displayed on the right hand side.*

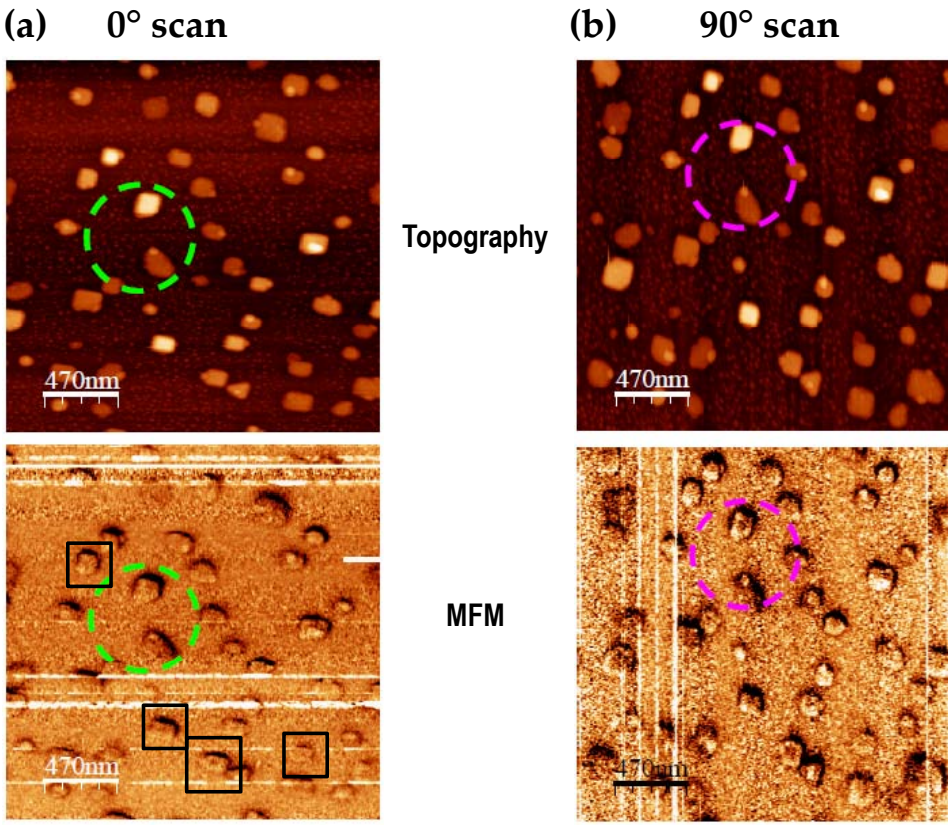


**Fig. 4.6:** *(a) 0° and (b) 90° scanning of the self-assembled LSMO nanoislands with applied out-of-plane magnetic field. The dark contrast on the island edges is more intense at one of the island sides. This is presumably caused by a certain inclination of the cantilever and hence of the tip with respect to the island. Such inclination induces the island walls to interact differently with the two-side coating of the tip (which is a point dipole only in a simplistic approximation). The fact that the darkest side remains the same during the two scans reveals the magnetic nature of this contrast. If it were an artifact, the dark side would change together with the scanning direction.*

From the faint contrast we have seen above, it seems clear that the magnetic interaction between the tip and the islands is too low to enable further analysis. By using a tip with higher magnetic moment the contrast should in principle increase, despite also risking to influence the sample magnetic structure with the tip. Fig. 4.7 displays the resulting magnetic contrast using a tip of higher magnetic moment under 30 mT, in remanence, and under -20 mT out-of-plane applied field. When the 30 mT are applied parallel to the tip magnetic moment, some of the edge-contrast seen before is still present but now we may also see a blurry dark contrast, typical of magnetic contrast, throughout the entire island. This contrast fades a little in the remanence image [Fig. 4.7(b)], and seems even weaker when the field is applied in the opposite direction to the tip [-20 mT, Fig. 4.7(c)]. The change in the contrast is better seen in the line scans of an individual island [Fig. 4.7 (d)]. This behavior accounts for the magnetic nature of the islands: the larger dark contrast is seen when the magnetic moment of the island is parallel to that of the tip (attractive interaction); into the surface, in this case. By decreasing the field and changing its orientation, we expect the island to switch into an 'out-of-the-surface' magnetization. However, the field applied is not strong enough to achieve the reversal of $m$, otherwise we would see the bright contrast characteristic of the repulsive interaction. These results apparently contradict what we deduce from the SQUID magnetization loops of Chapter 3: according to them, 20 mT should be enough to saturate the island out-of-plane, which we do not see with MFM. Seemingly, under the influence of the stray-field of the tip, the effective field sensed by the nanoisland is less than 20 mT: i.e. the field, applied opposite to the stray field, only decreases the magnitude of the attractive interaction but it does not achieve the magnetization reversal. Therefore, although we have gained in sensitivity, the influence of the tip modifies our nanoislands and thus precludes the study of their spontaneous magnetic structure.

**Assessing the optimal magnetic tip**

The above experiments underline the critical role of the magnetic tip and illustrate some of the tests done using both commercial magnetic and in-house sputtered Si tips. Among the tips tested, the commercial tips from Nanosensors proved to be the most appropriate for our samples, and will be used in the following experiments. Their relevant parameters are listed in Tab. 4.1. The majority of the tips used in MFM are Si-based tips coated with magnetic layers that are tens of nm thick. The higher the magnetic moment of the material or the thicker the coating, the larger the tip magnetic sensitivity will be. On the other hand, as we already mentioned, the high stray field caused by a highly magnetic tip may modify the original domain pattern of the sample. Also, for thick coatings, the large tip radius may decrease the resolution. An exhaustive study of the characteristics of a large number of magnetic tips is reported in [231]. The only difference between the two tips used from now on is the thickness of the coating , which is made of a CoCr alloy (see Tab. 4.1). This means that the thinnest coated tips have a lower magnetic moment (LM) and a smaller radius (see Fig. 4.8).

According to what we said in section 4.1, non-destructive MFM imaging implies that the magnetic sample and tip should fulfill Eqs. 4.8 and 4.9, where the parameters involved are the tip and sample saturation magnetizations $M_S$ and anisotropy fields $H_K$. In Chapter 3 we presented the SQUID values for the saturation magnetization and coercive field ($H_C$) of our system of LSMO nanoislands grown on YSZ. For room temperature in the in-plane

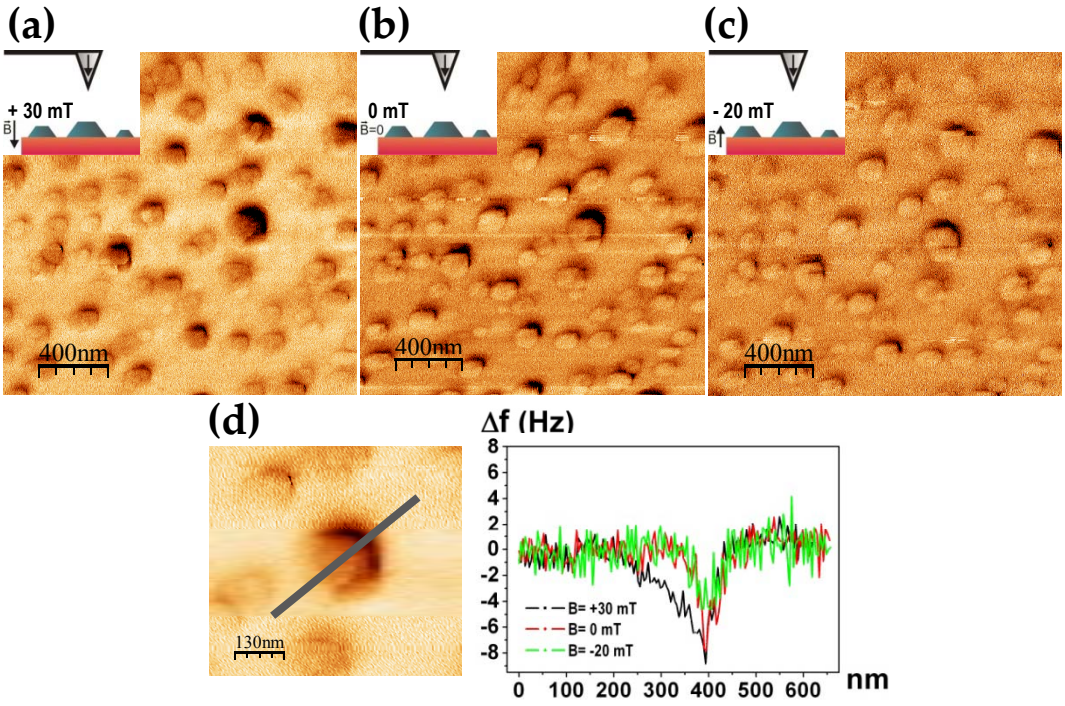


**Fig. 4.7:** *MFM images of LSMO nanoislands using a high magnetic moment tip under 30 mT (a), 0 mT (b) and -20 mT (c) out-of-plane magnetic field. (d) Zoomed image of a single nanoisland and its corresponding MFM contrast line scan under the different applied fields.*

**Tab. 4.1:** *Technical parameters of the two tip models utilized.*

| Tip | $f_0$ (Hz) | k (N/m) | Radius (nm) | Coating (nm) | $H_c^{th}$ (Oe) | $H_c^{exp}$ (Oe) | $M_S$ (emu/cm$^3$) |
|---|---|---|---|---|---|---|---|
| **1.** | 75 | 2.8 | $\lesssim$30 | 20 | 250 | 280 | 150 |
| **2.** | 75 | 2.8 | $\lesssim$50 | 40 | 350 | 380 | 300 |

*Data are from [233] except for $H_c^{exp}$, which is deduced experimentally. Tip 1 stands for PPP-LM-MFMR tip, known as the low-moment (LM) tip, and Tip 2 is the standard PPP-MFMR tip. The given $H_c^{th}$ and saturation magnetization $M_S$ values are from measurements on a flat surface. In contrast, $H_c^{exp}$ is the result of the real tip-end characterization obtained from measuring a magnetic hard disc with* in-situ *applied field [231].*

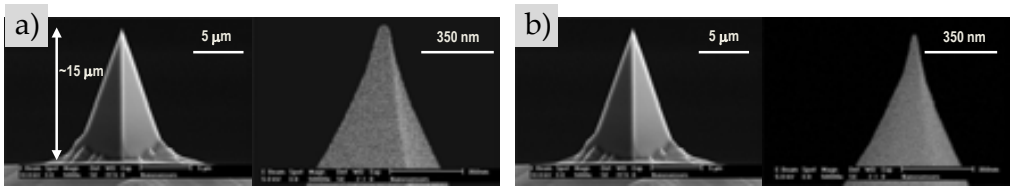


**Fig. 4.8:** *Scanning Electron Microscopy micrographs of the employed Nanosensors MFM commercial tips. (a) PPP-MFMR tip. Full front view of the tip (left) and zoom of the tip-end with radius∼50 nm (right). (b) PPP-LM-MFMR tip. Full front view of the tip (left) and zoom of the tip-end with radius∼30 nm (right). From [233].*

configuration, the estimated $M_S$ was 300±40 emu/cm$^3$, and the coercive field value $H_C$ ∼20 Oe, for nanoislands grown from 0.03 M precursor solutions (see Tab. 3.3). The latter is a large value compared to soft magnetic materials like Iron (1 Oe) and Permalloy (0.05 Oe for $Fe_{21.5}Ni_{78.5}$) [234], but very low compared to hard materials like Alnico V (640 Oe) [234], Cr-Co-Pt hard disk drives (1700 Oe) [235], or Nd-Fe-B alloys (10,000 Oe) [236]. It is also considerably smaller than the coercive fields of our CoCr-coated tips [280 Oe (22.3 kA/m) for low moment LM Tip 1 and 380 Oe (30.2 kA/m) for Tip 2]. We can deduce the anisotropy fields of the sample from the in-plane and out-of-plane hysteresis cycles of Chapter 3, which give a value of around ∼4225 Oe (∼336 kA/m). For the anisotropy field of the tip we may take the value of the coercive field, since its hard-ferromagnet cycle is reasonably squared. Regarding the saturation magnetization values, instead of them we take the remanence magnetization values of tip and sample: it seems more appropriate in this case, since we initially look at the tip-sample interaction in remanence. For the tip, in any case, the remanence magnetization equals the saturation magnetization value, because of its hard-magnet square hysteresis loop. For the sample, in contrast, the measured remanence magnetization is far lower than the saturation value: we take the value measured with SQUID for the system of self-assembled LSMO nanoislands, i.e. 61 kA/m. Consequently:

$$\text{From Eq. 4.8 } \frac{H_K^{samp}}{M_{rem}^{tip}} \geq 1 = \begin{array}{lrcl} \text{Tip 1:} & 336\ \frac{kA}{m} & > & 150\ \frac{kA}{m} \\ \text{Tip 2:} & 336\ \frac{kA}{m} & > & 300\ \frac{kA}{m}; \end{array}$$

$$\text{From Eq. 4.9 } \frac{H_K^{tip}}{M_{rem}^{samp}} \geq 1 = \begin{array}{lrcl} \text{Tip 1:} & 22\ 3\ \frac{kA}{m} & > & 61\ \frac{kA}{m} \\ \text{Tip 2:} & 30\ 2\ \frac{kA}{m} & > & 61\ \frac{kA}{m} \end{array}$$

From the above lines we may see that both tips fulfill the first condition and neither the second. Thus, in principle, the tip is not expected to modify the sample while, conversely, we could expect the sample to modify the tip magnetic structure. In either case, however, the compared values are quite close to each other and, very importantly, those of the sample are values averaged over a large amount of different nanoislands featuring a variety of sizes and aspect ratios. Therefore, the real anisotropy field and magnetization values of the sample will vary from island to island and the tip to sample interaction will change accordingly. Tip modifications are also to be taken into account: the loss or roughening of the magnetic coating and changes in the tip geometry are quite common during the scanning process. In summary, this simple estimation indicates that the chosen tips are in the range of the appropriate values but also that we will have to look critically at the specific measurements we do in order to discard any possible artifacts.

Given the analysis presented above, it is useful to assess the performance of the chosen tips in some representative measurements, to ascertain that the aforementioned potential artifacts are under control. Fig. 4.9 displays the magnetic force micrographs of the LSMO nanoislands grown on YSZ (Sample 1) using Tip 1 in (a) remanence, and (b) & (c), after applying opposite in-plane magnetic fields of 21 mT. Image (a) is, as expected, identical to the one shown in Fig. 4.5: islands are mainly identified by their edge-contrast; the contrast within the island is otherwise difficult to detect. We need to apply as much as 21 mT in order to be able to distinguish the white and dark contrasts within each island, which are the signature of a saturated island, i.e. of a single magnetic domain. The contrast is reversed for oppositely applied field, as expected, proving that it is not an artifact due to tip-sample interaction. On the contrary, tip-sample interaction is very weak, as evidenced in the small remanence magnetic signal in (a) and by the fact that we were not able to detect intermediate stages between the remanence and saturation regimes. As expected, there is no influence of the tip on the magnetization of the sample. However, we cannot fully rule out the converse effect. Especially after a long scanning time, it is possible that the sample stray field may influence the tip magnetization. This would go in the direction of reducing the effective tip $|\vec{m}_z|$, with a corresponding decrease in the tip-sample interaction strength. The line scan of a single island in (d) quantitatively shows the variations of the magnetic contrast. Such differences are small, yet clear. The magnitude of the magnetic contrast is also very modest, with a frequency variation no larger than 3-4 Hz, which is not far from the background noise.

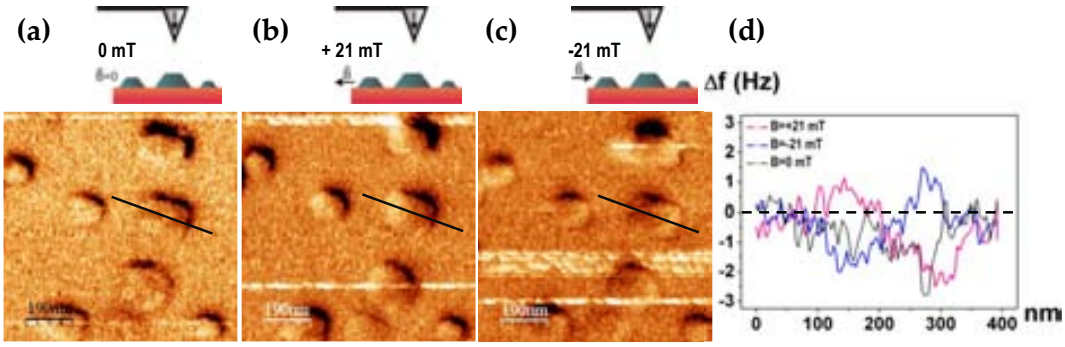


**Fig. 4.9:** *MFM images of LSMO nanoislands taken with a low-moment tip (Tip 1) in remanence (a) and after saturating the sample by applying in-plane 21 mT (b) and -21 mT (c) fields. The contrast within the islands, unnoticeable in (a), arises as a left to right bright-dark (b), and dark-bright (c), contrast characteristic of saturated single domains. (d) Magnetic contrast profile of an individual island at the different magnetization states shown in (a), (b) and (c).*

Fig. 4.10 shows the topography and magnetic images of Sample 1, as in Fig. 4.9 but now scanned using Tip 2. These images were done after saturating the tip and the sample in opposite directions by applying *ex-situ* an out-of-plane magnetic field of 500 mT. In contrast to the previous case, the use of the thicker-coated Tip 2 yields a very clear magnetic contrast at the nanoisland locations already in remanence. Furthermore, we found no evidence of tip changes caused by the stray field of the islands, which could happen due to the low anisotropy field of the tip (as stated previously in the application of Eq. 4.9). Successive scans of the same area with different scan directions always led to the same island contrasts (not shown), confirming that the tip remained unchanged. The color scale in the MFM image shows a frequency shift range of around 10 Hz, after having appropriately re-

stricted the scale. This is not much larger than the 3-4 Hz range we saw before. However it does make a clear difference. As a matter of fact, it allows us to clearly resolve the magnetic structures of the nanoislands, which have, until now, remained hidden. A close inspection of the image reveals that such different magnetic structures can actually be grouped into three categories, which we name *low contrast*, *vortex state* and *multidomain*, as we will explain in the following. The next section is precisely devoted to the description and analysis of these magnetic structures.

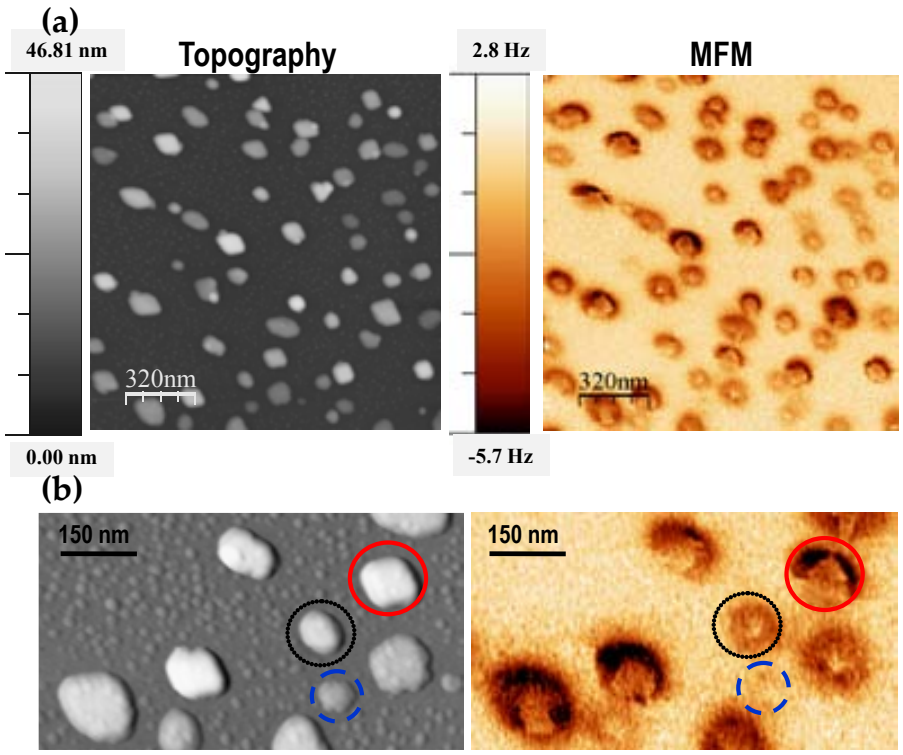


**Fig. 4.10:** *(a) Topographic and magnetic images of LSMO nanoislands, taken with Tip 2 after having saturated,* ex-situ, *tip and sample in opposite directions. The retrace distance for the MFM scanning was 30 nm. Images were recorded in remanence and at room temperature. The color scale in the MFM image is restricted to comprise only the majority of the values shown by the nanoislands. (b) Detailed topographic and magnetic images of a smaller region with LSMO nanoislands. The dashed (blue) line, dotted (black) line and solid (red) line circles highlight nanoislands with low-contrast, vortex and multidomain magnetic configurations, respectively.*

## 4.3 Unveiling the magnetic configuration of self-assembled LSMO nanoislands

### 4.3.1 Nanoisland shape-Magnetic structure correlation

Three different magnetic structures, named *low-contrast* islands, *vortex*, and *multidomain* configurations have emerged from the imaging of LSMO samples with Tip 2 (see previous section). These magnetic structures are, in fact, not randomly linked to the various islands,

but appear correlated to the island size and morphology. We can use the average lateral size $D$ and thickness $t$ of the islands to calculate the average section $S_a$ of every nanoisland configuration. The smaller islands ($S_a$~$0.75\times10^3$ nm$^2$), are those exhibiting *low-contrast*, and their domain structure cannot be determined due to the small interaction with the magnetic tip. The medium size nanostructures ($S_a$~$1.33\times10^3$ nm$^2$) typically present in-plane anisotropy with *vortex state*, showing the characteristic out-of-plane magnetic contrast in the center of the nanoisland, the so-called vortex core. Finally, the larger structures ($S_a$~$2.50\times10^3$ nm$^2$) present *multidomain* magnetic configuration. The existence of not only in-plane but also out-of-plane components of the magnetic moment in these larger islands is in agreement with the macroscopic hysteresis loops measured in the out-of-plane configuration. These, although small, still show remanence magnetization and non negligible coercive field values. It should also be noted that no correlation between the states of adjacent islands was observed. This fact suggests that the interaction between neighboring islands may be disregarded and that they can be treated as independent objects.

Fig. 4.11 shows an example of how the size and geometry of nanoislands determines their magnetic structure. In (a), a medium size nanoisland ($D$~90 nm, $t$~30 nm) displays a *vortex* configuration, with the out-of-plane core in the middle. The topography and magnetic contrast line profiles are shown below the image. Conversely, the island in (b), with a similar lateral size but with a smaller thickness, does not give a measurable magnetic signal: this is what we understand by *low-contrast*.

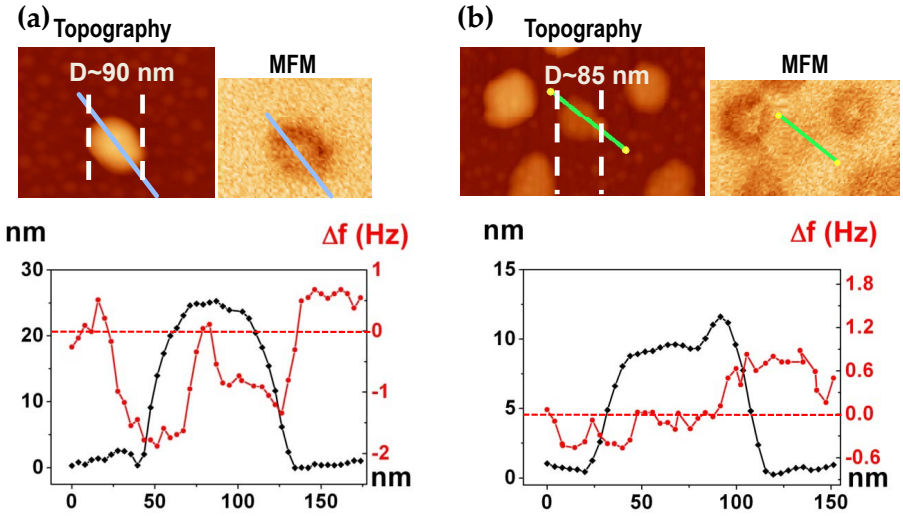


**Fig. 4.11:** *(a) Topography and MFM images of one LSMO nanoisland and its corresponding line scan across the vortex core. (b) The same as in (a) but for an island with similar width but less than half thick. This island represents the so-called low contrast nanoislands.*

Statistical processing of several areas of about $2\ \mu m \times 2\ \mu m$ results in three distinct regimes, as shown in Fig. 4.12 (a). The magnetic configuration of the islands depends on their lateral size $D$ and thickness $t$. Although the spread in geometries and shapes is considerable, each of the three magnetic structures appears well confined to certain regions of this map. The larger nanoislands display a *multidomain* configuration and the smallest present a low contrast that seemingly corresponds to a *single domain* state with homogeneous in-plane magnetization. In between, we find the *vortex* state, displaying an out-of-

plane central core, and which we will discuss soon. These three configurations are clearly seen in graph (b), where the histogram shows how many islands of a given volume present each of the three magnetic configurations. The same is done in Fig. 4.12 (c), using the aspect ratio $D\ \ t$ of the islands. At a first glance, the *D* and *t*-defined distinct regions from (a) suggest that the aspect ratio may be the determining factor leading to one magnetic structure or the other. However, it follows from the graph in (c) that both multidomain and vortex configurations show similar aspect ratios. This suggests that island volume is eventually deciding between the two configurations.

The *low-contrast* nanoislands, which we assume to be single domains, are at the limit of detection with our experimental set-up. To be able to estimate the interaction between the tip and these small islands, we first assume a dead layer of thickness ∼2 nm (recall the discussion regarding the presence of a magnetic dead layer in Chapter 3). The ferromagnetic section of the low-contrast islands would then have a thickness of about 8 nm (the average thickness for these islands is ∼12 nm). Such nanoislands can be divided into individual ∼8 nm diameter spherical elements that interact with the MFM tip. The force gradient between each element and the tip, separated *z*∼30 nm, is then about $4.8\times10^{-5}$ N/m *. The total magnetic interaction between the Co coated MFM tip and a LSMO island can be estimated as the sum of the interactions between each element and the Co tip: considering the typical island lateral size to be around ∼80 nm in the case of the small islands, this gives a total value of $\sim4.8\times10^{-4}$ N/m. Meanwhile, the noise of the MFM signal, evaluated as the signal fluctuation when the tip lies away from the islands, is around $\sim4\times10^{-5}$ N/m. Hence, our estimation is around an order of magnitude above the noise limit. Nevertheless, the average experimental contrast that we measure for the *low-contrast* islands is around $\sim8\times10^{-5}$ N/m, only a factor 2 higher than the background noise, which is the reason why it is hardly detected. The estimated theoretical value, $\sim4.8\times10^{-4}$ N/m, nearly an order of magnitude larger than the experimental, thus sets an upper limit for the magnetic signal between the tip and the low-contrast small nanoisland. The discrepancy between the theoretical estimation and the experimental signal may be due to various facts. First, during the experiments, especially under ambient conditions, the tip is most probably oxidized, which increases the effective tip-to-sample distance. Second, because of the scanning process, the magnetic coating might have worn out slightly, decreasing its magnetic moment. Third, an important decrease from the theoretical value could be also expected in case of in-plane magnetic moments, since the theoretical calculation assumes the moments are out-of-plane. From here, the discrepancy between the theoretical and the experimental value could be taken as an indirect confirmation that the magnetization in the ferromagnetic nanoisland lies indeed in-plane. Anyhow, this diversity in the magnetic configuration cannot be inferred from the SQUID hysteresis loops. In such macroscopic measurements the size-dependent magnetic behaviors all add up and reflect the average magnetic characteristics of the nanoisland ensemble.

It is well known that the geometrical constraints determine up to a great extent the magnetic configuration of small structures, taking *small* as "of the order of the characteristic magnetic length scale" (e.g. in the order of the magnetic exchange length). The magnetization pattern of nanoelements represents the lowest total energy configuration, which is the

*We have estimated the interaction between a Co coated tip (with a radius of 10 nm and magnetization value of $M_S$(Co) = 1440 kA/m) and a LSMO nanoisland divided into 8 nm size elements with $M_S$(LSMO at 300 K) ∼300 kA/m, using the following equation: $\frac{\partial F}{\partial z} = \sum_i \frac{\mu_0 6 m_{tip} m_i}{\pi z^5}$ where $m_{tip}$ and $m_i$ are the magnetic moment of the tip and the magnetic moment of each of the elements of the nanoisland, respectively, and $z$ is the distance between the tip and each nanoelement.

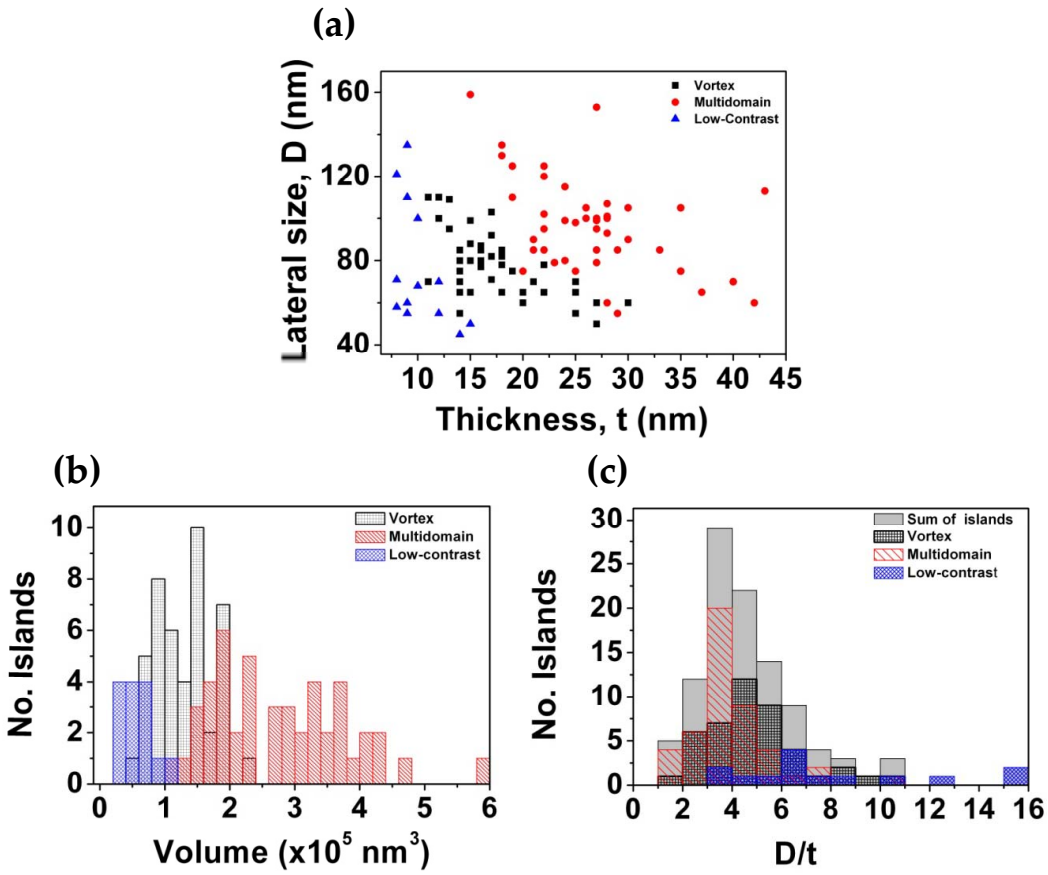


**Fig. 4.12:** *(a) Magnetic phase diagram extracted from MFM measurements displaying the three magnetic configurations as a function of the nanoisland lateral size* D *and thickness* t. *(b) The volume of the islands against the number of nanoislands, separated in terms of the three possible magnetic configurations. (c) The island population distribution in terms of the aspect ratio* D t.

compromise among the different competing terms, i.e. exchange energy, magnetostatic or shape energy, magnetoelastic and magnetocrystalline anisotropy energies, and the interaction energy between individual islands. If we consider an isotropic (no preferential crystal orientations for the magnetization) and free-standing magnetic structure (no strain), its magnetic ground state will be uniquely determined by the competition of the *exchange energy*, which tends to align the spins of the atoms, and by the *magnetostatic energy*, which tries to reduce the field in the surrounding space through flux-closure configurations. Below a certain lateral size in the order of $10^{-8}$-$10^{-11}$m, such competition requires that nanostructures display a single domain structure of parallel atomic spins, giving rise to a giant spin [237]. With increasing volume, however, the increase in the magnetostatic energy triggers the particle to break into differently oriented magnetic domains which permit to reduce the stray fields. In between the single-domain and multidomain structures, for particles of a certain aspect ratio, the ground state is the so-called vortex state [10, 38, 44, 238].

The magnetic moments within the vortex curl in-plane, keeping parallel to the side of the nanoelement-in order to reduce the magnetostatic energy- and slowly curve towards the interior of the particle. The large exchange energy around the center gives rise to a singularity known as the vortex core, which exhibits out-of-plane magnetization. The vortex configuration provides a good flux-closure and it is a highly stable magnetic configuration. It may display four different and energetically equivalent magnetic states depending on its *chirality* or *circulation* (the clockwise or counterclockwise sense of the in-plane magnetization) and *polarity* (the outwards or inwards out-of-plane sense of the core magnetization). The hysteresis loops for such a magnetic configuration were first measured in supermalloy ($Ni_{80}Fe_{14}Mo_5$) nanodiscs by Cowburn et al. [38]. The vortex core was later observed in real space by MFM [10], and also with spin polarized scanning tunneling spectroscopy in Fe nanodots [44]. The vortex magnetic configuration has also been measured in submicron patterns defined in LSMO thin films grown by pulsed laser deposition on (001)-$SrTiO_3$ substrates, where the shape of the islands dominates over the crystal field and the epitaxial strain effects to finally determine the domain structure under zero applied magnetic field [66].

In our system of self-assembled LSMO nanoislands we can rule out the magnetoelastic energy contribution because we know from the structural analysis of Chapter 3 that the islands are strain-free. Regarding the magnetostatic interaction between nanoislands, our analysis did not show any correlation between the nanoisland magnetic structure and their spatial distribution, even if some islands sit very close to each other (less than one diameter away). Besides, it is as an extremely challenging task to include an island-island interaction in such a non-uniform distribution of nanostructures; only for regular arrays of elements, such as those obtained from lithography methods, the interaction component could be realistically modeled [239, 240]. Nevertheless, we do need to include the cubic magnetocrystalline anisotropy in the energy expression of our system. This was inferred from the Ferromagnetic Resonance experiments: the in-plane easy axis lies in the <110>$_{LSMO}$ direction, which is the projection of the <111>$_{LSMO}$ magnetocrystalline easy axis. Summarizing the above, the energy of our LSMO nanoislands can be expressed in the following way:

$$E_{total} = E_{exchange} + E_{shape} + E_{magnetocrystalline} \tag{4.10}$$

The above contributions were taken into account in the simulation of the stable magnetization configurations, performed with micromagnetic elements using the OOMMF 3D code [241] by Oscar Iglesias-Freire from the group of Dr. Agustina Asenjo at ICMM-CSIC.

We consider our pyramidal nanoislands as rectangular prisms in a first approximation, and the following LSMO parameters: the magnetocrystalline anisotropy constant $K_1$ measured in the FMR experiments, the saturation magnetization $M_S$ at 300 K as deduced from hysteresis cycles, and the exchange stiffness $A$= 1.73×$10^{-12}$ J/m taken from the literature [242]. Three different typical islands sizes were evaluated: small (lateral size 50 nm, 10 nm thick), medium-size (lateral size 100 nm, 15 nm thick) and large nanoislands (lateral size 120 nm, 30 nm thick). The obtained results, displayed in Fig. 4.13, reveal what we already saw in the MFM image analysis: the domain configuration depends on nanoisland size. In the case of the smaller islands, we always find a single-domain configuration with in-plane magnetization. Due to the in-plane magnetization of these islands, the MFM contrast (which is proportional to the divergence of the magnetization) is lower than the estimated interaction between the tip and an island magnetized out-of-plane. The majority of the medium-size nanoislands present vortex configuration [Fig. 4.13 (b)] with an out-of-plane component of the magnetization in the center of the island. Finally, the larger islands show a complex magnetization configuration [Fig. 4.13 (c)] with an out-of-plane component of the magnetization in different regions of the island, in agreement with the MFM measurements. It is worth noting how in the vortex-state, where the magnetization is supposedly in-plane except for the core, the magnetic moments exhibit non-zero out-of-plane component (expressed by the presence of red and blue colors throughout the island). A certain out-of-plane component arises in square geometries, due to 90° domain walls that form at the regions where the magnetization vector changes direction. Also, the <111>$_{LSMO}$ easy magnetization axis could contribute to the out-of-plane component of the magnetization. For large islands, the presence of out-of-plane regions gains weight, thus forming domains.

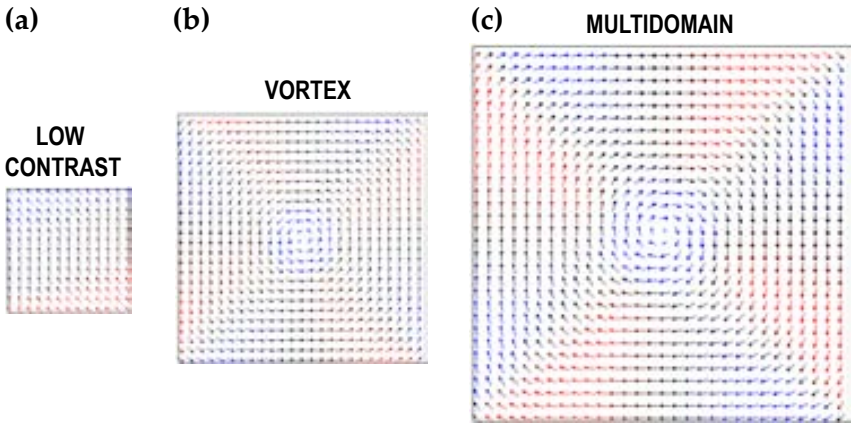


**Fig. 4.13:** *Results of micromagnetic simulations performed with the OOMMF 3D code. Nanoislands correspond to the following geometries: (a) 50 nm × 50 nm and 10 nm thick, (b) 100 nm × 100 nm and 15 nm thick and (d) 120 nm × 120 nm and 30 nm thick. The data scale for all the simulated images is 25 kA/m. The blue and red colors correspond to the out of plane magnetization (outwards and inwards, respectively). The magnetization configurations were obtained after saturating along the +Z (outwards) direction. Courtesy of O. Iglesias-Freire.*

In conclusion, the MFM results, supported by the above explained micromagnetic simulations, allow for the prediction of the geometries that, in LSMO, yield the single-domain, vortex, and multidomain configurations. The uniform magnetization of single-domain nanoparticles, for instance, is a promising candidate for high density hard disk drive data

storage and magnetoelectronic device applications [243–245]. In turn, the four possible independent vortex states could be used as magnetic bits for data storage. Furthermore, the chirality and polarity control necessary for technological applications has triggered a lot of interest, with recent works reporting the electrical and magnetic switching of the vortex core magnetization and the tuning of the chirality [43, 246–248].

### 4.3.2 Analysis of the vortex state in sub-200-nm LSMO nanoislands

The analysis shown in the previous section focused on a specific sample that we named *Sample 1* to distinguish it from *Sample 2*, on which we focus in this section. *Sample 2* also displays an homogeneous self-assembly of well-faceted LSMO nanoislands on a YSZ substrate. Note the remarkable number of vortices that can be observed in the $5\ \mu\text{m} \times 5\ \mu\text{m}$ MFM image of Fig. 4.14. Measurements were done in remanence, after saturating tip and sample in opposite directions. At a first glance, the vast majority of the islands show a bright spot, corresponding to the outwards orientation of the vortex core, although a closer look reveals the presence of some dark spots in the center of some islands (marked with arrows). The predominance of bright spots is due to the prior *ex-situ* saturation, where the islands are first magnetized opposite to the tip (i.e. repulsively interacting with the tip, thus exhibiting bright contrast). When the field is turned off, the island relaxes into the in-plane curling vortex state, with its core pointing preferably outwards.

In addition to the vortex configuration, note that this sample displays a high number of $(111)_{\text{LSMO}}$ oriented nanoislands, crystallized in the form of triangles. Fig. 4.15 shows the MFM forward and backward scan of a group of islands with different magnetic structure. The $(111)_{\text{LSMO}}$ nanoislands exhibit clear magnetic contrast, often the darkest contrast in the image. However, their contrast is influenced by the field of the tip. This is evidenced by the changing of the magnetic pattern with the scanning direction. A reasonable hypothesis is that the tip may trigger a reversible domain wall displacement caused by the small coercive field of the triangles with respect to the tip magnetization.

Unlike the triangular islands, the vortex configuration remains undisturbed during the scanning [see the vortex next to the triangle in Fig. 4.15 (b)]. Note also that, except for the bright core, the vortex state exhibits a dark contrast, characteristic of an attractive tip-island interaction. Recalling that MFM is sensitive to the *out-of-plane* variation of the field generated by the sample, and that the magnetic moments within the vortex are curled *in-plane*, there should not be an appreciable contrast where we actually observe an evident dark contour. There are two issues here to be considered. On one hand, it is not strictly true that no contrast should arise from the region outside the core. The latter indeed holds for perfectly circular structures, where the magnetization swirls continuously within the $xy$ plane. For square geometries, however, a contrast arises at the 90° domain walls of the square diagonals, as commented in relation with micromagnetic simulations of Fig. 4.13. On the other hand, the tip stray field may modify the sample magnetic moments towards the field direction in such a way that the vortex outer region interacts attractively with the tip (dark contrast) [249, 250]. This local modification may happen reversibly, in a way that does not permanently affect the magnetic state of the island. The closer to the sample and the larger the magnetic moment of the tip, the stronger this effect will be. Fig. 4.16 (a) is a simulated MFM image of a permalloy element (1 μm × 1 μm × 10 nm), where the gray scale represents the contrast to be seen in MFM (proportional to $\cdot M$) and the superposed arrows represent the magnetization distribution. Note at how a black (attractive) and a

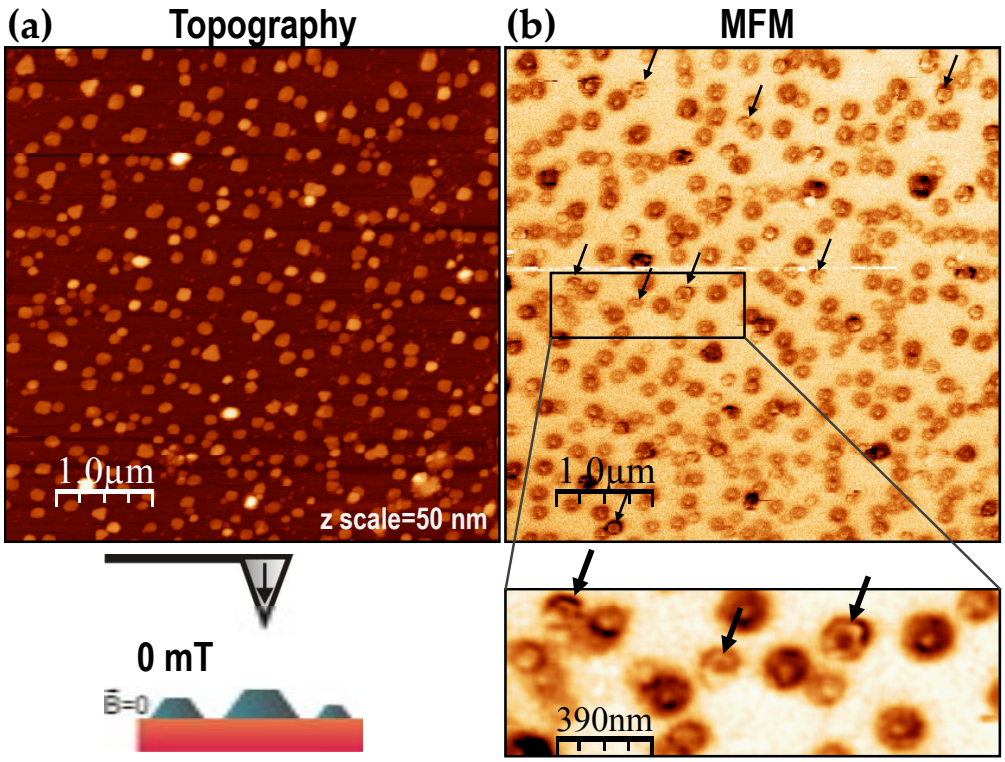


**Fig. 4.14:** *Topography image (a) and its corresponding MFM image (b) of self-assembled LSMO nanoislands displaying a majority of vortex configuration. Images were taken at zero applied field, after saturating tip and sample in opposite directions. The arrows in (b) mark some of the islands which show dark contrast in the vortex core, namely, inwards magnetization (parallel to the tip). (c) Zoom image from (b). A gaussian filter was applied in order to better distinguish the dark and bright vortex cores.*

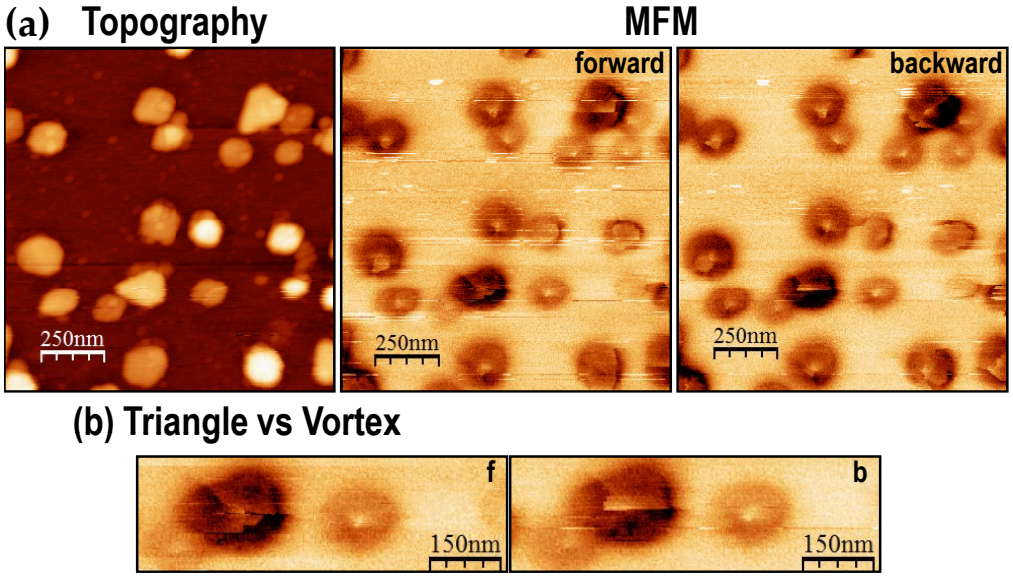


**Fig. 4.15:** *(a) Topography image (left) and MFM images (center and right), the latter corresponding to the forward and backward scan of the tip. (b) Zoom of a triangular and a square island showing how the magnetic structure of the first varies with the tip scanning direction, as opposed to the vortex configuration, which remains unchanged. Images were taken in remanence, after saturating tip and sample in opposite directions. 'f' and 'b' stand for 'forward' and 'backward' scanning direction, respectively.*

white (repulsive) contrast arise at the four domain walls, different to the gray background where $M$ is uniform [228]. In Fig. 4.16 (b) we may see the experimental result of the MFM imaging of such permalloy squares [250]. Fig. 4.16 (c) shows the micromagnetic calculation of a permalloy disk ($D$=300 nm, $t$=50 nm). The size of the arrows reflects the magnitude of the in-plane component (from [249]). Image (d) in Fig. 4.16 corresponds to the MFM measurement of a 400 nm diameter permalloy dot exhibiting a bright core (outwards polarization) and a dark outer core region, consequence of the tip-sample interaction (from [250]).

From the above discussion it is reasonable to think that our square LSMO nanoislands may combine both of the effects described. The influence of the tip stray field in orienting the in-plane magnetic moments parallel to the tip would hence add to the contrast due to the domain walls, which, considering the MFM resolution and the small lateral size of our nanoislands [150 nm vs the 1000 nm of Fig. 4.16 (a) and (b)], cannot be as well-defined as in Fig. 4.16 (b).

Regarding the vortex core, some authors have deduced, using analytical and numerical tools, that it grows wider with increasing island thickness. This is a consequence of the relative decrease in magnetostatic energy due to the reduced out-of-plane demagnetization field in thicker elements. The core $M_z$ distribution thus widens to lower the exchange energy . In our results we do not see such a correspondence between the core lateral size and the island thickness $t$. Fig. 4.17 (a) shows the $D$ vs $t$ diagram of the measured vortex configuration, indicating islands with a *narrow* core $\leq$100 nm (solid dots), and those with a $\geq$100

For instance, the core can display a domain-like $\geq$100 nm-wide central region within 200 nm diameter (0001)-Co circular dots of $D/t$ $\leq$8 aspect ratio [251].

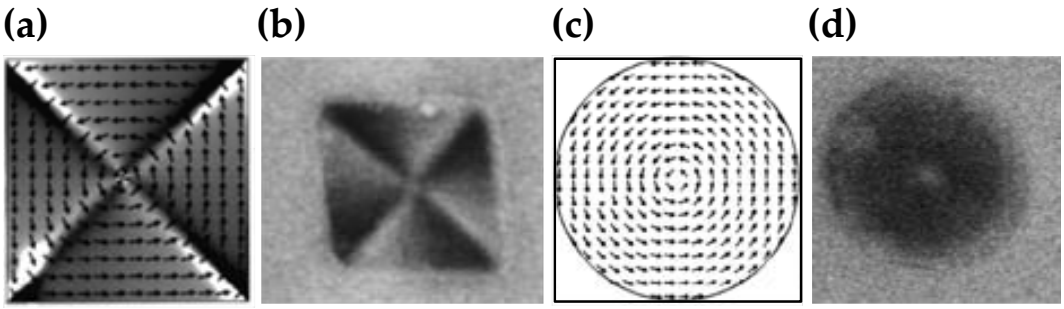


**Fig. 4.16:** *(a) Calculated magnetization distribution (arrows) and the expected MFM contrast, proportional to $\cdot M$ (grey-scale) in a 1 $\mu m$ × 1 $\mu m$ × 10 nm square permalloy element [228]. (b) Real MFM image of a 1 $\mu m$ × 1 $\mu m$ × 50 nm permalloy structure exhibiting the flux-closure structure contrast linked to the presence of domain-walls [250]. (c) Micromagnetic simulation of the magnetization in a D=300 nm and t=50 nm permalloy disk [249]. (d) MFM image of a D=400 nm and t=50 nm disk exhibiting the global attractive tip-sample interaction in the outer region of the vortex. The vortex core is the bright spot in the center of the dot [250].*

nm *wide* core (open dots), which could suggest the concentric-ring structure discussed in reference [251]. Fig. 4.17 (a) evidences that neither *narrow* nor *wide* cores appear related to a higher or a lower aspect ratio region of the diagram. The MFM image in Fig. 4.17 (b) and the corresponding line scans in Fig. 4.17 (c) illustrate what we mean by *narrow* and *wide* cores: their average width $w$ is ∼30 nm and ∼100 nm, respectively. Particularly, these two islands have very similar $D$ and $t$ values yielding aspect ratios in the 9-10 range. The trend described in the literature, hence, is not visible in our MFM results.

A word of caution is in order here regarding the comparison between literature and our experimental results. Theoretical models and experimental studies available in the literature concern different materials and different measuring techniques. The energies involved and the approximations made in them might thus not be applicable to our specific case. For example, the islands reported to show a larger core width with increasing thickness are *hcp* Co cylinders [251], while our LSMO nanoislands are square pyramids with beveled facets, at a 54.7° angle from the substrate surface. The higher the islands, in this case, the smaller the top facet will be. Therefore, it is not evident that the demagnetizing field will decrease in such a geometry, not at least in the manner simulated in reference [251].

An important fact that we have not mentioned yet is that the vortex core sizes deduced from our MFM images are the convolution of the tip-sample interaction, and thus they are likely to be overestimated. Moreover, it appears that the major influence of the tip stray field over the stable vortex configuration is precisely the broadening of the vortex core we discussed above. Fig. 4.18 (a) shows that such broadening is caused by tip-sample interaction, since it varies depending on the scan direction. Such a modification was not detectable in the islands from Fig. 4.17, suggesting that both a real and a tip-induced broadening coexist. The effect of making the vortex core appear wider than it is in reality is a well known issue, intrinsically linked to scanning probe techniques. The tip-sample convolution responsible for the lateral resolution limit is greater in MFM measurements than in topography measurement, due to the *larger* effective tip size: the sample interacts with the stray field of the tip, which is less localized when farther away from the sample surface. From our images we find that the lateral size of the vortex core takes values in the ∼30-

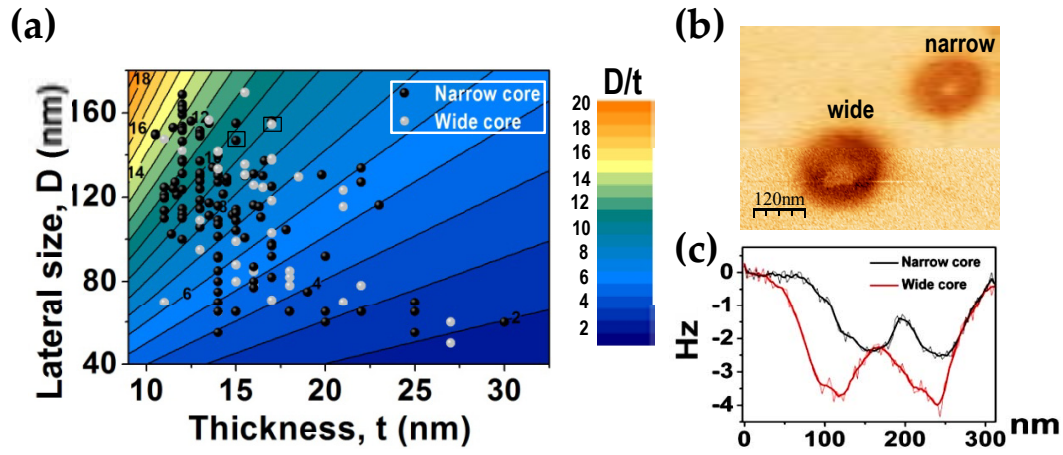


**Fig. 4.17:** *(a) Diameter* D *and thickness* t *of nanoislands displaying vortex state, separated according to the size of their cores as seen with MFM. Narrow core vortices (solid dots) and wide core vortices (open dots), exhibit core lateral sizes below or above ∼100 nm, respectively. The blue to red color scale expresses ascending* D t *values. (b) MFM zoom image of two representative islands exhibiting a narrow and a wide vortex core. They correspond to two islands within the 9-10* D t *range highlighted inside black squares in graph (a). (c) Line profiles across the two vortex cores shown in (b). The lines marked strongest correspond to the smoothing of the real signal, noisier, also drawn. The values measured are ∼40 nm (narrow core) and ∼100 nm (wide core).*

150 nm range. Values in the literature are also in this range for permalloy [10, 249, 250] or Nickel [248] nanostructures observed by MFM. Improvements to MFM measurements have made it possible to achieve 15 nm and even 10 nm lateral size resolution, although measuring at very low temperatures (5.2 K) [252]. To go beyond these limit requires the use of other techniques. An estimation of the real vortex core diameter $w$ of soft ferromagnetic (FM) materials, in the thin-film limit, can be obtained by comparing the exchange and the magnetostatic energies (the two main contributions that dominate the vortex formation).

$$w_t \quad _0 = 2 \quad \overline{A \;\; K_d} \tag{4.11}$$

where $A$ is the *exchange stiffness* and $K_d = \mu_0 M_S^2 \;\; 2$ [44]. Using a value of $A$=1.73×10$^{-12}$J/m for the exchange stiffness of LSMO [242] and $M_S$(300 K)= 300 kA/m, as calculated from SQUID, $w_t \quad _0 \sim$11 nm. In their 2002 work, Wachowiak and co-workers showed the first experimental evidence of a 9±1 nm size vortex core in Fe islands achieved using spin-polarized scanning tunneling microscopy (SP-STM), which is reasonably close to the 6.4 nm value obtained from the theoretical estimate [44].

The vortex core dimension can also be derived from the analytical description of the magnetization distribution within the core. Following the recent work by Mejía-López and co-workers, one can replace the discrete distribution of magnetic moments with a continuous $M(r)$ distribution.The vortex core profile is then described by the $z$ component of $M(r)$, i.e. $M_z(\omega)$, where $\omega = \quad \overline{x^2 + y^2}$ [253]:

$$M_z(\omega) = M_S \;\; 1 - \frac{\omega^2}{l_{ex}^2}[1\;83 + 1\;35(\frac{t}{l_{ex}})^{0.4}]^{-2 \;\; 4} \tag{4.12}$$

In the above expression, $M_S$ is the saturation magnetization, $l_{ex}$ is the *exchange length* and $t$ is the dot thickness. The exchange length $l_{ex}$=5.5 nm was calculated from $l_{ex} = \quad \overline{\frac{2A}{\mu_0 M_S^2}}$

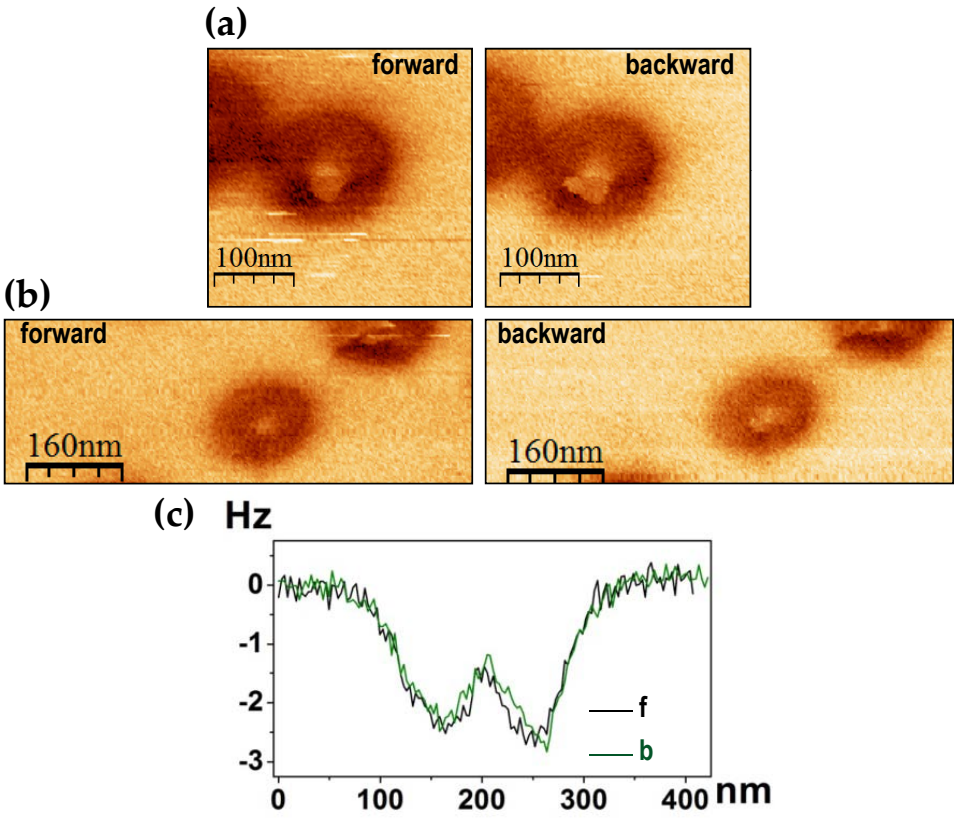


**Fig. 4.18:** *(a) Forward and backward scan MFM images of a zoomed vortex structure. The bright contrast arising from the out-of-plane core appears somewhat diffuse and its appearance changes with the scan direction, indicating the influence of the tip. (b) Forward and backward MFM scans showing a vortex structure. The definition of the core is slightly worse in the backward scan and thus appears slightly wider. (c) Line scans along the vortex cores of (b). In agreement with the observation in (b), the vortex core is a bit wider during the backward scan. The core appears to be ∼80 nm in diameter. The calculated diameter is ∼11 nm at 300 K (see text).*

[51, 254] where $M_S$(300 K)=300 kA/m, $A$ the exchange stiffness of LSMO [242]. Eq. 4.12 is derived for non-interacting cylindrical polycrystalline dots, after minimizing the total energy consisting solely of the magnetostatic and exchange contributions (i.e. neglecting the magnetocrystalline anisotropy). Note that the core distribution is independent of the lateral size of the island. It is also assumed that the core shape does not depend on the $z$ coordinate. Fig. 4.19 (a) shows the 3D spatial distribution of the normalized $M_z$ component of the core, according to Eq. 4.12, for the particular case of our LSMO $t$=20 nm high islands. We have plotted the projection of the 3D graph on the $OXZ$ quadrant, for various $t$ values, in Fig. 4.19 (b). The vortex core lateral size is approximately the full width at half maximum (FWHM) value [253], which leads to $w$∼2×6.5=13 nm for the $t$=20 nm case. The larger the nanoisland thickness $t$, the wider the core will be, and vice versa, in agreement with the previously discussed reference [251]. Fig. 4.19 (c) shows the linear increase of the core lateral size $w$ with $t$, for the particular range of thicknesses displayed by LSMO nanoislands. In the thin film limit, the linear fit gives $w$∼10 nm, which is in very good agreement with the vortex core size as calculated from Eq. 4.11. It follows from here that the theoretical core width values lie well below our MFM experimental resolution

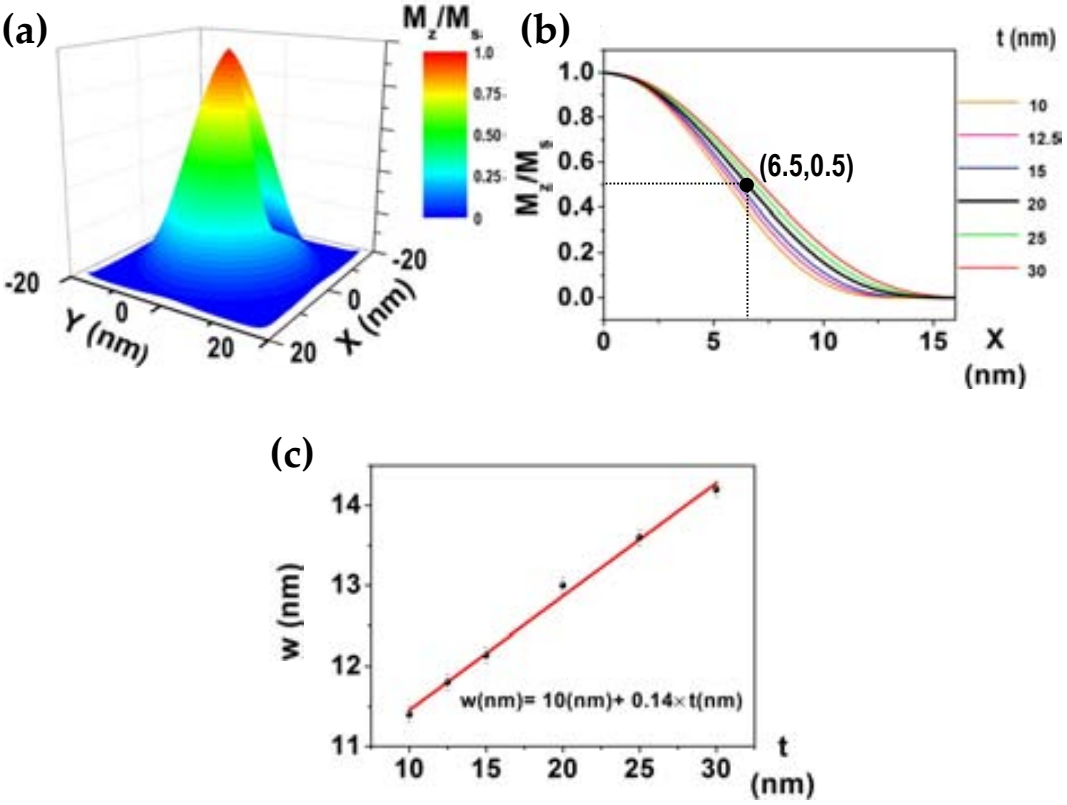


**Fig. 4.19:** *(a) 3D plot of the $M_z$ spatial distribution within the vortex core, according to the Eq. 4.12 derived by Mejía-López et al. [253]. We took island thickness* t = 20 *nm. (b) Projection of the graph in (a) on the OXZ quadrant. The $M_z$ distribution is calculated for the different set of* t *values shown by LSMO nanoislands. The vortex core width* w *is taken at the FWHM value. Variation of $M_z$ (c) Vortex core width* w *plotted against the nanoisland thickness* t*, extracted from graph (b). At the thin film limit (*t ∼0*)* w *approaches 10 nm.*

Integration of Eq. 4.12 over the whole island volume yields the total magnetization

produced by the vortex core. This calculation provides an upper limit in our case, since the expression from reference [253] assumes cylindrical shape. Fig. 4.20 (a) shows that the magnetization within the core constitutes a sizable fraction of the total $M_S$ in the case of nanoislands with small $D$, and rapidly decreases for larger diameters. Note that for thicker islands the core magnetization is slightly larger. This latter tendency is illustrated in Fig. 4.20 (b) for different lateral sizes. We can deduce from there that the variation of $M_z$ with thickness is small for the particular thickness range we are interested in. Only for the case of very small diameters ($D$=40-50 nm) does $M_z$ show an appreciable increase.

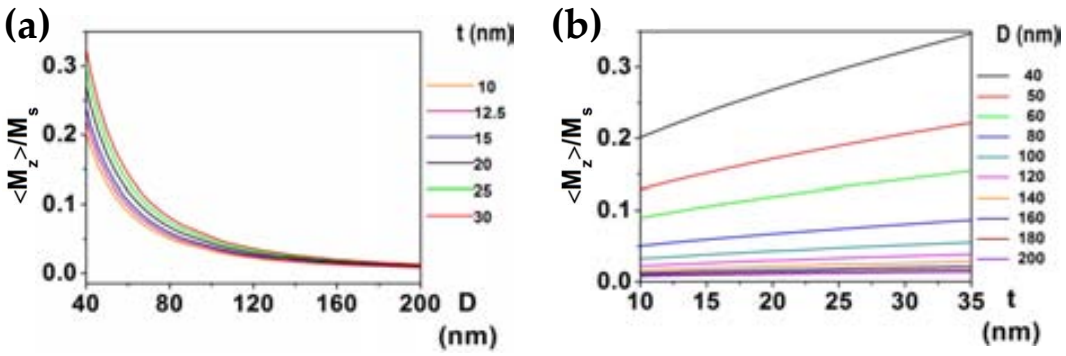


**Fig. 4.20:** *(a) The total $M_z$ produced by the vortex core within the island rapidly decreases for increasing island lateral size. (b) Evolution of normalized $M_z$ with nanoisland thickness. $M_z$ /$M_S$ varies very little with* t *except for the narrowest islands with* D $\leq$*60 nm.*

### 4.3.3 Completing the magnetic structure landscape in sub-200-nm LSMO nanoislands

In addition to the contrast-changing triangles and the vortex state, we may identify two more magnetic structures in *Sample 2*: i) some very small islands with low-contrast and ii) other high square-pyramid islands with an undefined contrast, exhibiting alternate bright and dark areas that sometimes depend on the scanning direction. We can identify the latter with a multidomain configuration. The different appearance with respect to the previously discussed *Sample 1* multidomain islands may stem from their slightly different morphology: in *Sample 2* they show larger thickness values and lower aspect ratios. A representative example of both i) and ii) islands is marked inside colored squares in Fig. 4.21 (a). The graph in (b) shows the sample aspect ratio distribution as a function of the magnetic configuration of more than a hundred islands. This graph is equivalent to the Fig. 4.12 (c) graph obtained from the statistical processing of *Sample 1*, except that the present additionally features $(111)_{\mathrm{LSMO}}$ oriented nanoislands. Note also that the multidomain islands appear in this case limited to low aspect ratio values [Fig. 4.12 (c)], which explains why they exhibit a rather different contrast from the multidomain islands observed in *Sample 1*. In fact, the cubic magnetocrystalline anisotropy of the system, with the $<111>_{\mathrm{LSMO}}$ easy directions [82, 255], could be playing a key role here: since the trend towards in-plane magnetization is weakened for low $D$ $t$ values, the magnetocrystalline anisotropy contribution, which pulls the magnetic moments parallel to the $<111>_{\mathrm{LSMO}}$ directions, would be favored, resulting in the magnetic configuration that we observe.

Vortex states are mainly observed in soft ferromagnetic polycrystalline nanoelements

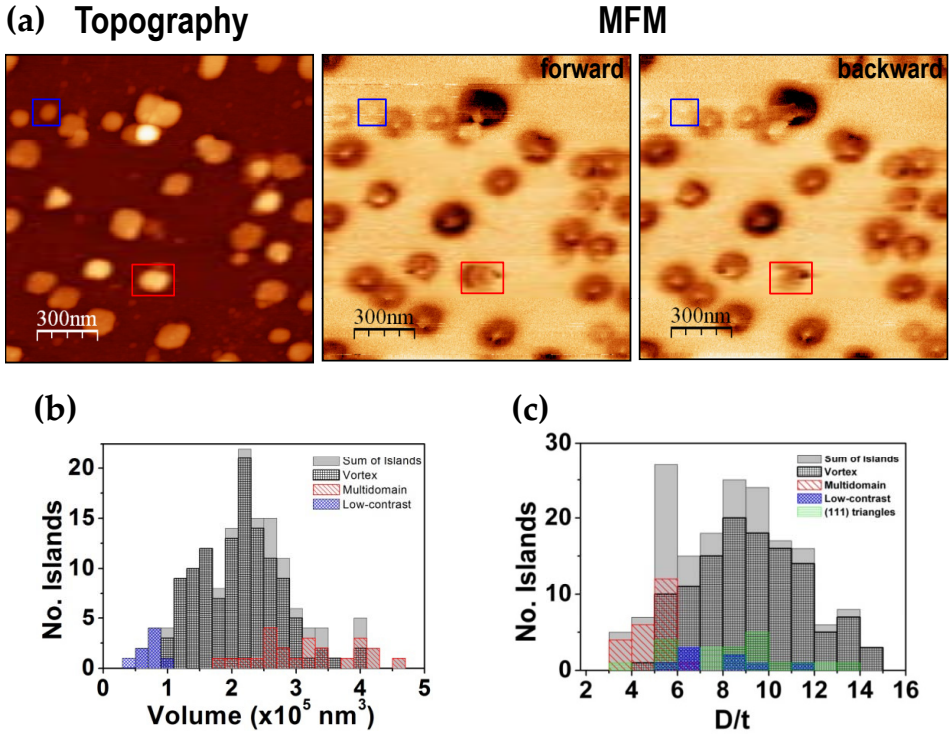


**Fig. 4.21:** *(a) 1.5$\mu m$ $\times$ 1.5$\mu m$ topography and MFM images of a LSMO nanoisland ensemble. Examples of each a small low-contrast island (blue square) and a high changing-contrast island (green square) are given. (b) The volume of the islands against the number of nanoislands, separated in terms of their possible magnetic configurations as seen by MFM (triangles not included). The large volume nanoislands (in red) we have named multidomain. (c) $D\ t$ aspect ratio distribution of the nanoislands separated in terms of their magnetic structure. While the vortex configuration is the most easily stabilized, those showing the largest volume (named multidomain) exhibit the lowest $D\ t$ values.*

sometimes called platelets because of their high $D/t$ values, often above 10 [256–258]. It is worth noting that LSMO nanoislands display vortex configuration also at $D/t$ values as low as 4. A very recent work has proposed that a beveled geometry of the nanoislands, obtained by cutting their edges away, promotes vortex nucleation in permalloy submicrometre disks. This is explained in terms of a symmetry breaking introduced by the beveled edges, which lowers the energy barrier for vortex nucleation within a saturated single domain state [258]. Fig. 4.22 (a) collects the results from the MFM analysis of the two types of LSMO/YSZ samples measured. Full dots stand for *Sample 1* and open dots for *Sample 2*. A symbol of the same color and shape represents the same magnetic configuration. The plot illustrates the consistency of the observed magnetic structures, leading to a complete magnetic phase diagram of the solution-derived LSMO nanostructures. Note that *Sample 2* exhibits thinner and wider nanoislands in general, in addition to the $(111)_{\mathrm{LSMO}}$ oriented triangular nanoislands islands (in green). We have plotted the latter only to illustrate their usual sizes, because they have different crystallographic orientation and hence they are not expected to comply with the tendency shown by the rest of the nanoislands.

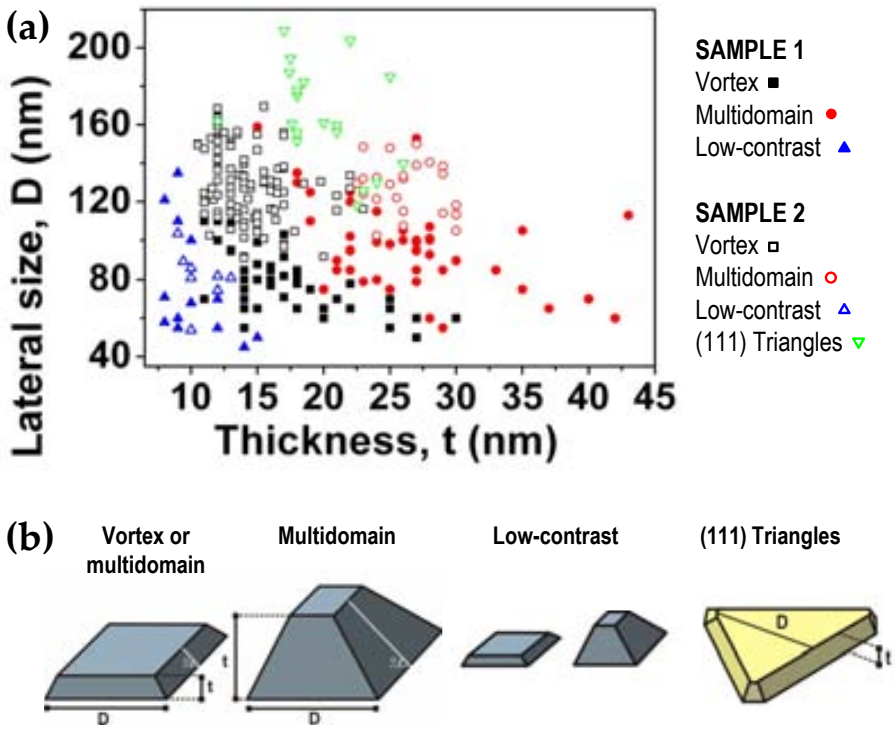


**Fig. 4.22:** *(a) Magnetic phase diagram relating the nanoisland magnetic structure and its shape. Both the contributions of nanostructures from* Sample 1 *and* Sample 2 *were taken into account. Except for a certain ambiguity in large and high islands showing either vortex or multidomain configuration, the magnetic structure of the vast majority of nanoislands is defined by its shape. Triangles are included for the sake of completitude. (b) Sketched geometries of the nanoislands displaying the different nanomagnetic behaviors.*

In order to further investigate the effect of increasing island thickness on the magnetic structure of nanoislands, mentioned before, we discuss here one last example, where nanoislands were grown onto a Zr-doped Cerium Oxide (CZO) buffer layer (∼20 nm thick-

ness) on YSZ. The LSMO on CZO/YSZ system is equivalent to the LSMO on YSZ system, in terms of LSMO island morphology and their crystallographic orientation, except that they tend to display larger thickness values. Note that Cerium Oxide displays a fluorite structure, the same as YSZ. The great majority of the LSMO islands grown on top of the CZO buffer layer of Fig. 4.23 have heights above 50 nm and aspect ratios in the $D\ \ t\sim$3-4 range. Both the MFM forward and backward scan images are shown, giving evidence that the magnetic contrast does not vary too much with the scanning direction (except for the (111) triangular island, where the contrast varies, as in the previous cases). The majority of islands are, once more, square-base pyramids, but we observe no vortex states for these specific geometries. Fig. 4.23 (c) is the same graph as in Fig. 4.22, but now including the data from a few dozens of LSMO islands on a CZO buffer layer. From the MFM images it is not straightforward to determine the magnetic configuration, although the different shades within each island suggest a multidomain structure (not fully resolved due to the limited resolution). Further micromagnetic simulations, taking into account the real shape of the island, would be required to shed some light on the specific magnetic structure of these islands.

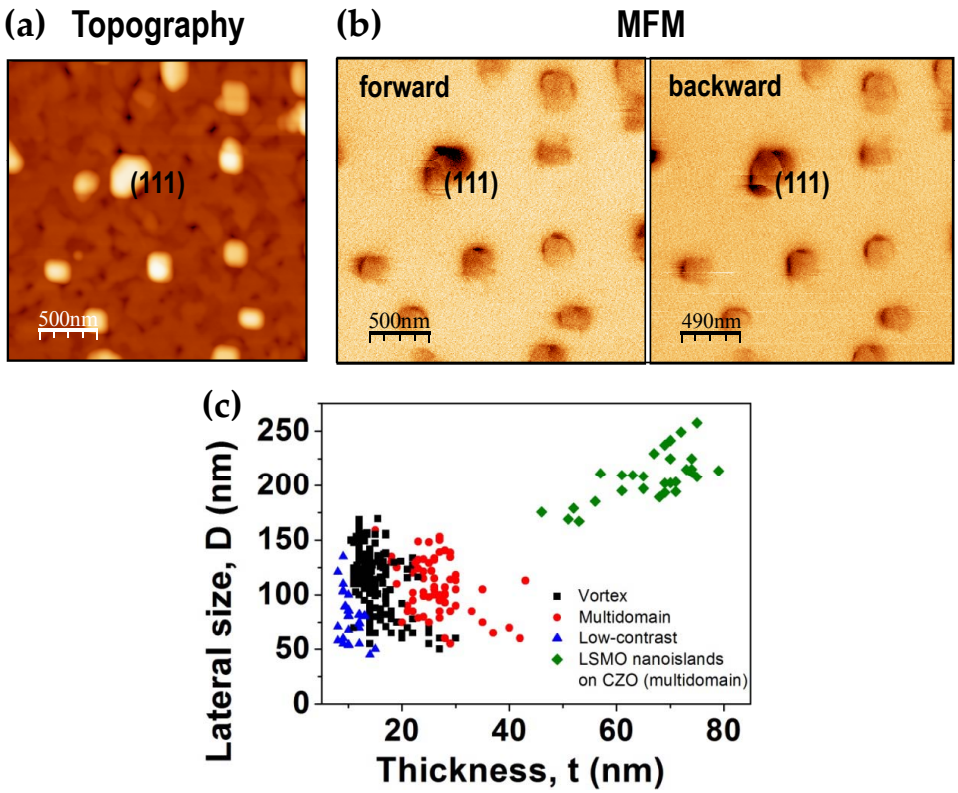


**Fig. 4.23:** *(a) Topography and (b) MFM images of LSMO nanoislands grown on CZO buffer layer. (c) Graph from Fig. 4.22, included the* D − t *correlation of LSMO nanoislands grown on top of a CZO buffer layer.*

## 4.4 System evolution under applied magnetic field

### 4.4.1 General considerations

Throughout the previous section we have described the rich variety of magnetic structures adopted by solution-derived LSMO nanoislands. In particular, we showed that the vortex-state is the preferred configuration for a broad range of LSMO nano-sized geometries. It is now of great interest to study the field stability of these LSMO vortices and, more generally, the behavior of LSMO nanoislands under applied magnetic field. The magnetization reversal process in ferromagnetic nanoelements is very important, not only from a fundamental perspective but also from a technological point of view. The implementation of magnetic nanostructures in modern applications requires knowing, for instance, under what fields the configuration is stable and when it switches magnetization. These processes are governed by the competing energies listed in Eq. 4.10, to which we must now add the Zeeman contribution due to the presence of an external applied field:

$$E_{total} = E_{exchange} + E_{shape} + E_{magnetocrystalline} + E_{Zeeman} \tag{4.13}$$

We could deduce, from the imaging of our LSMO nanoislands, that the vortex configuration is very stable, as proved by successive scans with a relatively high-moment magnetic tip. In their 2002 paper, Shinjo and co-workers revealed the stability of magnetic vortices subject to *out-of-plane* applied magnetic fields [259]: the application of 0.25 T in the direction opposite to previously saturated vortex cores left the core magnetization of circular permalloy dots unaffected. Raising the field up to 0.35 T reversed the magnetization of only the 24% of the cores. Their measurements for constant thickness dots of different aspect ratios ($D$ $t$=4, 8 and 20) showed that the necessary field to switch the vortex core, $\sim$0.4 T, did not depend on the lateral size of the dot, further proving that the core is an independent entity within the surrounding in-plane magnetic structure (recall what we commented regarding the expression for its magnetization, Eq. 4.12).

By contrast, the evolution of the vortex state under *in-plane* magnetic field offers wider possibilities with much smaller fields involved. It is well known that the magnetization reversal in such a case proceeds via vortex nucleation, displacement, and annihilation [38, 260]. The new ground state is no longer the centered vortex state but a new state, now stabilized by the Zeeman contribution (Eq. 4.13). Fig. 4.24 illustrates how the vortex state evolves under in-plane magnetic field, both for a cylindrical (a) and a square (b) prism: the domain with the magnetic moments parallel to the applied field grows at the expense of the rest while trying to keep a flux-closure configuration. The core of the vortex is hence gradually pushed to the edge of the element, where it is annihilated, and a saturated single domain state is reached. The left panel of Fig. 4.24 (a) shows the canonical hysteresis cycle of a vortex, adapted from [260], for a permalloy cylindrical nanodot with $D$=200 nm and $t$=30 nm: the saturated state (A) is followed by the vortex nucleation (B), where a sudden loss of magnetization occurs until the dot adopts the centered-vortex ground state at zero applied field (C). Under increasing opposite field, the core moves in order to minimize the Zeeman term (D) i.e., in the direction determined by its chirality. Finally, the vortex is annihilated, under fields typically in the thousands of Oersted range [38, 260], yielding the saturated single domain state (E).

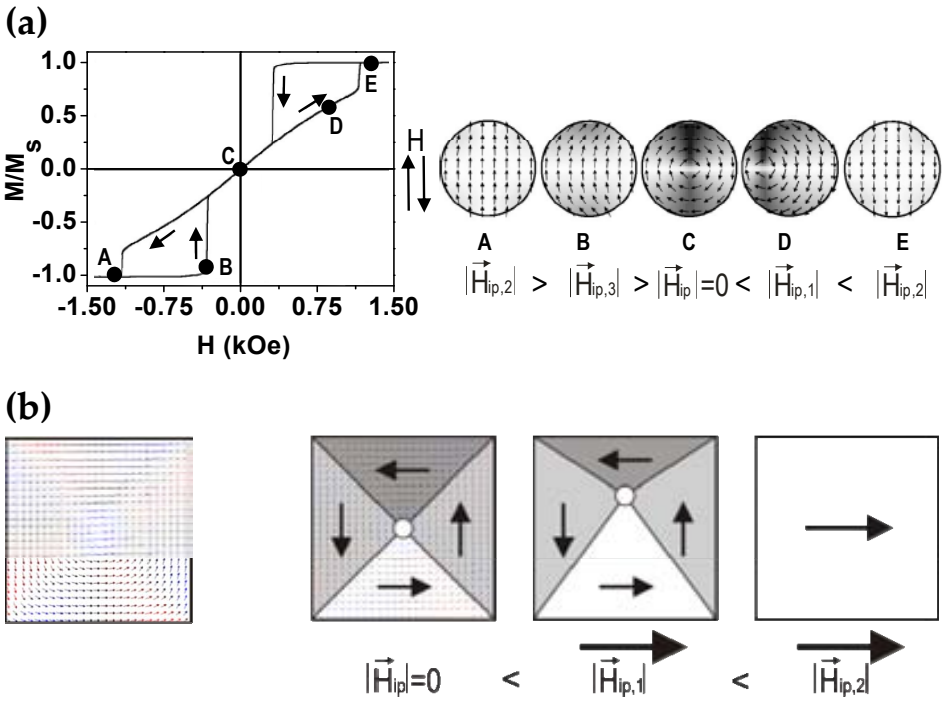


**Fig. 4.24:** *(a) Typical hysteresis loop showing the vortex nucleation, displacement, and annihilation process and the simulated magnetization reversal in a D=200 nm and t=30 nm isolated permalloy dot (adapted from [260]). (b) Simulated vortex configuration for a LSMO square 3D dot, with D=100 nm and t=15 nm (left panel). The vortex structure is simplified in terms of the four main domains and the central core within the square geometry (right panel, left). Under in-plane applied field, the vortex core displaces and finally disappears. These steps would correspond to stages (C), (D) and (E) in the magnetization loop (a).*

### 4.4.2 Experimental results

Fig. 4.25 (b) shows the MFM images of a group of LSMO nanoislands in remanence, and under opposite in plane magnetic fields [(c) and (d)]. The amplitude image in Fig. 4.25 (a) recalls the topography shape of the islands, and a black triangle on the left side of every picture serves as reference, since successive scans cause the tip to shift from its original position due to thermal drift. The remanence image was taken in the usual manner, i.e. after saturating tip and sample *ex-situ* in opposite directions. We were able to apply a maximum *in-plane* field of ∼450 Oe. Note that the general shift of the bright vortex cores is in the direction of the applied field.

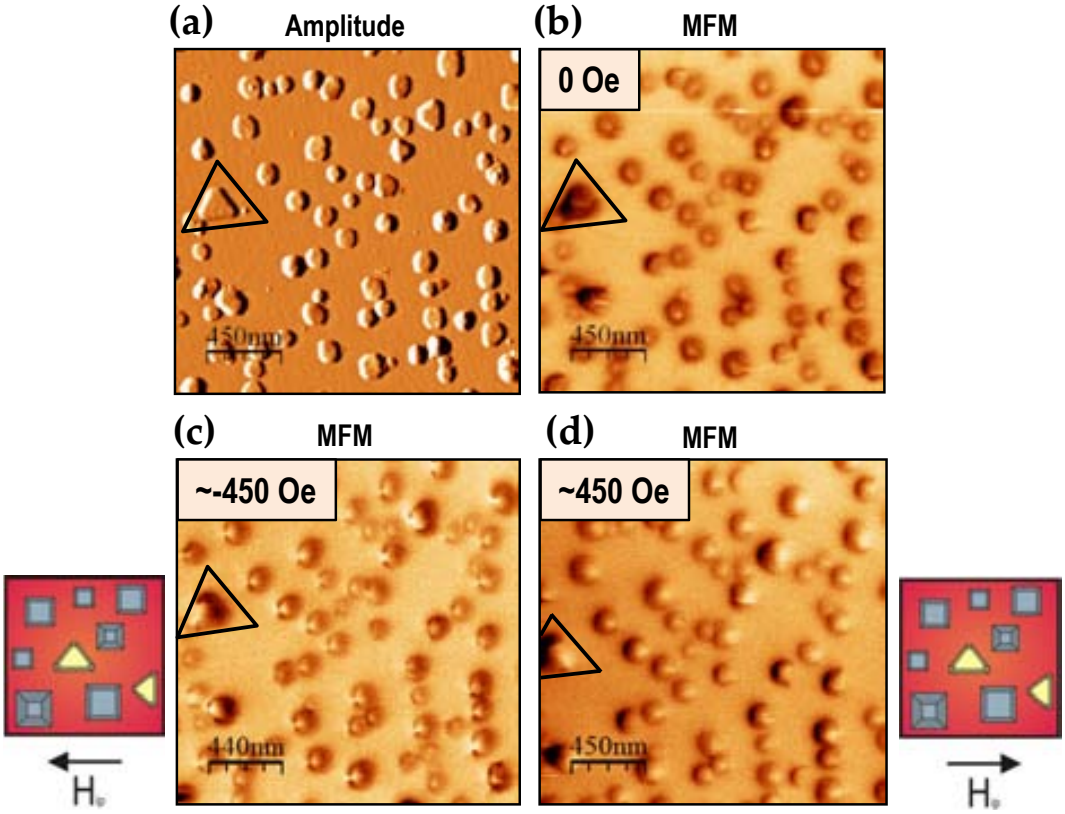


**Fig. 4.25:** *(a) Amplitude image of Sample 2 LSMO nanoislands showing their faceted geometries. (b) MFM image of the same region taken in remanence. Note the presence of different magnetic structures, previously described, including a large number of vortices. (c)&(d) MFM images of the same region under ∼450 Oe external field applied parallel to the substrate edge. The sketches at each side of the figure illustrate the direction of the in-plane magnetic field. A large triangular nanoisland is marked in every image for reference.*

A closer inspection of the magnetic behavior of nanoislands, displayed in Fig. 4.26 confirms the general tendency observed in the low-magnification images of Fig. 4.25. Three regions, labeled *1*, *2*, and *3* are marked with white squares in the topography image at the top of the figure. Zoomed-in magnetic contrast images of such regions are displayed below, along with their topography and MFM line scans. A representative example of each of the different magnetic behaviors found in the nanoislands has been analyzed: The **vortex-state** (V) in *Region 1* shows the leftwards and rightwards shift of its core under leftwards and

rightwards applied magnetic field, respectively. The line scan reveals the presence of the bright core at 0 Oe, and a seemingly dipolar bright-dark contrast under 450 Oe, characteristic of a saturated single domain state [248, 257]. Note that the dipolar contrast appears clearer at 450 Oe, whereas at -450 Oe it has a horse-shoe structure. This asymmetry is most likely due to the presence of a remanent field at zero applied current, which causes the effective field in both directions not to be identical. In other words, the values we give of the fields are approximate, and -450 Oe is in practice less in magnitude than 450 Oe, so the latter does not saturate the island. The small island in between the two medium-size islands in *Region 1* is an example of low-contrast island, which are at the limit of sensitivity of our equipment, and which we know from micromagnetic simulations to display a **single-domain** (SD) structure. Indeed, its weak magnetic contrast, less than 1 Hz in magnitude, shows no observable structure change when imaging at different magnetic fields. *Region 2* gathers a series of vortices and also a **triangular** (T) $(111)_{\mathrm{LSMO}}$ island. The remanence image of the triangle may resemble that of a vortex, but we cannot confirm it, since the backward scan is different from the forward scan shown in the image; as we already explained, the stray field of the tip sweeps the domain walls within the triangle back and forth during the scan. In any case, it appears clear that the island reaches saturation for both -450 Oe and 450 Oe, as indicated by the bright-dark dipolar contrast. The fact that the two saturated states show a contrast of similar magnitude (opposite in sign) confirms our belief that these are magnetically *softer* islands. Finally, the high square (SQ) islands in *Region 3*, with the undefined **multidomain** structure, also show a tendency towards a single domain saturated magnetic state under external in-plane field.

Field values below the $\sim$450 Oe yield slightly off-centered vortices, as shown in Fig. 4.27. The intermediate states between -450 Oe and 450 Oe reveal the gradual displacement of the vortex core, from the aforementioned horse-shoe structure to that of the saturated nanoisland. The change in the location of the core apex in the example from *Region 1* changes imperceptibly for fields in between -200 Oe and 200 Oe. This is not unexpected, since the lateral MFM resolution, around 50 nm, does not allow to resolve the exact location of the $\sim$10 nm wide core. Notice, nevertheless, the presence of a dark spot near the bright vortex core. This spot most likely indicates the attractive interaction between the tip and the field distribution within the core. The fact that it shifts position with changing magnetic field is a clear signal that the structure of the core is rearranging under the influence of the field, although we cannot resolve this movement. The island in *Region 2* exhibits the same magnetization reversal process as the island in *Region 1*, although it appears somewhat noisier and the dipolar contrast expected at 450 Oe appears less clear. Furthermore, it would appear that the bright vortex core, although weak, can still be distinguished at 450 Oe. The island in *Region 2* exhibits a lower aspect ratio than the previous *Region 1* island ($\sim$7.7 against $\sim$11), suggesting that, the lower the aspect ratio, the higher is the field required to annihilate the vortex. In the following we will see that this is in agreement with theoretical predictions.

### 4.4.3 Theoretical analysis

We can compare our experimental observations with the theoretical prediction of vortex evolution under applied field. Guslienko and co-workers have long treated this problem for the case of cylindrical soft FM nanodots, reaching the analytical expressions for the magnetic fields required to nucleate a vortex out of an in-plane saturated state ($B_n$, nu-

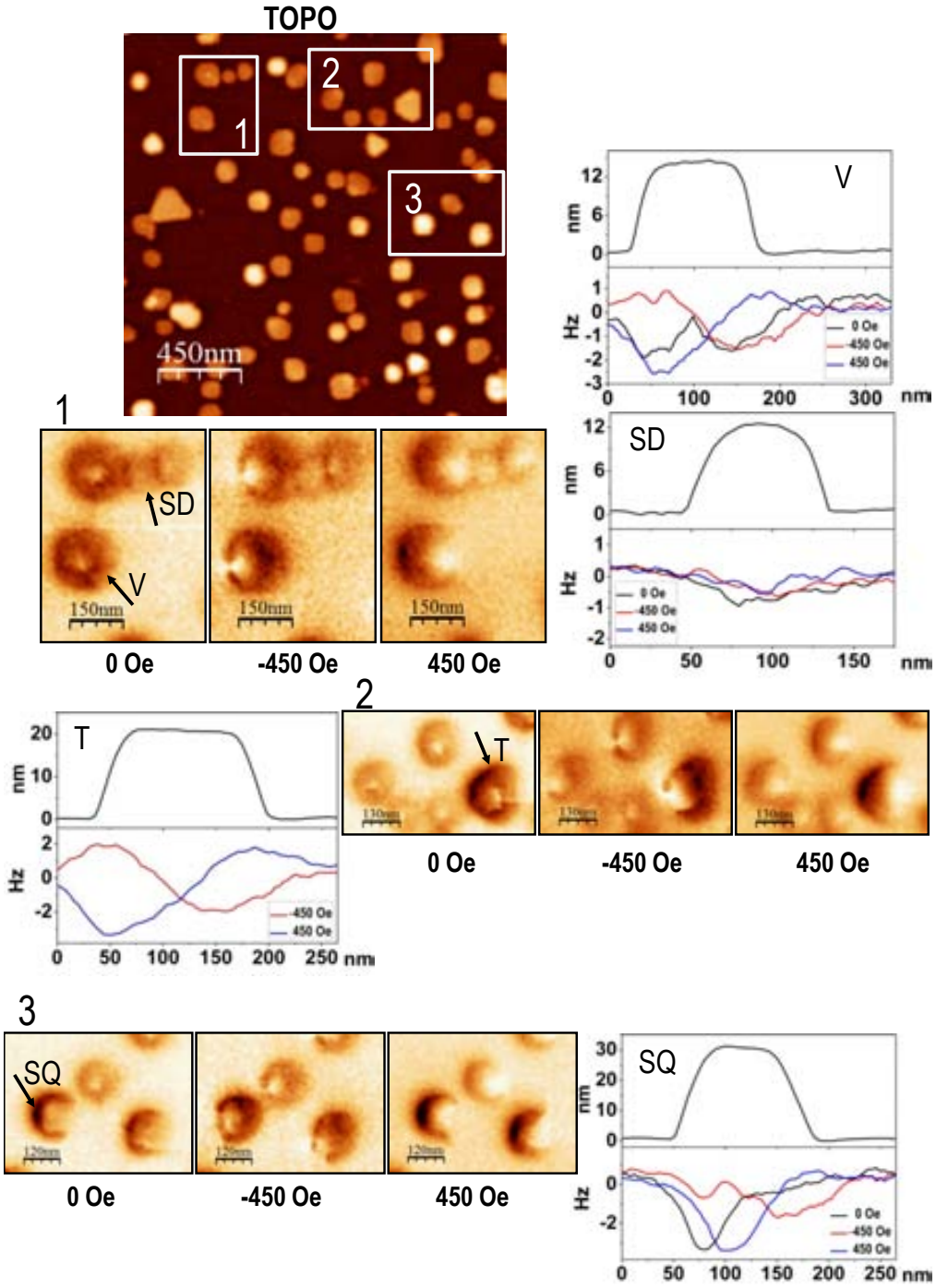


**Fig. 4.26:** *Topography and MFM analysis of LSMO nanoislands in remanence and under in-plane magnetic field. Three white squares in the upper 1.5$\mu$m $\times$ 1.5$\mu$m topography image mark the zoomed-in* 1*,* 2*, and* 3 *regions displayed below. Vortex (V) and single domain (SD) structures are shown in Region* 1*, a triangle (T) appears in Region* 2 *and the high square multidomain island (SQ) is shown in Region* 3*. Their corresponding topography and magnetic contrast line scans are displayed on the sides of the MFM images.*

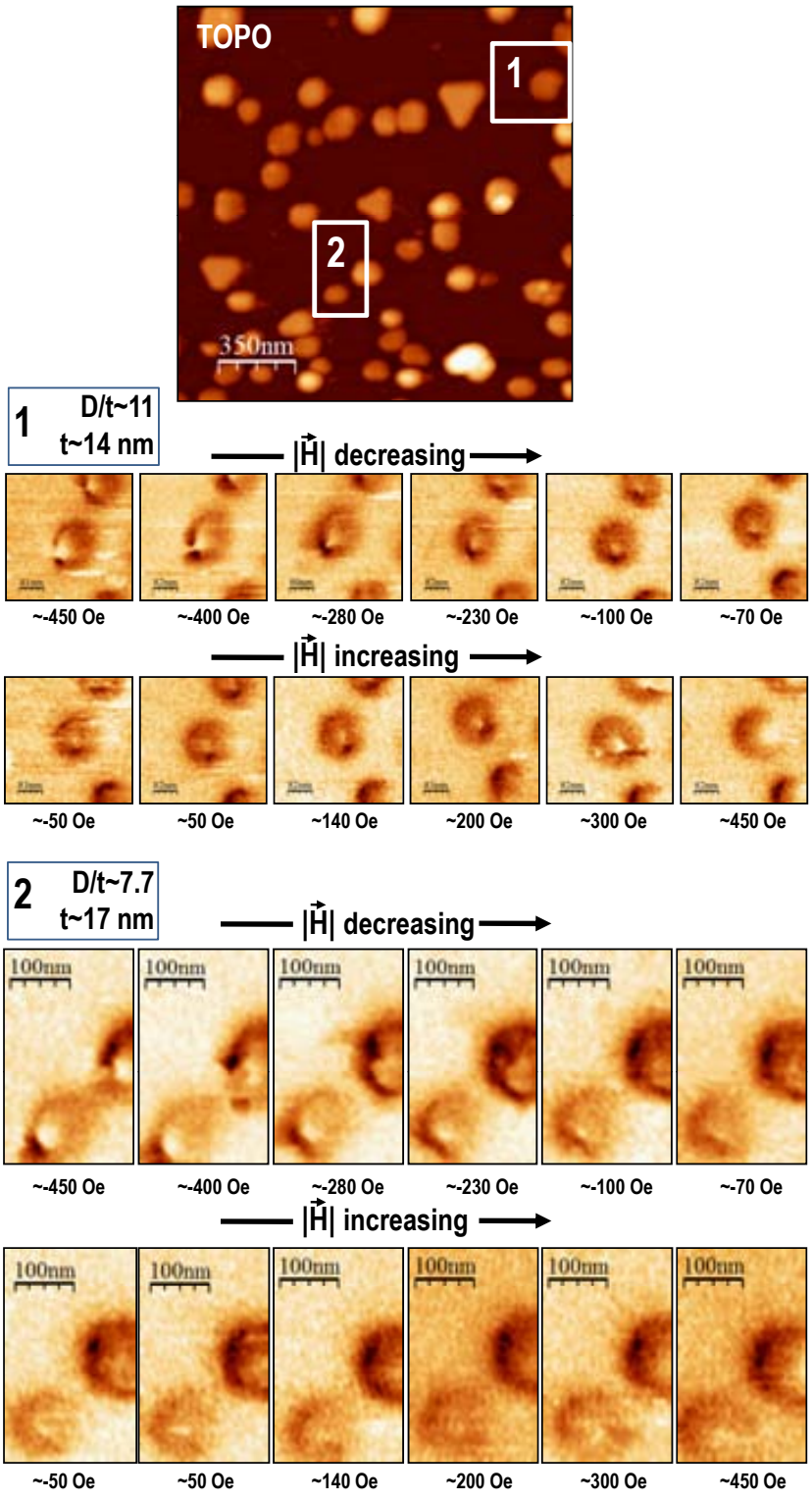


**Fig. 4.27:** *Evolution of the magnetic contrast of LSMO nanoislands under in-plane magnetic field. The MFM images are zooms from the Regions marked 1 and 2 in the above topography image. Note how the dipolar contrast, characteristic of a saturated island, appears clearly in the island with aspect ratio ∼11 whereas the island in Region 2, with lower aspect ratio, does not exhibit a saturated state.*

cleation field) and for the magnetic fields required to expel the vortex from the dot ($B_{an}$, annihilation field) [39, 260]. Starting from the remanence state where the vortex core sits at the center of the disk, $B_n$ and $B_{an}$ are calculated by minimizing the total energy of the shifted vortex state with respect to the relative vortex core displacement $s = 2l \ D$, with $l$ the displacement of the core and $D$ the dot diameter. The sum of magnetostatic, exchange and Zeeman energy contributions for a given vortex core displacement $s$ then leads to the following analytical expressions of the nucleation and annihilation fields (in Gauss) [39, 260]:

$$B_{an} = 2M_S \ 2^{\rightarrow} F_1(\beta) - \frac{1}{2}\left(\frac{2l_{ex}}{D}\right)^2 \tag{4.14}$$

$$B_n = 4^{\rightarrow} M_S \ F_1(\beta) - F_2(\beta) - \frac{1}{\rightarrow}\left(\frac{2l_{ex}}{D}\right)^2 \tag{4.15}$$

where $\beta = 2t \ D$ and $F_n(\beta) = \ _0 \ \frac{dx}{x}\left(1 - \frac{1-e^{-\beta x}}{\beta x}\right) J_n^2(x)$, with $n = 1 \ 2$. $J_1(x)$ and $J_2(x)$ stand for the Bessel function of the first kind and order 1 and 2, respectively. We evaluated the above equations in the $t$ and $D$ range of our LSMO nanoislands and taking the values $M_S(300K)$=300 kA/m and $l_{ex}(300K)$=5.5 nm. The result is plotted in Fig. 4.28, which shows the dependency of annihilation and nucleation field values with respect to the island aspect ratio. According to these graphs, around 120 mT would be required to expel a vortex from a cylindrical polycrystalline LSMO nanodot. This value could go down to 40 mT for the case of an aspect ratio of 10. On the other hand, 40 mT is the greatest value necessary to nucleate a vortex starting from a saturated island, however nucleation values decrease fast when reducing the island thickness $t$. Both the annihilation and nucleation fields show a similar behavior against $D \ t$, with a sharp increase at very small values and a slower decrease for the great majority of higher $D \ t$-s. For the larger $t$-s the curve maxima fall below $D \ t = 1$ but in the plot only those $D \ t \geq 1$ are shown, since in our islands the aspect ratio is always above one. In fact, more realistic expressions for our system would be the ones shown in Fig. 4.29. In the latter, plots from Fig. 4.28 have been confined according to the possible aspect ratio values every island with thickness $t$ can exhibit. This is obtained considering the real $D$ values measured from our AFM studies, i.e., between 40 nm and 180 nm. Tab. 4.2 collects the $D \ t$ ranges for each $t$. The dashed line in Fig. 4.29 (a) represents the maximum field value of 45 mT (450 Oe) we applied in the experiments. This line intersects the set of graphs at a $D \ t \sim 7.8$, meaning that we should be able to expel the vortex and saturate those islands with aspect ratio above $\sim$7.8.

**Tab. 4.2:** *Range of* D t *values found for a given island thickness* t*, considering that the island lateral size* D *varies between 40 and 180 nm.*

| **t (nm)** | | **10** | **15** | **20** | **30** | **40** |
|---|---|---|---|---|---|---|
| **D/t** | min | 4 | 2.7 | 2 | 1.33 | 1 |
| | max | 18 | 12 | 9 | 6 | 4.5 |

The above theoretical analysis is useful to understand the evolution of the vortex state under in-plane magnetic field. We must recall, however, that such analysis oversimplifies our system; the real beveled-edge pyramids are approximated as a parallelepiped, and the influence of magnetocrystalline anisotropy is neglected. Hence, its results should be

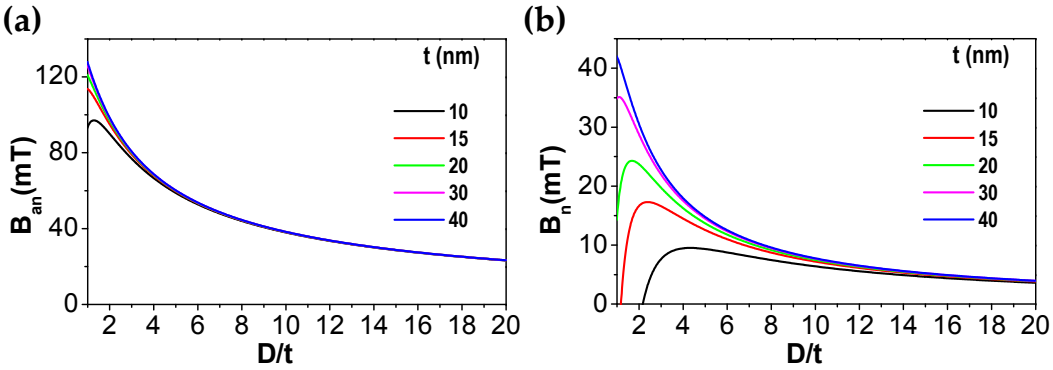


**Fig. 4.28:** *(a) Vortex annihilation $B_{an}$ and (b) nucleation $B_n$ fields for varying island aspect ratios. The larger* D t*, the lower the fields required to expel and nucleate a vortex.*

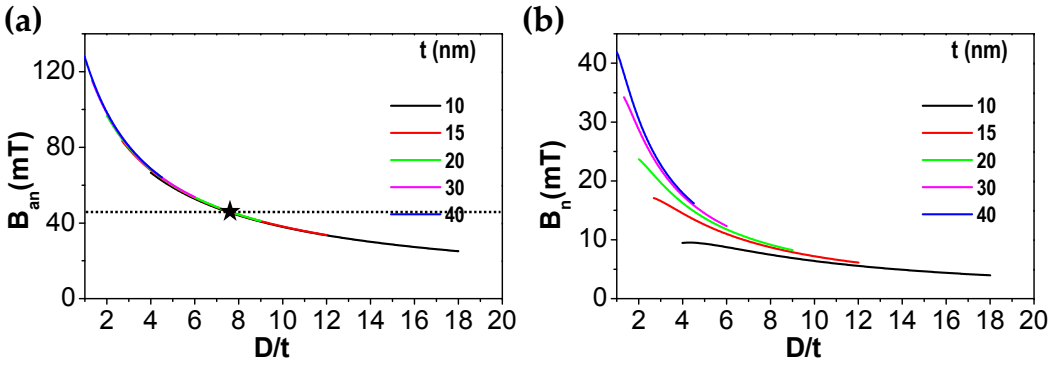


**Fig. 4.29:** *(a) Vortex annihilation $B_{an}$ and (b) nucleation $B_n$ fields for varying island aspect ratios, restricting the* D t *range to the possible values exhibited by the nanoislands, in accordance with Tab. 4.2. The dashed line in (a) represents a field value of 45 mT, which intersects the curves in (a) at* D t*∼7.8. Hence, vortex state is to be annihilated in nanoislands with* D t *values above 7.8.*

considered qualitatively. Furthermore, these neglected factors could also be influencing the movement of the vortex core, which appears to have a motion parallel to the applied external field, instead of perpendicular to it, as we explained in section 4.4.1 that is the common rule. Indeed, in Figs. 4.25, 4.26, and 4.27 all the observed vortex cores shift parallel to the applied magnetic field. The resolution of the MFM does not permit to resolve with enough accuracy whether the core displacement is perfectly parallel or it exhibits a slightly diagonal shift. However, it is clear that the movement is not perpendicular to the applied field, as it would be expected from the theory (see Fig. 4.24 and related text). The *expected* behavior of the vortex core described there, however, does not consider the role of magnetocrystalline anisotropy. The $< 111 >_{\mathrm{LSMO}}$ easy axis of our LSMO nanoislands, responsible for out-of-plane magnetic moment components in our simulated vortex-state configuration, will certainly affect the domain wall movement, although the way it does so is unclear. The influence of the magnetocrystalline anisotropy could be further reinforced by a small out-of-plane component of the external magnetic field: although the experiment is set up to apply in-plane field, a misalignment, either in the sample position (pasted to the sample-holder) or due to some spatial inhomogeneity in the field, cannot be completely ruled out. Nevertheless, it is unclear how these contributions, other than reducing the efficiency of the parallel field, could produce a 90° orientation change in the core motion.

In addition to the magnetocrystalline anisotropy and to the beveled edges of our nanoislands there are other factors that could be influencing the domain wall motion and hence the core displacement. In our analysis we have always neglected the role of magnetoelastic anisotropy, since the islands appear strain-relaxed. Nevertheless, the presence of strain fields due to misfit dislocations at the island-substrate interface could be affecting the movement of domain walls. Moreover, the likely presence of twin planes due to the fact that the LSMO is not truly a cubic but a rhombohedral structure, could also modify the wall motion .

Very few of the effects listed here, not to say all of them simultaneously, are considered in the vast majority of the reported works on ferromagnetic nanomagnets. As we mentioned in the Introduction of this thesis, the traditionally studied nanomagnets, both experimentally and through simulations, typically refer to regularly spaced polycrystalline prisms. All of the previous factors, unique to our system, plus other possible effects that go beyond our control, make it delicate to derive conclusions on the magnetic behavior of our system. As a consequence, simulations that take into account all of the necessary ingredients are highly desirable in order to get insight into the physical mechanisms leading to our experimental observations.

## 4.5 Conclusions and outlook

A detailed study of the nanoscale magnetic structure of solution-derived self-assembled LSMO nanoislands has been carried out by means of MFM imaging at room temperature and ambient atmosphere. We have shown that the successful imaging of the system relies on the adequate tuning of the experimental conditions, and, specifically, on the appropriate choice of the magnetic tip. A commercial CoCr coated tip (40 nm thick coating) was found to be the best compromise between sensitivity and sample modification, revealing

{100} and {110} type twins have been observed in solution-derived LSMO thin films using diffraction contrast TEM [160], p.125.

a clear correlation between the magnetic structure of LSMO nanoislands and their geometrical characteristics. These LSMO nanostructures, featuring lateral sizes $D$ $\sim$40-180 nm and thicknesses $t$ $\sim$10-40 nm, exhibit three main magnetic structures, namely, single domain islands, multidomain islands, and islands with a vortex configuration. These configurations are consistent with micromagnetic simulations. From the analysis of more than two hundred islands we have built an experimental magnetic phase diagram showing the geometric stability of each of the magnetic states in remanence. A remarkable tendency towards the vortex-state has been identified in islands with a wide range of aspect ratios $D$ $t$ 5-15, provided that the island thickness was sufficiently small (below $\sim$20 nm).

In the magnetic vortex state magnetic moments curl in-plane, parallel to the nanoobject edges, in a flux-closure configuration. At the center of the structure, the singularity in the exchange energy is avoided by pulling the magnetization out-of-plane, forming the vortex core. In fact, the observation of the out-of-plane core, represented in most cases by a bright spot at the center of our islands, has been crucial in identifying the vortex state. The small lateral size of the nanoislands ($D$<200 nm) together with the low resolution ($\sim$50 nm) and the tip-sample interaction issues of the MFM, prevented us from resolving the in-plane domain structure of the vortex. We have further studied the vortex core as a function of the nanoisland $D$ and $t$, comparing our observations to analytical expressions derived for the expected core width. These give a theoretical value below 15 nm, well below our experimental resolution. Finally, we have analyzed the evolution of our LSMO nanoislands under an in-plane applied magnetic field, reaching values up to $\sim$45 mT. These have shown the *parallel* motion of the vortex core with respect to the applied field, in contrast to the expected *perpendicular* movement. Using analytical expressions derived for polycrystalline soft cylinders, we have argued that the fields required to nucleate ($B_n$) and annihilate ($B_{an}$) a vortex rapidly decrease with increasing aspect ratios. However, application of the existing models must be regarded with caution. First, the vast majority of them are derived for isotropic prism geometries, whereas our LSMO nanoislands exhibit a beveled pyramid shape and a $< 111 >_{\mathrm{LSMO}}$ easy magnetization axis. Second, it is reasonabe to expect that the specific relaxation mechanisms present in our islands (e.g. misfit dislocations, twin planes...) may also influence the domain wall displacement within our nanoislands. These factors could possibly account for the observed parallel vortex movement, although further evidence is required. A way to accomplish this objective is through more exhaustive micromagnetic simulations that consider all the unique ingredients of our system. These are currently underway, through a collaboration with Prof. A. Sánchez and Dr. C. Navau from the Universitat Autònoma de Barcelona (UAB).

In addition to simulations, there are a number of accessible experiments that could, in the near future, help unveil the nature of the vortex state in our solution-derived LSMO nanoislands. It would be very interesting, on one hand, to be able to apply higher in-plane magnetic fields. By reaching values of 500 mT , we would be sure of having saturated the islands in both directions. Although our calculations show that the applied 45 mT are enough to annihilate a vortex, we also mentioned that the numbers are a rough approximation and that should be regarded with caution. No doubts on reaching the saturation state would exist by applying a field as high as 500 mT. After having saturated the islands, decreasing the field towards the remanence state we would see whether the nucleation of the vortices happens similarly to what we have observed after reaching $\sim$45 mT, i.e. whether

We know from SQUID measurements at 300 K that at such field values the whole nanoisland ensemble is fully saturated.

the core of the vortices shows only bright or, conversely, both bright and dark contrasts. Theory predicts that after saturating a nanomagnet the out-of-plane vortex core nucleates randomly either outwards or inwards. In our experiments up to date we have always recovered the initial bright core, as shown in the chapter. This is probably another property that is specific to our system, where the beveled-edge geometry breaks the symmetry of the geometry and somehow influences vortex nucleation. By applying very high field values this could be unambiguously ascertained.

Another experiment that would be interesting to perform is to carry out the same study as we did in here but from different starting conditions: we have mainly analyzed our system in remanence, after saturating tip and sample in opposite directions. Another option would be to investigate what is the relaxed magnetic structure achieved after having saturated the sample in-plane. In this case the exchange energy would favor in-plane magnetic moments, with the help of the flat nanoisland shape, while the magnetocrystalline anisotropy would pull the magnetization along the easy $< 111 >_{\mathrm{LSMO}}$ directions, and the demagnetizing field would tend to produce a flux-closure configuration. Although we know from micromagnetic simulations that the ground state of certain islands is the vortex state, a different, although metastable magnetic structure can also be achieved. Indeed, the magnetic structure dependency upon the magnetic history has already been reported for (0001) flat Co dots with a strong perpendicular anisotropy [257]: they have shown to display a vortex state in remanence after out-of-plane saturation (the ground state), and, by contrast, a single domain state (a local minimum), also in remanence, after in-plane saturation. Observing the behavior in our LSMO islands could help further unveiling the precise role of each of the energy terms. Furthermore, the broad range of aspect ratios found in our islands would allow us to observe the cross-over between different behaviors. For instance, regaining the vortex state after such in-plane saturation would underline the significance of the magnetocrystalline anisotropy in our system.

# Chapter 5

# Advanced local characterization of LSMO nanoislands: PEEM and KPFM

The present chapter is devoted to the investigation of self-assembled ferromagnetic $La_{0.7}Sr_{0.3}MnO_3$ (LSMO) nanoislands by means of two cutting-edge nanoscale characterization techniques. Photoemission electron microscopy (PEEM) combines the high spatial resolution provided by electron imaging with the chemical, electronic and magnetic information attainable from X-ray-matter interaction. Meanwhile, Kelvin Probe Microscopy (KPFM) is based on the contact potential measurement between materials brought into electrical contact, as originally first achieved by Lord Kelvin back in 1898 [261]. Developed 30 years ago, KPFM is a powerful scanning probe technique, capable now of lateral atomic resolution in the mapping of local contact potential differences [262, 263]. These two distinct techniques have in common their rapid and continuous development, caused by the need to characterize increasingly small objects as well as new and complex materials systems. In this regard, both PEEM and KPFM characterization of solution-derived LSMO self-assembled nanoislands constitute a notable challenge, principally due to the insulating character of the substrates where the nanoislands lie. This makes KPFM measurement and its interpretation non-straightforward. On the other hand, feasible PEEM experiments require the a priori metal capping of the insulating samples, greatly reducing the intensity of the signal coming from the sub-200 nm size LSMO nanoisland. Under this experimental conditions, we will see, we are close to the resolution limit of the technique. To the best of our knowledge there are no attempts in the literature concerning the study by PEEM and KPFM of systems of these particular characteristics. This chapter presents the efforts in pushing the potential of these techniques towards the characterization of self-assembled nanoscale magnetic systems.

## 5.1 Photoemission Electron Microscopy measurements of self--assembled LSMO nanoislands

PEEM offers simultaneous imaging and spectroscopic characterization of material surfaces with high spatial resolution. Being able to probe the local chemical composition of the sample, it allows one to independently study the surface of the nanoislands in the case of self-assembled nanostructured templates, or even to chemically map individual nanoscale objects. In addition to elemental selectivity, PEEM also enables the study of the magnetic domain structure of surfaces of films and nanostructures. The recent technological interest and advances in the fabrication of novel and miniaturized magnetic devices, and the corresponding necessity for their fundamental understanding, makes PEEM a very valuable nanoscale magnetic characterization technique.

### 5.1.1 Basics on PEEM

In photoemission electron microscopy an intense light such as X-ray radiation, is directed into a sample triggering the excitation of core-level electrons into unoccupied states. The holes in the corelevels are subsequently filled by electrons from higher energy states, either radiatively i.e. with the emission of fluorescence rays, or by Auger electrons that can suffer multiple scattering and yield a cascade of secondary electrons. The core-level photoemitted electrons (photolectrons) and the cascade of elastically and inelastically scattered secondary electrons escaping the sample surface, are then accelerated under high voltages (typically 20 kV). Then, these electrons are carried along an electron-optical system which generates, transfers, and magnifies the image, finally formed onto a phosphor screen. The electron image is converted there into a visible image by means of a CCD camera (see Fig. 5.1 below). The energy spectra of the PEEM-transmitted electrons is considerably broad, ranging from directly emitted photoelectrons to low-energy secondary electrons. This is one of the main factors that limit the resolution (known as chromatic aberration). Other lens aberrations include astigmatism or spherical aberration, in which rays at different angles are focused at different distance from the focal plane. Increasing the acceleration voltage or decreasing the contrast apertures are some of the strategies used to enhance the lateral resolution, presently at around ∼30 nm, and further improving [264].

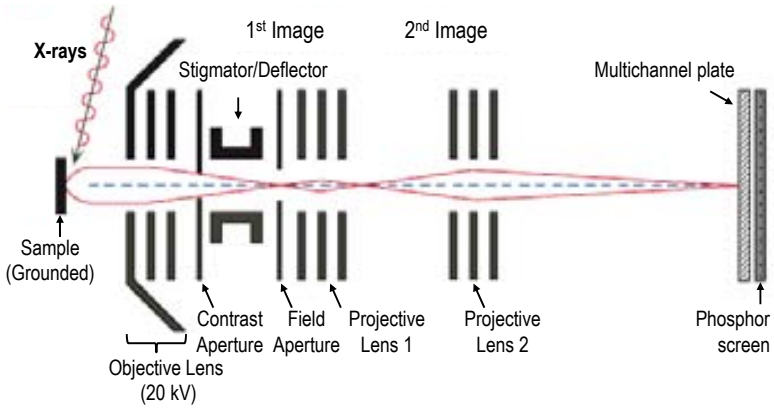


**Fig. 5.1:** *Electron-optics layout within the PEEM chamber. Adapted from [265].*

X-ray PEEM (X-PEEM) experiments are performed in synchrotron-radiation facilities, which provide intense, naturally polarized light, with wavelengths ranging from micrometers (infrared) up to Angstroms (hard X-rays). X-PEEM is typically operated in the soft X-ray regime, i.e. with radiation energies in the 100-2000 eV range, where many of the most important magnetic transition metals like Fe, Co, Mn, and Ni have their $L$-absorption edges (the $2p \quad 3d$ transition). The $K$-edge of light elements (O, C, Si...) and the $M$-edge of rare-earth metals also fall in this energy range. Fig. 5.2 shows a schematic drawing of the fundamental instrumental parts constituting a X-PEEM experiment. X-rays, generated by the deflection of relativistic electrons within the synchrotron storage ring, are directed into the specific PEEM beamline, after choosing their polarization (either linear, circular or elliptical). The monochromator in the line selects the energy of the beam, in minimum steps of 0.1 eV, and a mirror system brings the light onto the sample surface. After the X-ray interacts with matter, the escaping electrons enter the PEEM electron-optical system depicted in Fig. 5.1.

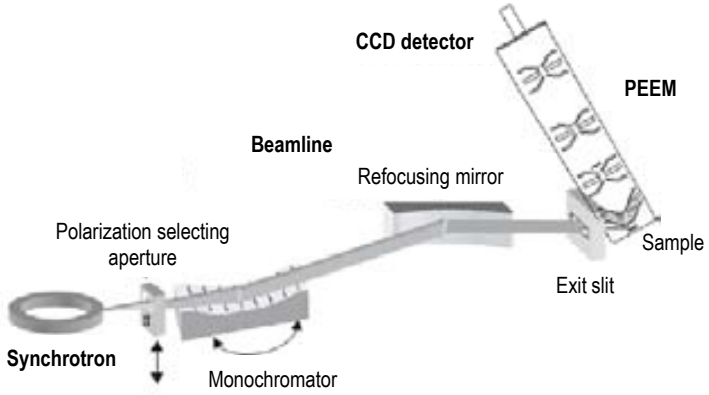


**Fig. 5.2:** *Schematic drawing of the PEEM integration in a synchrotron facility. Reproduced from [266].*

### Chemical and Magnetic contrast in X-PEEM

The fundamental characteristic of X-PEEM is that it provides spatially-resolved chemical and magnetic contrast in the *nm* range. This is done by simultaneously recording the emitted electrons, at a certain energy, for every point of the imaged sample. By changing the energy (in steps as small as 0.1-0.5 eV), the changes in $e^-$ emission are monitored in the form of a darker or brighter contrast. The usual working mode consists in collecting all of the electrons (directly photoemitted and secondary) that escape from the sample due to the de-excitation process initiated by the X-ray absorption. This mode is known as Total Electron Yield (TEY) mode. When the energy of the arriving photons meets that of a certain electronic transition in a particular element, the absorption is greatly enhanced and this, in turn, augments the cascade of electrons emitted from that particular spot of the sample (the spot is seen with bright contrast). It can be demonstrated that if the penetration depth of the X-rays is larger than the escaping depth of the electrons, $\Delta$, the absorption is directly proportional to the electron yield signal [265, 267, 268]. The escaping depth is determined by the average depth from which low energy secondary electrons (the great majority) leave the sample. This distance is measured experimentally, taking values from 1.5 nm to 2.5 nm

in ferromagnetic metals (for instance, $\Delta\sim$21 Å and 17 ($\pm$2) Å have been measured for Fe [268, 269]). Therefore, X-PEEM is essentially a surface-sensitive technique. By recording the intensity maps (which constitute the PEEM images) at several energies, and integrating the stack of images within the area of interest, we obtain the X-ray Absorption Spectrum (XAS) of that specific sample region. By tuning the energy range and the energy resolution adequately, not only the general aspects of the XAS spectra but also their fine structure can be studied. The latter, known as X-ray Absorption Near Edge Structure (XANES) allow one to discern different valence states of the studied element, as well as to learn about the chemical environment of the analyzed atoms, since their characteristic spectra depend on it.

The other major characteristic of X-PEEM is the possibility of imaging the magnetic domains of ferromagnetic surfaces using X-ray magnetic circular dichroism (XMCD). XMCD is based on the distinct absorption of left- and right-handed circular polarized light by the electrons of a ferromagnet. The interaction with the illuminating X-rays causes the spin of photoelectrons to change polarization. This change depends on the helicity of the light and on the spin state of the excited core-electron and may be expressed in the following way [265]:

$$P(\phi^+) = -P(\phi^-) \tag{5.1}$$

$$P(2p_{3/2}) = -k \cdot P(2p_{1/2}) \tag{5.2}$$

Here $P$ stands for polarization and $\phi^+$ ($\phi^-$) for the left-handed (right-handed) circularly-polarized light. Eq. 5.1 indicates the change in polarization direction when the helicity of the incident light is opposite. As regards Eq. 5.2, it expresses the dependency of polarization with the core-electron spin. The splitting of the $2p$ level due to spin-orbit interaction gives rise to the $L_3$ and $L_2$-edges in transition metals, which correspond to $2p_{3/2}$ $3d$ and $2p_{1/2}$ $3d$ transitions, respectively. According to Eq. 5.2, the polarization changes sign and magnitude from one $2p$ level to the other. Besides, in the case of a ferromagnetic material, the probability for an electron to be excited into an unoccupied state depends precisely on its polarization, i.e. on whether it is a minority spin with a large available unoccupied Density of States (DOS) above the Fermi level ($E_F$), or, conversely, a majority spin with a low DOS above $E_F$. As the polarization depends on the helicity of the light (Eq. 5.1) and, from what we have just said, the transition probability of electrons in a ferromagnet depends on the polarization of the photoelectrons, it follows that the intensity $I$ of the absorption edge will be different for opposite light helicities:

$$I(\phi^+) = I(\phi^-) \tag{5.3}$$

Fig. 5.3 shows the XAS for the Mn $L_3$ and $L_2$ edges in a $La_{0.7}Sr_{0.3}MnO_3$ thin film at 100 K, measured with the light helicity either parallel or antiparallel to the magnetization. The XMCD spectrum below, also known as the *dichroic spectrum*, is then calculated from the difference between I($\phi^+$) and I($\phi^-$) [270]. The integration of intensities and the application of the so-called *sum rules* can be further used to calculate the magnetic orbital and spin moments of the specific elements measured [271, 272].

Regarding magnetic domain imaging, the usual procedure is to collect PEEM images at fixed photon energies where the magnetic contrast is maximum, i.e. at the $L_3$ or $L_2$ absorption edges for the case of ferromagnetic (FM) transition metals. Contrary to FM materials, for non-magnetic materials there is no absorption change with circular polarization,

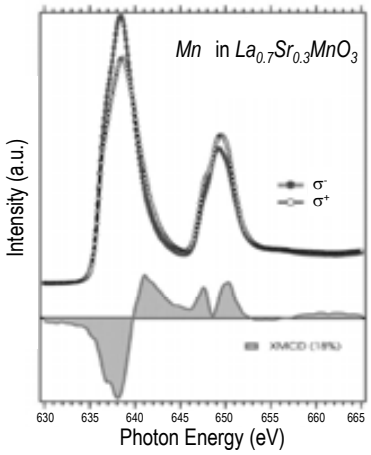


**Fig. 5.3:** *XAS for Mn $L_{3,2}$-edges in a $La_{0.7}Sr_{0.3}MnO_3$ thin film for light helicity aligned either parallel or antiparallel to the magnetization vector. The difference between the two spectra yields the XMCD signal below. The measurement was done at 100 K. Adapted from [270].*

i.e. $I(\phi^+) = I(\phi^-)$. Consequently, the common way of enhancing the magnetic contrast in PEEM images is by getting rid of the non-magnetic contrast by subtracting two images taken at the same energy but with opposite helicities:

$$A_\sigma(x\ y) = \frac{I_{\sigma^+}(x\ y) - I_{\sigma^-}(x\ y)}{I_{\sigma^+}(x\ y) + I_{\sigma^-}(x\ y)} \tag{5.4}$$

where $A_\sigma$(x,y) is known as the *asymmetry image* [265]. Equivalently to Eq. 5.4, the XMCD image can be obtained by subtracting two images taken with the same helicity but opposite magnetization directions. A clear example of such contrast enhancement is illustrated on the left panel of Fig. 5.4 (a) and (b), in which the nickel rectangular structures (12 µm equivalent diameter) of Fig. 5.4 (b) (the asymmetry image) display purely FM contrast, after eliminating non-magnetic contributions (chemical, topographical...etc.) exhibited in Fig. 5.4 (a) [265]. The black and white contrast and the gray shades in between account for the relative orientation of the magnetization vector with respect to the light helicity. Indeed, the intensity of the contrast may be expressed as $I \sim M \cdot \phi \sim I_0 \cos(\alpha)$ with $M$ the magnetization vector of the sample and $\alpha$ the angle between the helicity vector and $M$. Fig. 5.4 (c) on the right shows the magnetic domain pattern of a (001)-Fe (001) surface obtained at the iron $L_{2,3}$ edge [265]. The arrows display the in-plane magnetization direction within each domain. In addition to FM samples, X-PEEM can also probe technologically important antiferromagnetic materials such as Ni and Co oxides or complex oxides like $LaFeO_3$ [273], taking here advantage of X-ray Linear Magnetic Dichroism.

### 5.1.2 Experimental procedure: on the metal capping of insulating substrates

We conducted the PEEM measurements at the UE49-PGM-1-SPEEM Beamline at the synchrotron light source BESSY II (Berlin), in the context of the scientific collaboration with Dr. S. Valencia (BESSY) and with the technical support and supervision of Dr. J. Herrero-Albillos and the Beamline scientist Dr. F. Kronast. A beam time of 3 weeks in total, separated in three periods, was devoted to our samples. We measured self-assembled ferro-

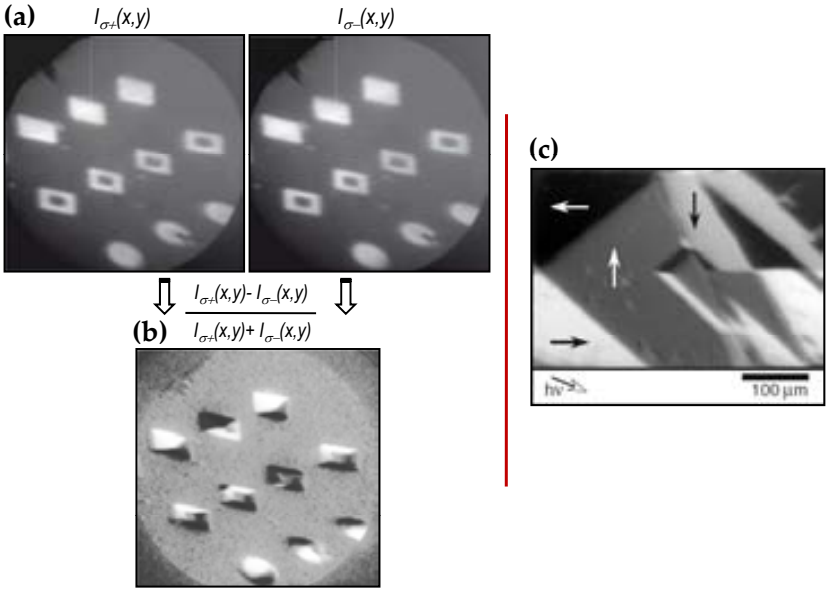


**Fig. 5.4:** *(a)&(b) Example of the ferromagnetic contrast PEEM image obtained from the subtraction of two consecutive images taken at the same photon energy but with opposite helicities. The subsequent normalization further enhances the FM contrast. The sample consists of rectangular Ni structures, with ∼12 µm equivalent diameter [265]. (c) (001)-Fe thin film PEEM magnetic contrast image. The various shades of gray are caused by the relative angle between magnetization and the incident light propagation vector [265].*

magnetic LSMO nanoislands on YSZ substrates, grown from 0.03 M precursor solutions, and heat-treated at 900°C for 1 h to 3 h. These nanoislands are small, near the PEEM resolution, with thickness $t$∼10-60 nm and lateral sizes $D$∼40-200 nm, and a variety of aspect ratios. Among the two possible nanoisland morphologies, we selected the *regular-square* nanoislands, described in Chapter 3, mainly because they are larger and appear separated at larger distances than the *rotated-square* nanoislands. Recall that samples exhibiting the $(001)_{\mathrm{LSMO}}$-oriented *regular-square* nanoislands also display a minority population of $(111)_{\mathrm{LSMO}}$-oriented triangle-base nanoislands.

With PEEM we can explore both the absorption edges of individual nanoislands and averaged signals of nanoisland collections. As shown in previous chapters, these ferromagnetic islands have a $T_C$∼350 K and display various possible nanoscale magnetic configurations, revealed by MFM. As compared to MFM, PEEM offers complementary information regarding the ferromagnetic structure of nanoislands: it is sensitive to the in-plane magnetization direction rather than to the out-of-plane stray field sensed by MFM (recall the intensity dependence $I \sim M \cdot \phi$). Furthermore, in PEEM we avoid the influence of the tip on the magnetic contrast of the sample, and we may thus observe the unperturbed magnetic structure. Nevertheless, the small island size makes it difficult to resolve their magnetic domains.

### In uence of the capping on photoemission experiments

Before going through the chemical and magnetic investigation of the nanoislands our first objective is to overcome the most important experimental factor limiting the measure-

ments: the insulating nature of the single crystal YSZ substrates. To bring the electrons emitted from the sample into the microscope, we mentioned earlier that a high voltage (20 kV) is applied between the sample surface (the cathode) and the first part of the objective lens, called the extractor electrode (the anode). Consequently, the sample surface, in contact with the grounded sample-holder, must be conducting. To circumvent this issue we explored the coating of our LSMO/YSZ nanostructured samples using different non-ferromagnetic metals: platinum, copper, and aluminum. In the following we explain the details of this strategy and some of the difficulties it introduces.

First of all, X-rays must get across the metal capping layer into the LSMO nanoislands without a significant intensity loss. Aluminum cappings are very common in electron emission microscopies precisely because they are highly transparent to X-rays, compared to other denser metals like copper or platinum. The latter, in turn, offers a greater conductivity. Fig. 5.5 (a) shows the attenuation length of X-rays*, impinging at a 16° angle with respect to the substrate horizontal, for Al, Cu and Pt, as a function of different photon energies in the 500 eV to 700 eV range [274]. We have chosen to plot this energy range because it comprises the manganese absorption edge. Additionally, we have selected the 16° X-ray incidence angle because it is the angle (±3°) used in the experimental set-up of our PEEM measurements . The larger this angle, the farther the X-rays will penetrate [see Fig.5.5 (b), plotted for the case of Pt]. From Fig. 5.5 (a) it is evident that X-rays penetrate long distances in Al, while for photons of 700 eV, Pt coatings larger than 15 nm produce a decrease in X-ray intensity above 37%. .

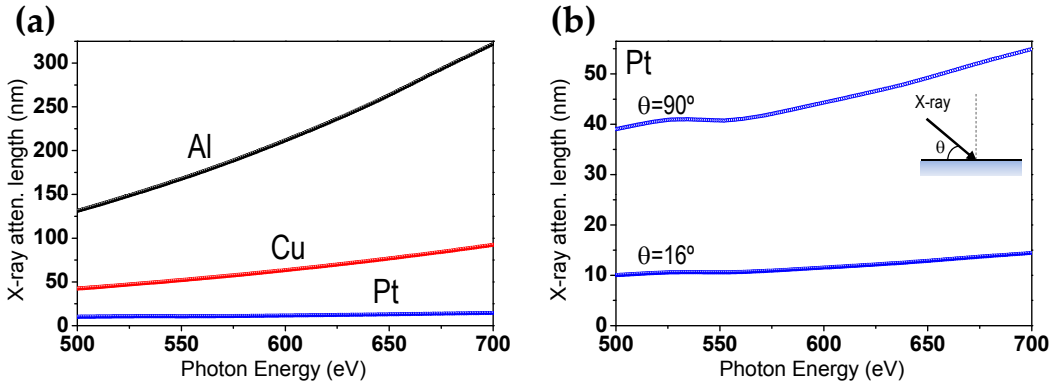


**Fig. 5.5:** *X-ray attenuation lengths as a function of photon energy, for energies in the 500-700 eV range. (a) Comparison for Al, Cu, and Pt coatings. The X-ray incidence angle was taken 16° with respect to the surface horizontal. (b) X-ray attenuation length notably increases with higher incidence angles. The plot shows the case for Pt at θ=16° and θ=90°.*

In order not to decrease the photon intensity substantially, therefore, we should keep the Pt coating thickness below 15 nm, below 50 nm in the case of Cu, and around a few hundreds of *nm* for Al. We knew from previous PEEM experiments in thin LSMO films [140] that a resistance of the order of 10 kOhms, measured with a two-probe tester, was sufficiently low to make the PEEM measurement feasible. For electron-beam sputtered

*X-ray attenuation length is defined as the depth into the material, measured along the surface normal, at which the X-ray intensity has decayed 1/e (∼37%) with respect to its value at the material surface.

Selecting an X-ray incidence angle of 16° is common procedure in PEEM experiments. It gives a compromise between having a large signal for in-plane magnetization and being able to detect out-of-plane magnetization components.

Pt layers, for instance, we achieved such values with ∼2-5 nm thick coatings. Hence, regarding photon penetration, the metallic coating does not hamper the measurement. The critical point, as we shall see next, relies in the great loss of collected electrons caused by the capping.

We already mentioned that PEEM is mainly a surface-sensitive technique, since only electrons ejected within a few *nm* from the sample surface will be able to leave the sample and reach the detector. Such electron *mean escape depth* ($\Delta$), in turn, depends on the inelastic mean free path ($\lambda_i$) of electrons (which is a material-dependent quantity), and of the electron emission angle ($\alpha$). This dependence is expressed as $\Delta = \lambda_i \cos\alpha$. The intensity due to the surface-emitted electrons, in turn, decays with the increasing capping thickness $t$ according to the exponential law [275]

$$I_S = I_S^0 e^{-\frac{t}{\lambda_i \cos\alpha}} \tag{5.5}$$

In reality, electrons also undergo elastic-scattering events that change their trajectories. To take into account such effects one needs to replace $\lambda_i$ with $L$, the *effective attenuation length*, which varies with sample thickness and emission angle [275]. In Fig. 5.6 we plot the decay of the electron intensity (in percents) as a function of the metal capping thickness for the three metals used (Al, Cu, Pt), and for two different electron energies i.e., 200 eV [Fig. 5.6 (a)] and 1000 eV [Fig. 5.6 (b)] . These energy values are far apart from each other and therefore set the boundaries for what the decay is like at intermediate energies.The detector, as in our experiment, is considered parallel to the substrate surface. Note also that two different emission angles, $\alpha$=0° and 55°, were considered. Recall that the electron mean escape depth varies with the emission angle, and that the majority of our nanoislands are square-base pyramids faceted in the (111) planes, hence at 55° from the substrate horizontal (see the schematic diagram at the top right corner of Fig. 5.6). The intensity decay is stronger for electrons leaving the sample at inclined angles than for normal emission ($\alpha$=0°). Aluminum is the metal showing the slowest decay, and Pt the most rapid, close to Cu in the case of slow electrons. Anyhow, the thickness values necessary to prevent an excessive loss of electron intensity are very low: for a Pt capping of $t$=2 nm the intensity falls to 10% in the case of 1000 eV electrons, and a capping as thin as $t$∼1 nm is required to achieve the same signal in the case of slower electrons. The best situation is found for Al capping, which allows the same intensity (10%) at twice the thicknesses (∼5 nm for 1000 eV). In addition to the loss due to the capping we should keep in mind that the electron intensity will first decay within the LSMO sample before reaching the metal overlayer. Fortunately, this decay is not as strong as in Pt; for the fastest electrons, an intensity loss of 90% corresponds to values of 4 and 6 nm, for $\alpha$=55° and 0°, respectively (not shown).

### Capping selection experiments

Copper and aluminum capping were performed at the BESSY Synchrotron facility, using the evaporator system and a separate chamber dedicated to sample sputtering and metal deposition available in the PEEM. The main advantage is the possibility of starting with very thin deposits, enter the sample in the PEEM, check whether it conducts, and, if not, realize further depositions and checks. The disadvantage is that, when the sample does

We have calculated these plots through simulations available from the NIST Electron Effective Attenuation Length Database [276]. These data are based on Eq. 5.5, revised as to take into account $L$ values instead of $\lambda_i$. They calculate the electron mean escape depth $\Delta$ values for a given $\alpha$, $L$ and $\lambda_i$.

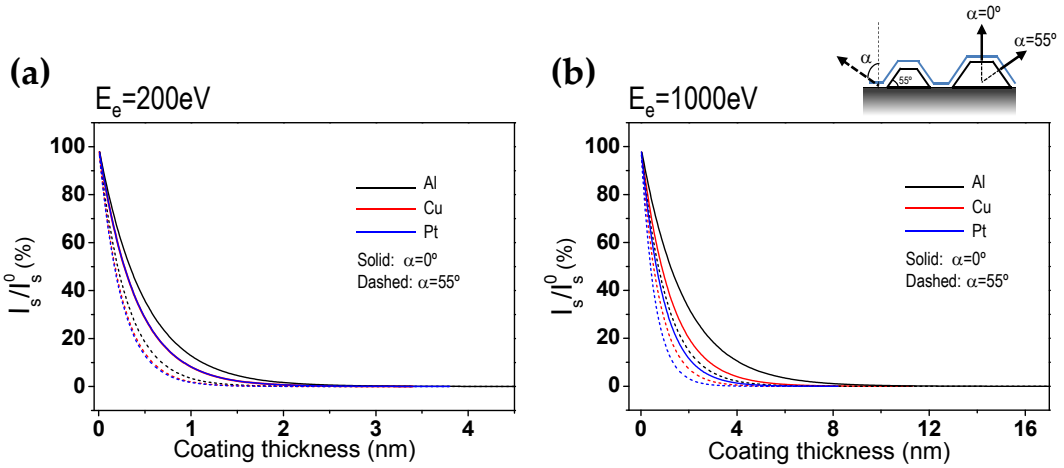


**Fig. 5.6:** *Relative decay of the emitted electron intensity as a function of the coating thickness for 200 eV (a) and 1000 eV (b) electron energies. Al, Cu and Pt capping and two possible emission angles $\alpha$=0° (solid lines) and $\alpha$=55° (dashed lines) are considered. The sketched diagram at the top right corner illustrates the geometry of such emission processes.*

not conduct, we cannot know whether the thickness is insufficient, or whether the problem stems from the lack of electrical contact between the sample-holder cap and the sample surface. To verify this, we need to remove the sample from the chamber (thus first undo the vacuum), check the contact, reposition the cap in the case cap and sample do not make electrical contact, and re-insert the sample in the PEEM. These checks require successive venting and pumping down of the load-lock chamber, and ensuring the ultra-high vacuum (UHV) chamber does not lose its vacuum. On the other hand, Pt-coated samples were electron-beam evaporated *ex-situ* (at the Scientific Services of the UAB, Barcelona). Thus, the sample was known to make electrical contact before introducing it into the PEEM. In turn, we could not a priori ascertain whether the capping was too thick to be able to detect any signal until the PEEM measurement was performed.

Among the series of experiments we made to optimize the capping experiments for enhanced PEEM signal, *ex situ* evaporated *platinum* yielded the best results. The next sections will in fact be based on Pt-coated samples. *Copper* capping, starting from $t$=1 nm up to 5 nm layers did not work: the initial thin layers (1-1.5 nm) produced sparks in the PEEM, indicative of sample charging, i.e., of insufficiently conducting capping. Moreover, these sparks did not disappear with increasing coating thickness. This suggests that such sparks removed part of the Cu layer producing a rough surface with possible bare substrate spots that did not improve in quality upon further Cu deposition. Regarding *aluminum*, this was a priori the best option, according to the X-ray attenuation length and the electron intensity decay studies described above (Figs. 5.5 and 5.6). However, the strong tendency of Al towards oxidation (its oxidation potential is the highest of all elemental metals except K, Ca, Na and Mg) can trigger depletion of oxygen from the LSMO upper layers, with the consequent loss of ferromagnetism [277].

To prevent the Al-triggered LSMO de-oxigenation, we deposited 1.5 nm of Cu prior to the 5 nm Al capping. Fig. 5.7 (a) shows a PEEM 5 µm field of view (meaning 5 µm diameter) image of a LSMO/YSZ nanostructured sample, taken at E=639.2 eV. The image is normalized first by subtracting the detector background image, and second, with the

subtraction of an image taken at the pre-edge of the Mn $L$-edge. The latter is often used to enhance the signal from a particular element [266] and will be invariably applied in all of the PEEM images shown hereafter. A bright contrast emerges from the island structures as opposed to the dark YSZ substrate, indicating the presence of Mn within the islands. Fig. 5.7 (b) displays the TEY XAS for the Mn $L$ edge, obtained by integrating the intensities within a certain area, selected from the image of Fig. 5.7 (a), for a stack of images running from the Mn $L$ pre-edge (635 eV) up to 660 eV in the present case. The XAS in the top row of Fig. 5.7 (b), very noisy, corresponds to a single island, with area around (166 $\times$ 120) nm$^2$, comprising $\sim$126 pixels. If we sum the contribution of a large number of spectra, which is done by selecting simultaneously a large number of islands, the signal to noise ratio of the resulting *averaged* spectrum increases substantially, revealing more detailed absorption features. Note that the highest peak corresponds to E=639.2 eV, precisely the energy at which the island contrast is brightest.

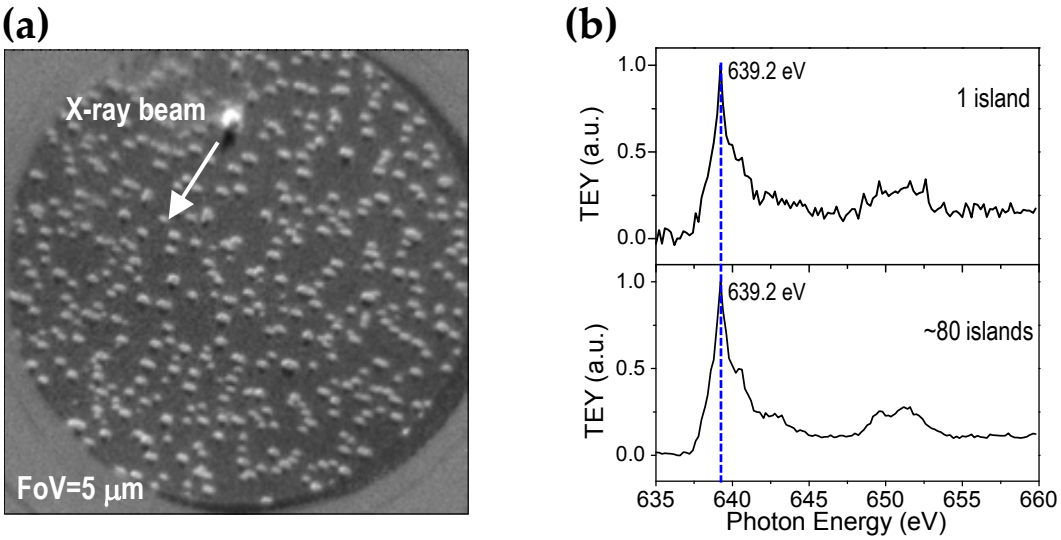


**Fig. 5.7:** *(a) PEEM image at E=639.2 eV of a LSMO on YSZ nanostructured template coated with 1.5 nm Cu (in contact with the sample surface) and 5 nm Al. Field of view FoV=5 μm. (b) XAS of the Mn $L_{2,3}$-edges obtained for a single nanoisland (top panel) and for a large number of them (lower panel). The integration of many nanoislands largely increases the signal to noise ratio.*

The difference between the XAS of Fig. 5.7 and that corresponding to stoichiometric $La_{0.7}Sr_{0.3}MnO_3$ (LSMO), in Fig. 5.3, is remarkable. Although we can recognize some features from the ferromagnetic LSMO spectrum in Fig. 5.7 (b), such as the presence of the double-step background, the general shape of the two spectra differ notably. Moreover, in measurements on LSMO ferromagnetic thin films done the same day under identical experimental conditions, the Mn $L_3$ edge was found at $\sim$641 eV, well above the energy shown by the highest peak in Fig. 5.7 (b) (639.2 eV) . Our results hence indicate a departure from the $Mn^{3+}/Mn^{4+}$ valence composition expected for LSMO. A peak in the XAS at lower energies than the main $L_3$ peak has been identified in the literature as the fingerprint of $Mn^{2+}$ in the case of de-oxygenated LSMO and LCMO surfaces [278–281]. In these works, the presence of $Mn^{2+}$ appears superimposed to the original $Mn^{3+}/Mn^{4+}$ composition (i.e. coexisting with the ferromagnetic manganite). Also, the $Mn^{2+}$ is predominantly related to

The energy resolution was kept at 0.1-0.3 eV for the majority of the spectra.

the film surface and grain boundaries, i.e. the places more likely to suffer the effect of atmosphere exposure, defects...etc. The $Mn^{2+}$ fingerprint of our spectra is even more evident, suggesting that the de-oxidation of LSMO in our case is more pronounced; this, in turn, would reduce the fraction of $Mn^{3+}/Mn^{4+}$ consequently destroying the ferromagnetism of the compound. Effectively, no XMCD signal could be measured for this sample. In Fig. 5.8 we compare our data (bottom graph) with the XAS for the Mn $L$ edge in two cases having purely $Mn^{2+}$. Our results agree much better with this latter spectra than with the spectrum for LSMO in Fig. 5.3. We can therefore conclude that the copper coating does not prevent the LSMO de-oxidation caused by the Al capping.

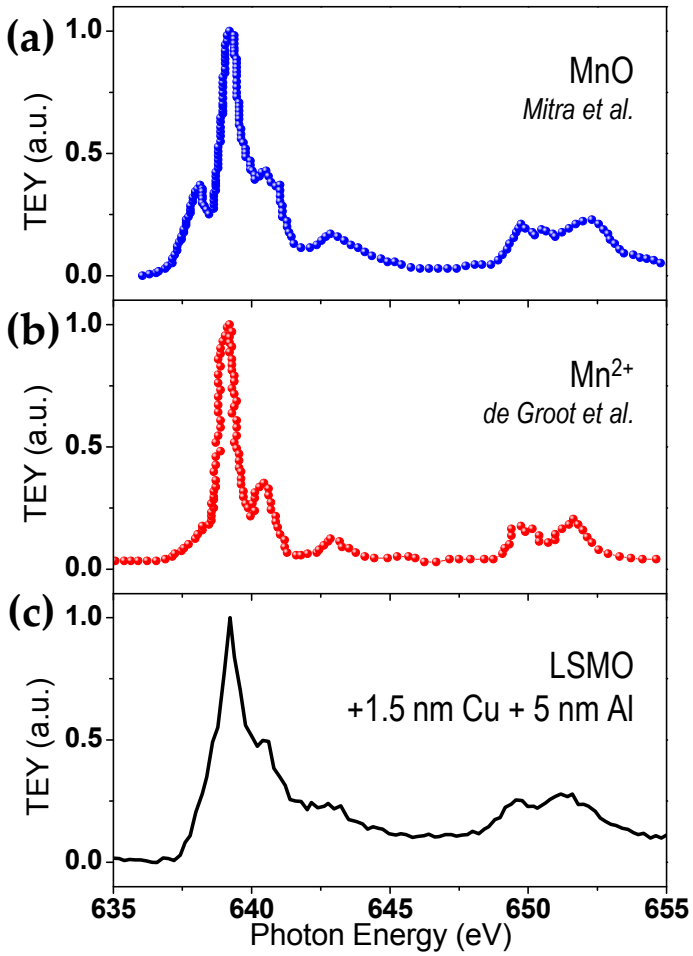


**Fig. 5.8:** *Mn L-edge XAS for (a) MnO compound [282], (b) $Mn^{2+}$ in a cubic crystal field, with field splitting of 0.6 eV [283], (c) LSMO on YSZ nanostructured sample with 1.5 nm Cu + 5 nm Al capping.*

Based on the above study we discarded the copper and aluminum cappings for further measurements. Therefore, the following analyses are focused on platinum-coated samples, with estimated thickness between 2 and 4 nm.

### 5.1.3 Chemical analysis: probing the nanoscale chemical features

**Surface and bulk composition of LSMO nanoislands**

The images in Fig. 5.9 were taken at the Mn $L_3$-edge (E=641.3 eV). The 5 μm field of view PEEM image shown in Fig. 5.9 (a) reveals a dispersion of black spots on a gray background. The digital zoom (below) shows that these dark dots have elongated shape in the direction of the illuminating X-rays. Moreover, one can also notice that the black dot is accompanied by a slightly brighter contrast. This image is the result of merging 10 images taken at the same energy, and the only normalization done is against the detector. By further subtracting the background image acquired at the Mn $L$ pre-edge, we significantly enhance the contrast, as evidenced by Fig. 5.9 (b). The dark spots are still there, but now the bright contrast can also be clearly perceived.

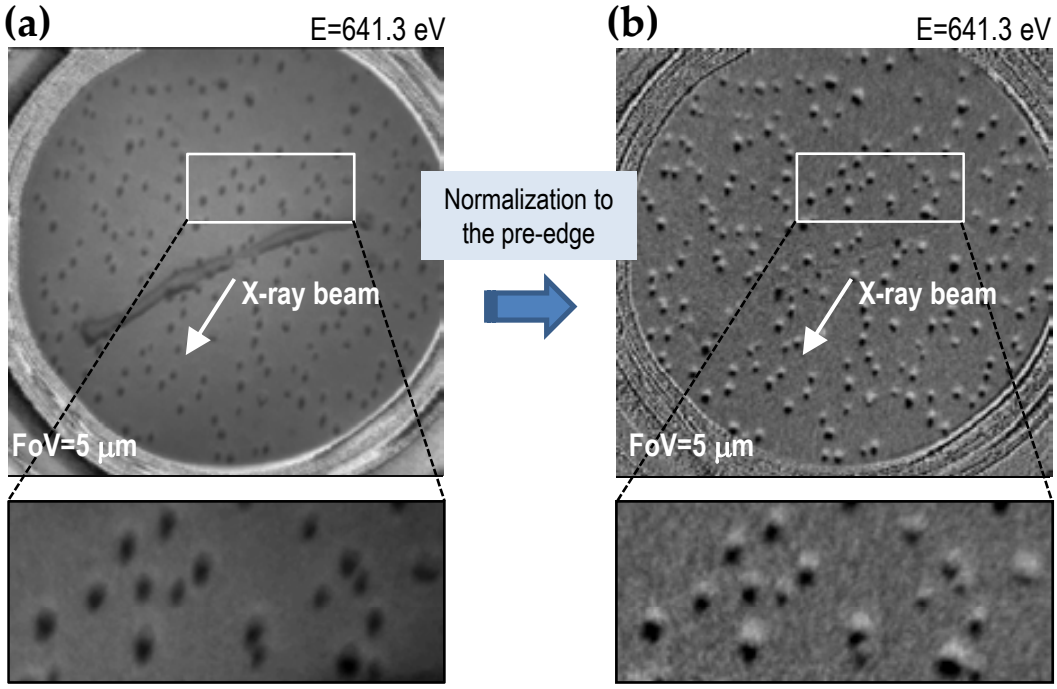


**Fig. 5.9:** *PEEM images (5 μm field of view) of a Pt-coated LSMO nanostructured sample taken at the Mn L-edge. They are the result of merging 10 images. (a) After subtracting the detector image. (b) After further subtracting the Mn L- pre-edge image.*

By illuminating our sample with X-rays at the Mn $L$-edge energy, we expect the Mn-rich regions to give a bright contrast, indicative of the $2p \quad 3d$ transition and of the subsequent secondary electron emission (see section 5.1.1). In Fig. 5.9 we do, in fact, observe bright spots, but these appear linked to a black *shadow*, which is even easier to see [Fig. 5.9 (a)]. The spatial distribution of the structures and their lateral sizes are in agreement with what one expects from the topology of the self-assembled LSMO nanoislands, which we checked with AFM beforehand. The presence of the island *shadow*, in turn, is the consequence of the X-rays 16° grazing angle with respect to the sample surface. PEEM investigations of nanoislands, although still very scarce and mostly involving semiconductor nanocrystals, have already identified the shadow effect, which is caused by low X-ray

incident angles on *nm* size objects [284–286]. Beyond considering the impact of such geometrical effects on the intensity of XAS spectra [284], however, no further importance was ascribed to the presence of the island shadow. Fig. 5.10 (a) shows the same PEEM data as Fig. 5.9 (b), using a different color scale to better distinguish the *island* and *island-shadow* features. Blue corresponds to the highest TEY values (island) and red to the lowest (shadow), with white in between. In Fig. 5.10 (c) we plot the laterally resolved spectra obtained from integrating the selected areas in (b) for a number of images running from the Mn $L$ pre-edge up to the post-edge. While the top graph in Fig. 5.10 (c) shows the expected absorption spectrum, the bottom graph displays the reversed Mn $L_{3,2}$ edges characteristic of a transmission experiment. The origin of these two information sources, simultaneously obtained in our case, relies on the experiment geometry, as we will discuss next.

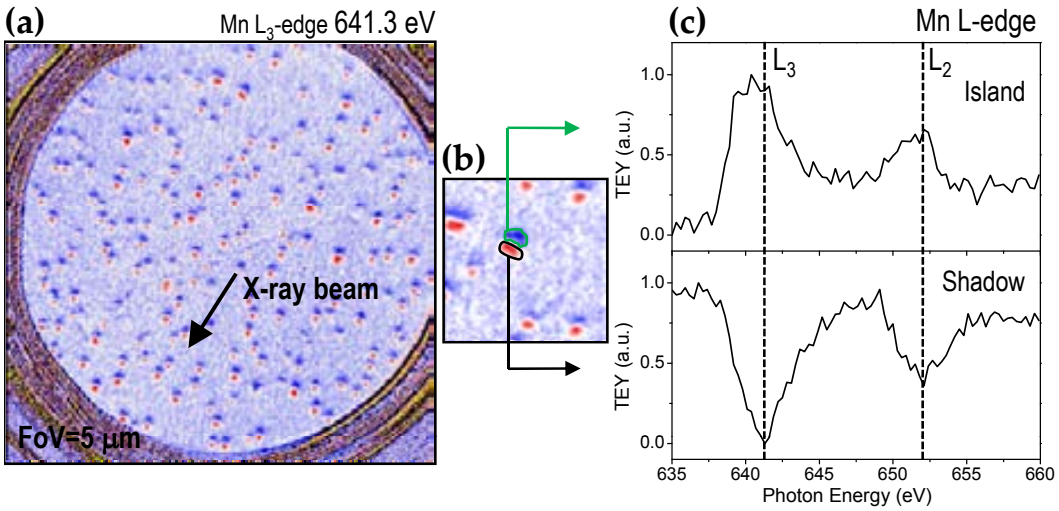


**Fig. 5.10:** *(a) PEEM image from Fig. 5.9 (b), displayed now with a blue-red color scale. Blue corresponds to bright contrast (enhanced TEY signal) and vice versa. (b) Island and island-shadow regions for a single nanostructure. (c) Laterally-resolved spectra corresponding to the island and island-shadow regions marked in (b).*

We plot the schematic diagram of our experimental configuration in Fig. 5.11 (a). The light impinges on the island at a 16° angle, goes through the Pt coating (not drawn to scale) and part of it passes through the whole nanoisland reaching the opposite side. The LSMO nanostructure in the sketch exhibits the 55° inclined (111) facets, as in the real case, and its proportion (lateral size $D$=3.5 times the island thickness) is also within the measured nanoisland aspect ratio statistics. When the energy of the X-rays matches the Mn $L$-edge, absorption processes occur throughout the entire island, triggering the cascade of electrons that produce the TEY signal. Because of the small mean escape depth of electrons, especially in Pt, many of them won't be able to leave the island; only very few, the most superficial of the LSMO island, will escape and be collected to form the image. Meanwhile, the X-rays will have traversed the entire island since the attenuation length of X-rays is much larger than the electron escape depth. In the process, however, the Mn atoms located deep within the bulk of the island will undergo the same absorption processes we just mentioned. The result of such a large number of photons being absorbed is that the light that reaches the other end of the structure is less intense. And it is more or less intense depending on the degree of absorption suffered in the bulk, i.e. depending on the energy value.

This is precisely what happens in a transmission experiment. Therefore, due to the grazing incidence, we have the negative image of what happens in the island bulk. The secondary electrons that do not come from the Mn-rich places form the grayish background, with much smaller intensities. At the shadow places, however, the electrons that reach the detector are less than those coming from the background, simply because the X-ray intensity reaching that places is less.

In brief, thanks to the grazing angle of light, which permits some rays to reach the substrate surface at the opposite end of nanoislands, we have access to the chemical information of the *bulk* of the nanostructure. The Pt capping, although greatly reducing the incoming signal, further restricts the information depth of the TEY signal to the very *surface* of the island. The latter, instead of a limitation, appears in the present case as an advantage, because it gives us access to the information of the island surface, which is complementary to the bulk characterization obtained by the transmission results. In Fig. 5.11 (b) we plot the result of integrating both island and island-shadow areas, as we did in Fig. 5.10 (c), but now for a total of ∼85 nanostructures in order to enhance the signal to noise ratio [we have also reversed the transmission spectrum (bottom panel) to better compare its features with the spectrum from the nanoisland surface (top panel)]. Let us once more underline that we identify the *island* (bright and blue contrasts in Figs. 5.9 and 5.10, respectively) with the *surface* information, and the *shadow* (dark and red contrasts in Figs. 5.9 and 5.10, respectively) with the *bulk* information. The *bulk* spectrum in Fig. 5.11 (b) displays the shape of the expected Mn $L_{2,3}$ edges XAS for $Mn^{3+}/Mn^{4+}$ composition according to the 0.7:0.3 La-Sr ratio in $La_{0.7}Sr_{0.3}MnO_3$. It is remarkable its good agreement with the XAS for $La_{0.7}Sr_{0.3}MnO_3$ reported by de Jong et al. [278]. In contrast, the *surface* spectrum displays larger differences. In addition to being noisier (the intensity counts were ∼43% of the intensity of the bulk spectrum) it also shows a new peak at around 639.5 eV, which does not appear in the bulk spectrum.

In the previous section we discussed the peak at low energy of the Mn $L$-edge spectrum (∼639.2 eV) in terms of $Mn^{2+}$ formation due to the aluminum capping. At variance with that sample, where the $Mn^{2+}$ signal was dominant, the results here show that the low energy (∼639.5 eV) peak is a secondary feature superimposed to the characteristic bulk LSMO spectrum. Meanwhile, the nanoisland bulk shows no traces of such low-energy peak, as confirmed by the transmission spectra. Hence it appears that, in agreement with previous experiments [279, 280], if that peak is related to the $Mn^{2+}$ ion, its presence is limited to the surface, where it coexists with the $Mn^{3+}/Mn^{4+}$ mixed valence composition. Moreover, $Mn^{2+}$ formation, which occurs at expenses of destroying the $Mn^{3+}/Mn^{4+}$ stoichiometric ratio in $La_{0.7}Sr_{0.3}MnO_3$, is expected to decrease the ferromagnetic signal of the compound. Therefore, its presence can be related to the ferromagnetic dead layer concept already introduced in Chapters 3 and 4. In other words, the loss of ferromagnetic signal observed in manganite nanoislands on YSZ (with respect to bulk LSMO), which we argued in terms of the generally accepted concept of a surface/interface dead magnetic layer, could be rooted in the presence of $Mn^{2+}$. It should be noted, nevertheless, that the subtraction of the bulk spectrum from that associated to the surface did not yield as clear a $Mn^{2+}$ fingerprint as the ones reported in the literature [279, 280] (not shown). It turns out that the signal from the surface is too weak and noisy with respect to the bulk signal to be able to discern a clean signal.

The origin of $Mn^{2+}$ ion was claimed to be related to oxygen vacancies found at the surface [280]. In turn, the surface de-oxygenation was explained as a consequence of

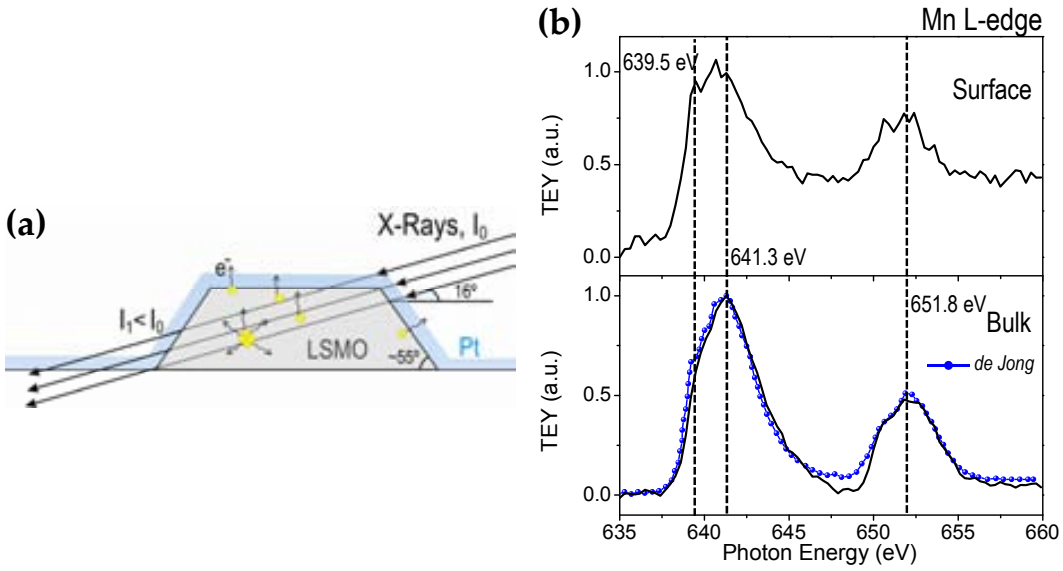


**Fig. 5.11:** *(a) Schematic diagram of the X-rays impinging at 16° on a LSMO nanoisland. The yellow circles illustrate absorption events from which electron cascades are generated. The X-rays that manage to cross the entire island are less than those at the beginning. (b) The particular experiment geometry enables discerning island surface and island bulk XAS for the Mn, averaged among ∼85 islands in these particular graphs. The reported XAS corresponding to the $Mn^{3+}/Mn^{4+}$ ratio in $La_{0.7}Sr_{0.3}MnO_3$ [278] has been plotted for comparison.*

vacuum annealing [278, 280], or of reduction processes during ambient exposure to CO [281]. Other origins of spectral variations in the Mn $L$-edge were ascribed to changes in the $Mn^{3+}/Mn^{4+}$ ratio and in the crystal field strength [283]. Our results suggest that a certain amount of $Mn^{2+}$ is present at the surface of nanoislands, but a number of tests, left for future work would be needed to ascertain such hypothesis. One could i) check whether upon annealing under different oxygen partial pressures the low-energy peak changes, ii) perform the PEEM experiment on different days and check for variations in the ambient-sensitive $Mn^{2+}$ peak (the present measurements were performed two months after the sample synthesis), iii) check the low energy peak of the oxygen $K$-edge (∼530 eV), which is related to the hybridization of O $2p$ orbital with the Mn $3d$ orbitals. A hypothetical decrease in the intensity of such peak could be related to a higher $3d$ level occupancy due to the presence of $Mn^{2+}$. In fact, we did attempt this latter study but our oxygen spectra did not yield any useful information, mainly due to the small intensities we were dealing with. Also, note that mirrors (and other objects along the beam trajectory towards the sample), have oxygen contamination: the oxygen spectral features of our sample were thus not clearly discernible from those caused by absorption processes before reaching the sample.

### Comparison of $(001)_{\mathrm{LSMO}}$ and $(111)_{\mathrm{LSMO}}$ nanoislands

One of the strengths of PEEM regarding nanostructured samples is that, because of its space resolution, it allows one to identify, select, and study distinct features. We exploited this potential for the individual study of the spectral shapes corresponding either to $(001)_{\mathrm{LSMO}}$-oriented and $(111)_{\mathrm{LSMO}}$-oriented nanoislands. The former constitute the majority of the population, with square-base truncated pyramidal shape and $(111)_{\mathrm{LSMO}}$ inclined facets [we

referred to them in the description of the shadow origin in Fig. 5.11 (a)]. The $(111)_{\mathrm{LSMO}}$ nanoislands, by contrast, are the triangular-base nanoislands, which we have already introduced in the previous chapters. As they are different both in morphology and crystal structure, we aim now at verifying whether there is a sizable difference in their chemistry. Fig. 5.12 (a) shows a PEEM image taken at the Mn $L_3$-edge with circularly polarized light. We show this image because it facilitates the identification of nanoislands in terms of square or triangular. The XAS data displayed in Fig. 5.12 (c), however, are calculated from measurements with linear polarized light, the same kind of measurements done to calculate the XAS data shown in Figs. 5.10 and 5.11. Islands that could be distinguished unambiguously are marked in red (square nanoislands) and blue circles (triangular nanoislands) in Fig. 5.12 (a), and are the ones used for building the laterally-resolved spectra on the right. The small differences between squares and triangles we can observe in the spectra of Fig. 5.12 (c) spectra are of the same order as the differences that arise from one individual island spectrum to another, regardless of its geometry. Thus, no measurable differences emerge from the Mn spectra of these two types of nanostructures. Note that, although a little noisier, the Mn island surface and bulk $L$-edges here presented show the same trends as depicted in the previous XAS analysis.

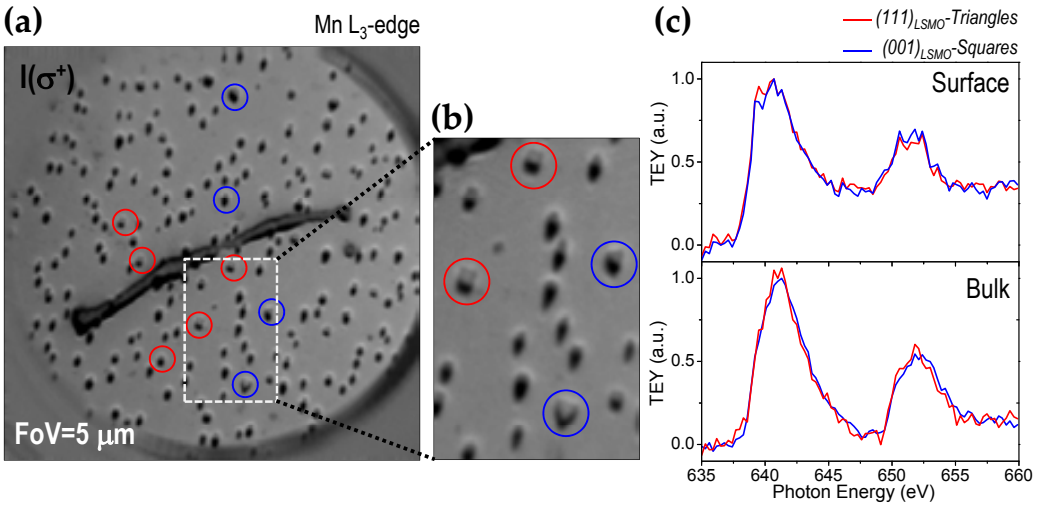


**Fig. 5.12:** *PEEM analysis of $(001)_{LSMO}$ and $(111)_{LSMO}$-oriented LSMO nanoislands reveals no differences in their chemistry. (a) 5 µm field of view image taken at the Mn $L_3$ edge with circularly polarized light. A few recognizable square and triangular islands appear within red and blue circles, respectively. (b) Enlarged image of the area marked with dashed lines in (a). (c) Mn L-edge XAS corresponding to the square and triangular islands, further separated in terms of their surface and bulk contributions.*

### La $M$-edge

Contrary to the Mn $L$-edge, the XAS features of the lanthanum $M$-edge, which involves $3d_{5/2}$ $3d_{3/2}$ $4f$ transitions, reveal little of the specific chemical composition of LSMO. This is mainly because of the great valence stability of the lanthanum ion, which exhibits a single oxidation state, $La^{3+}$. Fig. 5.13 (a) shows the PEEM image, after normalization, taken at the La $M_5$-edge. As for Mn, this image is also the result of 10 merged images. The

XAS at the right side show the surface (top panel) and bulk (bottom panel) contributions obtained by selecting either *island* or *shadow* regions, respectively. We have also plotted the TEY spectrum from the literature corresponding to lanthanum in $LaAlO_3$, where La displays the same 12-fold coordination as in LSMO [287]. One can notice that there is a considerable difference between the intensities of the $M_5$ and $M_4$ peaks. Otherwise, the main information we extract from the lanthanum XAS is the presence of La on the substrate surface. This is consistent with the observation that the substrate exhibits residual material in the form of small dots [see the AFM topography image in Fig. 5.13 (c)]. As we saw in Chapter 3, such material diffuses towards the islands upon longer annealing times and higher temperatures.

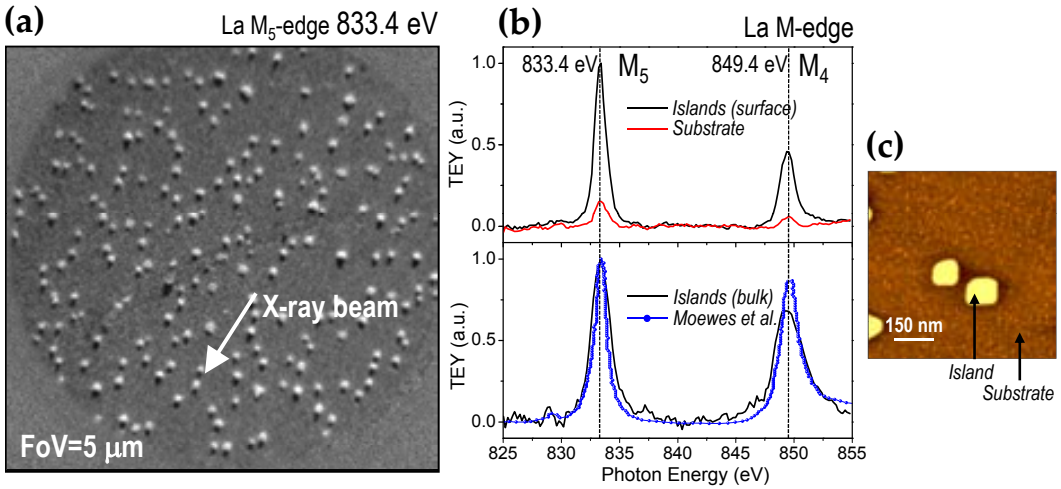


**Fig. 5.13:** *(a) PEEM 5 µm field of view image taken at the La $M_5$-edge showing the bright and dark contrasts characteristic of our experiments. (b) La M-edge XAS of the island surface (top panel) and bulk (bottom panel). The absorption spectra show no significant differences. A La M-edge for $LaAlO_3$ is also plotted for comparison [287]. Analysis of sites without islands reveal the presence of lanthanum on the substrate surface. This is in agreement with the AFM study of the sample (c), which reveals residual material on the substrate surface.*

In summary, throughout this section we have investigated the manganese $L$-edge XAS of LSMO self-assembled nanoislands on YSZ. The small nanoisland sizes ($t$ below ∼40 nm and $D$ below ∼200 nm), along with the X-ray 16° incidence angle, have made the nanoisland surface and its bulk contribution separately accessible. Thanks to this fact we can confirm that the majority of the island, corresponding to the bulk contribution, displays the manganese XAS expected for bulk LSMO. Hence this result supports our assumption, in the previous chapters, that the ferromagnetic signal obtained from SQUID and MFM measurements effectively stems from the actual $La_{0.7}Sr_{0.3}MnO_3$ compound. Meanwhile, a certain de-oxigenation has been detected on the surface of the nanoislands, evidenced by means of a slight peak at low energy values, which suggests $Mn^{2+}$ formation. This could be related to the loss of magnetic moment obtained from macroscopic SQUID magnetometry, i.e. to the dead layer concept we introduced in previous chapters. The individual chemical analysis of $(001)_{\mathrm{LSMO}}$ and $(111)_{\mathrm{LSMO}}$-oriented nanoislands, has shown that no detectable differences exist between the two populations. Finally, lanthanum $M$-edge XAS has shown no remarkable features but for the detectable presence of La on the YSZ substrate. The latter is in agreement with the presence of small particles between the LSMO

nanoislands shown by AFM measurements.

### 5.1.4 Magnetic analysis: the limits of XMCD in nanoscale metal-coated LSMO nanoislands

Now that we have investigated the absorption spectra for individual and LSMO nanoisland ensembles, we move on to study their magnetism. As we explained in section 5.1.1, we collect PEEM images at the Mn $L$-edge with circular-polarized light of opposite helicities. The result of subtracting two images taken with opposite helicities, the so-called *asymmetry image* (Eq. 5.4), will reveal the ferromagnetic contrast present in our sample. One should keep in mind that the intensity of such contrast goes like $I \sim I_0 \cos\alpha$, with $\alpha$ the angle between the sample magnetization vector and the light helicity vector. Hence, if the magnetic moments, despite being in-plane, they are oriented 90° with respect to the X-rays, the contrast will be null. In order to enhance the contrast as much as possible, we saturate the samples in-plane, prior to inserting them in the PEEM chamber, using a 1 T permanent magnet. Then, in remanence after retiring the magnet, we place the sample in the magnetic sample-holder, making sure that the saturation direction is parallel to the in-plane projection of the 16° impinging light. Fig. 5.14 shows a schematic diagram of how the sample is located with respect to the X-rays and to the coils of the magnetic sample-holder.

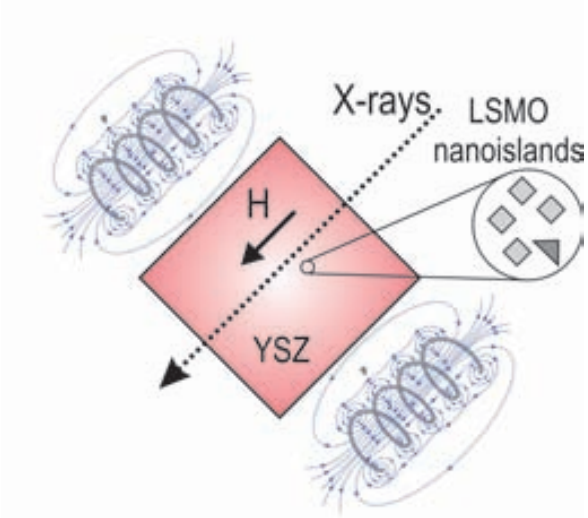


**Fig. 5.14:** *Illustration of the sample placed with respect to the incident X-rays and to the magnetic field H generated by the sample-holder coils.*

#### XMCD at room temperature

Our LSMO/YSZ self-assembled nanoislands are ferromagnetic, as we have seen by SQUID magnetometry and MFM. Fig. 5.15 shows the hysteresis loop, at 300 K, of the 0.03 M 900°C heat-treated LSMO/YSZ nanostructured sample that we will study with PEEM. We place it on the sample-holder with no applied field. Considering the magnetic volume derived from the estimated thickness ($t_{eq}$∼3.5 nm), the magnetization takes a value of ∼308 kA/m

at saturation ($\sim 2.7\times10^{-5}$ emu, see Chapter 3). At zero applied field, in contrast, the magnetic moment value falls a $\sim 80\%$ from its saturation value, i.e. down to $\sim$57 kA/m. A maximum field of $\pm$178 Gauss was applied for room temperature measurements. For these field values, according to the macroscopic magnetization loops, the magnetic moment exhibits a value of 1.9 $(\pm 0.1)\times10^{-5}$ emu ($\sim$217 kA/m); the $\pm$0.1 error stems from whether we are on the upper or lower branch of the loop. Hence, the drop from saturation is now of $\sim 30\%$. Although notably improving with respect to the remanence regime, we do not achieve complete saturation of the sample with these fields.

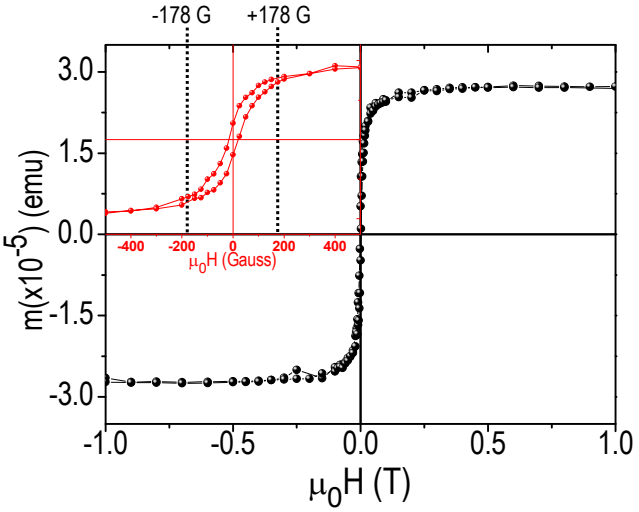


**Fig. 5.15:** *Magnetic moment vs. magnetic field hysteresis loop at 300 K for the LSMO/YSZ nanostructured sample measured by PEEM (0.03 M, 900°C heat-treated). The field was applied in-plane. The augmented view of the center region is displayed on the inset, in red. The signal decrease from saturation is of $\sim 80\%$ for remanence, and of $\sim 30\%$ for the maximum 178 G applied field within the PEEM.*

The result of XMCD measurements in **remanence** are shown in Fig. 5.16. For each XMCD image (1 stack), we recorded 60 images with one helicity and other 60 images with the opposite helicity, with an exposure of $\Delta t$=3 s per image. Fig. 5.16 (a) displays the PEEM image at the Mn $L_3$-edge taken with left-handed circular polarized light, after merging 7 different stacks collected in the above mentioned way. Thus, Fig. 5.16 (a) is the result of averaging 420 images. To this image we subtract the opposite helicity image, identically obtained, which yields the XMCD image of Fig. 5.16 (b). In the red-blue color scale, red indicates magnetic moments $m$ oriented antiparallel to the X-rays (negative contrast), and blue means that $m$ is parallel to the incident light direction (positive contrast). White indicates no magnetic contrast.

Some of the nanoislands evidenced by small squares in Fig. 5.16 (a) appear in the corresponding XMCD image as dark-blue spots, which is the evidence of the ferromagnetic nature of islands. A careful inspection of the images allowed us to determine that the blue contrast in Fig. 5.16 (b) stems from the shadows of Fig. 5.16 (a). Recall that the intensity of the transmitted signal (the shadow) is twice as large as the intensity coming from the island surface. Hence, it is reasonable to think that the signal we observe is in fact the difference between the two more intense signals, i.e. those coming from the transmission. Note that, since the transmission signal is identical but opposite in sign to the absorption

signal, the XMCD will also be opposite in sign. In other words, if blue contrast means magnetic moments parallel to the incident light, the islands we observe in Fig. 5.16 (b) are magnetized antiparallel to the X-rays. The line scan across an individual nanoisland, Fig. 5.16 (c), shows that the amplitude of the signal is only ∼3.3 times the noise peak-to-peak amplitude, despite the large number of scans we have averaged. Regarding the XAS measurements, the intensity signal we measured was barely a 5% of the total available intensity, due to the Pt coating. The magnetic signal is now a ∼20% of that 5%, i.e., a ∼1% of the total signal. We are therefore very close to the detection limit.

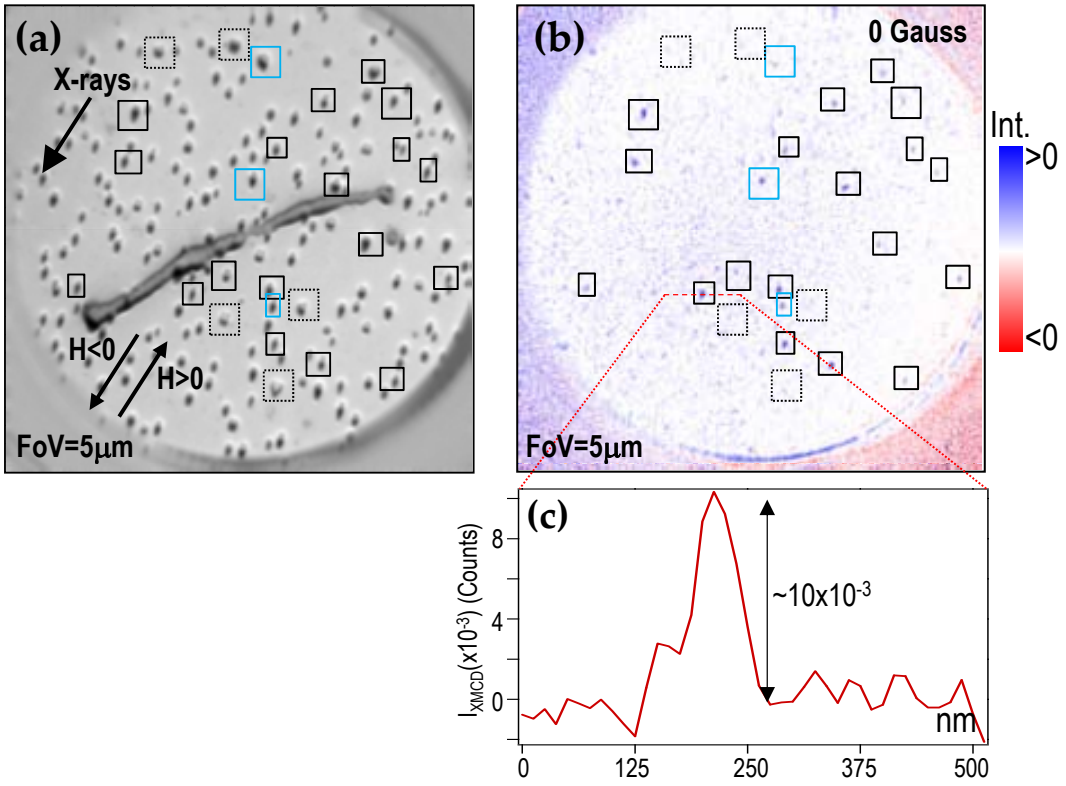


**Fig. 5.16:** *(a) 5 μm field of view PEEM image taken with left-handed circular polarized light. (b) Remanence XMCD image of the region in (a), after ex-situ saturation of the sample. The islands giving ferromagnetic contrast are marked inside black squares. Some examples of large islands giving no XMCD signal are indicated with dashed-line squares. Within light-blue squares we have marked a few islands showing simultaneous blue and red contrast (see text). (c) Line profile showing the intensity of the signal at one of the blue-contrast islands (red dashed line in (b)).*

We know from SQUID magnetometry that the magnetic signal in remanence is very low, ∼57 kA/m. By XMCD too, it appears that few of the islands (in blue) are contributing to the magnetic signal parallel to the initial saturation field. We cannot properly tell the inner distribution of the magnetic domains in such islands, e.g. whether they are single domain or multidomain, because of the limited resolution. This limit can be estimated by the smallest lateral size of the observed contrasts, which is around ∼150 nm [see Fig. 5.16 (c)]. Considering the exceedingly small signal, and the loss of precision in the island shapes caused by the Pt capping, even achieving such a resolution is quite remarkable. Other islands give no contrast, presumably because their magnetic moments are oriented

90° with respect to the incident light. Finally, a few islands displaying both blue and red contrast have been marked inside light-blue squares in Fig. 5.16 (b). Note that this *double contrast* is related to individual islands, i.e. from the correspondence between Fig. 5.16 (a) and Fig. 5.16 (b) we can rule out the possibility that it might originate from two different adjacent nanostructures with opposite magnetic moments. In fact, there are no isolated red islands: in remanence, none of the islands have reversed magnetization. The red contrast we observe appears next to the blue contrast of the same island. Such a contrast fits well with an in-plane swirling magnetic configuration, i.e. with a vortex flux-closure state. We shall come back to this point later on.

By applying **in-plane magnetic field** we expect to change the magnetic configuration of the LSMO nanoislands. From the averaged SQUID data (Fig. 5.15) we expect a significant increase in the magnetization signal with applied magnetic field; such increase should be somehow reflected in the XMCD contrast. Fig. 5.17 (a) shows the XMCD image, at the Mn $L_3$-edge, that results under an in-plane applied field of 178 Gauss. Since the contrast we observe is positive we know from $I \sim I_0 \cos(\alpha)$ that magnetic moments and incident X-rays are parallel. As these magnetic signal comes from the *island shadow*, however, what we have in reality is the magnetic field applied anti-parallel to the X-ray beam. Note that, compared to Fig. 5.16, a greater number of dots appear with the blue contrast here: the magnetic field enhances the alignment of the magnetic moments. However, the contrast is quite weak and noisy. This is because the images in Fig. 5.17 are averages of two stacks of images, instead of the seven stacks used for Fig. 5.16. When we switch the applied field direction, Fig. 5.17 (b), we observe a reverse in the contrast: nanoislands are now seen as red spots. This provides further evidence on the ferromagnetic origin of the contrast. The line scans below each PEEM image display this reversal in terms of a change from positive to negative signal, implying that the relative orientation of magnetic moments with respect to the light has reversed.

It is also noteworthy that Fig. 5.17 (b) appears noisier than Fig. 5.17 (a) (the red spots are harder to detect from the background). This loss of contrast is further evidenced in the decrease of intensity (from $14\times10^{-3}$ to $10\times10^{-3}$) observed in the line scan. A possible reason for this loss could be that the field we are applying is not really -178 Gauss but somewhat less, caused by some remanent magnetic field at zero applied current. Another source of contrast loss could be some kind of *sample damage* due to the prolonged exposure of the region to continuous radiation. This particular region was exposed to no less than 1.5 h of X-ray irradiation, since the first image of Fig. 5.17 (a) until the last of Fig. 5.17 (b). We shall discuss this point in the following.

#### In uence of X-ray irradiation time on the XMCD signal

A potential loss of magnetic signal with increasing X-ray sample irradiation is not a minor issue. We cannot expect to address physical changes in the magnetic signal of our LSMO nanoislands with varying magnetic field, if such variations are, in part, due to the signal degradation caused by X-rays.

Fig. 5.18 displays the lower left-corners of the images that comprise the XMCD image of Fig. 5.16 (b) (recall that the latter is the result of merging 7 XMCD images collected in sequence). Each of the 7 images of Fig. 5.18 have a line scan corresponding to one individual island. We observe that there are fluctuations in the intensity of the magnetic signal of the island investigated, but these are random fluctuations, i.e. there is no monotonic decay

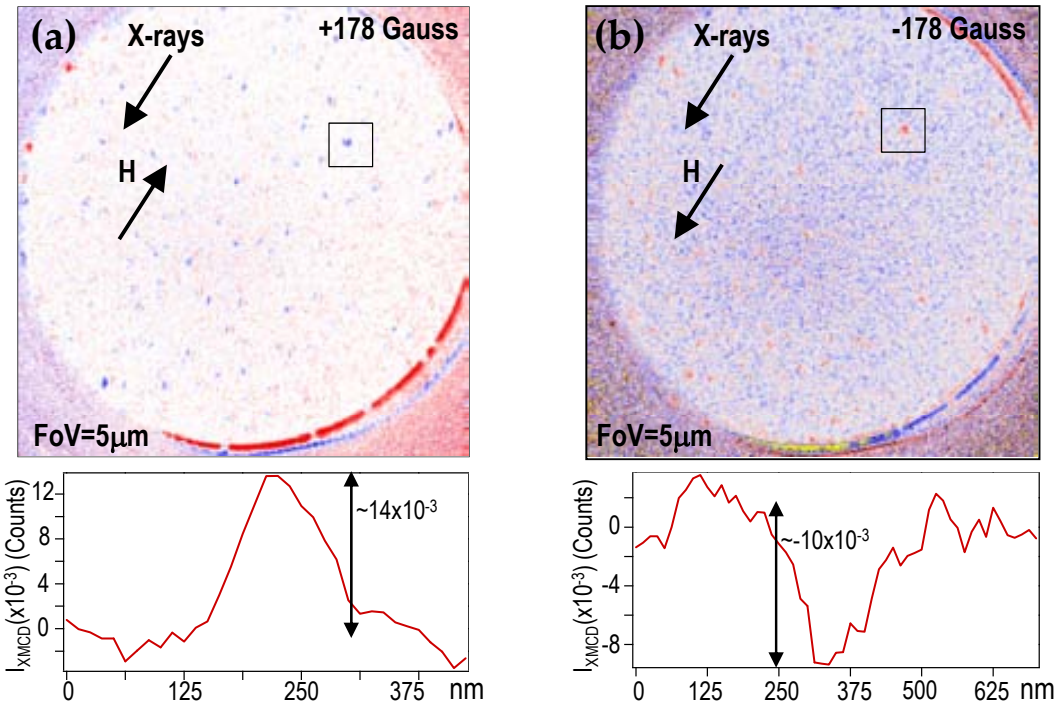


**Fig. 5.17:** *(a)&(b) 5 μm field of view XMCD images taken with opposite applied fields of± 178 Gauss. The change of field direction is accompanied by a change in the magnetization direction of nanoislands. This is evidenced by a blue to red contrast change and the associated sign reversal in the line scan.*

of the intensity that could suggest a gradual loss of the signal. We can thus conclude that, throughout the ∼45 min of continuous irradiation from image 1 to image 7, the X-rays do not affect the magnetism of the islands.

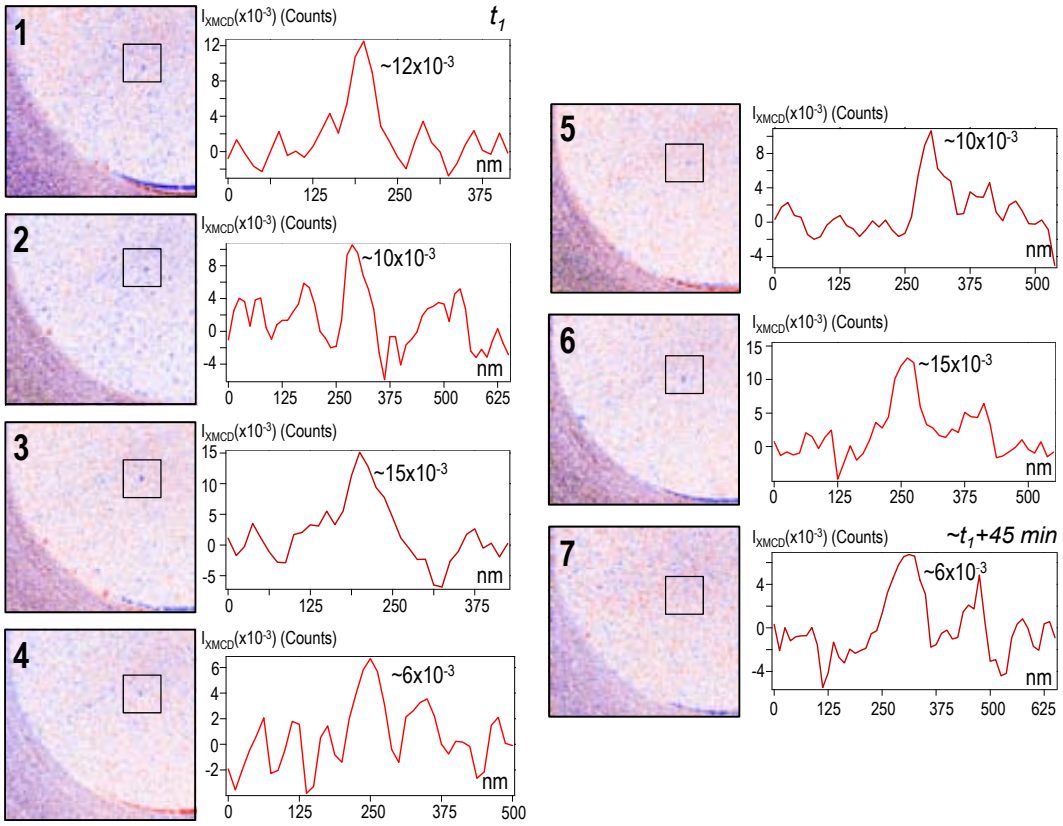


**Fig. 5.18:** *Left-bottom corner of each of the 7 images that conform Fig. 5.16 (b), numbered in chronological order. The set of accompanying line-scans express the intensity evolution of the XMCD contrast with time, corresponding to a single island (marked within black squares).*

If we now study what happens after longer exposure times, however, we find conclusive evidence that the XMCD signal can completely fade away. On the left hand side of Fig. 5.19 we have the same XMCD image as shown in Fig. 5.16 (b), displaying the nanoisland contrast at zero applied field. On the right, the same sample spot is imaged, at 178 Gauss, after a large number of experiments were done in between. We have estimated that the area was exposed to X-ray irradiation for a total of ∼15 h, with 2 breaks of a few hours in between due to the synchrotron beam injection. The sample was therefore steadily illuminated for about 7 h. The result of such exposure is the total loss of XMCD signal in the area, even at an applied field of 178 Gauss. Besides, by moving the illuminated spot to other sample regions, we regained the XMCD signal. Hence, the apparent *sample damage* after such long exposure times is due to X-ray irradiation.

Next, we want to check whether upon X-ray irradiation there are sizable changes in the chemical spectra of manganese. If we compare the Mn $L$-edge XAS features of a group of nanoislands at a certain time and ∼45 min after continuously irradiating the same spot, we observe no relevant differences [see Fig. 5.20 (a)]. This is in agreement with the fact that no magnetic signal loss was observed after ∼45 min of steady irradiation. Fig. 5.20 (b), in

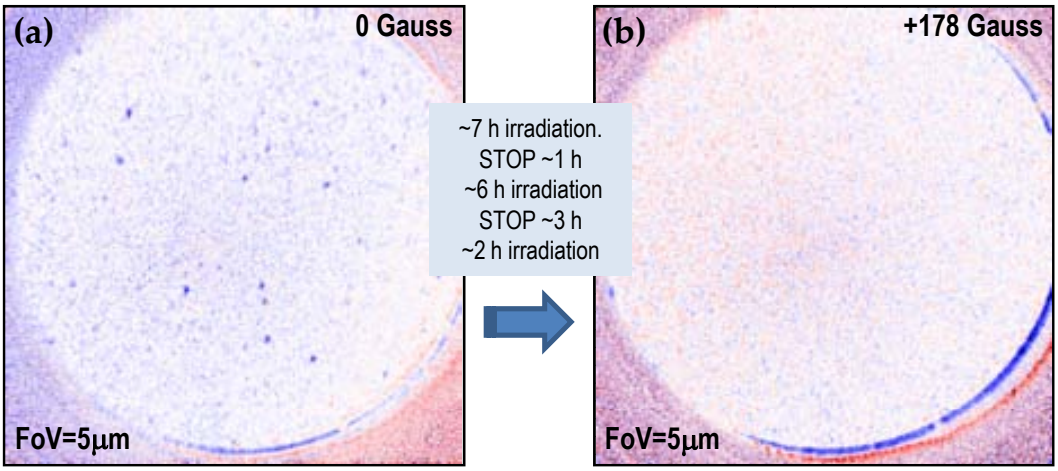


**Fig. 5.19:** *(a)&(b) 5 µm field of view XMCD images of the same sample spot showing the loss of magnetic signal upon 7 h of continuous X-ray irradiation.*

turn, compares the Mn $L_3$-edge XAS for a nanoisland ensemble at a moment when XMCD signal was measurable, with a XAS of the same group of nanoislands at an instant when the signal was no longer detectable (after 7 h of irradiation).Although for fine-structure considerations a better signal to noise ratio is required, it appears evident that the Mn $L_3$-edge is still present after having lost the magnetic signal. Furthermore, we do not find a decrease in the signal intensity nor the low-energy peak, at ∼639.2 eV, characteristic of $Mn^{2+}$ formation. Hence, apparently, the lack of magnetism is not caused by having chemically altered the manganite.

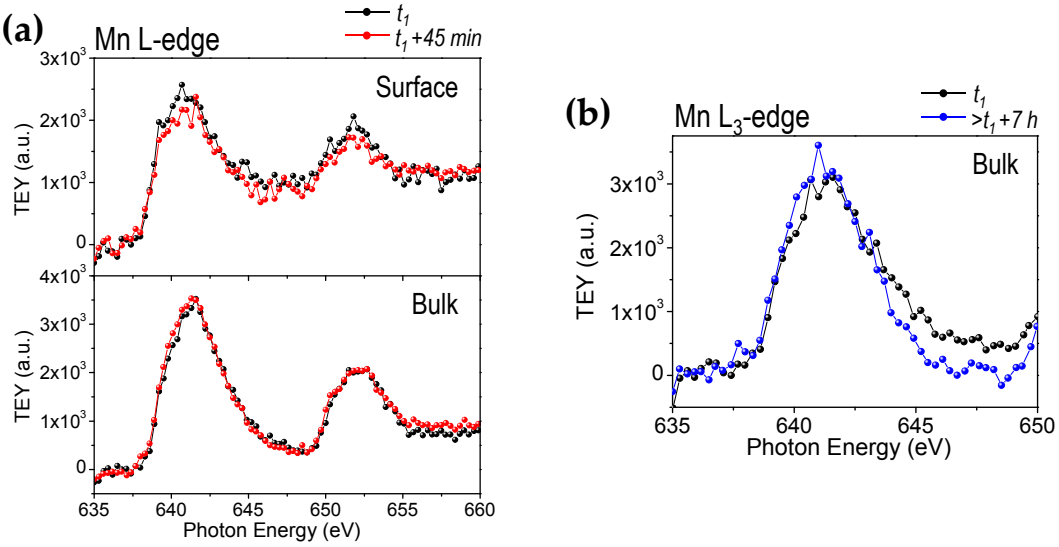


**Fig. 5.20:** *(a) Mn L-edge XAS of a LSMO nanoisland ensemble after X-ray irradiation during ∼15 min ($t_1$, black) and ∼60 min ($t_1$+ 45, red). The spectra exhibit no appreciable variations. (b) Mn $L_3$-edge XAS of a LSMO nanoisland ensemble after X-ray irradiation during ∼15 min (black) and for more than 7 h (blue).*

After the previous results, we can now think of a different mechanism that could lead

to the fading of the magnetic signal. Pt is a good thermal conductor, with thermal conductivity values of around $\kappa_{Pt}$(300 K)∼71.6 W/m×K [288], and it is hence expected to easily lead the X-ray power, in the form of heat, into the LSMO nanoislands, which have a poor thermal conductivity of $\kappa_{LSMO}$(300 K)∼2.4W/m×K [289]. The heat within the small LSMO nanoisland cannot easily dissipate since islands stand on top of an extremely good thermal insulator, YSZ [$\kappa_{YSZ}$(300 K)∼2.2-2.6 W/m×K [290]], and thus the nanoisland is expected to rise its temperature a lot, which would not happen if it were epitaxially grown onto a metallic substrate. Therefore, LSMO nanoislands under prolonged X-ray irradiation could undergo the ferromagnetic to paramagnetic transition, by being heated above their Curie temperature $T_C$∼350 K.

### XMCD at 110 K

The interest of measuring our LSMO nanoisland system at low temperatures is two-fold: on one hand, the magnetic signal is stronger below 300 K, so we expect to enhance the faint magnetic contrast we obtain at room temperature (RT). On the other hand, this study will clarify whether the magnetic signal loss observed at RT is effectively caused by heating the LSMO above its Curie temperature. Our experimental set-up allows us to reach a minimum temperature of 110 K. The magnetic hysteresis loop of the LSMO nanoisland ensemble (0.03 M) at 110 K, as measured with SQUID magnetometry before the PEEM experiments, is plotted in Fig. 5.21. The saturation magnetic moment is ∼4.6×$10^{-5}$ emu (∼526 kA/m) while, in remanence, the magnetization value drops a ∼50% from the saturation value.

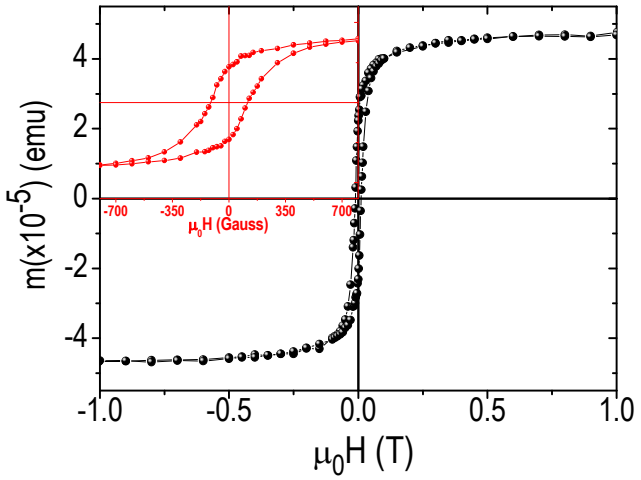


**Fig. 5.21:** *Magnetic moment vs. magnetic field hysteresis loop at 110 K for the LSMO/YSZ nanostructured sample measured by PEEM (0.03 M, 900°C heat-treated). The field was applied in-plane. The augmented view of the center region is displayed on the inset, in red. The signal decrease from saturation is of ∼50%.*

Fig. 5.22 (a) displays a 5 μm field of view PEEM image taken at the Mn $L_3$-edge. The interesting thing about this image is that the Pt capping has worn out a little, in the form of horizontal scratches; this results in a greatly increased brightness for nanoislands next to

The low thermal conductivity of YSZ makes it the material of choice for thermal barrier coating applications, where the ceramic is required to protect metallic parts of engines subject to very high operational temperatures of around 1200°C.

these scratches. One can notice, in the areas where the capping layer is intact, that the island and shadow contrast is identical to that shown earlier in the chapter (a representative island with its associated shadow is indicated in the figure). Conversely, near the thinned Pt, the island surface signal is remarkably improved, confirming the critical role of the capping in the collected electron intensity. Note also that the shadow can still be detected next to the bright islands, as expected, since its origin is exclusively due to the grazing X-ray angle and the nanoisland geometry. The direction of the incident light, as well as the two possible application directions of the magnetic field, are depicted in Fig. 5.22 (a).

Fig. 5.22 (b) shows a 3 μm zoomed XMCD image, taken in remanence, of the region marked within dashed white lines in Fig. 5.22 (a). We have numbered some of the large islands in both images, to better see the image correspondence. With respect to our RT measurements, the present low $T$ XMCD image shows a considerable contrast enhancement. Note that the most intense contrasts, those of the large triangular islands, coincide with the scratched-capping sites. For the islands located below the numbered islands, the contrast is notably weaker. Nevertheless, even at these sites we can easily discern many double spots, aligned with the light direction, and with opposite colors. These double spots correspond to a single island, in particular, to the island and the island-shadow. This confirms our previous hypothesis that the contrast arising from island and island-shadow should be opposite, with the difference (with respect to RT measurements) that we are now able to see them both, thanks to the enhanced intensity conditions. Note that not all of the nanostructures exhibit the same island and island-shadow sizes; this depends on the specific nanoisland geometry and orientation. In fact, for the islands at the very thin Pt capping sites (the scratches) the shadow loses relevance with respect to the bright island signal, and we mostly observe a single large spot coming from the island [some of these single spots have been marked with stars in Fig. 5.22 (b)]. In the following, we will refer exclusively to the contrast arising from the island, not from the island-shadow.

Along with the double-spots we have just described, we find single islands giving adjacent blue and red double spots, for instance the triangular nanostructure numbered *3*. Instead of one on top of the other, these spots are located one next to the other, perpendicular to the X-ray incidence direction. Such contrast arrangement is in agreement with two antiparallel magnetization vectors, next to each other, characteristic of a magnetic vortex. The perpendicular magnetic moments necessary to achieve the flux-closure configuration, being 90° oriented with respect to the X-rays, give no contrast. We have therefore the evidence of magnetic vortices in some of these nanoislands, which we already suggested in the RT results. Furthermore, we have the first confirmation that the magnetic configuration of triangles may also be that of a vortex. Remember that, by means of Magnetic Force Microscopy, we could not resolve their magnetic structure due to the influence of the tip, which wiped the magnetic domains within the triangles back and forth upon scanning (Chapter 4). Some of the vortices (V) are indicated with red squares in Fig. 5.22 (b). The rest of the nanoislands exhibit either a blue or a red contrast, characteristic of a single domain (SD) state (some of them are also marked with squares). It is highly possible that these apparently uniform contrasts might comprise a mixture of differently oriented domains (i.e. a multidomain structure), considering the large size of some of those islands. However, detecting these variations is beyond our experimental resolution.

In addition to an enhanced magnetic contrast, no critical magnetic contrast loss was detected upon continuous X-ray irradiation of the same spot at low temperatures. We can thus confirm our hypothesis that the X-rays are not intrinsically damaging the LSMO but

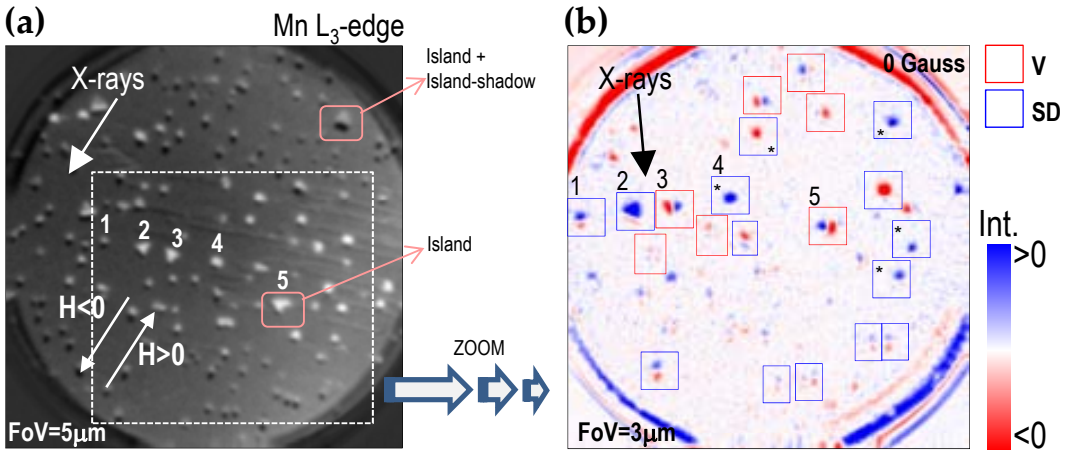


**Fig. 5.22:** *(a) 5 μm field of view PEEM image at the Mn $L_3$-edge showing a large increase in the intensity signal at the central part, i.e. where a thinning of the Pt capping occurred. (b) Remanence XMCD image of the zoomed-in region, approximately indicated with dashed lines in (a). Numbered nanostructures serve as reference with respect to (a). Vortex configurations (V) and single domain configurations (SD) can be distinguished. Some representative examples are marked within red and blue squares, respectively.*

producing a temperature gradient that makes the system non-ferromagnetic when measured at RT. Therefore, we may now safely study the changes in the magnetic configuration of individual nanostructures under applied field. This time, magnetic fields up to ±700 Gauss could be applied within the PEEM chamber. The maximum field applied in the course of imaging was, nevertheless, ±350 Gauss.

Fig. 5.23 exhibits a number of XMCD images of the same spot taken at different stages throughout the magnetic history of the sample. The XMCD image in the top row, taken in remanence, corresponds to the same region shown in Fig. 5.22 (b). Some representative vortex and single domain configurations are marked with red and blue squares, respectively. The sample was previously saturated with a negative field ($H$<0). This can be deduced from the fact that the majority of the single domain islands we observe in remanence show a blue (positive) contrast, which indicates magnetic moments aligned parallel to the incident X-rays [i.e. $H$<0, see Fig.5.22 (a)]. The three XMCD images of the bottom row were taken at the same magnetic field, ∼260 Gauss, but at different times, i.e. following different magnetic states. The sequence that was carried out is illustrated by *A*, *B*... letters on different points of the 110 K macroscopic hysteresis loop of the sample, indicating the magnitude of the field and the order in which it was applied.

By increasing the magnetic field from 0 to +260 Gauss, opposite to the incident light, some of the nanoislands magnetic configurations undergo detectable variations. The same islands within squares in the remanence **A** image, are also marked with squares in **B**. Those showing detectable changes with respect to the previous image are marked with black solid lines, while the rest are enclosed in gray dashed squares. Notice, for instance, how the two islands named *1* and *2* in image **B** lose the blue contrast shown in **A**, under the influence of a +260 Gauss field opposite to their magnetization [1]. This lack of contrast, even more evident in image **D**, could indicate that a coherent rotation demagnetization process is taking place, with the magnetic moments aligning close to perpendicular to the X-rays

[1] Recall that we refer only to the island (not island-shadow) contrast.

at that particular stage. Even clearer is the vanishing contrast in island *3* of image **B** with respect to its blue contrast in **A**. Applying a considerably larger field, i.e. ∼450 Gauss (point **C** in the hysteresis cycle), we achieve the total reversal of that island, which, going back to 260 Gauss (image **D**), does not regain the faint contrast of image **B**.

Regarding islands *4*, *5*, and *6* in image **B**, these were all vortices in the remanence image **A**. In the case of *5* and *6* they were already non-centered vortices, with non-compensated parallel and antiparallel domains. The domain parallel to the applied field (red) spreads to the whole nanoisland in **B**, until reaching a single-domain state. The vortex evolution is more clearly seen in nanoisland *4*, where the applied field makes the red domain grow at expenses of the blue, but the vortex is not yet annihilated. In fact, this suggests that the vortex core movement (the middle part between blue and red), moves perpendicular to the applied field, as generally expected. The evolution of nanoisland *4* towards a single domain configuration is further evidenced in **D**. Other significant transformations one can observe include the total reversal, in image **D**, of the large triangular island *7*: in the increase from 260 Gauss up to 450 Gauss and back to 260 gauss the nanostructure undergoes a 180° change in magnetization. Identical behavior, although only after reaching higher fields (∼700 Gauss), is exhibited by island *11* in image **F**.

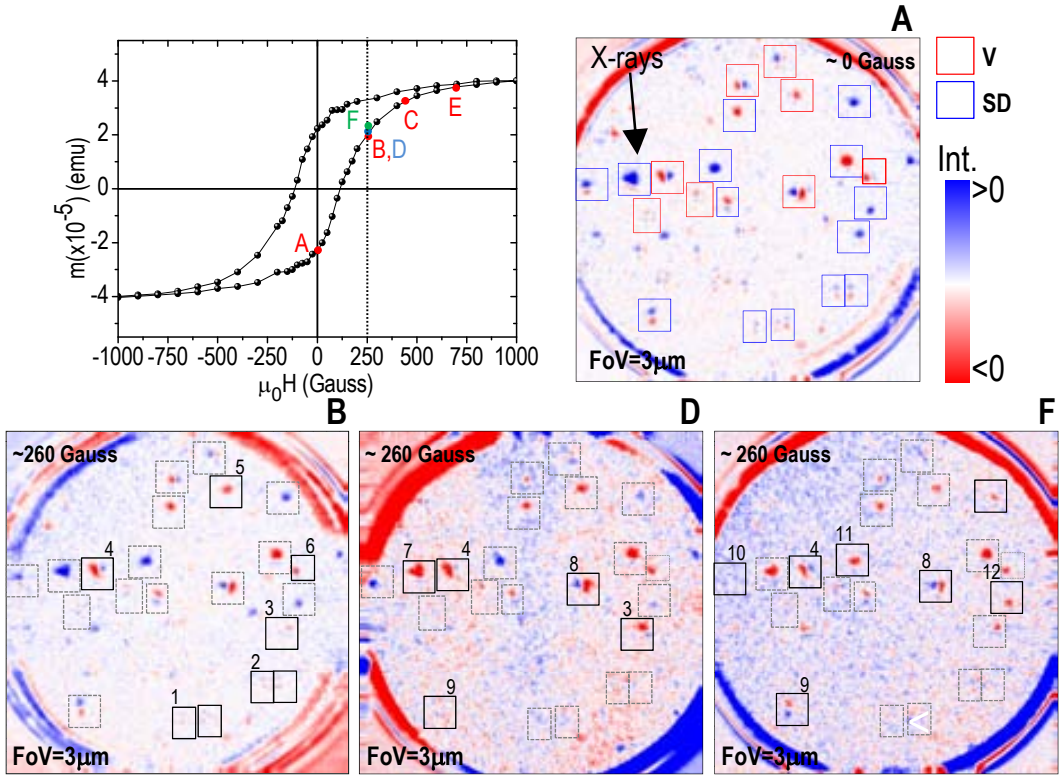


**Fig. 5.23:** *XMCD study of the magnetic configuration evolution of LSMO nanoislands with applied magnetic field. Images are labeled A, B...etc. in chronological order and in correspondence with the applied fields pointed in the 110 K hysteresis loop. Black solid squares mark nanoislands that have undergone a transformation in their magnetic configuration with respect to the previous image, and gray-dashed squares mark those which remain the same.*

Fig. 5.24 displays another set of XMCD images at various magnetic fields, as illustrated by the different points marked on the hysteresis cycle. The 5 μm field of view XMCD im-

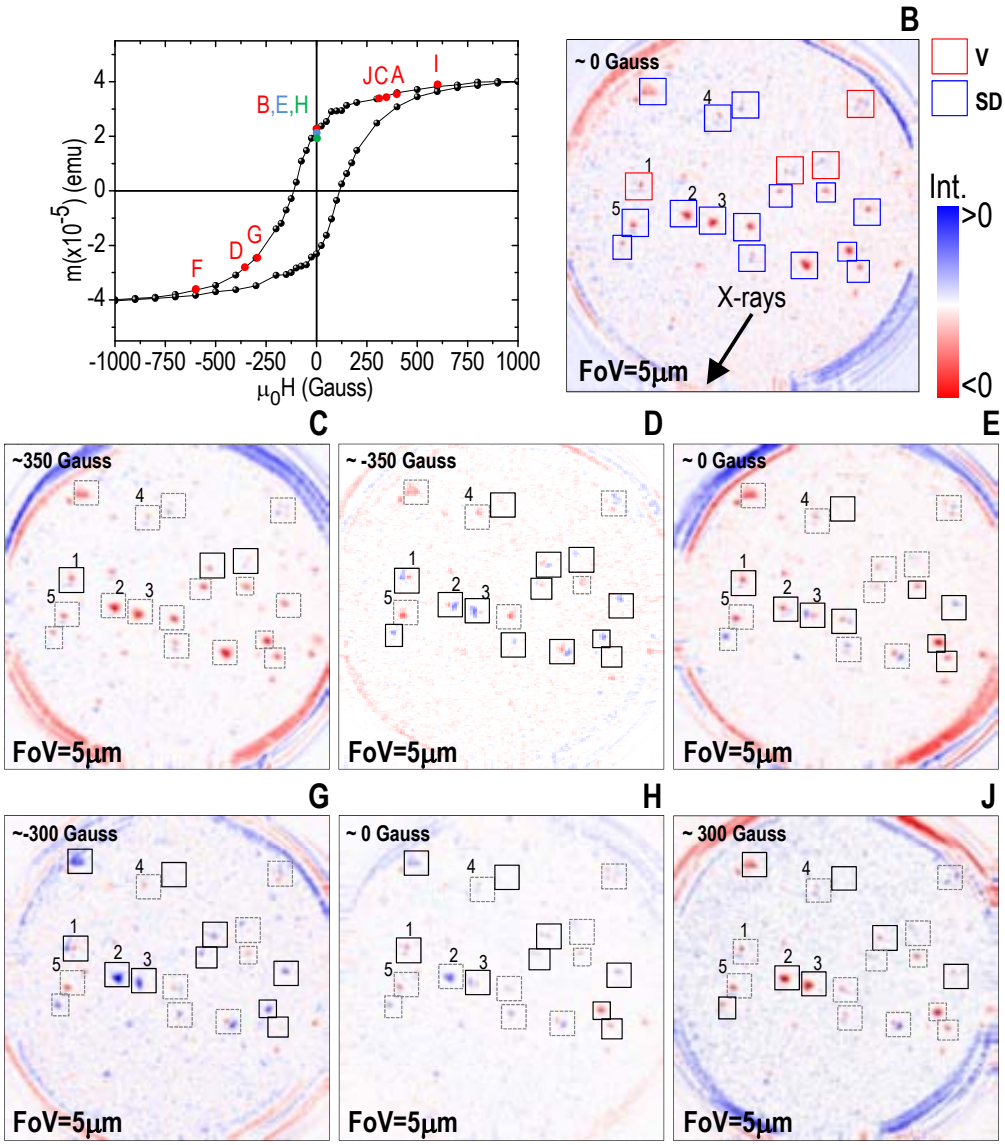


**Fig. 5.24:** *Similar XMCD study as the one presented in Fig. 5.23, although now the fields do not surpass 350 Gauss and hence their corresponding XMCD image is measurable. Islands labeled 1, 2, and 3 are large triangles which exhibit easily detectable changes in their magnetic configuration. By contrast, islands 4 and 5 exemplify other smaller islands which show no appreciable change in their magnetic structure within the range of applied magnetic fields.*

ages show the same PEEM image of Fig. 5.22 (a). Again, the islands that have changed their magnetic configuration with respect to the previous image are marked with solid black squares, and gray dashed-line squares denote those that remain unaltered. From the study of this set of XMCD images one can see that large triangular nanoislands, in the middle of the image, easily change their magnetic configuration upon application of a magnetic field. Take, for instance, nanoislands *1*, *2*, and *3*. Nearly at every registered magnetic field variation we see a change in their magnetic configuration: from single domain to vortex, vortex evolution, reversed single domain etc. This behavior suggests a magnetically soft nanostructure, whose magnetic configuration is easily perturbed. During MFM imaging of triangles in Chapter 4, in fact, we also observed such "softness", manifested in the influence of the magnetic tip on the nanoisland original magnetic configuration. At the other extreme we find examples like those of islands *4* and *5*: they exhibit an initial red single-domain contrast, which, upon multiple changes in magnetic field direction and magnitude, does not suffer any detectable alteration.

In conclusion, the XMCD studies presented here highlight once more the rich variety of nanoscale magnetic behaviors exhibited by the solution-derived self-assembled LSMO nanoislands. This landscape can only be revealed from a nanoscale spatially-resolved technique that allows one to individually characterize each nanostructure, and identify details that appear hidden in the averaged macroscopic magnetometry measurements. This scenario was already extensively described in the previous chapter, devoted to the investigation of the nanoisland magnetic structure by Magnetic Force Microscopy. We there could correlate the nanoisland size and aspect-ratio to its preferential magnetic ground state. The present PEEM investigation, in turn, has allowed us to answer some of the questions that raised during the MFM study: for example, we have seen that triangular nanoislands can display a magnetic vortex configuration, and, additionally, the evolution of the contrast under an applied magnetic field is consistent with the expected behavior of a vortex core, i.e. is perpendicular to the field. Regarding the vortices in the square-shape nanoislands, which we saw in Chapter 4 to move parallel to the external field, we could not determine their behavior by PEEM. On one hand, it is not straightforward to characterize square islands displaying a vortex state (they tend to be smaller islands). On the other hand, a motion parallel to the field implies subtle contrast changes difficult to resolve. Once more, one should rely on micromagnetic simulations that take into account the real shape of the nanoislands. These, as already commented in Chapter 4, are currently in progress.

### 5.1.5 Conclusions

Along the previous pages we have explained and discussed the PEEM experiments and their results on the system of ferromagnetic self-assembled LSMO nanoislands on YSZ. Special emphasis was given to the metallic capping required to accomplish the measurements, since samples must be electrically conducting (YSZ is a good insulator) and because, as we showed here, a successful capping is crucial and not straightforward. After demonstrating the suitability of platinum against copper and aluminum, we have moved on to the XAS study of the manganite nanoislands. We have taken advantage of the geometrical shadow-effect caused by the 16° X-ray incidence angle impinging on the small nanoislands ($D \lesssim 200$ nm and $t \lesssim 40$ nm), to simultaneously and separately analyze their surface and bulk composition. We have thus seen that the Mn XAS within the nanoisland (the bulk part) exhibits the spectral features expected for stoichiometric $La_{0.7}Sr_{0.3}MnO_3$. In

contrast, there is evidence of a certain $Mn^{2+}$ formation at the island surface, which supports the hypothesis of a superficial ferromagnetic dead layer on the LSMO nanoislands, discussed in previous chapters. It was also proved that, within experimental accuracy, the chemistry of the nanoislands does not depend on its crystallographic orientation. Magnetic measurements by means of XMCD have shown that the islands are indeed ferromagnetic. Nevertheless, we have seen that the Pt capping in such small nanostructures substantially reduces the intensity signal in the XMCD experiments, especially at high temperatures, where the magnetization value of manganite is small. The exposure to X-rays, for as long as seven hours and at room $T$, has been proved to heat the irradiated spot above the manganite $T_C$, with the corresponding loss of magnetic signal. In order to avoid the heating and to enhance the signal to noise ratio, we have performed experiments also at 110 K. The greater intensities, especially at places where the capping appears to have slightly worn out, has evidenced the presence of magnetic vortices in the $(111)_{\mathrm{LSMO}}$-oriented triangular-shaped nanoislands, which magnetic state was not accessible in the MFM experiments of Chapter 4 (recall that the tip stray field modified its magnetic configuration). Moreover, these vortices move, as theoretically predicted, perpendicular to the applied field. We have finally studied the magnetization processes of individual islands subject to different external magnetic field values. Our observations reveal that the variety of island shapes and sizes comprising the system of self-assembled LSMO nanoislands implies a correspondingly varied landscape of magnetization processes. It is also worth remarking that in the evolution of nanoislands with applied field there is no evidence that the magnetic state of an island should influence that of its neighbour islands. This agrees well with our hypothesis of Chapter 4 that the magnetic interaction between nanoislands is negligible. A more detailed study considering XMCD imaging at many different field values, given an island large enough to resolve its structure can, in a future work, provide full hysteresis cycles of individual LSMO nanoislands.

## 5.2 Kelvin Probe Force Microscopy study of self-assembled LSMO nanoislands

KPFM is the scanning force microscopy tool used for measuring the work functions of different metals with nanometer spatial resolution [291, 292]. The work function values of a metal are known to sensibly vary with contaminants, adsorbed layers, different reconstructions and defect structures on the surface, and such variations can be locally addressed with KPFM [293]. Increasingly during the past decade, the use of KPFM has been extended to other materials, being applied in the characterization of semiconductor nanostructures and devices [294–296] as well as to measure charge-related phenomena on insulating surfaces [297–300]. The precise mechanisms acting between the tip and the sample are often complex and difficult to understand, and hence the interpretation of KPFM results is not trivial and straightforward [301, 302]. In this section we focus on the KPFM study of self-assembled LSMO nanoislands on insulating YSZ substrates, detailing the experimental procedure and, from a critical perspective, analyzing the obtained results.

### 5.2.1 Basics on KPFM

KPFM measures the contact potential difference (CPD) between the sample and a sharp metallic tip placed a few *nm* above its surface. CPD (or $V_{CPD}$) is defined as the electric potential difference between two points in vacuum, each of them close to the surface of a different metal, while these metals are uncharged and electrically contacted. KPFM is a Scanning Probe Microscopy technique which relies on the Kelvin method [261]: when two metals, arranged in a parallel plate capacitor geometry as illustrated in Fig. 5.25, are contacted, electrons will flow from the material with lowest to the material with highest work-function, until the Fermi level of the two equilibrate [Fig. 5.25 (b)]. At that point, an electrostatic field develops between the two conductors. We can nullify this field by applying a certain voltage, $V_{CPD}$, which equals the work-function difference between the two materials, i.e. $eV_{CPD} = \Delta\theta = \theta_{tip} - \theta_{sample}$ [Fig. 5.25 (c)], with $e$ the electron charge. Strictly speaking, this expression only holds for the case of metals [261, 291, 303]. For insulating samples, the $V_{CPD}$ does not equal the difference in work functions between the tip and the sample, since the electrically contacted conductors in that case are the tip and the sample-holder, not the sample. Moreover, the voltage applied to nullify the electric field will counteract, in addition to the $V_{CPD}$, any potential difference that may build-up as a consequence of the bulk insulator in-between the tip and the sample-holder [297].

As a type of Scanning Probe Microscopy (SPM), KPFM senses the interaction, in particular the electrostatic interaction, of the *nm* lateral-size tip with the sample underneath [293]. As we also commented for magnetic force microscopy (MFM) in Chapter 4, the critical point in SPM is to be able to separate the specific interaction we want to measure, in this case electrostatic, from the number of short and long-range forces that are present between the tip and the sample. These interactions include short-range repulsive forces due to the overlapping electron wave functions, Van der Waals attractive forces, adhesion and friction forces...etc. In order to separately measure the electrostatic force with the Kelvin method, the vibrating capacitor method is used [304], first implemented into a Force Microscopy by Nonnenmacher and co-workers [291]: either the tip or the sample are biased by applying an alternating voltage $V_{ac}$ at a frequency , along with a continuous voltage $V_{dc}$. The energy in a parallel plate capacitor is given by $U = \frac{1}{2}C(\Delta V)^2$, where $C$ is the local capacitance between the tip and the sample and $\Delta V$ is the potential difference between them. Because of the existence of the CPD, the potential difference is given by: $\Delta V = (V_{dc} - V_{CPD}) + V_{ac}\sin t$. The electrostatic force is the gradient of the energy:

$$F_{el} = -\frac{1}{2}\frac{C}{z}(\Delta V)^2 \tag{5.6}$$

where the $z$-axis is the direction perpendicular to the sample surface. Substituting the explicit expression of $\Delta$V in Eq. 5.6, developing it, and rearranging the result in terms of the dependency with , three different terms arise: $F_{el} = F_{dc} + F_{\omega} + F_{2\omega}$, where

$$F_{dc} = -\frac{1}{2}\frac{C}{z}\left[(V_{dc} - V_{CPD})^2 + \frac{V_{ac}^2}{2}\right] \tag{5.7}$$

$$F_{\omega} = -\frac{C}{z}V_{ac}(V_{dc} - V_{CPD})\sin t \tag{5.8}$$

$$F_{2\omega} = \frac{V_{ac}^2}{4}\frac{C}{z}\cos 2 t \tag{5.9}$$

The first term, $F_{dc}$, contributes to the topography signal by the static deflection of the tip, and the time-dependent $F_{\omega}$ and $F_{2\omega}$, can be separately measured by lock-in techniques.

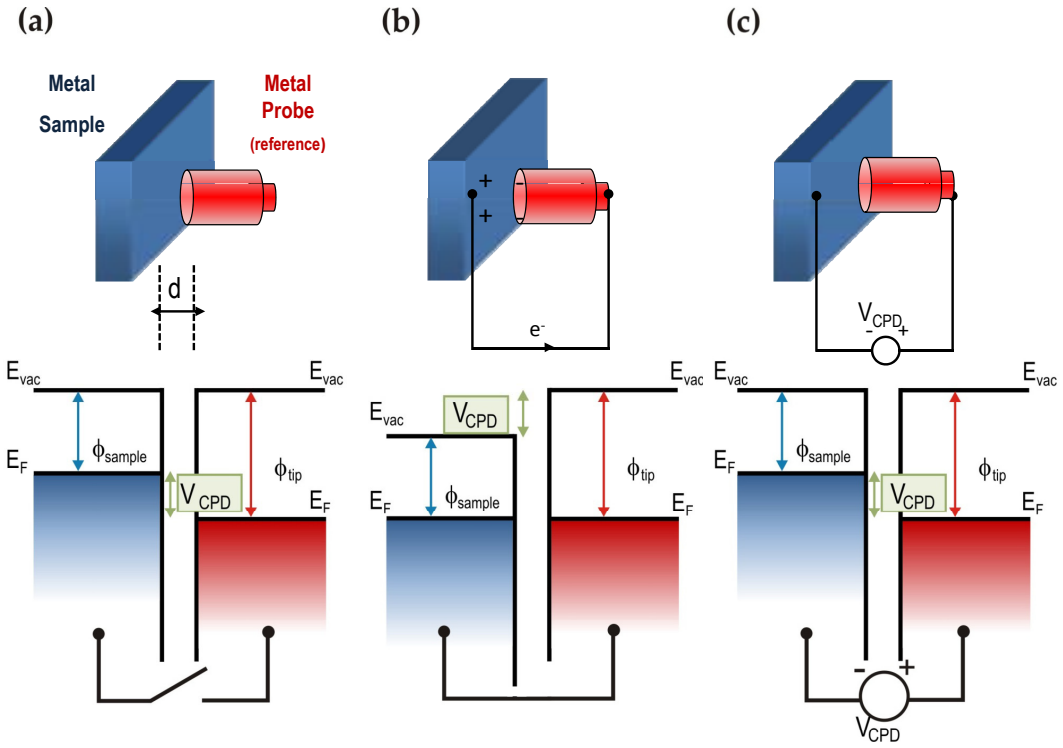


**Fig. 5.25:** *Schematic illustration of the Kelvin method for CPD measurement. (a) Two conductors, sample and probe, are arranged as a parallel plate capacitor separated a distance* d*. (b) Upon electrical contact, electrons flow from the material with lowest work-function to the material with the highest work-function until the Fermi levels of the two equilibrate, leaving both conductors charged which yields an electrostatic field to develop between them. (c) Such electrostatic force can be nullified by application of the Contact Potential Difference, which equals the difference between the work-function of the two metals.*

The term $\frac{\partial C}{\partial z}$ depends on the probe-sample geometry and on the dielectric characteristics of the sample, so it will change with varying sample topography, tip-sample distance, and with the dielectric properties. The term $F_{2\omega}$, which exclusively depends on this derivative ($V_{ac}$ is an externally set constant), can be used for capacitance microscopy [305, 306]. $F_{\omega}$ causes the cantilever to vibrate and is the signal used in KPFM measurements: the voltage value $V_{dc}$ we need to apply to make $F_{\omega}$=0 is, precisely, the CPD value between the tip and the sample, $V_{dc}$=$V_{CPD}$. Therefore, by monitoring the voltages that make $F_{\omega}$=0 at each *(x,y)* point of the sample, we obtain a CPD map of the scanned area.

Simultaneously to the CPD image, during KPFM operation we obtain the topography image of the studied surface. In fact, one of the uses of KPFM is the imaging of *real* topographical features, free from electrostatic artifacts that may cause errors in the estimation of the lateral and vertical dimensions. To be able to measure topography and KPFM simultaneously we need to disentangle the influence due to Van-der-Waals attractive forces (responsible for topography) and the long-range electrostatic interactions. Generally, the cantilever first resonance frequency ($f_0$) is used for topography imaging while the alternating voltage $V_{ac}$ is set at a frequency $f_{ac} =$ $2^{\rightarrow}$ well separated from $f_0$: some experiments use small frequencies in the 1-10 kHz range [307–309] while others enhance the resolution of the measurement by tuning to the second cantilever resonance frequency ($f_2 \sim 6 f_0$) [310–312]. In either case we have two feedback loops, one for the height control which gives us the topography signal, the other for detecting and subsequently enforcing $F_{\omega}$=0.

The same concepts related to the *Dynamic mode* operation explained in section 4.1 of Chapter 4 are applied in KPFM measurements. In brief, the interactions between the tip and the sample are measured by detecting the variations in the characteristic parameters of the oscillating cantilever: its amplitude, its phase, and its frequency. The shift in frequency, for instance, is given by: $\Delta f \approx -\frac{f}{2k}\frac{\partial F}{\partial z}$, with $k$ the cantilever spring constant. The Scanning Probe Microscope then works by utilizing these parameters as feedback parameters so that any deviation from the set-point value is followed by a response to restore such set-point. Such response is recorded at every *(x,y)* point during the scanning of the sample, and hence, we obtain the spatially-resolved image of the desired physical property.

### 5.2.2 Experimental procedure

The KPFM measurements described here were done in the context of a short three month stay at Prof. M. Salmeron's group at the Materials Science Division of Lawrence Berkeley National Laboratory (LBNL), under the supervision of Dr. A. J. Katan. A UHV AFM instrument (model 350AFM/STM) equipped with a SPM100 control electronics (RHK Technology) was used, operated at room temperature and with a base pressure of around p$\sim 10^{-8}$ Torr. We worked in the Dynamic Non-Contact mode using the resonance frequency of the cantilever as the feedback parameter for topography measurements (Frequency modulated-AFM). An independent demodulator was employed for such purpose (EasyPLL from Nanosurf). For Kelvin operation we used a Lock-in Amplifier (Perkin Elmer) and a PID feedback controller (SIM960, Stanford Research Systems). Fig. 5.26 displays the main parts of the experimental set-up we employed. The sample, a 0.5 mm thick YSZ insulating substrate, was pasted with Ag paint to the grounded sample-holder, and the voltages were applied to the conducting tip.

Frequency modulated operation mode is the usual working mode for topography feedback in UHV, after the pioneering work by Albrecht et al. [313]. In the general *Dy-*

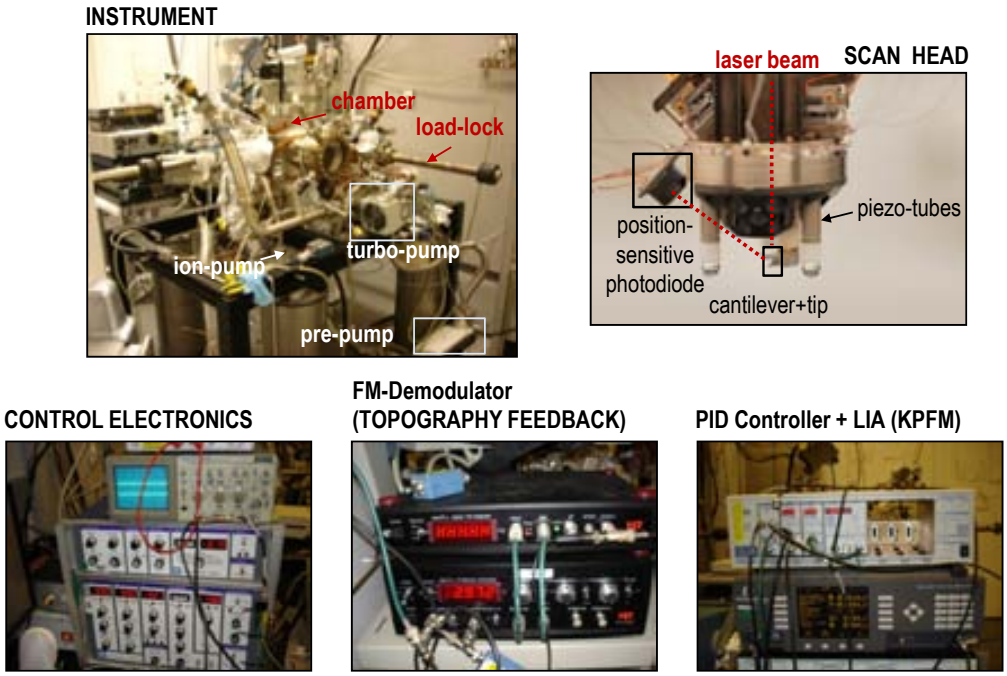


**Fig. 5.26:** *Experimental set-up for simultaneous Frequency modulated-AFM and KPFM measurements using the UHV AFM/STM (RHK Technology) from Prof. Salmeron's group at LBNL.*

*namic* AFM, a cantilever far from the sample surface, which oscillates at its free resonance frequency $f_0$, is set to oscillate slightly off-resonance (at its set-point value $f$). The tip will then approach the sample until it reaches that precise oscillation frequency (set-point). Topography variations of the sample surface will cause the oscillation amplitude to change and the frequency value to deviate from the set-point value $f$. In the Frequency modulated-AFM mode the feedback loop will then adjust the tip to sample distance in order to restore the set-point frequency $f$. In other words, the feedback reacts to keep the frequency shift $\Delta f = f - f_0$ value constant and thus topography images are constant frequency-shift images. One could also work in Amplitude-Modulated AFM or 'slope detection' mode, in which the feedback parameter is the amplitude of the oscillation. However, the time necessary for the amplitude to reach, after its change, a steady state (necessary for feedback purpose) is $\chi$=2$Q$/ $_0$, where $Q$ is the cantilever quality factor and $_0$ its resonance frequency [222]. Such value results unsuitably large in UHV systems, where $Q$ is $\sim 10^4$-$10^5$ In Frequency modulated-AFM, by contrast, this problem is avoided because the immediate change in frequencies is detected.

All of the images reproduced in the following were done using Si tips from Budget Sensors with an electrically conducting chromium/platinum coating (5 nm Cr + 25 nm Pt, with Pt the outward layer) [314]. Their resonance frequency is found in the $f_0 \sim$68-75 kHz range and the spring constant $k$ is around 2.5-3 N/m. The nominal radius is $R \leq$25 nm. Typical peak-to-peak oscillation amplitudes, measured through the register of the cantilever thermal spectrum and the oscillation amplitude in the oscilloscope, were in the range of $A_{p-p} \sim$2-10 nm.

Fig. 5.28 displays the main channels, significant for the Kelvin Probe signal analysis, that we recorded on a LSMO/YSZ self-assembled nanoisland system. As explained

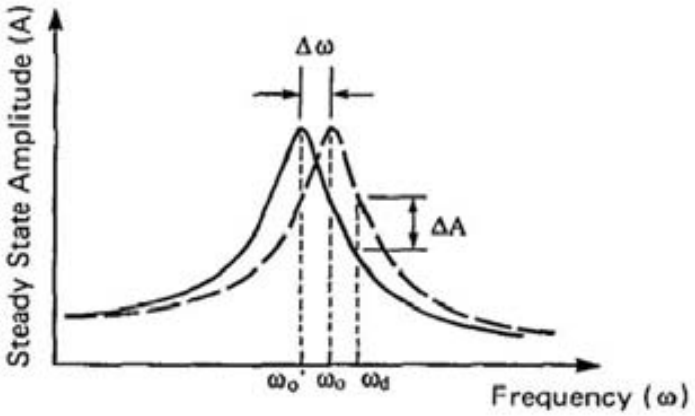


**Fig. 5.27:** *The resonance curve for a cantilever shifts its resonance frequency value from* $_0$ *to* $_0$ *due to the tip-sample interaction (*$\Delta$ $\frac{\partial F}{\partial z}$*). Such variation causes a variation in the amplitude,* $\Delta A$*, as measured in the set-point value* $_d$*. Reproduced from [313].*

above, the topography signal registers the piezo changes in order to keep the frequency-shift constant. The frequency shift map to its right, hence, records the error due to the feedback, which is always more evident at the edges of abrupt structures. The CPD channel corresponds to the DC voltage (applied to the tip in our case) necessary to make the $F_\omega$ component equal to zero, i.e. this is the CPD or Kelvin signal. We measured the Kelvin signal in the Amplitude Modulated-KPFM mode, which means that we measured and nullified the *amplitude* of the $F_\omega$ component. In analogy to the aforementioned Amplitude modulated-AFM and Frequency modulated-AFM, Amplitude modulated-KPFM and Frequency modulated-KPFM use the *amplitude* of $F_\omega$ component and its *gradient* for feedback in Kelvin operation, respectively (see for instance reference [293]). To the right of the CPD image we show the Kelvin Error image, which registers the feedback error in nullifying $F_\omega$, and hence will be accentuated where large CPD changes are present. When the Kelvin feedback is OFF, this channels gives the measure of the electrostatic force between the tip and the sample. For every image we recorded both forward and reverse scans to be able to separate true contrasts from scanning artifacts (only the forward scan is shown in Fig. 5.28.) The resolution of the images was typically 256×256 pixels.

Before performing the Kelvin measurement, an important step is the **tuning of the feedback parameters** (Proportional, Integral, and Derivative gains of the PID controller) to make sure that the feedback is working fast enough with respect to the scanning speed. For this reason also the scanning speed was generally kept notably low, at values ∼0.15-0.2 Hz (∼5-6.5 s/line). Fig. 5.29 shows the time-dependent oscilloscope behaviors of the CPD, Kelvin Error, and Topography signals, at the moment of turning the Kelvin feedback on, and off again. The abrupt change of the CPD and of its error signal indicates that the PID parameters are working fast enough (otherwise the change with time would be progressive). The values of the Kelvin error axis, both absolute and relative, depend on the sensitivity of the lock-in at the time of scanning, as well as on its output voltage (2.5 V), and hence are not meaningful. In contrast, although the absolute values in the CPD

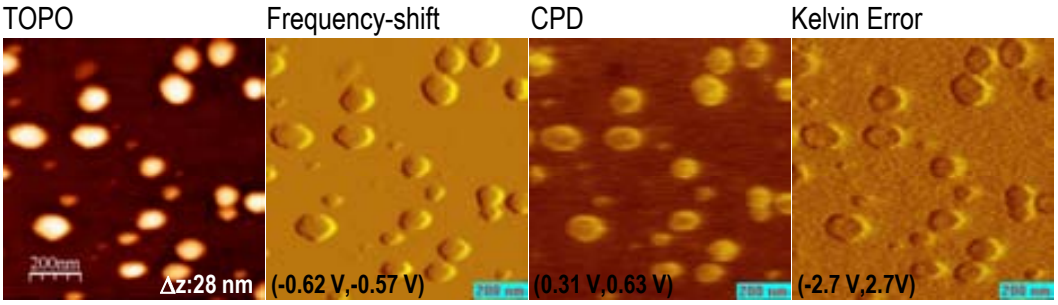


**Fig. 5.28:** *Principal channels to be recorded throughout KPFM measurements. In addition to the simultaneous topography and CPD images, their corresponding error signals are also displayed. The images are 1 $\mu m \times$ 1 $\mu m$.*

signal varied notably in both magnitude and sign (sometimes during the course of the same image), the relative island to substrate CPD variations remained roughly constant. These variations in the absolute value of the voltage to be nullified, however, made it necessary to constantly check and re-tune the feedback operation, which at times was difficult. We believe that these variations could arise from trapped charges on our insulating substrate, which may be inhomogeneously distributed at defect sites or kinks of the YSZ surface. The electric field generated by such charges in the tip 'image' charges varies with the tip-sample distance, and so does the voltage required to nullify such field [300]**.

The optimal set-points for our measurements of LSMO nanoislands on YSZ substrates ranged from $\Delta f \sim$-35 Hz to $\Delta f \sim$-60 Hz, corresponding to typical tip to sample distances ranging from less than 5 nm to slightly above 8 nm, as measured from Force-Distance curves. We routinely adjusted the set-point, so we expect different tip to sample distances for different measurements. Note that none of these PID tuning difficulties arose when we performed preliminary KPFM measurements on LSMO thin conducting films (not shown in this work). The stability of these samples during the KPFM was ideal, the CPD absolute voltages were identical, before and after tip-withdrawal, experiment after experiment etc. This observation supports our ascribing the former voltage variations to trapped charges on the insulating YSZ sample. Regarding the topography signal, it is worth commenting on the $\sim$1 nm height change produced by the ON-OFF turning of the Kelvin feedback. This is precisely the evidence of an electrostatic force, in this case repulsive, between the tip and the sample, which is present when there is no Kelvin feedback. At the moment the electrostatic force is made zero, with the turning ON of the feedback, the tip increases its distance from the sample (by$\sim$1 nm) so that the $\Delta f$ is kept constant (otherwise $\Delta f$ would fall to lower values due to the absence of repulsion).

### 5.2.3 Origin and evidence of the KPFM contrast in LSMO on YSZ nanostructured samples

The following sections are devoted to the results concerning the KPFM measurements on self-assembled LSMO nanoislands on insulating YSZ substrates, with particular emphasis on the experimental concerns related to their physical interpretation. A small 240 nm $\times$ 240

**In their KPFM study of alkali halide surfaces Barth and Henry ascribe the observed potential contrasts, which are typically observed at kink sites of steps of the sample surface, to negative net charges, caused by impurities within the crystal [300].

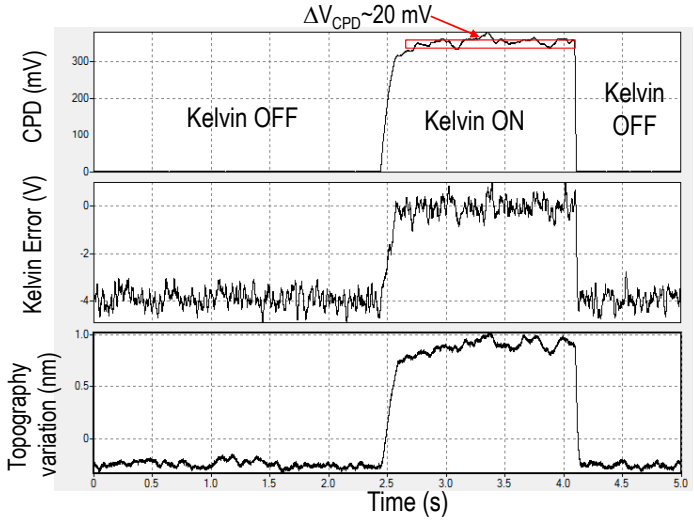


**Fig. 5.29:** *Kelvin feedback testing through the time response signal analysis. Tip and sample are at the set-point distance, and the topography feedback is kept ON, i.e $\Delta f$=constant, the whole time. The abrupt changes in time evidence that the PID controller is doing well. The change registered in topography reveals the presence of the electrostatic force.*

nm area, containing a single LSMO nanoisland, is imaged in Fig. 5.30. The top row shows the topography-related information of a well-defined LSMO nanoisland with a thickness $t\sim$22 nm and a lateral size $D\sim$100 nm. Note that the island displays a rotated-square morphology, one among the two main morphologies observed in LSMO/YSZ nanostructured samples (see Chapter 3).The simultaneous Kelvin measurement of the island is shown at the bottom row of Fig. 5.30. A clear bright contrast, as compared to the dark YSZ substrate, emerges from the island in the potential image $V_{dc}$. Meanwhile, the Kelvin error signal exhibits very low contrast, featuring the expected changes where abrupt contrast variations occur, i.e. at the edges of the island in this case. A line scan across the $V_{dc}$ image shows that the potential difference between substrate and island is $\sim$120 mV. Statistical analysis of a large number of pixels at substrate and island spots give also a very similar potential jump of $\Delta V$=110$\pm$10 mV. Note that we have named the Kelvin image $V_{dc}$, instead of $CPD$, as we did in Fig. 5.28, despite being exactly the same channels, identically measured. $V_{dc}$ is the bare continuous potential applied to the tip in order to make $F_\omega$=0. On the other hand, $CPD$ entails a physical meaning, the Contact Potential Difference between the tip and the sample electrode. According to Eqs. 5.7 to 5.9, routinely used to explain the bases of KPFM, $V_{dc}$ equals the $CPD$. This, however, is not strictly true for our case, as we will explain shortly. In the following, we will refer to $V_{dc}$ images as *potential images*.

We plot a schematic diagram of the system under study in Fig. 5.31. Tip and sample, separated a distance $z$, are there the capacitor plates. At variance with the canonical KPFM operation example where the sample surface is metallic, in our system the capacitor architecture is formed by the tip and the sample-holder, which is grounded. On top of the sample-holder lays a massive 0.5 mm thick insulator, the YSZ substrate, which supports a dispersion of comparatively tiny LSMO nanoislands on its surface. Hence in the expression for the electrostatic force between the capacitor plates (Eq. 5.6) the capacitance $C$ and the potential $V$ will include the combined effect of the two dielectric media in between: vacuum (or air) and the YSZ substrate. In other words, the voltage we apply in order to

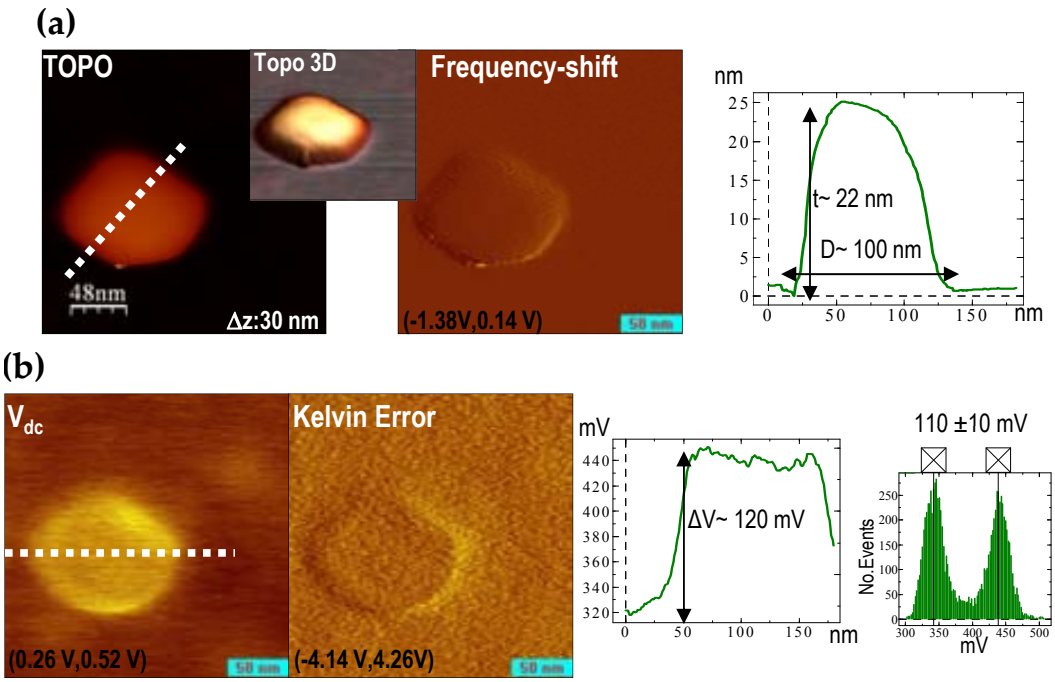


**Fig. 5.30:** *Simultaneous topography (top row, (a)) and KPFM measurements (bottom row, (b)) of an individual LSMO nanoisland on YSZ. The surface potential variation between island and substrate is ∼110 mV.*

make $F_\omega$=0 depends not only on the CPD due to the tip and the sample-holder surfaces but also on the dipoles or charges, that may develop at the LSMO/dielectric, vacuum/YSZ interfaces [297].

If we consider the simplified picture of the parallel plate capacitor and disregard border effects, we may write the potential drop along the two dielectrics in between, vacuum and YSZ, in the following way:

$$\Delta V_{dielect.} = E_1 z + E_2 l \tag{5.10}$$

where $E_1$ and $E_2$ are the electric fields in the vacuum (between the tip and the YSZ surface) and within the YSZ, respectively, both of them perpendicular to the vacuum-YSZ interface. $z$ and $l$ are the corresponding dielectric thicknesses (see Fig. 5.31). As there is no free electric charge on the insulator surface, the boundary conditions for the displacement vector at the vacuum-YSZ interface require that $\epsilon_0\epsilon_r E_2 - \epsilon_0 E_1 = 0$, where $\epsilon_r$ is the relative permittivity of YSZ (which takes values around ∼25 [315] and ∼29 [316]). If we now insert a conductor of thickness $t$ in between the two plates at a distance $(z-t)$ from the tip, the voltage difference will vary accordingly:

$$\Delta V_{dielect.'} = E_1(z-t) + E_2 l \tag{5.11}$$

where now $E_1$ and $E_2$ are defined by the condition of no electric field within the conductor, i.e. $E_1 = \frac{-\sigma}{\epsilon_0}$ and $E_2 = \frac{\sigma'}{\epsilon_0\epsilon_r}$ for the fields in vacuum and within the YSZ, respectively. $\phi$ and $\phi$ refer to the free surface charge density on the top and bottom plates of the conductor, respectively. Adding the potential drops in Eq. 5.10 and 5.11 to the expression $\Delta V$=($V_{dc}$-$V_{CPD}$)+$V_{ac}$sin $t$, and substituting the new potential difference in the expression for the electrostatic force (Eq. 5.6), we may derive the expressions for the component of the

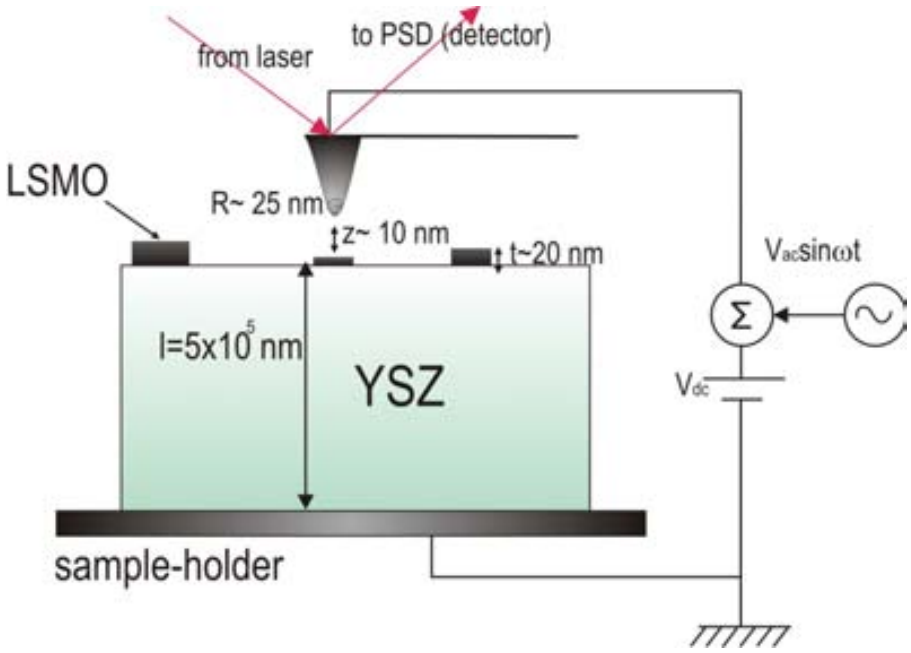


**Fig. 5.31:** *Schematic diagram of the experimental set-up for the KPFM measurement of LSMO on YSZ nanostructured system.*

force, $F_\omega$, both for the tip positioned on top of the bare YSZ substrate and on top of the LSMO nanoisland:

$$F_\omega^{YSZ} = -\frac{C}{z}V_{ac}\left[V_{dc} - V_{CPD} - E_1 z - \frac{E_1 l}{\epsilon_r}\right]\sin\ t \tag{5.12}$$

$$F_\omega^{LSMO} = -\frac{C}{z}V_{ac}\left[V_{dc} - V_{CPD} + \frac{\phi(z-t)}{\epsilon_0} - \frac{\phi\ l}{\epsilon_0\epsilon_r}\right]\sin\ t \tag{5.13}$$

where $C$ and $C$ correspond to the capacitances of each of the two architectures (dielectric and dielectric+ conductor). The voltages required to make that component equal to zero over the YSZ substrate or the LSMO island will hence be:

$$V_{dc}^{YSZ} = V_{CPD} + E_1\left(z + \frac{l}{\epsilon_r}\right) \tag{5.14}$$

$$V_{dc}^{LSMO} = V_{CPD} - \phi\frac{z-t}{\epsilon_0} + \frac{\phi\ l}{\epsilon_0\epsilon_r} \tag{5.15}$$

And the difference between the two leads to

$$\Delta V_{dc}^{LSMO-YSZ} = -\phi\frac{z-t}{\epsilon_0} + \frac{\phi\ l}{\epsilon_0\epsilon_r} - E_1\left(z + \frac{l}{\epsilon_r}\right) \tag{5.16}$$

Note that the $V_{CPD}$ voltage term due to difference in work function between the tip and the sample-holder is canceled, i.e. we do not have a dependence with respect to the sample-holder. In contrast, we obtain an expression which is dependent upon the distinct charge distributions at the LSMO surfaces. Note that this picture is a rude oversimplification of the real experimental set-up, as we have considered that the LSMO conductor in-between the two dielectrics consists of two infinite parallel plates. In reality, the LSMO nanoislands are finite solids, with well-defined crystal planes that connect the upper and lower parallel surfaces. Instead of charge distributions, in a faceted finite size metal in equilibrium

such as these nanoislands it is generally talked of the *surface dipole* of a specific surface, which is the origin of its work function and thus it is directly related to the geometric and, in consequence, the electronic structure of that specific surface [317, 318]. This issue will be discussed later in the chapter. The above oversimplified view, however, is useful to illustrate the role of the bulk insulator, while it highlights that the relative potential differences between the substrate and the LSMO islands do not depend on the sample-holder electrode.

In addition to a remarkable contrast difference between the LSMO nanoislands and the YSZ surface of Fig. 5.30, careful measurements of some islands, which generally imply very low scanning speeds (∼5-6.5 s/line), enable the observation of contrast variations within one island. The potential images of Fig. 5.32, for instance, evidence a brighter contrast at the lower half of the island. This potential variation is quantitatively shown in the line-scans of Fig. 5.32 (c): we have plotted the nanoisland topography (top row) and potential (bottom row) profiles, corresponding to the white dashed lines in the images. A potential jump of around ∼80 mV is measured within the island, in agreement with the statistical $V_{dc}$ distribution study of the regions marked in blue squares and numbered *1*, *2*, and *3*. After verifying that the Kelvin feedback is working correctly, a number of tests are available to assess whether this is a physical effect or an artifact: we can repeatedly scan the island, combining different directions, e.g. back and forth downwards [Fig. 5.32 (b), top row] or upwards, changing the angle of the tip with respect to the sample [from 0° in Fig. 5.32 (b) top to 90° in Fig. 5.32 (b) bottom row etc. Other tests include slight variations of the tip to sample distance, or playing with the scanning speed. After taking such precautions we can thus conclude that there is a real difference in the potential between those two island halves. According to what we saw earlier this could be linked to a difference in the charge distribution within the upper facet. In turn, such charge inhomogeneities could have multiple origins: different surface reconstructions of the facet yielding distinct charge distributions or the presence of defects on the surface promoting the adsorption of contaminants, are only some of the possible scenarios.

Fig. 5.33 shows the KPFM measurement of three different LSMO nanoislands from the same sample as above. The top panel displays the topographical information of the nanostructures, i.e. the topography and its corresponding error image, plus a line scan along the dotted white line drawn in the topography image. The line profile displays a $t$∼20 nm thick island next to a small $t$∼10 nm island. The simultaneous potential and its error measurements are shown in the lower panel [Fig. 5.33 (b)]. The two largest islands are now characterized by a bright halo at their edges, surrounding a darker contrast in the middle; the latter is still ∼60 mV above the substrate contrast [see the line profile in Fig. 5.33 (b')]. The potential we measure at the edges is around ∼60 mV above the value at the center of the island (i.e. 120 mV above the substrate surface). If we perform a statistical analysis of the potential difference between the substrate and the whole island (including both edges and center), we obtain the distribution plotted in Fig. 5.33 (b''), where two clear peaks are separated ∼100 mV; this is roughly the value expected from averaging the potential values of the island edge and center. All these observations point at possible differences in the electrical nature of the lateral and top facets of some of the islands. The fact that the bright halo at the island edges does not appear always (we do not see it, for instance, in the island of Fig. 5.32, although it has a similar thickness) suggests that it is not a measurement artifact. Indeed, the small nanoisland of Fig. 5.33 does not exhibit the *edge feature*. Instead, it shows a homogeneous ∼60 mV potential difference with respect to

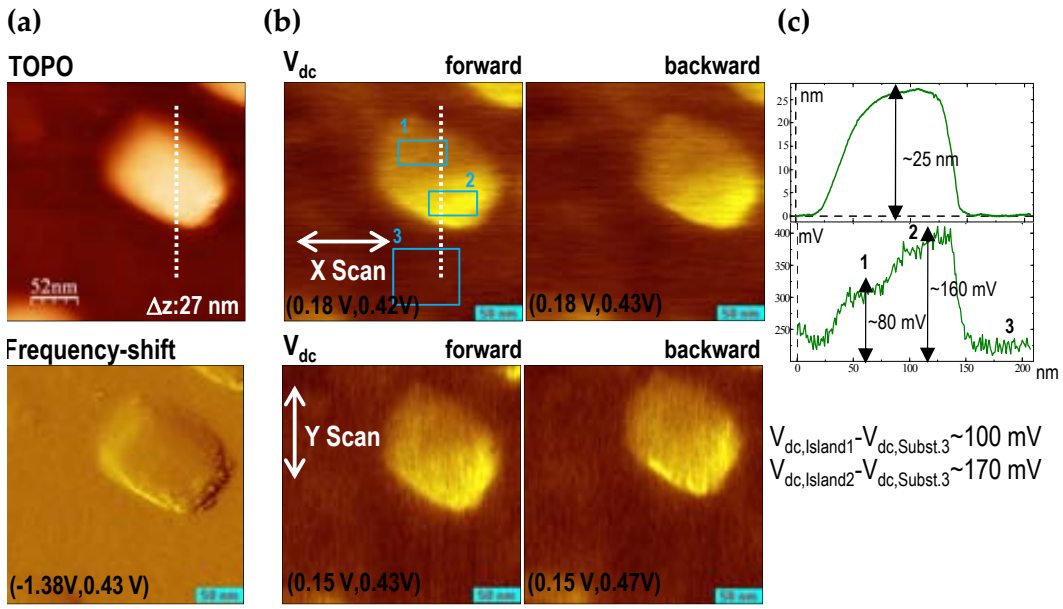


**Fig. 5.32:** *260nm×260nm images of a LSMO nanoisland on YSZ. (a) Topography and frequency-shift images. (b) Potential images acquired with the tip scanning in the X (0°, usual way) and Y (90°) directions. (c) Line profiles of the topography and $V_{dc}$ images, corresponding to the white dotted lines across the island. The values below are the potential differences of the two distinct halves of the island with respect to the substrate, calculated from statistic evaluation of the squares numbered 1, 2, and 3 in the $V_{dc}$ image.*

the YSZ substrate. In the $V_{dc}$ image it appears that the tip, with a radius of around $R$∼25 nm rapidly widening away from the apex, cannot fully resolve the small lateral separation between the large and the small island. A hypothetical effect of the lateral edges is thus not discernible. The small height of the island, however, implies very small lateral facets which suggest that the contrast we observe is mainly caused by the planar top facet. Note that this island, half the thickness of the previous discussed, exhibits the same ∼60 mV potential difference, which can be taken as a further indication that the signal we measure does not come from the topography.

As a matter of fact, the 'leakage' of topographical information into the potential channel is a major issue of concern, since it can lead to physical interpretation of measurement artifacts. It is especially challenging to disentangle the topography influence from purely electrostatic signals in cases like the present one, where the abrupt changes in the topography are accompanied by a change of material. The problem of the tip-sample convolution, common to all scanning force microscopies and already mentioned for MFM in Chapter 4, is indeed also present in KPFM. For the case of the electrostatic interaction, not only the tip apex contributes to the contrast observed at a certain *(x,y)* position, but other parts of the tip, further separated from the sample surface, will also contribute, since the electrostatic force is long ranged and the whole tip is conducting. Consequently, the contrast exhibited by a particular *(x,y)* spot will display a certain proportion of contrast belonging to other spots in the sample, which is one of the reasons why achieving lateral resolution in KPFM is harder than in topography measures, and why long tips with small opening angles are ideally required. In addition to lowering the resolution of the potential image, it was demonstrated that the convolution due to the tip-sample geometry may result in a

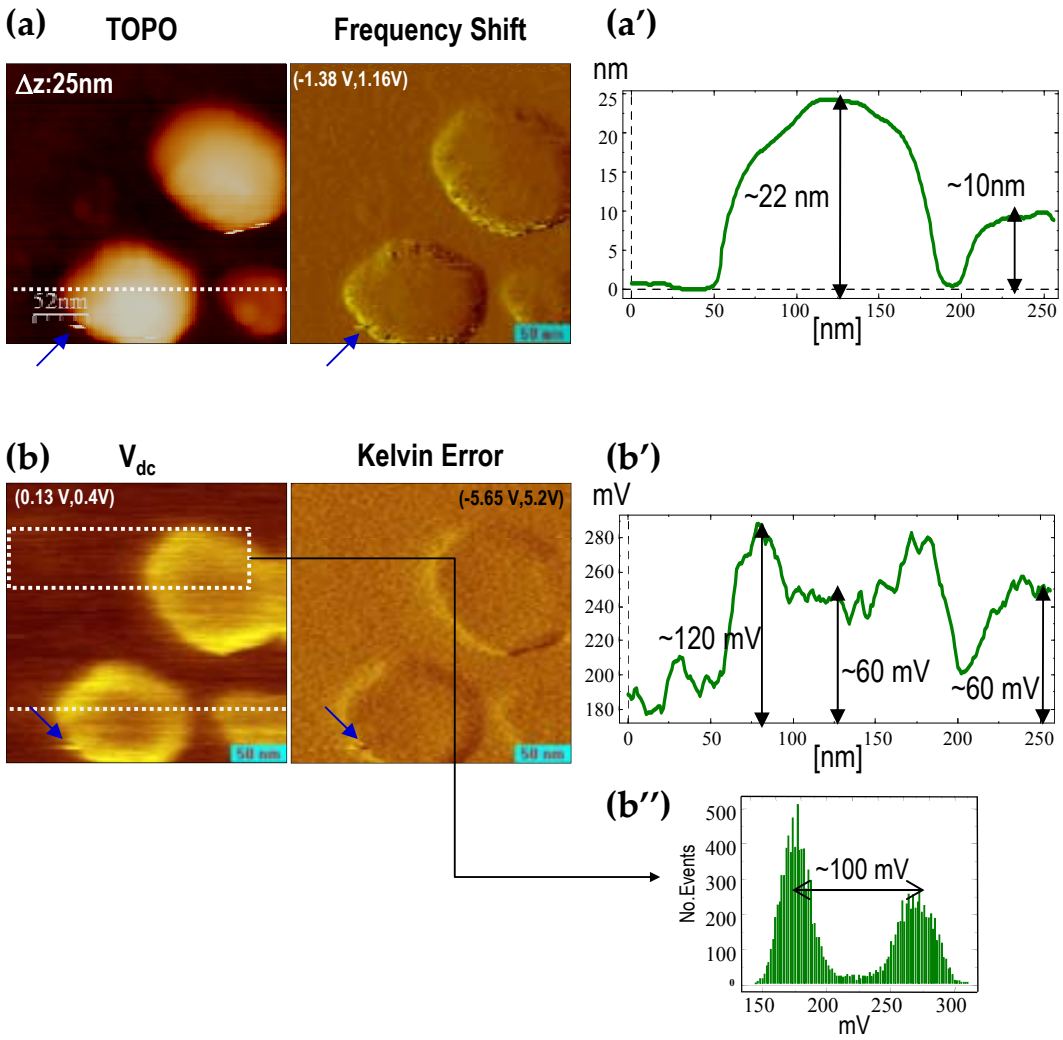


**Fig. 5.33:** *260nm×260nm images of LSMO nanoislands on YSZ. (a) Topography and frequency-shift images. (a′) Line scan corresponding to the dotted white line in the topography image (a). (b) Potential and Kelvin error images. (b′) Potential profile along the line marked in the $V_{dc}$ image in (b), revealing a higher potential at the island edges with respect to the center. No such feature is observed in the contrast belonging to the lowest (t∼10 nm) island, which exhibits a potential difference of ∼60 mV, analogously to the large island center. (b″) Potential distributions of the island and substrate regions within the dotted square area marked in (b). The mean difference between substrate and island (edges and center) is around ∼100 mV.*

certain cross-talk of the potential signal with the topography signal; this was named the 'topography artifact' by Morita and co-workers [319]. Such effects are mainly observed in the case of granular films with grain sizes of the order of or smaller than the radius of the tip [320]. In the case of our nanoislands ($D$∼100-250 nm), although we cannot fully rule out a partial contribution from the topography, it will emerge clearly from the analysis throughout this chapter that this is a secondary effect compared to the main signal. In line with this issue, Fig. 5.34 shows the topography and potential images of a LSMO nanoisland on top of a $CeO_2$ buffer layer. The topography image shows an ill-defined amount of material protruding from the darker substrate. By comparison with other islands in this sample (not shown) we are able to distinguish the squared shape of an island as the brightest contrast in topography, at the far edge of the protruding material (precisely on the position that says *c*). The material to the left of the island, in the spot *b*, is probably dirt attached to the island. The important fact here is that, although such unidentified material protrudes from the sample at least 30 nm, the potential contrast it shows is darker than that of both the real island contrast (the brighter spot, *c*) and of the substrate background. In brief, a protruding object does not necessarily lead to a bright contrast, which confirms that in the potential image we are not measuring topography but electrostatic interaction.

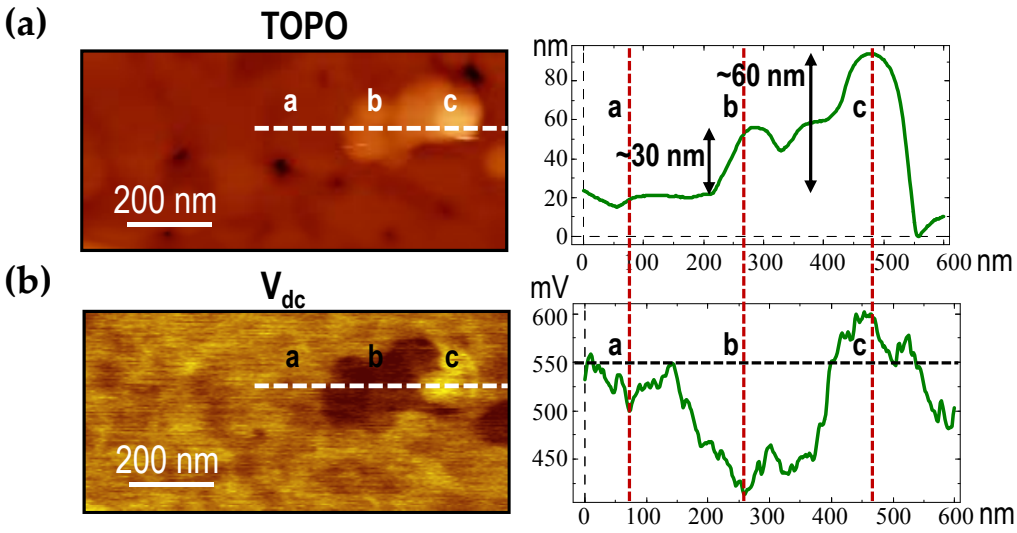


**Fig. 5.34:** *Topography (a) and potential (b) analysis of a LSMO nanoisland on a $CeO_2$ buffer layer. The line profiles at the right hand side correspond to the dashed white lines drawn in the images.* a, b *and* c *along the profile indicate positions on the buffer layer and on the protruding material.*

It is also pertinent at this point to mention the presence of topography-related artifacts in the potential images which result from feedback failures. The failure of the topography feedback will give erroneous normal force ($F_N$) values, which are the values that feed both the topography and the Kelvin feedback. This will thus be reflected in the component of the force $F_\omega$, responsible for the Kelvin feedback. Such feedback failures are of course more likely to occur at sudden height changes, as those taking place at the island-substrate boundaries. An example is evidenced with blue arrows in the images of Fig. 5.33. That kind of feature indicates a feedback failure, and one can find its fingerprint not only in the topography channels, but also in the potential images. Moreover, we may also note that it produces a bright yellow contrast in the $V_{dc}$ channel, which actually enhances the bright appearance of the island edges. Still, we may look at other places of the same island

edges where the substrate to island transition (most easily observed in the frequency-shift channel) is smooth, and is still accompanied by bright contrast in the $V_{dc}$ image. Consequently, although present, the feedback failures do not account for the great majority of the measured potential variations.

### 5.2.4 Analysis of the facet contrast in large LSMO nanoislands

The contrast variations between the insulating YSZ substrate and the LSMO nanoislands illustrated in the previous examples appear notably enhanced when looking at substantially larger LSMO islands, with thickness $t$ that go up to 80 nm and lateral sizes $D$ of around 200 nm. Fig. 5.35 exhibits the topography and potential images of three LSMO nanoislands of this type. The potential image in Fig. 5.35 (b) features a clear bright-dark double contrast within each island. We can also note that the dark contrast of the substrate surface is not uniform, but exhibits a certain 'color roughness', as if it were mixed with some kind of bright contribution. In fact, topography images of the substrate surface as the one shown in gray shades in the inset of Fig. 5.35 (a), give evidence of small islands on the YSZ substrate surface. These are very likely related to the presence of La and Mn on the YSZ surface, as we already pointed out in our discussion of the PEEM results (section 5.1.3). Consequently, comparison with samples characterized by a clean YSZ surface (e.g. the case discussed in the previous section) must be done with some caution.

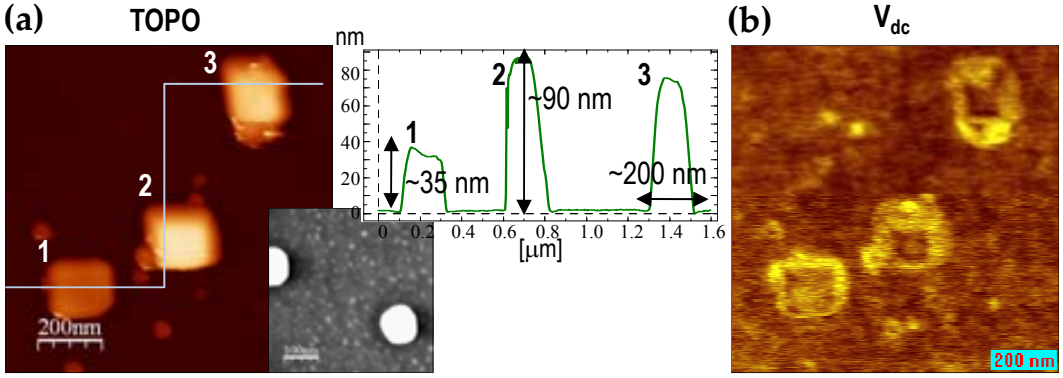


**Fig. 5.35:** *1$\mu$m×1$\mu$m topography (a) and potential (b) images of 'large' LSMO nanoislands on YSZ. The topography profile of the three islands, along the light-blue line in (a), shows the typical island sizes. The inset in gray shades, with saturated intensities, evidences the presence of material on the substrate surface in the form of little islands.*

A closer look at the nanostructures of Fig. 5.35 reveals the details of the contrast variation within them. Fig. 5.36 shows the topography and potential images of the island numbered *2* in Fig. 5.35 (a). This is a *regular-square* type of LSMO nanoisland (see Chapter 3) that exhibits $(001)_{\mathrm{LSMO}}$ top and lateral $(111)_{\mathrm{LSMO}}$ facets. The potential image in Fig. 5.36 (b) shows that these two inequivalent planes yield different potential values with respect to the bottom reference line: ∼50 mV for $(111)_{\mathrm{LSMO}}$ and ∼10 mV for the $(001)_{\mathrm{LSMO}}$. Statistical analyses of a large number of pixels within substrate, the top $(001)_{\mathrm{LSMO}}$ facets, and the lateral $(111)_{\mathrm{LSMO}}$ facets, give $V_{dc}^{subst.}$∼-9±10 mV, $V_{dc}^{top}$∼-11±10 mV, and $V_{dc}^{lat.}$∼35±10 mV, respectively. The voltage distributions for each are plotted in 5.36 (b''). From these values we can deduce that the substrate and the island top facets yield similar potential values

(within the error bars), while the potential necessary to nullify the $F_{el}$ on the $(111)_{\mathrm{LSMO}}$ facets is ∼45-50 mV larger.

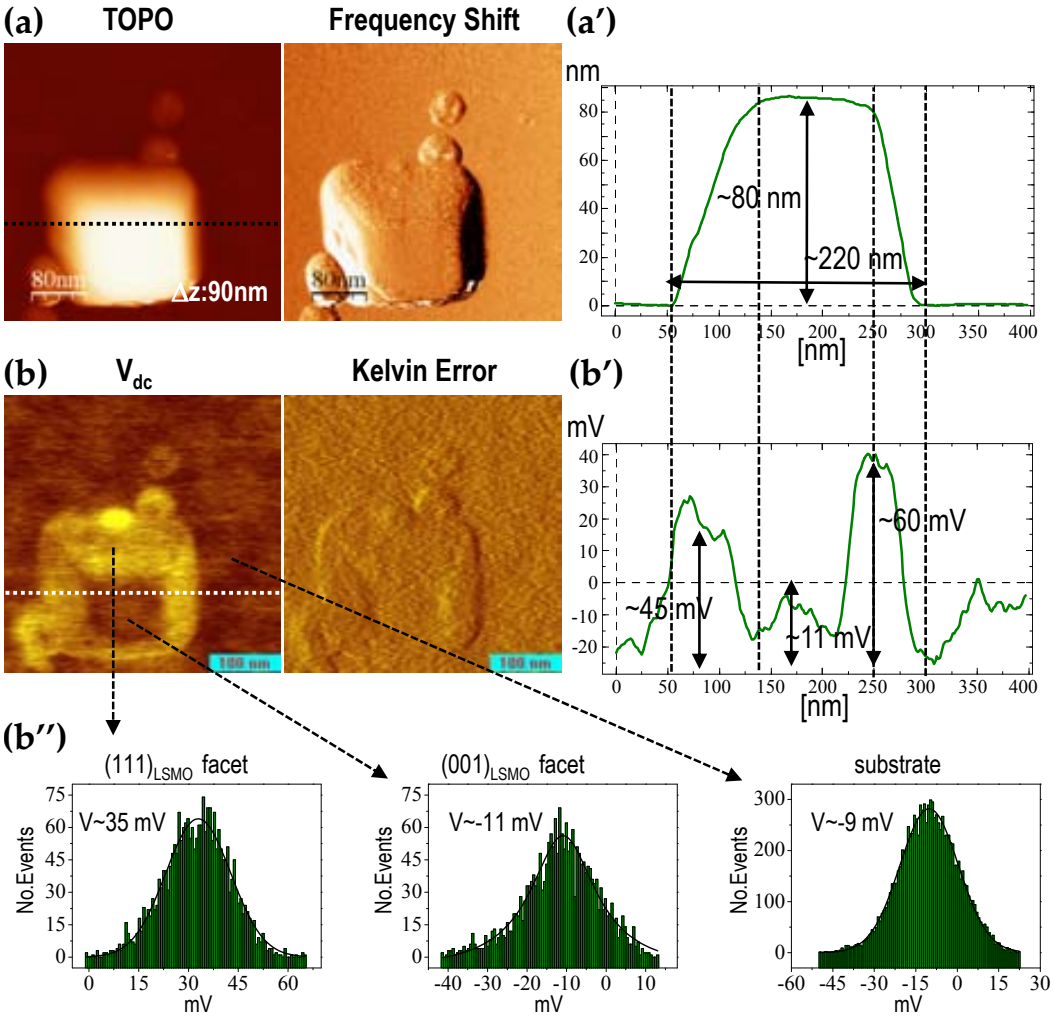


**Fig. 5.36:** *400nm×400nm topography (a) and potential (b) images corresponding to the 'large' nanoisland named 2 in Fig. 5.35. The dark to bright contrast variation, in the order of ∼40 mV, appears linked to the nature of the LSMO facet. The line scans in (a') and (b') are simultaneous topography and potential profiles, i.e. they correspond to the same spatial region, marked in dotted lines on the topography and $V_{dc}$ images (a) and (b). The graphs in (b") belong to the statistical potential distributions on the $(111)_{LSMO}$ facet, the $(001)_{LSMO}$ facet, and on the substrate.*

Fig. 5.37 shows the measurements of the island numbered *1* in Fig. 5.35. It is one of the *low* islands found in the present sample, with thickness $t$∼35 nm and a lateral size $D$∼225 nm. As in the island from Fig. 5.36, the top $(001)_{\mathrm{LSMO}}$ and the lateral $(111)_{\mathrm{LSMO}}$ facets yield different potential values. These contrast variations are quantitatively analyzed in the line-scan below the image, and also by comparing statistical analysis of the potential distributions within the regions with the same contrast; the resulting absolute values along with their standard deviation are shown in the potential images. Note, for instance, that the potential value of the $(111)_{\mathrm{LSMO}}$ facet is $V_{dc}^{lat.}$∼35±10 mV, i.e. ∼45 mV ($V_{dc}^{subst.}$∼-10±10 mV) with respect to the substrate potential. This is in excellent agreement with the contrast

variation observed in the island of Fig. 5.36, even if these two structures are remarkably different: $t$∼80 nm vs. $t$∼35 nm, which means that the $(111)_{\mathrm{LSMO}}$ facets have very different extension. These observations are in line with the assumption that the topography signal is not responsible for the observed contrast variations.

In addition to the orientation-dependent facet potential, we can also distinguish different types of contrasts within the top $(001)_{\mathrm{LSMO}}$ facet: the upper part shows a slightly darker contrast as compared to the lower part. Such contrast variation is identically observed in the backward scan (not shown) and in the 170 nm×170 nm potential image shown in Fig. 5.37 (b'). The latter scan was measured ∼1 h after the scan of Fig. 5.37 (b) and entirely reproduces the contrast variations there observed. In fact, by restricting the scan to the island center (plus a bit of the lateral facets) we avoid the abrupt transition of the tip from the substrate surface to the nanoisland. Consequently, the measurement is free of topography feedback failures, and, being identical to that of Fig. 5.37 (b), further supports our claim that the observed potential variations, exemplified in the previous images, have a real physical origin.

Although its thickness is not far from the values displayed by the islands of the previous sample [e.g. $t$∼22 nm in Fig. 5.33], the island of Fig. 5.37 features a notably larger lateral size. Such a difference in lateral size could explain why here the lateral facets can be clearly discerned from the top flat facet, while in the case of Fig. 5.33, the tip-nanoisland convolution precludes resolving these features. It is well likely, in fact, that a facet-dependent contact potential occurs in both samples, even if it's not well-resolved in Fig. 5.33 due to the smaller island sizes of that sample. We should note, nevertheless, that the lateral facets of the *rotated-square* morphology islands are not $(111)_{\mathrm{LSMO}}$ planes as in the present case (see Chapter 3). Therefore, such difference in the crystal nature of the facets, along with the fact that our reference substrate is also different in both samples (recall the presence of small islands in the second sample), should be noted before attempting to compare the magnitude of both contrast variations.

The facet-dependent contrast discussed above raises the natural question of what contrast yield the triangular LSMO nanostructures, which top facet and long lateral facets belong to the $111\ _{\mathrm{LSMO}}$ family of planes. Fig. 5.38 shows the simultaneous measurement of two interpenetrating square islands and a triangular LSMO nanostructure. The potential image of Fig. 5.38 (b) shows the average potential values inferred from the statistical analysis of the potential distributions within each blue square. Note that this latter measurement was performed on a different day, and that these values are at first sight very different from those of Figs. 5.36 and 5.37. However, the absolute numbers are not meaningful, as we have emphasized earlier in this KPFM section. Only the *differences* are important. We observe that, indeed, the tendency of 'dark top facet' and 'bright lateral facets' is reproduced for the square islands. In particular, the mean potential value of the top facets of the two merged square islands is $V_{dc}^{top}\sim -35\pm20$ mV [note that this is an average value, since there is a graduation of contrast from the upper (darker) to the bottom (brighter) part of the facets]. Taking this value as a rough estimate, the difference with respect to the brighter lateral $(111)_{\mathrm{LSMO}}$ facets ($V_{dc}^{lat}\sim -85$ mV, see the line scan) is of ∼50 mV, which is in good agreement with the variations between lateral $(111)_{\mathrm{LSMO}}$ and top $(001)_{\mathrm{LSMO}}$ facets measured in the square islands from the previous examples.

Moving now to the triangle, the contrast of the top facet appears fairly bright and uniform, and we do not see the clear change in contrast between the lateral and the top facets characteristic of square islands. Both the line scan and the statistical analysis show values

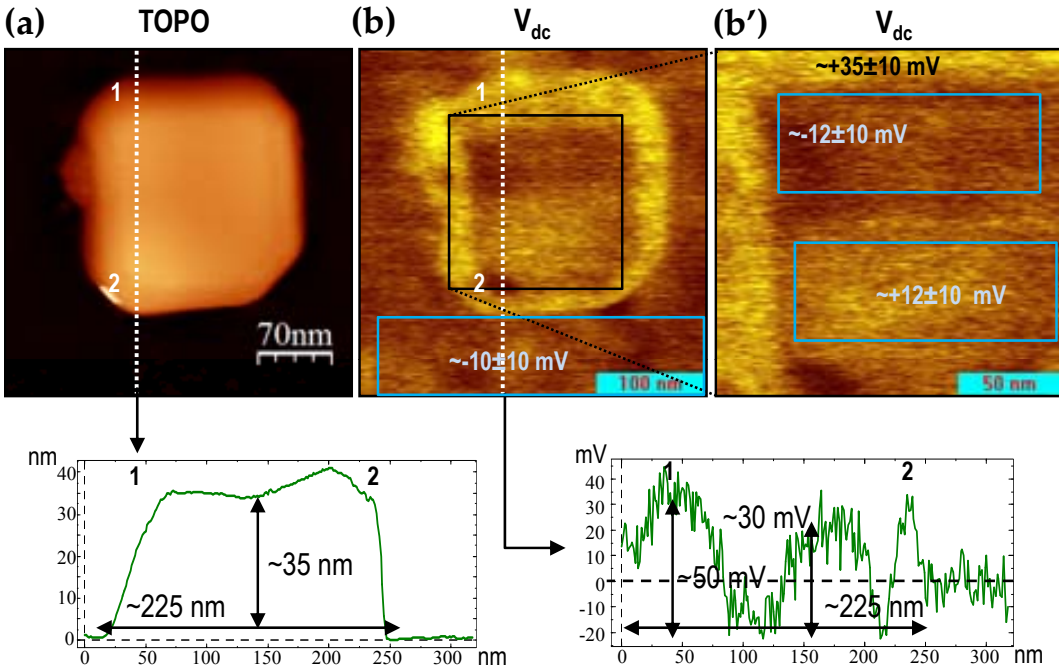


**Fig. 5.37:** *(a)&(b) 320nm×320nm topography and potential images corresponding to the nanoisland numbered* 1 *in Fig. 5.35. The line scans along the vertical dotted-lines in both images are plotted below. (b′) A new scan (170 nm×170 nm, potential image) shows the interior of the nanoisland potential distribution. The numbers given in (b) and (b′) represent the potential values at each distinct region of the nanoisland.*

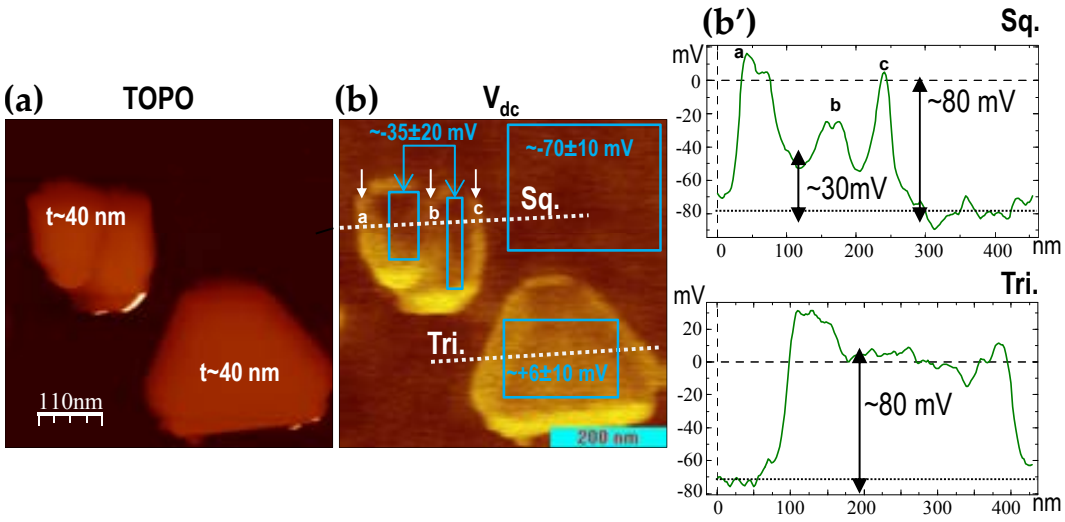


**Fig. 5.38:** *570nm×570nm topography (a), and potential (b) images of two merged square islands and a triangular (111) out-of-plane oriented island. The mean potential values of the distinct regions, marked in blue squares, are also indicated. (b′) Potential line scans of the square and triangular islands across the dotted white lines in (b).*

for the triangle $(111)_{\mathrm{LSMO}}$ top facet that differ by ∼80 mV with respect to the substrate surface. This value is much larger than that of the $(001)_{\mathrm{LSMO}}$ top facet of the square islands, both in the present image and in the previous examples. Conversely, it is in remarkable agreement with the value we obtain for the $(111)_{\mathrm{LSMO}}$ lateral facets of the square islands in Fig. 5.38, which is around ∼85 mV. Fig. 5.39 displays the topography line scans corresponding to the triangle and square islands in Fig. 5.38 [Fig. 5.39 (a) and (b), respectively] and the profile of the square island of Fig. 5.37. Note that the angle of the facets inferred from the line scans ($\alpha_{exp}$) is the result of the tip-radius/nanoisland-facet convolution: the angle of ∼71° between the 111 LSMO facets of the triangle is reduced to around ∼56°, while the $(111)_{\mathrm{LSMO}}$ lateral facets in the (b) and (c) square islands, at a theoretical angle of ∼54.7° from the substrate horizontal, differ from one another. We have already commented that the experimentally measured angles with this kind of tips and measurements does not provide for the real values. Nevertheless, the fact that the three islands in Fig. 5.39 exhibit very similar heights, lateral sizes, and experimental angles, supports the fact that the brighter contrast obtained for the triangular top-facet is due to its crystallographic nature. In other words, would the effect be topographical, we would expect, since the geometry of the islands and the resolved experimental angle are very similar, that the triangular island exhibited a depressed potential value in its central region, as in the case of the square islands. Instead, such central value, corresponding to the $(111)_{\mathrm{LSMO}}$ facet, remains higher, by around ∼50 mV, with respect to the potential exhibited by the $(001)_{\mathrm{LSMO}}$ facets.

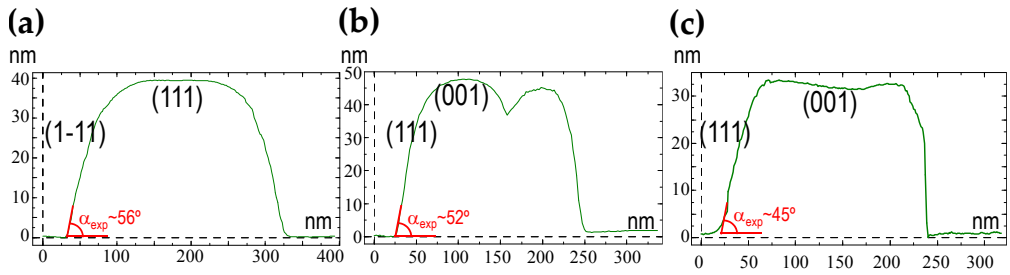


**Fig. 5.39:** *Topography line-scans comparing the geometrical features of: (a) the triangular island in Fig. 5.38, (b) the square islands in Fig. 5.38, and (c) the square island of Fig. 5.37. The lateral and top facets are labeled, as well as the experimentally measured facet angle.*

### 5.2.5 On the origin of the facet contrast: work function anisotropy

The results discussed until now reveal that there is a difference in potential of ∼50 mV between the $(111)_{\mathrm{LSMO}}$ and the $(001)_{\mathrm{LSMO}}$ crystal planes. We will see next that such potential difference can be related to the so-called *work function anisotropy*, i.e. the dependence of the work function $W$ of metal single crystals on the crystallographic orientation of the surface.

The work function $W$ of a finite-size metal is defined as the energy necessary to remove an electron from its Fermi energy level $E_F$ to a point in the vacuum just outside the solid. By the term 'just outside' we refer to a distance far larger than the interatomic distances but small with respect to the sample size [321]. The vacuum level *just outside* a solid $V_{vac}(s)$, depends on the chemical, atomic, and electronic structure of its surface layers through the so-called *electronic surface dipole* of the specific surface. Conversely, the vacuum level at infinity $V_{vac}(\quad)$ is invariant, and describes the energy of an electron at rest at infinite distance

from the solid [322]. This $V_{vac}(\quad)$ is not experimentally accessible [322, 323] and thus it is not relevant in real measurements, and in the following we shall therefore exclusively refer to $V_{vac}(s)$. The energy difference between these two levels is caused precisely by the presence of the surface dipole layer , which, in general, causes the vacuum level of the solid to raise from that at infinity.

The surface dipole has its origin on the spreading of the electronic charge density towards the vacuum, which occurs at the surface of a solid [324] [see Fig. 5.40 (a)]. In a nearly-free electron metal (which is not the case of LSMO), this is typically explained through the simple jellium model. Within the bulk of the crystal there is no dipole since the constant background positive charge, modeling the ion cores, is neutralized by an equal and opposite electronic charge. At the surface, however, due to their quantum-mechanical nature, electrons prefer to penetrate slightly into the vacuum region to lower their kinetic energy. A surface dipole thus forms. This 'spilling out' of the electron cloud causes a negative pole to stick out of the surface, inducing a potential step or dipole barrier $V_e$ [see Fig. 5.40 (b)] [317]. In order to escape from the metal, the electron must overcome such barrier. For the electrons in the last occupied energy level, $E_F$, the barrier they must surmount is precisely the work function of the metal $W$=$V_e$-$E_F$. Notice that in Fig. 5.40 (b) we have written explicitly $V_{vac}(s)$ in relation to the electrostatic potential just outside the solid. According to what we said above, for distances far away from the solid such level will converge into the $V_{vac}(\quad)$ [323]. The reference energy in the diagram is $< V >$, the average electrostatic potential within the bulk of the metal [325], i.e. $V_e$=$V_{vac}(s)$-$< V >$.

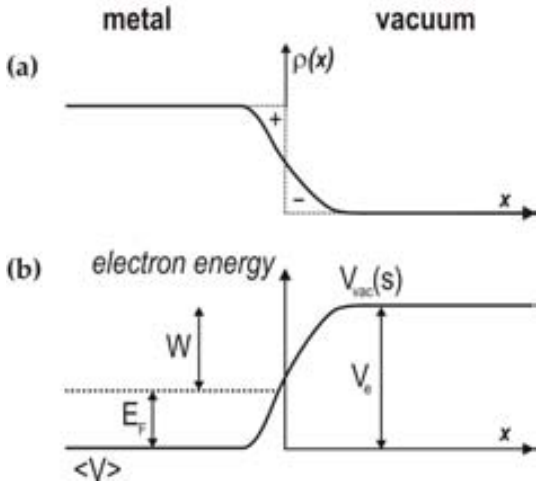


**Fig. 5.40:** *(a) Electronic density distribution at the surface of a metal. The spreading of the electron cloud gives rise to the surface dipole. The 'thickness' of the dipole layer is in the order of some angstroms [324, 326].(b) Energy levels at the metal/vacuum interface. The work function of the metal, W, is directly related to its surface dipole ($W$=$V_e$-$E_F$).*

Nevertheless, this simple model is not sufficient to explain the work function anisotropy: a jellium surface is a flat and structureless plane. An elegant solution to this problem was given in 1941 by Smoluchowski [327]. The idea is quite intuitive: one just needs to consider, instead of a flat jellium surface, a *corrugated* one. The conduction electrons will slightly penetrate in the vacuum, as before, giving rise to the surface dipole. In addition to this surface

And, in insulating materials, also by extra charges on the sample surface [322].

dipole, which sticks out of the surface normal to the surface and increases $W$, however, electrons will also redistribute laterally (a corrugated electron cloud costs energy, i.e. better to 'smooth it out'). This means that some negative electron charge will 'drip inwards', leaving the positively charged ions of the jellium surface 'uncovered'. In other words, the so-called Smoluchowski smoothening [325] causes a *reverse dipole* which tends to lower the work function. The more corrugated the surface (i.e. less close-packed), the lower the work function, as a result of this effect. Therefore, for SC, BCC, and FCC Bravais lattices it is expected that the work functions $W$ of (100), (110), and (111) facets, respectively, to be the largest. These predictions were theoretically [324] and experimentally [328] confirmed .

In the case of KPFM on LSMO nanoislands, work function variations from one crystal facet to another should be probed, provided that the tip to sample distance $z$ is short compared to the lateral size of the facet, but large enough that the image potential effects are negligible there. Under such conditions we can detect the corrugation of the electrostatic potential related to the work function anisotropy discussed above. We talk in this case of local work function measurements (see references [325, 326] for in-depth treatments of this issue). In contrast, when the probe is drawn far from the sample (or, analogously, the sample is very small with respect to tip-sample distance) the local potential becomes isotropic, i.e. at sufficient distance from the metal the sample has only one well-defined work function [318, 323, 326]. Fig. 5.41 shows a sketch drawn at scale of the KPFM measurement of a LSMO nanoisland. Note that our parameters meet the criteria for local work function measurements, and thus we expect our data to give reliable indications about the work function anisotropy in LSMO.

The general concepts outlined above to explain the nature of the surface dipole and of work function anisotropy are best suited for nearly-free electron metallic systems. Complex oxide metals such as LSMO are, however, very different metals. Note that LSMO surfaces have remained vastly unexplored until now, and the microscopic mechanisms leading to the formation of a surface dipole in LSMO are still unknown. For example, it is likely that the electron spill out, or even the Smoluchowski effect might not be relevant at all in this system, given the nature of the metallic state in LSMO (definitely not free-electron like). Conversely, there are other effects here that are absent in elemental metals, e.g. lattice distortions, and the possibility of having many different terminations or reconstructions for a given surface orientation. Also, the fact that we are dealing with a multicomponent compound raises concerns about the possibility of surface segregations, or yet other phenomena related to structural and/or chemical defects, added to a possible surface contamination (like water or carbon). All these effects are likely to be essential for determining the final surface dipole. Addressing this subject, therefore, would require further experimental and, very importantly, substantial theoretical efforts.

Also, concerning our specific experimental setup, we cannot be sure that the island remains at a fixed potential during the scan; indeed (see Fig. 5.41) the sample-holder is grounded, but the island lies electrically isolated, separated by the YSZ substrate. This means that one should use some care when interpreting the contact potential differences. On the other hand, the degree of repeatability of our measurements and the sharp contrast between facets suggest that the above (i.e. that the island remains at a constant potential) might be a reasonable assumption. If this is the case, our data indicate a difference in local work function of $\sim$50 meV between the $(111)_{\mathrm{LSMO}}$ and $(001)_{\mathrm{LSMO}}$ facets of the LSMO

Exceptions to this are found, for instance, in Al and Pb, FCC metals, in which the (100) plane exhibits the largest $W$ [324].

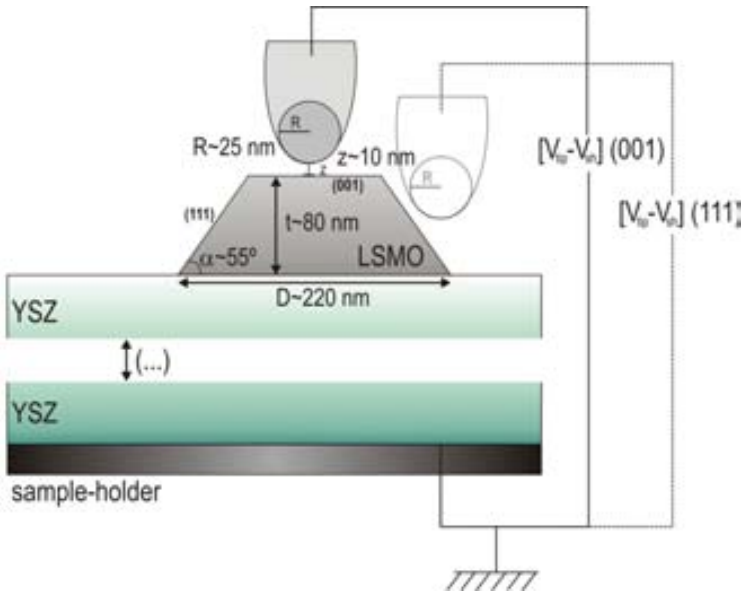


**Fig. 5.41:** *Schematic diagram, drawn at scale, of the KPFM measurement of a LSMO square-base pyramid nanoisland. We have selected the island thickness $t$ and lateral size $D$ to be those of the nanoisland of Fig. 5.36, since its potential image shows a clear contrast between the $(111)_{LSMO}$ and the $(001)_{LSMO}$ facets. The tip to sample distance $z$ and the tip radius $R$ are also drawn at scale. Note how the extension of the LSMO facet is large enough to contain the whole probe width. On the other hand, $z$ is small enough to probe $V_{vac}(s)$, i.e. the electrostatic potential 'just outside' the facet.*

nanoislands. The contact potential was higher at the $(111)_{\mathrm{LSMO}}$ facet, which implies a larger work function at the $(001)_{\mathrm{LSMO}}$ facet (taking into account the negative sign of the electron charge).

### 5.2.6 Conclusions

Throughout this section we have studied the KPFM measurements on self-assembled LSMO nanoislands grown on YSZ substrates. After a general overview of the technique, we have described the experimental set-up used for sample imaging. Particular emphasis was given to the fact that the LSMO nanoislands lie on an insulating massive substrate. This makes the measurement especially challenging, both from a practical point of view (concerning the stability of the imaging process) and from a conceptual perspective. Regarding the latter, we have shown that the measured potential difference between the YSZ substrate and the LSMO nanoisland is independent from the contact potential difference between the tip and the sample holder, as deduced from considering the metallic tip and sample-holder as a parallel-plate capacitor system, with the YSZ/LSMO system sandwiched in between. Careful measurements of individual islands have revealed a contrast difference of $\sim$50 mV among the $(111)_{\mathrm{LSMO}}$ and $(001)_{\mathrm{LSMO}}$ crystallographic planes. This contrast is especially clear in the largest nanoislands, where the tip can better resolve the potential variations due to a smaller tip-island convolution. The difference in work function between the different crystal facets of a metal is a well known issue, which has been widely investigated in simple metals but very little in complex oxides. Differences in the electric surface dipole, caused by variations in the spreading of the electronic density towards vacuum, lie at the

base of such work function anisotropy. According to our results, the $(001)_{\mathrm{LSMO}}$ facet exhibits a higher work function than the $(111)_{\mathrm{LSMO}}$ by around $\sim$50 mV. LSMO is a multicomponent oxide and thus its facets can display different terminations [e.g. either (La,Sr)-O or Mn-$O_2$, or a mixture of the two in the case of the $(001)_{\mathrm{LSMO}}$ plane]. The specific characteristics of the LSMO nanoisland facets are unknown at this stage. To ascribe the measured potential differences to a particular combination of terminations and to further assess the implications of our findings require for joint experimental and theoretical efforts.

# General Conclusions

In this work we have explored nanoscale $La_{0.7}Sr_{0.3}MnO_3$ heteroepitaxial systems grown by a solution-based methodology onto different oxide single crystal substrates, including STO, LAO, YSZ, and MgO. The main results of this study are summarized in the following:

First, we have demonstrated that chemical solution deposition (CSD) is a successful approach for the fabrication of high quality epitaxial ferromagnetic LSMO ultra-thin films and 3D nanostructures. We have seen that, following identical growth procedures based on ultradiluted LSMO precursor solutions, the final system configuration relies on the choice of the substrate. In particular, ultra-thin LSMO films with thickness below $\sim$10 nm are obtained on STO and LAO perovskite substrates, whereas onto YSZ fluorite and MgO rock-salt substrates, homogeneous dispersions of self-assembled nanoislands are achieved. These results are the experimental evidence of the key parameters ruling heteroepitaxial growth: elastic strain energy, and surface and interface energies. In the heteroepitaxy formed by two perovskite structure crystals, where the interface energy is expected to be low and the lattice mismatches are below 2%, LSMO grows in a thin-film configuration (onto STO and LAO). Conversely, the structural dissimilarity between LSMO and YSZ and MgO, along with the high lattice mismatches, brings the manganite to build into a 3D form.

Ultra-thin LSMO films on STO and LAO exhibit remarkably flat surface morphologies, with the tendency to reproduce the underlying substrate's step-terrace architecture. This trend is more pronounced for STO substrates, which display a very low $\epsilon\sim$0.9% lattice mismatch against LSMO ($\epsilon\sim$-2% for LAO). As a matter of fact, the role of elastic energy is univocally manifested in that LSMO grows fully strained onto STO, while the larger mismatch with respect to LAO triggers LSMO to partially relax through misfit dislocations. The latter result contrasts with fully strained LSMO on LAO thin films, grown by vapor deposition techniques, reported in the literature. Furthermore, it highlights how the crystallization pathways and, consequently, the film microstructure, deeply depend on the processing route. Solution-derived LSMO ultra-thin films are found to be highly crystalline and epitaxial, and show no secondary phases. The versatility of CSD, in turn, is evidenced in the ability to tune the system of self-assembled nanoislands (i.e. the island size and density) by acting upon the solution concentration, the annealing times, and temperatures. Optimal precursor solution concentrations in the 0.015 M to 0.03 M (in Mn) range, and typical heat treatments at 900°C for 1 h to 3 h, yield highly uniform nanoisland ensembles. The amount of material in the nanostructured templates is given in terms of the equivalent thickness parameter, which varies from 1.5 to 3.5 ($\pm$0.5) nm for the above concentrations. In general, dense nanoisland dispersions are formed on MgO, featuring islands with mean thickness $t\sim$7 nm and lateral sizes $D\sim$50 nm. Nanostructures on YSZ typically exhibit larger thickness values of $t\sim$20 nm and lateral sizes $D$ of around 100 nm. Anyhow, for these processing

conditions, nanoislands do not surpass the 200 nm of lateral size, which is already below the sizes commonly reached by lithography methods.

XRD pole-figure analyses have shown that LSMO nanoislands on YSZ exhibit a majority population of $(001)_{\mathrm{LSMO}}$ out-of-plane oriented nanoislands, which exhibit two possible morphologies, regular-square and rotated-square, suggesting that distinct manganite crystal planes have similar surface energies. A minority triangle-shaped population was seen to display the $(111)_{\mathrm{LSMO}}$ out-of-plane orientation. Meanwhile, LSMO on MgO shows a single population of cube-on-cube grown $(001)_{\mathrm{LSMO}}$ nanoislands, with an in-plane rotated-square morphology displaying edges parallel to the <110>$_{MgO}$ substrate step edges. TEM investigations have demonstrated that LSMO nanoislands on YSZ and MgO are highly relaxed.

Concerning the magnetic properties of the solution-derived LSMO ultra-thin films and nanoislands, we have shown evidence of Curie temperature values around $\sim$350 K, i.e. close to reported bulk LSMO values, whether fully strained LSMO on STO, partially relaxed LSMO on LAO, or LSMO sub-200 nm lateral size nanoislands on YSZ. These are remarkable results considering the well documented tendency of vapor-deposited LSMO thin films to show depressed $T_C$ values at very low film thicknesses, as well as taking into account the sub-200 nm lateral size of the nanoislands. Transport measurements in ultra-thin LSMO/STO and LSMO/LAO systems have shown that above average thicknesses of $\sim$5.5 nm such films exhibit a metal-insulator transition which occurs at $T_{MI}$ values well below their ferromagnetic-paramagnetic transition (measured at $T_C\sim$350 K). Increased MR values have also been measured. An Anderson type of 2D localization in this very thin films, and the presence of structural or chemical disorder may be at the basis of these findings. To be able to shed more light into the physical mechanisms responsible for these results a deeper study is, however, in order.

The saturation magnetization in both ultra-thin LSMO films and LSMO nanoislands on YSZ was seen to be in the order of the reported values. For the LSMO on YSZ nanoisland system, however, we have found a trend towards lower magnetization with decreasing solution concentrations, i.e. with decreasing nanoisland size. The latter was explained in terms of a ferromagnetic dead-layer on the surface/interface of the nanoislands, which effect is enhanced for smaller islands (larger surface to volume ratios). We have also calculated the role of the different anisotropy contributions on the LSMO/YSZ nanoisland system, which features a biaxial in-plane anisotropy with the [110]$_{LSMO}$ in-plane easy axis, and a magnetocrystalline anisotropy constant value $K_1$(150 K)=-(5$\pm$1) kJ/m$^3$, measured for the first time in LSMO nanoislands. The exception to the good magnetic properties of these heteroepitaxial systems was found in the LSMO on MgO nanoislands. Their depressed magnetic behavior was discussed in terms of the strain state around dislocation cores, of the presence of a dead layer, and of the chemical interdiffusion between Mn and Mg. The latter mechanism is suggested by recent STEM-EELS evidence of Mn in the MgO substrate, and is currently under study.

The system of self-assembled ferromagnetic sub-200 nm lateral size LSMO nanoislands grown onto YSZ comprises a novel and challenging system. Moreover, it features many of the characteristics that are required from building blocks of potential devices, as discussed in the introduction of this work. These include room temperature ferromagnetism, high spin polarization, and sub-200 nm lateral size. Unveiling the functional nanoscale properties of these nanoislands was thus found of utmost interest, and has lead us to investigate them using MFM, PEEM and KPFM . These are all advanced techniques, in the sense that they are continuously evolving, they implement cutting-edge technologies, and in that

their characterization potential is at the frontier of knowledge, thus yielding both new discoveries and insight into them. We have given a general overview of these techniques, as well as emphasized the optimization of the experimental procedure. This has implied tuning the MFM operation through the choice of the appropriate magnetic tip, optimizing the necessary metal capping for PEEM experiments, and dealing with the challenge of an insulating substrate and its implications in KPFM measurements.

The MFM study of self-assembled LSMO nanoislands on YSZ has shown that different magnetic configurations arise from the interplay between nanoisland lateral size and thickness. This information is not accessible from macroscopic magnetometry measurements. In particular, we have identified single domain, multidomain, and vortex state configurations, in agreement with micromagnetic simulations. The vortex state appears in platelet-like nanoislands, when the competition between exchange energy and magnetostatic energy results in the in-plane curling of the magnetic moments, with an out-of-plane singularity at the center, known as the vortex core. The limited resolution of the MFM (around $\sim$50 nm) and the small size of the nanoislands prevent from discerning their internal domain structure. However, the presence of the vortex core is well defined, as we conclude from the series of analyses done for a large number of nanoislands. We have also investigated the evolution of the ferromagnetic nanoislands under in-plane magnetic field. The vortex core appears to move parallel to the applied field, instead of perpendicular, as expected from a canonical vortex state. Further experiments and simulations are underway to give insight into these observations, which could be triggered by the specific characteristics of the nanoislands (their magnetocrystalline anisotropy, the truncated pyramid shape...etc.).

With respect to PEEM, by means of XAS studies we have concluded that LSMO on YSZ nanoislands exhibit the $Mn^{3+}$ $Mn^{4+}$ ratio expected from the stoichiometric $La_{0.7}Sr_{0.3}MnO_3$ compound. We have also shown experimental evidence suggesting the presence of $Mn^{2+}$ on the topmost surface layers, which can be related to the ferromagnetic dead layer responsible for the overall magnetization decrease measured by SQUID. XMCD experiments at room temperature and at 110 K have demonstrated that $(111)_{\mathrm{LSMO}}$ out-of-plane oriented triangular nanoislands exhibit a vortex configuration, which we could not address by MFM because of the tip stray field. Furthermore, these vortices were seen to evolve towards a single domain state under in-plane external field, and to do so showing the expected vortex movement (core displacement perpendicular to the applied field).

Finally, KPFM measurements on LSMO nanoislands have opened the path to the local electrostatic characterization of nanoscale complex oxides, bringing interesting results and a number of questions regarding the underlying physical phenomena. In particular, we have observed that distinct crystallographic LSMO planes, namely $(001)_{\mathrm{LSMO}}$ and $(111)_{\mathrm{LSMO}}$, yield different electrostatic interaction with the conducting microscope probe. This is manifested in a relative potential variation of around $\sim$50 mV between the two facets, suggesting that $(001)_{\mathrm{LSMO}}$ crystallographic planes have a $\sim$50 meV larger work function than $(111)_{\mathrm{LSMO}}$ planes. The difference in work function among different crystal facets of simple metals is a well established issue, known as the work function anisotropy. This phenomenon, however, is best understood in the context of nearly-free electron metal systems. Hence, its implications in the complex multicomponent LSMO oxide are not straightforward and will require joint experimental and theoretical efforts.

In conclusion, this work has described the growth of nanoscale ferromagnetic manganite systems and their comprehensive characterization. On one hand, the scalability and cost-effectiveness of the solution-based approach, together with the nanometric dimension

and the magnetic properties of the manganite, meet the demands of the ever progressing nanotechnology field. On the other hand, the insight into the local properties of these systems opens new perspectives towards the exploration and understanding of nanoscale phenomena.

# List of Abbreviations

**2D** ..... Two-dimensional
**3D** ..... Three-dimensional
**AFM** ..... Atomic force microscopy
**BCC** ..... Body centered cubic
**CCD** ..... Charge-coupled device
**CMR** ..... Colossal magnetoresistance
**CPD** ..... Contact potential difference
**CSD** ..... Chemical solution deposition
**DE** ..... Double exchange
**DOS** ..... Density of states
**$E_F$** ..... Fermi energy level
**EELS** ..... electron energy loss spectroscopy
**FCC** ..... Face centered cubic
**FFT** ..... Fast Fourier transform
**FM** ..... Ferromagnetic
**FMR** ..... Ferromagnetic resonance
**FWHM** ..... full width at half maximum
**GMR** ..... Giant magnetoresistance
**GPA** ..... Geometric phase analysis
**HAADF** ..... High angular annular dark field
**HRTEM** ..... High resolution transmission electron microscopy
**KPFM** ..... Kelvin force probe microscopy
**LAO** ..... $LaAlO_3$ Lanthanum aluminate
**LSMO** ..... $La_{0.7}Sr_{0.3}MnO_3$ Strontium-doped lanthanum manganite
**LZO** ..... $La_2Zr_2O_7$ Lanthanum zirconate
**MBE** ..... Molecular Beam epitaxy
**MFM** ..... Magnetic force microsopy
**MOKE** ..... Magneto-optical Kerr effect
**MR** ..... Magnetoresistance
**(M)RAM** ..... (Magnetic) random access memory
**PEEM** ..... Photoemission electron microscopy
**PID controller** ..... Proportional Integral Derivative controller
**PLD** ..... Pulsed laser deposition

**PPMS** ..... Physical properties measurement system

**RMS** ..... Root mean square

**RT** ..... Room temperature

**SC** ..... Simple cubic

**SOFC** ..... Solid oxide fuel cells

**SP-STM** ..... Spin-polarized Scanning tunneling microscopy

**SPM** ..... Scanning probe microscopy

**SQUID** ..... Superconducting quantum interference device

**SRT** ..... Spin reorientation transition

**STEM** ..... Scanning transmission electron microscopy

**STM** ..... Scanning tunneling microscopy

**STO** ..... $SrTiO_3$ Strontium titanate

$T_C$ ..... Curie temperature

$T_{MI}$ ..... Metal-insulator transition temperature

**TEM** ..... Transmission electron microscopy

**TEY** ..... Total electron yield

**UHV** ..... Ultra-high vacuum

**XANES** ..... X-ray Absorption Near Edge Structure

**XAS** ..... X-ray absorption spectrum

**XMCD** ..... X-ray magnetic circular dichroism

**XRD** ..... X-ray diffraction

**XRD$^2$** ..... 2D X-ray diffraction

**YSZ** ..... $Y_2O_3$:$ZrO_2$ Yttria-stabilized zirconia

# Appendix A

# Experimental Techniques

In this section we briefly describe the main characteristics of the techniques that have been routinely used to characterize the $La_{0.7}Sr_{0.3}MnO_3$ (LSMO) nanoscale systems object of this work. These include: surface topography characterization by means of Atomic Force Microscopy (AFM), structural study using X-ray Diffraction (XRD) and Transmission Electron Microscopy (TEM), and magnetic and electrical characterization using Superconducting Quantum Interference Device (SQUID), Ferromagnetic Resonance (FMR), and transport measurements. Each of these techniques involves scientific and operating principles, as well as technical details that could lead to extensive descriptions. The aim of this appendix, however, is to provide the reader with a general idea of the working principles of these techniques and with the information of the specific measurements performed with them and of the instruments used.

## A.1 Atomic Force Microscopy

Atomic Force Microscopy, AFM, was created in 1986 [329] as a further development of Binnig and Rohrer's first scanning probe microscope (SPM), i.e. the Scanning Tunneling Microscope, in 1982 [330]. As part of the SPM family, AFM measures the interactions between a sharp probe (the *tip*) and the studied sample with nanometric or even atomic lateral resolution. The *nm* range distance between the tip and the sample enables sensing very small forces in the $10^{-13}$-$10^{-5}$ N range [221]. The specific property being measured depends on the nature of the force sensed by the tip (repulsive, attractive Van der Waals, magnetic, electrostatic...). This thesis widely treats the operation principle of SPM in its Magnetic Force Microscopy (MFM, Chapter 4) and Kelvin Probe Force Microscopy (KPFM, Chapter 5) variants, i.e. SPM techniques related to the measurement of magnetic and electrostatic properties, respectively. In turn, for the topography studies of LSMO ultra-thin films and 3D nanostructures described in Chapter 3 we have used systematically AFM, sensing the attractive Van der Waals forces between the tip and the sample in the Dynamic mode.

Sharp AFM tips typically have apex radii below the ∼20 nm, and are fabricated on Si or $Si_3N_4$. Their sharpness and the fact of approaching the tips at distances below the ∼30 nm from the sample enables lateral and vertical resolutions of around ∼0.1-0.2 nm and ∼1 nm, respectively [221, 230]. Tips sit at the end of a soft spring called the cantilever, also known as the force detector. The sensitivity of the cantilever to the interactions is determined by

its geometry and its mechanical stiffness. The force constant $k$ of the cantilever is therefore given by $k = Ew^3t/4l$, where $E$ is Young's modulus, $w$ is the lateral width (with typical values ∼10-30 m), $t$ is the thickness (∼3-5 m), and $l$ is the length (∼100-300 m). Cantilevers are also made of silicon or silicon nitride, by means of standard microfabrication techniques [331].

The forces between the tip and the sample are detected by measuring the bending and the torsion suffered by the cantilever due to the specific interactions at play. In the optical detection mode, a laser beam is focused on the rear side of the cantilever, at the end of which sits the tip, and its reflection is detected by a Position Sensitive Photo Diode (PSPD) (see Fig. A.1) The PSPD senses the shifts in position of the laser spot while the tip is scanning the sample. Upon comparing the signal measured with a user-specified set-point, an electronic feedback system sends the signal to the piezoelectric tubes under the sample to retract or expand in order to re-establish the value of the set-point. Such contractions/expansions are registered and form the topography images, which is hence a constant-deflection image. The piezoelectric tubes under the sample control not only the $z$ movement, but also the $xy$ scanning. Typical $x - y$ scan areas range from $0.5$ m $\times$ $0.5$ m up to $20$ m $\times$ $20$ m.

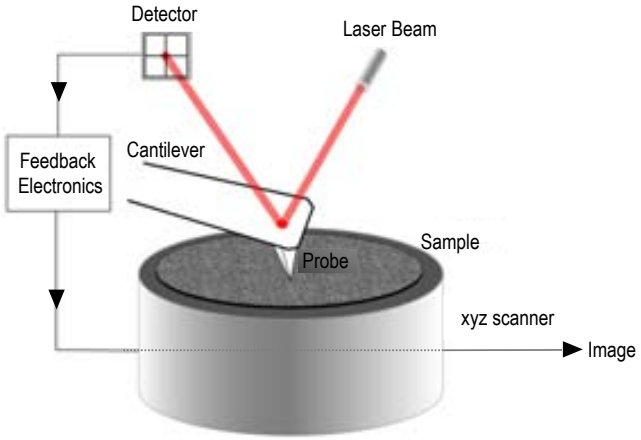


**Fig. A.1:** *Schematic diagram of a AFM set up featuring the optical laser-reflection detection mode. Adapted from [332].*

The AFM can operate in a variety of modes mainly depending on the environmental conditions and on the goal of the measurement [333]. In the *static* or *contact* mode, the tip is in mechanical contact with the sample surface and the forces are sensed through the bending and torsion of the cantilever mentioned above. The vertical deflection of the cantilever provides topography information while lateral deflection or torsion can be used to measure friction and wear properties of the sample. Electrical conduction measurements also require that tip and sample are in contact. Typical cantilever force constants for contact mode operation are very low, in the 0.01-1 N/m range. In the *dynamic* mode operation, which includes intermittent and non-contact modes, the cantilever is set to oscillate near its resonance frequency, at distances typically below the ∼30 nm from the sample surface. The forces between tip and sample are thus sensed by measuring the changes produced in the cantilever's oscillation amplitude, frequency, and phase, when the tip gets close to the sample [222]. Stiffer cantilevers are used, with force constants typically between 10-80 N/m and resonant frequencies in the 100-500 kHz range. Dynamic operation prevents tips

from wearing off so quickly and also damaging soft samples. It is used in ambient, liquid, and vacuum environment, and, besides providing topographical information, it can be used for the magnetic and electrostatic imaging of the sample with nanometric resolution (as explained in Chapters 4 and 5 of this thesis). Fig. A.2 shows the dependence of the tip-sample force with their separation, as well as the typical ranges where Contact and Non-Contact modes operate. Interleave refers to large distances usually used in lift-mode operation, where each line is scanned twice, one scan near the surface, the other scan away from it. At distances between ∼1 nm to ∼500 nm the interaction is attractive (<0) and below 1 nm it becomes repulsive due to the overlap of electronic orbitals upon decreasing the distance [334].

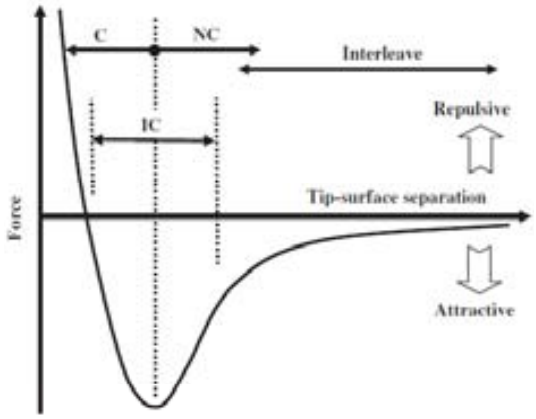


**Fig. A.2:** *Schematic diagram of the force dependence with sample-tip separation. The range of distances at which different modes operate are indicated: Contact (C), Intermittent contact (IC), and Non-Contact (NC). Reproduced from [334].*

Surface topography characterization of the nanoscale LSMO heteroepitaxys was performed in air, at room temperature, and, typically, in the intermittent contact mode. Three AFM equipments, located at ICMAB, were used for such purpose: an Agilent 5100, an Agilent 5500 LS (both from Molecular Imaging), and a Cervantes AFM (from Nanotec). Prior to imaging, samples were systematically cleaned with acetone and methanol in an ultrasonic bath. We used Si tips from Nanosensors, mounted onto rectangular Si cantilevers with force constants $k$ around 40 N/m, and resonance frequencies in the 300-400 kHz range. The suppliers give tip radius values below ∼10 nm [335]. Image processing was done using MountainsMap 5.1 (Digital Surf) and WSXM 5.0 [336] (Nanotec Electrónica) commercial softwares.

## A.2 X-Ray Diffraction

X-ray diffraction (XRD) is based on the scattering of incident X-ray waves by the electronic density surrounding each atom in a crystal. X-rays are electromagnetic waves with wavelength $\lambda$ in the 0.1-100 Å range. The atomic periodicity within crystals is also in the Å range. Diffraction phenomena occur when the spacing between the object (the crystal in this case) is in the order of the wavelength of the incident radiation, and, consequently,

X-ray diffraction is a powerful tool to characterize crystals. The scattered X-rays will destroy themselves except for the case in which the difference between the incident and the scattered wave vectors is a vector belonging to the reciprocal lattice. Or, more simply, according to Bragg's law, if the scattered rays are in-phase so that their difference in path is equal to an integer number $n$ of wavelengths [see Fig. A.3 (a)]

$$n\lambda = 2d_{hkl}\sin\theta \tag{A.1}$$

where $\lambda$ is the wavelength of the incident X-ray, $n$ is the reflection order (an integer number), $\theta$ is the angle of incidence between the X-ray and the sample plane, and $d_{hkl}$ is the interplanar spacing between the $(hkl)$ family of planes. When Bragg's law is fulfilled we have a constructive interference, i.e. the so-called diffraction peak or the Bragg reflection. The diffraction pattern is then composed by such Bragg reflections and their intensity and spatial distributions conform the fingerprint of the specific sample. XRD is thus routinely used for determining crystal structures, phase identification, crystalline quality, cell parameters, or the study of crystal texture and orientation of epitaxial thin films and nanostructures, among others.

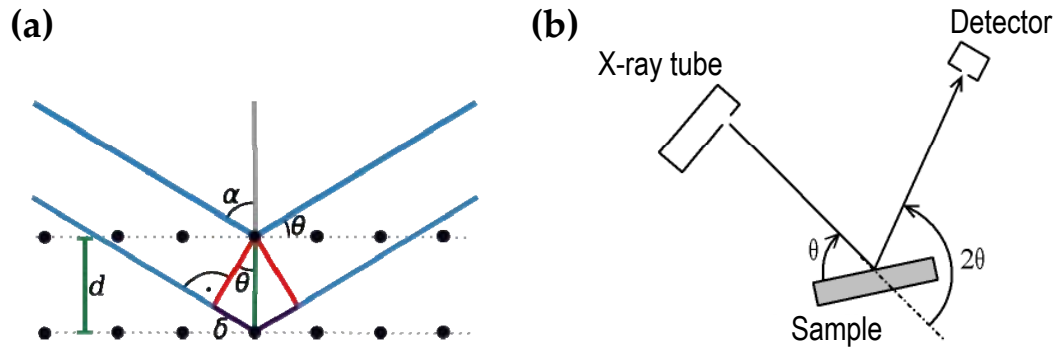


**Fig. A.3:** *(a) Sketch of the constructive interference (Bragg's law) between two incident X-rays on a crystal surface. (b) Geometry of the $\theta - 2\theta$ configuration.*

The rotation of the sample with respect to the incident angle and to the detector produces different XRD configurations from where different information can be obtained. In a $\theta - 2\theta$ scan [Bragg-Brentano geometry, Fig. A.3 (b)], the sample moves by the angle $\theta$ and the detector simultaneously moves by the angle $2\theta$ while the X-ray tube remains stationary. Only the atomic planes parallel to the surface plane will diffract in this configuration, i.e. we obtain information of the out-of-plane orientation of the crystal. Polycrystalline samples consist of randomly oriented crystallites in all possible orientations so for every crystal plane that fulfills the Bragg condition at a certain $\theta$ value there will be a diffraction peak. Conversely, in single crystals, the family of planes parallel to the sample surface is the only one giving a reflection peak. Information on the out-of-plane texture of crystallites can be obtained by ***scans***, also known as ***rocking curves***. A scan is a $\theta$ scan at a fixed $2\theta$ angle and provides information on the mosaic spread of the specific reflection being analyzed: the width of the peak obtained is proportional to the misorientation of the coherent domain being measured.

The $\theta-2\theta$ and scans performed in this thesis were done using either a Siemens D5000 or a Rigaku Rotaflex RU-200BV diffractometer located at ICMAB, using Cu $K_\alpha$ radiation [$\lambda(K^{Cu}_{\alpha1}) = 1\,5406$ Å and $\lambda(K^{Cu}_{\alpha2}) = 1\,5444$ Å]. Data acquisition was typically performed

with a 0.02° step size. The lattice parameters of the (001)-single crystal substrates used in this thesis (see Chapter 2) were obtained by the combination of $\theta - 2\theta$ and scans at two different (00l) reflections (which enables getting rid of the instrumental uncertainty $\theta_0$). We used $\theta - 2\theta$ scans to identify the $(001)_{\mathrm{LSMO}}$-oriented LSMO nanoislands on YSZ and MgO, and rocking curve measurements that gave information on the out-of-plane misorientation of the nanoisland ensemble. On the other hand, the proximity to the substrate $2\theta$ values prevented from resolving the LSMO reflection of ultra-thin LSMO films (concentrations $\leq$0.03 M, thickness $\leq$4 nm) grown onto STO and LAO.

The other XRD measurement routinely performed in the characterization of the LSMO nanoislands were ***pole gure*** measurements (also called phi-scans). In a Pole Figure we select a particular *hkl* reflection which is put in Bragg condition. In order to do so, if the $(hkl)$ planes are not parallel to the substrate, the sample has to be tilted a certain angle $\gamma$ and rotated an angle $\theta$. The rotation angles are displayed in Fig. A.4 (a). For instance, for epitaxial LSMO nanoislands growing $(001)_{LSMO}$-oriented with respect to a (001)-oriented single crystal substrate, to detect the $(011)_{LSMO}$ reflection the sample must be tilted 45° and rotated some degrees in $\theta$ in order to catch one of the 90° separated four poles (the multiplicity of the (001) out-of-plane orientation is $m$=4). Hence, the 360° rotation of the sample around the (001) sample plane results in the $(011)_{LSMO}$ pole figure of Fig. A.4 (b). Moreover, by comparing the relative orientation in $\theta$ of the poles of the substrate and of the islands (or film) on top we can deduce the in-plane orientation of the epitaxy. In summary, the $\gamma$ value indicates the out-of-plane orientation of the crystal, i.e. $(001)_{\mathrm{LSMO}}$ $(001)_{\mathrm{YSZ}}$ while the position of the poles in $\theta$ points out that, in-plane, LSMO grows 45° rotated with respect to the YSZ substrate, i.e. $[110]_{\mathrm{YSZ}}$ $[010]_{\mathrm{YSZ}}$.

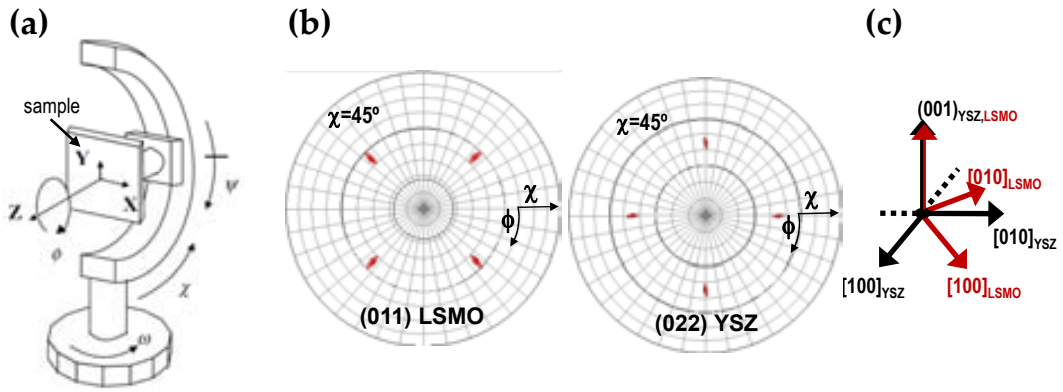


**Fig. A.4:** *(a) Sketch of the goniometer showing the different rotation angles. X, Y, and Z are the sample reference system. Reproduced from [337]. (b) Pole figure measurement of a LSMO nanoisland ensemble on YSZ showing the* $(001)_{\mathrm{LSMO}}$*[110]* $(001)_{\mathrm{YSZ}}$*[010] epitaxial orientation. (c) Sketch of the LSMO orientation relative to YSZ.*

We performed pole figure measurements using a 2D X-Ray Diffraction (XRD$^2$) system located at ICMAB, the GADDS D8 Advance System (Bruker), where GADDS stands for General Area Detector System. The sketched diagram of the GADDS mains components is shown in Fig. A.5 (a). In addition to the goniometer sketched in Fig. A.4, the most salient feature in the GADDS system is the 2D detector, which permits simultaneously measuring large $2\theta$ ($\sim$30°) and $\gamma$ ($\sim$70°) ranges. In consequence, in a single fast measurement we obtain not only the information relative to the $2\theta$ and $\gamma$ values in which we center the

sample, but also detect reflections at different $2\theta$ and $\gamma$ values that give information on the out-of-plane texture of the sample [337].

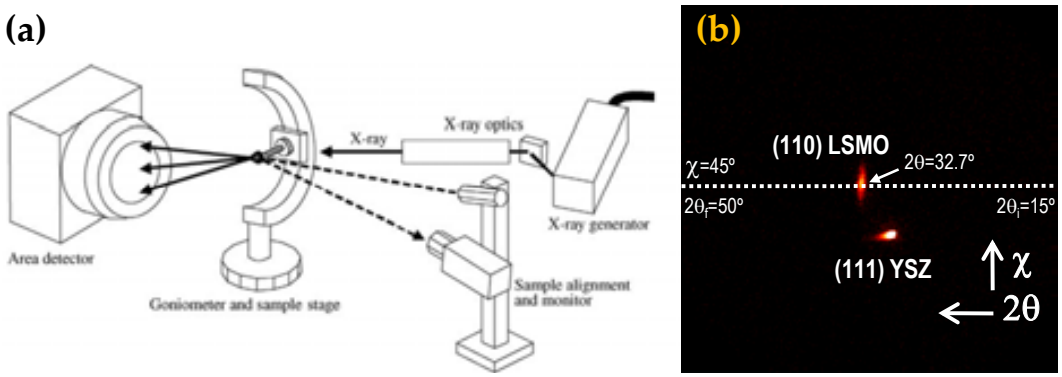


**Fig. A.5:** *(a) Main components of a XRD$^2$ GADDS system. Reproduced from [337]. (b) 2θ-γ frame obtained from a GADDS measurement on a LSMO thin film (thickness ∼25 nm) on a (001)-YSZ substrate.*

An example of a 2D XRD diffraction pattern obtained with the GADDS is displayed in Fig. A.5 (b). The sample was a thin LSMO film (thickness ∼25 nm) grown onto a (001)-YSZ substrate. The horizontal direction covers the $2\theta$ values and the vertical direction represents $\gamma$ values. The $2\theta$-$\gamma$ frame shown in Fig. A.5 (b) was obtained by centering the sample at the $(011)_{\mathrm{LSMO}}$ reflection (falling at $2\theta$=32.7°) and tilting it at a $\gamma$=45°. The bright reflection falling precisely at such $\gamma$ and $2\theta$ values indicates that the LSMO film grows with the $(001)_{\mathrm{LSMO}}$ out-of-plane orientation. To have the complete phi-scan we must rotate the sample about its normal axis (while tilted at 45°) and collect each of the frames. Integration in $\gamma$ for the whole set of frames then produces a pole figure such as the one in Fig. A.4 (b). The low intensities coming from our LSMO nanoislands required long exposition times (each frame would take 120 s). In order to better resolve the out-of-plane misorientations in some of the nanoislands we also played with the $\theta$ step sizes, reducing it from the standard $\Delta\theta$=2° to $\Delta$=$\theta$1° and even $\Delta\theta$=0.5°.

## A.3 Transmission Electron Microscopy and Scanning Transmission Electron Microscopy

The following lines are based on a complete description of Transmission Electron Microscopy (TEM) given in the thesis by P. Abellán [160]. The reader is directed to this piece of work and to the references therein for further details on the technique.

Transmission Electron Microscopy (TEM) and Scanning Transmission Electron Microscopy (STEM) are powerful tools for characterizing the internal structure of materials with sub-nanometer resolution [338]. In TEM a parallel beam of accelerated electrons (acceleration voltages ∼100-300 kV) is directed towards a thin specimen, giving rise to scattering events and diffracted beams. The electrons traversing the specimen contain the information of the sample's atomic structure (known as the projected crystal potential, $f(x\ y)$), and pass through an objective lens and a series of other lenses that focus and enlarge the information to finally build a magnified image of our sample. We can visualize the TEM

as a visible light microscope where the electron beam plays the role of light, and instead of glass lenses we have electromagnetic lenses which act upon the trajectories of the electrons. Fig. A.6 (a) shows a sketch of an ideal electron microscope. The analogy with the optical microscope is highlighted by illustrating the objective lens as a fictitious glass lens. The small wavelength of highly accelerated electrons permits very high lateral resolutions in the order of ∼1.5 Å-2.5 Å. Aberration-corrected microscopes can nowadays achieve resolution values of ∼0.5 Å. STEM is based on the same principles as TEM, with the difference that the specimen is hit by a convergent electron beam which scans the sample (instead of a parallel static beam). This is achieved by placing the objective lens before the specimen, as sketched in Fig. A.6 (b).

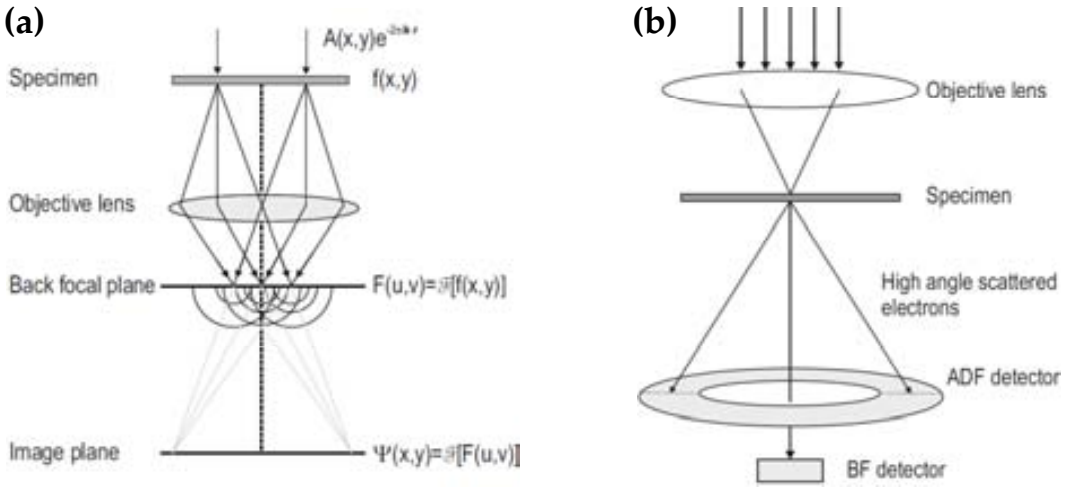


**Fig. A.6:** *(a) Main components of an ideal TEM microscope, showing the mathematical evolution of the projected crystal potential f(x,y). (b) Sketch of image formation within a STEM microscope. Illustrations reproduced from [160].*

In addition to imaging the sample, TEM provides for structural and chemical information by means of Electron Diffraction (ED) and spectroscopic techniques such as Electron Energy Loss spectroscopy (EELS). Whether the ED pattern or the image of the sample is the information projected and thus visualized, is selected by adjusting the strength of one of the electromagnetic lenses (the intermediate lens). In both ED and imaging modes the information comes from coherently scattered elastic electrons, i.e. electrons that after interacting with the specimen keep a certain phase relationship and do not loose energy. Conversely, for High Annular Dark Field (HAADF) STEM imaging high angle inelastically scattered electrons are used. These are generally incoherent electrons, and it can be demonstrated that their intensity is proportional to $Z^2$, where $Z$ is the atomic number [339]. During STEM operation the direct (non-scattered) beam can also be selected. In that case STEM imaging is similar to TEM Bright Field imaging. The $Z^2$ dependency in HAADF-STEM mode implies that heavy atoms will be seen brighter than light atoms. A consequence of this dependence is that in HAADF-STEM the interpretation of the contrast is straightforward. This is an advantage with respect to High Resolution TEM (HRTEM) imaging, which despite yielding atomic resolution images, their interpretation is not direct: in HRTEM the contrast arises from differences in the phase of the beams scattered through the specimen, i.e. HRTEM images are interference images which strongly depend on the sample thickness and the microscope defocus. HRTEM image interpretation thus often requires a posteriori

simulations to unambiguously determine the origin of the observed contrasts.

TEM and STEM imaging is limited in practice by lens aberrations (astigmatism, chromatic and spherical aberrations) and, very importantly, by the quality of the sample, which mainly refers to its thickness. Specimens must be 'electron-transparent', which requires thicknesses below the 200 nm. For high resolution imaging the optimal thickness goes down to a few tens of nm. The samples imaged by TEM and STEM in this thesis were all cross-section samples prepared by the tripod mechanical preparation technique. The sample is cut into different slices, two slices are glued face to face, and the tripod polishing is applied to one of the two faces parallel to the substrate/film interface, until a thickness of $\sim$20 μm is achieved. Further thinning down to electron transparency is obtained by $Ar^+$ ion bombardment on a Precision Ion Polishing System (PIPS), with low voltages in the 2-5 kV range (to minimize ion milling damage of the sample). The single crystal oxide substrates used in this thesis are very brittle and difficult to prepare. This process was principally carried out by Dr. P. Abellán in the context of her thesis, and also by F. Belarre and Dr. J. Gázquez.

A number of microscopes were used for the TEM and STEM images present in this thesis. LSMO thin films on STO and LAO substrates were imaged using two different aberration corrected STEMs: A VG Microscopes HB501UX and a Nion UltraSTEM at Oak Ridge National Laboratory (USA). Both of them were operated at 100 kV, equipped with NION aberration correctors (3rd order for the VG501and 5th order for the NION UltraSTEM). Low magnification and ED patterns for LSMO nanoislands on YSZ were acquired with a Jeol JEM-2011 (200 kV) microscope at UAB (Barcelona) and a Philips CM30 (300 kV) microscope at Serveis Cientifico Tècnics of the UB (Barcelona). High resolution TEM images of LSMO nanoislands on YSZ were obtained using a Jeol 2010 FEG (200 kV) at Serveis Cientifico Tècnics of the UB (Barcelona). An aberration ($C_S$) corrected F20-SACTEM Tecnai microscope at CEMES (Toulouse) was used for high resolution imaging of MgO on LSMO nanoislands. Image acquisition and interpretation was carried out by Dr. P. Abellán, Dr. J. Gázquez, and Dr. M. Roldán.

## A.4 Superconducting quantum interference device

Field and temperature dependent magnetization curves of LSMO ultra-thin films and self-assembled nanoislands were measured at ICMAB (B. Bozzo, Dr. C. Montón and J. Zabaleta) using a commercial SQUID DC-magnetometer (Quantum Design) equipped with a 7 T superconducting and a helium cryostat allowing temperature control between 1.8 K and 400 K. The isothermal magnetization curves showed a strong negative slope due to the diamagnetic contribution of the single crystal substrates. Data treatment involved getting rid of that contribution by linear fitting of the diamagnetic signal.

A SQUID consists of a superconducting loop with one or two non superconducting links inserted (the so-called Josephson junction). These devices give rise to an output voltage signal, which is a periodic function of the flux threading the superconducting loop. This geometry is known as DC-SQUID (constant bias current). The magnetometer includes a SQUID detection system and a precision temperature control unit in the bore of a high-field superconducting coil. The sample locates inside a set of pick-up coils, which in turn are placed inside the superconducting coil which provides a uniform dc-magnetic field at the sample location. The magnetized sample is then displaced inside the set of pick-up

coils inducing a current proportional to the variation of the magnetic flux. The signal is detected and amplified by means of the SQUID sensor (the superconducting loop with the weak link) in form of voltage. The magnetic moment of the sample is thus proportional to the voltage variations that the SQUID detects, which can resolve magnetic moments in the order of $10^{-6}$ emu. All the system is placed inside a helium cryostat which refrigerates the superconducting coil and allows precise temperature control.

## A.5 Transport measurements

The electric transport measurements in the ultra-thin LSMO films on LAO and STO were performed by Dr. A. Palau using a Physical Properties Measurement System (PPMS) from Quantum Design located at the ICMAB. The system has a 9 T superconducting magnet and a helium cryostat which allows a precise temperature control between 1.8 K and 400 K. During the magnetotransport measurements, the magnetic field was applied out-of-plane of the LSMO film. Silver metal contacts where evaporated on the films and post-annealed, ensuring resistance values below 10 $\mu\Omega$. The resistivity of the LSMO films was measured in a four-point configuration with an applied current of 5 nA. Vacuum grease was used when mounting the sample to ensure good thermal coupling during the measurement.

# Bibliography


[1] S. D. Bader, *Colloquium: Opportunities in nanomagnetism*, Rev. Mod. Phys. **78**, 1 (2006).

[2] G. Srajer, L. H. Lewis, S. D. Bader, A. J. Epstein, C. S. Fadley, E. E. Fullerton, A. Hoffmann, J. B. Kortright, K. M. Krishnan, S. A. Majetich, T. S. Rahman, C. A. Ross, M. B. Salamon, I. K. Schuller, T. C. Schulthess, and J. Z. Sun, *Advances in nanomagnetism via X-ray techniques*, J. Magn. Magn. Mater. **307**, 1 (2006).

[3] J. V. Barth, G. Costantini, and K. Kern, *Engineering atomic and molecular nanostructures at surfaces*, Nature **437**, 671 (2005).

[4] T. Ito and S. Okazaki, *Pushing the limits of lithography*, Nature **406**, 1027 (2000).

[5] M. N. Yoder, *Microelectronics/nanoelectronics and the 21st century*, in *University/Government/Industry Microelectronics Symposium, 2001. Proceedings of the Fourteenth Biennial* (2001) pp. 2–7.

[6] C. Moreno, P. Abellán, A. Hassini, A. Ruyter, A. P. del Pino, F. Sandiumenge, M. J. Casanove, J. Santiso, T. Puig, and X. Obradors, *Spontaneous outcropping of self-assembled insulating nanodots in solution-derived metallic ferromagnetic $La_{0.7}Sr_{0.3}MnO_3$ films*, Adv. Funct. Mater. **19**, 2139 (2009).

[7] P. Abellán, F. Sandiumenge, M.-J. Casanove, M. Gibert, A. Palau, T. Puig, and X. Obradors, *Interaction between solution derived $BaZrO_3$ nanodot interfacial templates and $YBa_2Cu_3O_7$ films leading to enhanced critical currents*, Acta Mater. **59**, 2075 (2011).

[8] A. Carretero-Genevrier, J. Gázquez, J. C. Idrobo, J. Oró, J. Arbiol, M. Varela, E. Ferain, J. Rodríguez-Carvajal, T. Puig, N. Mestres, and X. Obradors, *Single crystalline $La_{0.7}Sr_{0.3}MnO_3$ molecular sieve nanowires with high temperature ferromagnetism*, J. Am. Chem. Soc **133**, 4053 (2011).

[9] M. Gibert, P. Abellán, L. Martínez, E. Román, A. Crespi, F. Sandiumenge, T. Puig, and X. Obradors, *Orientation and shape selection of self-assembled epitaxial $Ce_{1-x}Gd_xO_{2-y}$ nanostructures grown by chemical solution deposition*, CrystEngComm **13**, 6719 (2011).

[10] T. Shinjo, T. Okuno, R. Hassdorf, K. Shigeto, and T. Ono, *Magnetic vortex core observation in circular dots of permalloy*, Science **289**, 930 (2000).

[11] A. Ohtomo and H. Y. Hwang, *A high-mobility electron gas at the $LaAlO_3/SrTiO_3$ heterointerface*, Nature **427**, 423 (2004).

[12] J. Gutiérrez, A. Llordés, J. Gázquez, M. Gibert, N. Romà, S. Ricart, A. Pomar, F. Sandiumenge, N. Mestres, T. Puig, and X. Obradors, *Strong isotropic flux pinning in solution-derived $YBa_2Cu_3O_{7-x}$ nanocomposite superconductor films*, Nat. Mater. **6**, 367 (2007).

[13] M. Stengel, D. Vanderbilt, and N. A. Spaldin, *Enhancement of ferroelectricity at metal-oxide interfaces*, Nat. Mater. **8**, 392 (2009).

[14] D. G. Schlom and J. Mannhart, *Oxide electronics: Interface takes charge over Si*, Nat. Mater. **10**, 168 (2011).

[15] R. K. Vasudevan, Y. C. Chen, H. H. Tai, N. Balke, P. P. Wu, S. Bhattacharya, L. Q. Chen, Y. H. Chu, I. N. Lin, S. V. Kalinin, and V. Nagarajan, *Exploring topological defects in epitaxial $BiFeO_3$ thin films*, ACS Nano **5**, 879 (2011).

[16] S. Jin, M. McCormack, T. H. Tiefel, and R. Ramesh, *Colossal magnetoresistance in La-Ca-Mn-O ferromagnetic thin films (invited)*, J. Appl. Phys **76**, 6929 (1994).

[17] Y. Tokura and Y. Tomioka, *Colossal magnetoresistive manganites*, J. Magn. Magn. Mater. **200**, 1 (1999).

[18] J. H. Park, E. Vescovo, H. J. Kim, C. Kwon, R. Ramesh, and T. Venkatesan, *Direct evidence for a half-metallic ferromagnet*, Nature **392**, 794 (1998).

[19] J. H. Park, E. Vescovo, H. J. Kim, C. Kwon, R. Ramesh, and T. Venkatesan, *Magnetic properties at surface boundary of a half-metallic ferromagnet* $La_{0.7}Sr_{0.3}MnO_3$, Phys. Rev. Lett. **81**, 1953 (1998).

[20] G. A. Prinz, *Magnetoelectronics*, Science **282**, 1660 (1998).

[21] S. D. Bader and S. S. P. Parkin, *Spintronics*, Annual Review of Condensed Matter Physics **1**, 71 (2010).

[22] F. Yang, N. Kemik, M. D. Biegalski, H. M. Christen, E. Arenholz, and Y. Takamura, *Strain engineering to control the magnetic and magnetotransport properties of* $La_{0.67}Sr_{0.33}MnO_3$ *thin films*, Appl. Phys. Lett. **97**, 092503 (2010).

[23] B. Kim, D. Kwon, J. H. Song, Y. Hikita, B. G. Kim, and H. Y. Hwang, *Finite size effect and phase diagram of ultra-thin* $La_{0.7}Sr_{0.3}MnO_3$, Solid State Communications **150**, 598 (2010).

[24] B. Kim, D. Kwon, T. Yajima, C. Bell, Y. Hikita, B. G. Kim, and H. Y. Hwang, *Reentrant insulating state in ultrathin manganite films*, Appl. Phys. Lett. **99**, 092513 (2011).

[25] J. Z. Sun, D. W. Abraham, R. A. Rao, and C. B. Eom, *Thickness-dependent magnetotransport in ultrathin manganite films*, Appl. Phys. Lett. **74**, 3017 (1999).

[26] Y. H. Sun, Y. G. Zhao, H. F. Tian, C. M. Xiong, B. T. Xie, M. H. Zhu, S. Park, W. D. Wu, and J. Q. Li, *Electric and magnetic modulation of fully strained dead layers in* $La_{0.67}Sr_{0.33}MnO_3$, Phys. Rev. B **78**, (2008).

[27] C. Kwon, M. C. Robson, K. C. Kim, J. Y. Gu, S. E. Lofland, S. M. Bhagat, Z. Trajanovic, M. Rajeswari, T. Venkatesan, A. R. Kratz, R. D. Gomez, and R. Ramesh, *Stress-induced effects in epitaxial* $(La_{0.7}Sr_{0.3})MnO_3$ *films*, J. Magn. Magn. Mater. **172**, 229 (1997).

[28] R. Desfeux, S. Bailleul, A. Da Costa, W. Prellier, and A. M. Haghiri-Gosnet, *Substrate effect on the magnetic microstructure of* $La_{0.7}Sr_{0.3}MnO_3$ *thin films studied by magnetic force microscopy*, Appl. Phys. Lett. **78**, 3681 (2001).

[29] J. Dho, Y. N. Kim, Y. S. Hwang, J. C. Kim, and N. H. Hur, *Strain-induced magnetic stripe domains in* $La_{0.7}Sr_{0.3}MnO_3$ *thin films*, Appl. Phys. Lett. **82**, 1434 (2003).

[30] J. Dho and N. H. Hur, *Thickness dependence of perpendicular magnetic anisotropy in* $La_{0.7}Sr_{0.3}MnO_3$ *films on* $LaAlO_3$, J. Magn. Magn. Mater. **318**, 23 (2007).

[31] Q. A. Pankhurst, J. Connolly, S. K. Jones, and J. Dobson, *Applications of magnetic nanoparticles in biomedicine*, J. Phys. D: Appl. Phys. **36**, R167 (2003).

[32] W. J. Gallagher and S. S. P. Parkin, *Development of the magnetic tunnel junction MRAM at IBM: From first junctions to a 16-Mb MRAM demonstrator chip*, IBM Journal of Research and Development **50**, 5 (2006).

[33] Y. Song and D. Zhu, *High Density Data Storage: Principle, Technology, and Materials* (World Scientific Publishing Company, 2009).

[34] S. N. Piramanayagam and T. C. Chong, *Developments in Data Storage: Materials Perspective* (John Wiley & Sons,, 2011).

[35] D. Weller and A. Moser, *Thermal effect limits in ultrahigh-density magnetic recording*, Magnetics, IEEE Transactions on **35**, 4423 (1999).

[36] A. Hubert and R. Schäfer, *Domain theory magnetic domains* (Springer Berlin Heidelberg, 1998) pp. 99–335.

[37] A. Aharoni, *Upper bound to a single-domain behavior of a ferromagnetic cylinder*, J. Appl. Phys. **68**, 2892 (1990).

[38] R. P. Cowburn, D. K. Koltsov, A. O. Adeyeye, M. E. Welland, and D. M. Tricker, *Single-domain circular nanomagnets*, Phys. Rev. Lett. **83**, 1042 (1999).

[39] K. Y. Guslienko and K. L. Metlov, *Evolution and stability of a magnetic vortex in a small cylindrical ferromagnetic particle under applied field*, Phys. Rev. B **63**, 100403 (2001).

[40] R. Wiesendanger, I. V. Shvets, D. Bürgler, G. Tarrach, H. J. Güntherodt, J. M. D. Coey, and S. Gräser, *Topographic and magnetic-sensitive scanning tunneling microscope study of magnetite*, Science **255**, 583 (1992).

[41] M. Bode, *Spin-polarized scanning tunnelling microscopy*, Reports on Progress in Physics **66**, 523 (2003).

[42] A. Schwarz and R. Wiesendanger, *Magnetic sensitive force microscopy*, Nano Today **3**, 28.

[43] K. Yamada, S. Kasai, Y. Nakatani, K. Kobayashi, H. Kohno, A. Thiaville, and T. Ono, *Electrical switching of the vortex core in a magnetic disk*, Nat. Mater. **6**, 269 (2007).

[44] A. Wachowiak, J. Wiebe, M. Bode, O. Pietzsch, M. Morgenstern, and R. Wiesendanger, *Direct observation of internal spin structure of magnetic vortex cores*, Science **298**, 577 (2002).

[45] S. B. Choe, Y. Acremann, A. Scholl, A. Bauer, A. Doran, J. Stohr, and H. A. Padmore, *Vortex core-driven magnetization dynamics*, Science **304**, 420 (2004).

[46] K. S. Buchanan, K. Y. Guslienko, A. Doran, A. Scholl, S. D. Bader, and V. Novosad, *Magnetic remanent states and magnetization reversal in patterned trilayer nanodots*, Phys. Rev. B **72**, 134415 (2005).

[47] V. Novosad, M. Grimsditch, K. Y. Guslienko, P. Vavassori, Y. Otani, and S. D. Bader, *Spin excitations of magnetic vortices in ferromagnetic nanodots*, Phys. Rev. B **66**, 052407 (2002).

[48] R. P. Cowburn, *Magnetic nanodots for device applications*, J. Magn. Magn. Mater. **242**, 505 (2002).

[49] B. Pigeau, G. De Loubens, O. Klein, A. Riegler, F. Lochner, G. Schmidt, L. W. Molenkamp, V. S. Tiberkevich, and A. N. Slavin, *A frequency-controlled magnetic vortex memory*, Appl. Phys. Lett. **96** (2010).

[50] V. S. Pribiag, I. N. Krivorotov, G. D. Fuchs, P. M. Braganca, O. Ozatay, J. C. Sankey, D. C. Ralph, and R. A. Buhrman, *Magnetic vortex oscillator driven by d.c. spin-polarized current*, Nat. Phys. **3**, 498 (2007).

[51] A. Ruotolo, V. Cros, B. Georges, A. Dussaux, J. Grollier, C. Deranlot, R. Guillemet, K. Bouzehouane, S. Fusil, and A. Fert, *Phase-locking of magnetic vortices mediated by antivortices*, Nat. Nanotechnol. **4**, 528 (2009).

[52] S. Kasai, K. Nakano, K. Kondou, N. Ohshima, K. Kobayashi, and T. Ono, *Three-terminal device based on the current-induced magnetic vortex dynamics with the magnetic tunnel junction*, Applied Physics Express **1**, (2008).

[53] T. Nozaki, H. Kubota, S. Yuasa, M. Shiraishi, T. Shinjo, and Y. Suzuki, *RF amplification in a three-terminal magnetic tunnel junction with a magnetic vortex structure*, Appl. Phys. Lett. **95**, (2009).

[54] J. I. Martín, J. Nogués, K. Liu, J. L. Vicent, and I. K. Schuller, *Ordered magnetic nanostructures: fabrication and properties*, J. Magn. Magn. Mater. **256**, 449 (2003).

[55] B. T. Jonker, K. H. Walker, E. Kisker, G. A. Prinz, and C. Carbone, *Spin-polarized photoemission study of epitaxial Fe(001) films on Ag(001)*, Phys. Rev. Lett. **57**, 142 (1986).

[56] N. C. Koon, B. T. Jonker, F. A. Volkening, J. J. Krebs, and G. A. Prinz, *Direct evidence for perpendicular spin orientations and enhanced hyperfine fields in ultrathin Fe(100) films on Ag(100)*, Phys. Rev. Lett. **59**, 2463 (1987).

[57] C. Liu, E. R. Moog, and S. D. Bader, *Polar Kerr-effect observation of perpendicular surface anisotropy for ultrathin fcc Fe grown on Cu(100)*, Phys. Rev. Lett. **60**, 2422 (1988).

[58] A. P. Popov, N. V. Skorodumova, and O. Eriksson, *Phenomenological model of the magnetic states of ferromagnetic film with competing surface and bulk anisotropies*, Phys. Rev. B **77**, 014415 (2008).

[59] R. P. Cowburn, A. O. Adeyeye, and M. E. Welland, *Configurational anisotropy in nanomagnets*, Phys. Rev. Lett. **81**, 5414 (1998).

[60] R. P. Cowburn and M. E. Welland, *Phase transitions in planar magnetic nanostructures*, Appl. Phys. Lett. **72**, 2041 (1998).

[61] R. P. Cowburn and M. E. Welland, *Micromagnetics of the single-domain state of square ferromagnetic nanostructures*, Phys. Rev. B **58**, 9217 (1998).

[62] Y. Suzuki, H. Y. Hwang, S. W. Cheong, T. Siegrist, R. B. van Dover, A. Asamitsu, and Y. Tokura, *Magnetic anisotropy of doped manganite thin films and crystals*, J. Appl. Phys. **83**, 7064 (1998).

[63] M. Bibes, L. Balcells, S. Valencia, J. Fontcuberta, M. Wojcik, E. Jedryka, and S. Nadolski, *Nanoscale multiphase separation at $La_{2/3}Ca_{1/3}MnO_3/SrTiO_3$ interfaces*, Phys. Rev. Lett. **8706**, (2001).

[64] J. L. Maurice , F. Pailloux, A. Barthélémy, O. Durand, D. Imhoff, R. Lyonnet, A. Rocher, and J. P. Contour, *Strain relaxation in the epitaxy of $La_{2/3}Sr_{1/3}MnO_3$ grown by pulsed-laser deposition on $SrTiO_3(001)$*, Philos. Mag. **83**, 3201 (2003).

[65] C. Adamo, X. Ke, H. Q. Wang, H. L. Xin, T. Heeg, M. E. Hawley, W. Zander, J. Schubert, P. Schiffer, D. A. Muller, L. Maritato, and D. G. Schlom, *Effect of biaxial strain on the electrical and magnetic properties of (001) $La_{0.7}Sr_{0.3}MnO_3$ thin films*, Appl. Phys. Lett. **95**, (2009).

[66] Y. Takamura, R. V. Chopdekar, A. Scholl, A. Doran, J. A. Liddle, B. Harteneck, and Y. Suzuki, *Tuning magnetic domain structure in nanoscale $La_{0.7}Sr_{0.3}MnO_3$ islands*, Nano Lett. **6**, 1287 (2006).

[67] M. Mathews, R. Jansen, G. Rijnders, J. C. Lodder, and D. H. A. Blank, *Magnetic oxide nanowires with strain-controlled uniaxial magnetic anisotropy direction*, Phys. Rev. B **80**, (2009).

[68] A. M. Haghiri-Gosnet and J. P. Renard, *CMR manganites: physics, thin films and devices*, J. Phys. D: Appl. Phys. **36**, R127 (2003).

[69] N. Suzuki, H. Tanaka, and T. Kawai, *Epitaxial transition metal oxide nanostructures fabricated by a combination of AFM lithography and molybdenum lift-off*, Adv. Mater. **20**, 909 (2008).

[70] E. Dagotto, *Complexity in strongly correlated electronic systems*, Science **309**, 257 (2005).

[71] E. Dagotto, T. Hotta, and A. Moreo, *Colossal magnetoresistant materials: the key role of phase separation*, Physics Reports **344**, 1 (2001).

[72] A. P. Ramirez, *Colossal magnetoresistance*, Journal of Physics-Condensed Matter **9**, 8171 (1997).

[73] C. N. R. Rao, A. Anthony, A. K. Cheetham, and R. Bernard, *Charge ordering in the rare earth manganates: the experimental situation*, Journal of Physics: Condensed Matter **12**, R83 (2000).

[74] M. B. Salamon and M. Jaime, *The physics of manganites: Structure and transport*, Reviews of Modern Physics **73**, 583 (2001).

[75] G. H. Jonker and J. H. Van Santen, *Ferromagnetic compounds of manganese with perovskite structure*, Physica **16**, 337 (1950).

[76] C. Zener, *Interaction between the d-shells in the transition metals. II. Ferromagnetic compounds of manganese with perovskite structure*, Phys. Rev. **82**, 403 (1951).

[77] P. W. Anderson and H. Hasegawa, *Considerations on double exchange*, Phys. Rev. **100**, 675 (1955).

[78] P. G. de Gennes, *Effects of double exchange in magnetic crystals*, Phys. Rev. **118**, 141 (1960).

[79] S. Jin, T. H. Tiefel, M. McCormack, R. A. Fastnacht, R. Ramesh, and L. H. Chen, *Thousandfold change in resistivity in magnetoresistive La-Ca-Mn-O films*, Science **264**, 413 (1994).

[80] M. N. Baibich, J. M. Broto, A. Fert, F. N. Van Dau, F. Petroff, P. Etienne, G. Creuzet, A. Friederich, and J. Chazelas, *Giant magnetoresistance of (001)Fe/(001)Cr magnetic superlattices*, Phys. Rev. Lett. **61**, 2472 (1988).

[81] H. Y. Hwang, S. W. Cheong, N. P. Ong, and B. Batlogg, *Spin-polarized intergrain tunneling in $La_{2/3}Sr_{1/3}MnO_3$*, Phys. Rev. Lett. **77**, 2041 (1996).

[82] A. Urushibara, Y. Moritomo, T. Arima, A. Asamitsu, G. Kido, and Y. Tokura, *Insulator-metal transition and giant magnetoresistance in $La_{1-x}Sr_xMnO_3$*, Phys. Rev. B **51**, 14103 (1995).

[83] R. A. de Groot, F. M. Mueller, P. G. v. Engen, and K. H. J. Buschow, *New class of materials: Half-metallic ferromagnets*, Phys. Rev. Lett. **50**, 2024 (1983).

[84] K. Schwarz, *$CrO_2$ predicted as a half-metallic ferromagnet*, Journal of Physics F: Metal Physics **16**, L211 (1986).

[85] R. J. Soulen, J. M. Byers, M. S. Osofsky, B. Nadgorny, T. Ambrose, S. F. Cheng, P. R. Broussard, C. T. Tanaka, J. Nowak, J. S. Moodera, A. Barry, and J. M. D. Coey, *Measuring the spin polarization of a metal with a superconducting point contact*, Science **282**, 85 (1998).

[86] J. M. De Teresa, A. Barthélémy, A. Fert, J. P. Contour, F. Montaigne, and P. Seneor, *Role of metal-oxide interface in determining the spin polarization of magnetic tunnel junctions*, Science **286**, 507 (1999).

[87] M. Bowen, M. Bibes, A. Barthelemy, J. P. Contour, A. Anane, Y. Lemaitre, and A. Fert, *Nearly total spin polarization in $La_{2/3}Sr_{1/3}MnO_3$ from tunneling experiments*, Appl. Phys. Lett. **82**, 233 (2003).

[88] A. Solignac, R. Guerrero, G. Agnus, C. Fermon, M. Pannetier-Lecoeur, and P. Lecoeur, *Magnetic tunnels junctions for all-oxide spin valves devices*, Journal of Physics: Conference Series **303**, 012059 (2011).

[89] M. C. Martin, G. Shirane, Y. Endoh, K. Hirota, Y. Moritomo, and Y. Tokura, *Magnetism and structural distortion in the $La_{0.7}Sr_{0.3}MnO_3$ metallic ferromagnet*, Phys. Rev. B **53**, 14285 (1996).

[90] K. Steenbeck, T. Habisreuther, C. Dubourdieu, and J. P. Senateur, *Magnetic anisotropy of ferromagnetic $La_{0.7}Sr_{0.3}MnO_3$ epitaxial thin films: Dependence on temperature and film thickness*, Appl. Phys. Lett. **80**, 3361 (2002).

[91] V. M. Goldschmidt, *The laws of crystal chemistry*, Naturwissenschaften **14**, 477 (1926).

[92] J. M. Phillips, *Substrate selection for high-temperature superconducting thin films*, J. Appl. Phys **79**, 1829 (1996).

[93] L. W. Martin, Y. H. Chu, and R. Ramesh, *Advances in the growth and characterization of magnetic, ferroelectric, and multiferroic oxide thin films*, Materials Science and Engineering: R: Reports **68**, 89 (2010).

[94] H. U. Habermeier, *Thin films of perovskite-type complex oxides*, Materials Today **10**, 34 (2007).

[95] R. Ramesh and N. A. Spaldin, *Multiferroics: progress and prospects in thin films*, Nat. Mater. **6**, 21 (2007).

[96] G. H. Kwei, A. C. Lawson, S. J. L. Billinge, and S. W. Cheong, *Structures of the ferroelectric phases of Barium-Titanate*, J. Phys. Chem. **97**, 2368 (1993).

[97] R. H. Buttner and E. N. Maslen, *Electron difference density and structural parameters in $CaTiO_3$*, Acta Crystallogr., Sect. B: Struct. Sci. **48**, 644 (1992).

[98] C. J. Howard, B. J. Kennedy, and B. C. Chakoumakos, *Neutron powder diffraction study of rhombohedral rare-earth aluminates and the rhombohedral to cubic phase transition*, J. Phys.: Condens. Matter **12**, 349 (2000).

[99] F. W. Lytle, *X-Ray diffractometry of low-temperature phase transformations in Strontium Titanate*, J. Appl. Phys. **35**, 2212 (1964).

[100] C. J. Howard and H. T. Stokes, *Structures and phase transitions in perovskites - a group-theoretical approach*, Acta Crystallogr., Sect. A: Found. Crystallogr. **61**, 93 (2005).

[101] R. H. Mitchell, A. R. Chakhmouradian, and P. M. Woodward, *Crystal chemistry of perovskite-type compounds in the tausonite-loparite series, $(Sr_{1-2x}Na_xLa_x)TiO_3$*, Phys. Chem. Miner. **27**, 583 (2000).

[102] S. Geller and V. B. Bala, *Crystallographic studies of perovskite-like compounds. II. Rare earth alluminates*, Acta Crystallogr. **9**, 1019 (1956).

[103] J. F. Scott, *Raman study of trigonal-cubic phase transitions in rare-earth aluminates*, Phys. Rev. **183**, 823 (1969).

[104] S. Bueble, K. Knorr, E. Brecht, and W. W. Schmahl, *Influence of the ferroelastic twin domain structure on the (100) surface morphology of $LaAlO_3$ HTSC substrates*, Surf. Sci. **400**, 345 (1998).

[105] G. W. Berkstresser, A. J. Valentino, and C. D. Brandle, *Growth of single crystals of lanthanum aluminate*, J. Cryst. Growth **109**, 457 (1991).

[106] C. H. Kim, J. W. Jang, S. Y. Cho, I. T. Kim, and K. S. Hong, *Ferroelastic twins in $LaAlO_3$ polycrystals*, Physica B: Condensed Matter **262**, 438 (1999).

[107] W. Langel and M. Parrinello, *Hydrolysis at stepped MgO surfaces*, Phys. Rev. Lett. **73**, 504 (1994).

[108] A. Wander, I. J. Bush, and N. M. Harrison, *Stability of rocksalt polar surfaces: An ab initio study of MgO(111) and NiO(111)*, Phys. Rev. B **68**, (2003).

[109] R. A. Evarestov and A. V. Bandura, *HF and DFT calculations of MgO surface energy and electrostatic potential using two- and three-periodic models*, International Journal of Quantum Chemistry **100**, 452 (2004).

[110] Y. Hao, M. Mihaylov, E. Ivanova, K. Hadjiivanov, H. Knozinger, and B. C. Gates, *CO oxidation catalyzed by gold supported on MgO: Spectroscopic identification of carbonate-like species bonded to gold during catalyst deactivation*, J. Catal. **261**, 137 (2009).

[111] J. Du, S. Gnanarajan, and A. Bendavid, *Influence of MgO surface conditions on the in-plane crystal orientation and critical current density of epitaxial YBCO films*, Physica C-Superconductivity **400**, 143 (2004).

[112] M. V. Jacob, J. Mazierska, N. Savvides, S. Ohshima, and S. Oikawa, *Comparison of microwave properties of YBCO films on MgO and $LaAlO_3$ substrates*, Physica C: Superconductivity **372-376**, 474 (2002).

[113] V. G. Tsirelson, A. S. Avilov, Y. A. Abramov, E. L. Belokoneva, R. Kitaneh, and D. Feil, *X-Ray and electron diffraction study of MgO*, Acta Crystallogr., Sect. B: Struct. Sci. **54**, 8 (1998).

[114] M. Yoshimura, *Phase-stability of zirconia*, Am. Ceram. Soc. Bull. **67**, 1950 (1988).

[115] C. Pascual and P. Duran, *Subsolidus phase-equilibria and ordering in the system $ZrO_2$-$Y_2O_3$*, J. Am. Ceram. Soc. **66**, 23 (1983).

[116] A. Weber and E. Ivers-Tiffee, *Materials and concepts for solid oxide fuel cells (SOFCs) in stationary and mobile applications*, J. Power Sources **127**, 273 (2004).

[117] X. Xia, R. Oldman, and R. Catlow, *Computational modeling study of bulk and surface of yttria-stabilized cubic zirconia*, Chemistry of Materials **21**, 3576 (2009).

[118] M. Yashima, S. Sasaki, M. Kakihana, Y. Yamaguchi, H. Arashi, and M. Yoshimura, *Oxygen-induced structural-change of the tetragonal phase around the tetragonal-cubic phase-boundary in $ZrO_2$-$YO_{1.5}$ solid-solutions*, Acta Crystallogr., Sect. B: Struct. Sci. **50**, 663 (1994).

[119] K. S. Lee, S. Choi, and S. K. Kim, *Radiation of spin waves from magnetic vortex cores by their dynamic motion and annihilation processes*, Appl. Phys. Lett. **87** (2005).

[120] C. Noguera, *Physics and chemistry at oxide surfaces* (Cambridge University Press, 1996).

[121] M. Kawasaki, K. Takahashi, T. Maeda, R. Tsuchiya, M. Shinohara, O. Ishiyama, T. Yonezawa, M. Yoshimoto, and H. Koinuma, *Atomic control of the $SrTiO_3$ crystal-surface*, Science **266**, 1540 (1994).

[122] G. Koster, B. L. Kropman, G. J. H. M. Rijnders, D. H. A. Blank, and H. Rogalla, *Quasi-ideal Strontium Titanate crystal surfaces through formation of Strontium Hydroxide*, Appl. Phys. Lett. **73**, 2920 (1998).

[123] R. Bachelet, F. Sanchez, J. Santiso, C. Munuera, C. Ocal, and J. Fontcuberta, *Self-assembly of $SrTiO_3$ (001) chemical-terminations: A route for oxide-nanostructure fabrication by selective growth*, Chemistry of Materials **21**, 2494 (2009).

[124] J. M. Huijbregtse, J. H. Rector, and B. Dam, *Effect of the two (100) $SrTiO_3$ substrate terminations on the nucleation and growth of $YBa_2Cu_3O_{7-\delta}$ thin films*, Physica C **351**, 183 (2001).

[125] J. Yao, P. B. Merrill, S. S. Perry, D. Marton, and J. W. Rabalais, *Thermal stimulation of the surface termination of $LaAlO_3$ (100)*, J. Chem. Phys. **108**, 1645 (1998).

[126] H. Kawanowa, H. Ozawa, M. Ohtsuki, Y. Gotoh, and R. Souda, *Structure analysis of $LaAlO_3$ (001) surfaces by low energy neutral scattering spectroscopy*, Surf. Sci. **506**, 87 (2002).

[127] D. A. Schmidt, T. Ohta, Q. Yu, and M. A. Olmstead, *Influence of perovskite termination on oxide heteroepitaxy*, J. Appl. Phys **99**, (2006).

[128] C. Duriez, C. Chapon, C. R. Henry, and J. M. Rickard, *Structural characterization of MgO (100) surfaces*, Surf. Sci. **230**, 123 (1990).

[129] I. D. Gay and N. M. Harrison, *A density functional study of water and methanol chemisorption on MgO(110)*, Surf. Sci. **591**, 13 (2005).

[130] K. F. Zheng, Y. H. Yu, Q. L. Guo, S. Liu, E. G. Wang, F. Xu, and P. J. Moller, *Coverage-dependent dissociation of $H_2O$ on Pd/MgO(100)/Mo(100)*, J. Phys.: Condens. Matter **17**, 3073 (2005).

[131] C. D. Daub, G. N. Patey, D. B. Jack, and A. K. Sallabi, *Monte Carlo simulations of the adsorption of $CO_2$ on the MgO(100) surface*, J. Chem. Phys. **124**, 9 (2006).

[132] S. C. Lee, H. J. Chae, S. J. Lee, B. Y. Choi, C. K. Yi, J. B. Lee, C. K. Ryu, and J. C. Kim, *Development of regenerable MgO-based sorbent promoted with $K_2CO_3$ for $CO_2$ capture at low temperatures*, Environmental Science & Technology **42**, 2736 (2008).

[133] A. B. Joshi and M. G. Norton, *The influence of annealing on the surface morphology of single crystal MgO*, Appl. Surf. Sci. **115**, 307 (1997).

[134] A. F. Degardin, F. Houze, and A. J. Kreisler, *MgO substrate surface optimization for YBaCuO thin film growth*, Ieee Transactions on Applied Superconductivity **13**, 2721 (2003).

[135] T. Thome, L. P. Van, and J. Cousty, *Evolution of yttria-stabilized zirconia (100) surface morphology with temperature*, Journal of the European Ceramic Society **24**, 841 (2004).

[136] R. G. Green, L. Barre, and J. B. Giorgi, *Nano-structures in YSZ (100) surfaces: Implications for metal deposition experiments*, Surf. Sci. **601**, 792 (2007).

[137] U. Hasenkox, C. Mitze, and R. Waser, *Metal propionate synthesis of magnetoresistive $La_{1-x}(Ca,Sr)_xMnO_3$ thin films*, J. Am. Ceram. Soc. **80**, 2709 (1997).

[138] R. W. Schwartz, T. Schneller, and R. Waser, *Chemical solution deposition of electronic oxide films*, C. R. Chim. **7**, 433 (2004).

[139] A. Hassini, A. Pomar, J. Gutierrez, M. Coll, N. Roma, C. Moreno, A. Ruyter, T. Puig, and X. Obradors, *Atomically flat MOD $La_{0.7}Sr_{0.3}MnO_3$ buffer layers for high critical current $YBa_2Cu_3O_7$ TFA films*, Supercond. Sci. Technol. **20**, S230 (2007).

[140] C. Moreno, *New features in solution derived $La_{0.7}Sr_{0.3}MnO_3$ thin films : spontaneous outcropping and nanoscale reversible resistive switching*, Ph.D. thesis, Universitat Autonoma de Barcelona (2010).

[141] L. B. Freund and S. Suresh, *Thin Film materials:stress, defect formation and surface evolution* (Cambridge University Press, Cambridge, 2003).

[142] M. Ohring, *Materials Science of thin films: deposition and structure* (Academic Press, 1992).

[143] E. Bauer, Z. Kristallogr. **110**, 372 (1958).

[144] F. C. Frank and J. H. Van der Merwe, Proc.Roy.Soc.London A **198**, 205 (1949).

[145] V. Volmer and A. Weber, Z.Phys.Chem **119**, 277 (1926).

[146] I. N. Stranski and L. Krastanov, Sitzungsberichte der Akademie der Wissenschaften Wien **146** (1938).

[147] V. A. Shchukin and D. Bimberg, *Spontaneous ordering of nanostructures on crystal surfaces*, Reviews of Modern Physics **71**, 1125 (1999).

[148] B. Voigtländer, *Fundamental processes in Si/Si and Ge/Si epitaxy studied by scanning tunneling microscopy during growth*, Surf. Sci. Rep. **43**, 127 (2001).

[149] J. Tersoff and F. K. LeGoues, *Competing relaxation mechanisms in strained layers*, Phys. Rev. Lett. **72**, 3570 (1994).

[150] C. Teichert, *Self-organization of nanostructures in semiconductor heteroepitaxy*, Physics Reports **365**, 335 (2002).

[151] H. T. Johnson and L. B. Freund, *Mechanics of coherent and dislocated island morphologies in strained epitaxial material systems*, J. Appl. Phys. **81**, 6081 (1997).

[152] F. Liu, A. H. Li, and M. G. Lagally, *Self-assembly of two-dimensional islands via strain-mediated coarsening*, Phys. Rev. Lett. **87**, 126103 (2001).

[153] J. A. Floro, G. A. Lucadamo, E. Chason, L. B. Freund, M. Sinclair, R. D. Twesten, and R. Q. Hwang, *SiGe island shape transitions induced by elastic repulsion*, Phys. Rev. Lett. **80**, 4717 (1998).

[154] J. Tersoff and R. M. Tromp, *Shape transition in growth of strained islands: Spontaneous formation of quantum wires*, Phys. Rev. Lett. **70**, 2782 (1993).

[155] J. C. Nie, H. Yamasaki, and Y. Mawatari, *Self-assembled growth of $CeO_2$ nanostructures on sapphire*, Phys. Rev. B **70**, 195421 (2004).

[156] O. L. Alerhand, D. Vanderbilt, R. D. Meade, and J. D. Joannopoulos, *Spontaneous formation of stress domains on crystal surfaces*, Phys. Rev. Lett. **61**, 1973 (1988).

[157] M. Gibert, *Self-assembled strain-induced oxide nanostructures grown by chemical solutions*, Ph.D. thesis, Universitat Autonoma de Barcelona (2009).

[158] M. J. Akhtar, C. R. A. Catlow, B. Slater, A. M. Walker, and S. M. Woodley, *Bulk and surface simulation studies of $La_{1-x}Ca_xMnO_3$*, Chemistry of Materials **18**, 1552 (2006).

[159] H. Boschker, M. Huijben, A. Vailionis, J. Verbeeck, S. v. Aert, M. Luysberg, S. Bals, G. v. Tendeloo, E. P. Houwman, G. Koster, D. H. A. Blank, and G. Rijnders, *Optimized fabrication of high-quality $La_{0.67}Sr_{0.33}MnO_3$ thin films considering all essential characteristics*, J. Phys. D: Appl. Phys. **44**, 205001 (2011).

[160] P. Abellan, *Interfacial structure and microstructural evolution of solution derived dissimilar oxide nanostructures. Implications on their functional properties*, Ph.D. thesis, Universitat Autònoma de Barcelona (2011).

[161] H. Zheng, Q. Zhan, F. Zavaliche, M. Sherburne, F. Straub, M. P. Cruz, L.-Q. Chen, U. Dahmen, and R. Ramesh, *Controlling self-assembled perovskite-spinel nanostructures*, Nano Letters **6**, 1401 (2006).

[162] F. Tsui, M. C. Smoak, T. K. Nath, and C. B. Eom, *Strain-dependent magnetic phase diagram of epitaxial $La_{0.67}Sr_{0.33}MnO_3$ thin films*, Appl. Phys. Lett. **76**, 2421 (2000).

[163] M. Angeloni, G. Balestrino, N. G. Boggio, P. G. Medaglia, P. Orgiani, and A. Tebano, *Suppression of the metal-insulator transition temperature in thin $La_{0.7}Sr_{0.3}MnO_3$ films*, J. Appl. Phys. **96**, 6387 (2004).

[164] Y. Takamura, R. V. Chopdekar, E. Arenholz, and Y. Suzuki, *Control of the magnetic and magnetotransport properties of $La_{0.67}Sr_{0.33}MnO_3$ thin films through epitaxial strain*, Appl. Phys. Lett. **92** (2008).

[165] M. Huijben, L. W. Martin, Y. H. Chu, M. B. Holcomb, P. Yu, G. Rijnders, D. H. A. Blank, and R. Ramesh, *Critical thickness and orbital ordering in ultrathin $La_{0.7}Sr_{0.3}MnO_3$ films*, Phys. Rev. B **78**, 094413 (2008).

[166] A. J. Millis, T. Darling, and A. Migliori, *Quantifying strain dependence in "colossal" magnetoresistance manganites*, J. Appl. Phys. **83**, 1588 (1998).

[167] L. F. Kourkoutis, J. H. Song, H. Y. Hwang, and D. A. Muller, *Microscopic origins for stabilizing room-temperature ferromagnetism in ultrathin manganite layers*, PNAS **107**, 11682 (2010).

[168] P. W. Anderson, *Absence of diffusion in certain random lattices*, Phys. Rev. **109**, 1492 (1958).

[169] P. Abellán, C. Moreno, F. Sandiumenge, X. Obradors, and M. Casanove, *Misfit relaxation of $La_{0.7}Sr_{0.3}MnO_3$ thin films by a nanodot segregation mechanism*, Appl. Phys. Lett. **98**, 041903 (2011).

[170] C. Moreno, P. Abellán, F. Sandiumenge, M. J. Casanove, and X. Obradors, *Nanocomposite lanthanum strontium manganite thin films formed by using a chemical solution deposition*, App. Phys. Lett. **100** (In press).

[171] M. Gibert, T. Puig, X. Obradors, A. Benedetti, F. Sandiumenge, and R. Huhne, *Self-organization of heteroepitaxial $CeO_2$ nanodots grown from chemical solutions*, Adv. Mater. **19**, 3937 (2007).

[172] J. Zabaleta, *Autoensamblaje dirigido de nanoestructuras de $Ce_{0,9}Gd_{0,1}O_{2-y}$ crecidas por vía química sobre sustratos nanoindentados*, Tech. Rep. (Universitat Autònoma de Barcelona, 2008).

[173] J. Zabaleta, N. Mestres, P. Abellan, M. Gibert, F. Sandiumenge, T. Puig, and X. Obradors, *Orientational ordering of solution derived epitaxial Gd-doped ceria nanowires induced by nanoscratching*, Nanotechnology **21**, (2010).

[174] W. Ostwald, *Lehrbruck der Allgemeinen Chemie*, Lehrbruck der Allgemeinen Chemie, Vol. 2 (Leipzig, 1896).

[175] J. Penuelas, P. Andreazza, C. Andreazza-Vignolle, H. C. N. Tolentino, M. De Santis, and C. Mottet, *Controlling structure and morphology of CoPt nanoparticles through dynamical or static coalescence effects*, Phys. Rev. Lett. **100**, 115502 (2008).

[176] C. J. Lu, S. Senz, and D. Hesse, *The influence of yttria-stabilized zirconia surface pits on the initial stage of reactive $La_2Zr_2O_7$ formation from $La_2O_3$ vapours and yttria-stabilized zirconia (001) substrates*, Philos. Mag. A **81**, 2705 (2001).

[177] F. F. Lange, H. Shubert, N. Claussen, and M. Ruhle, *Effects of attrition milling and post-sintering heat treatment on fabrication, microstructure and properties of transformation toughened $ZrO_2$*, J. Mater. Sci. **21**, 768 (1986).

[178] M. Gaudon, C. Laberty-Robert, F. Ansart, P. Stevens, and A. Rousset, *New chemical process for the preparation of fine powders and thin films of $LSM_x$-YSZ composite oxides*, Solid State Sci. **5**, 1377 (2003).

[179] A. N. Grundy, B. Hallstedt, and L. J. Gauckler, *Assessment of the La-Sr-Mn-O system*, CALPHAD: Comput. Coupling Phase Diagrams Thermochem. **28**, 191 (2004).

[180] M. Backhaus-Ricoult, K. Adib, T. St.Clair, B. Luerssen, L. Gregoratti, and A. Barinov, *In-situ study of operating SOFC LSM/YSZ cathodes under polarization by photoelectron microscopy*, Solid State Ion. **179**, 891 (2008).

[181] H. J. Deiseroth and H. Mueller-Buschbaum, *Ein beitrag zur pyrochlorstruktur an $La_2Zr_2O_7$*, Z. Anorg. Allg.Chem. **375**, 152 (1970).

[182] Y. Tabira, R. L. Withers, T. Yamada, and N. Ishizawa, *Annular dynamical disorder of the rare earth ions in a $La_2Zr_2O_7$ pyrochlore via single crystal synchrotron X-ray diffraction*, Zeitschrift fur Kristallographie **216**, 92 (2001).

[183] K. R. Whittle, L. M. D. Cranswick, S. A. T. Redfern, I. P. Swainson, and G. R. Lumpkin, *Lanthanum pyrochlores and the effect of yttrium addition in the systems $La_{2-x}Y_xZr_2O_7$ and $La_{2-x}Y_xHf_2O_7$*, J. Solid State Chem. **182**, 442 (2009).

[184] C. Clausen, C. Bagger, J. B. Bildesorensen, and A. Horsewell, *Microstructural and microchemical characterization of the interface between $La_{0.85}Sr_{0.15}MnO_3$ and $Y_2O_3$-stabilized $ZrO_2$*, Solid State Ion. **70**, 59 (1994).

[185] M. Backhaus-Ricoult, M. Badding, J. Brown, M. Carson, E. Sanford, and Y. Thibault, *Interface reactivity between yttria stabilized zirconia and strontium lanthanum manganites*, in *Developments in Solid Oxide Fuel Cells and Lithium Ion Batteries: Proceedings of the 106th Annual Meeting of the American Ceramic Society*, Ceramic Transactions Series, edited by A. Manthiram, P. N. Kumta, S. K. Sundaram, and S. W. Chan (Wiley-American Ceramic Society, 2004).

[186] A. Chen, G. Bourne, K. Siebein, R. DeHoff, E. Wachsman, and K. Jones, *Characterization of lanthanum zirconate formation at the A-site-deficient strontium-doped lanthanum manganite cathode/yttrium-stabilized zirconia electrolyte interface of solid oxide fuel cells*, J. Am. Ceram. Soc. **91**, 2670 (2008).

[187] Y. L. Liu, A. Hagen, R. Barfod, M. Chen, H. J. Wang, F. W. Poulsen, and P. V. Hendriksen, *Microstructural studies on degradation of interface between LSM-YSZ cathode and YSZ electrolyte in SOFCs*, Solid State Ion. **180**, 1298 (2009).

[188] C. W. Sun, R. Hui, and J. Roller, *Cathode materials for solid oxide fuel cells: a review*, J. Solid State Electrochem. **14**, 1125.

[189] S. Bernal, F. J. Botana, J. J. Calvino, C. López-Cartes, J. A. Pérez-Omil, and J. M. Rodríguez-Izquierdo, *The interpretation of HREM images of supported metal catalysts using image simulation: profile view images*, Ultramicroscopy **72**, 135 (1998).

[190] J. Pérez-Omil, Ph.D. thesis, University of Cadiz (2004).

[191] J. A. Venables, *Atomic processes in crystal growth*, Surf. Sci. **299-300**, 798 (1994).

[192] B. Fischer, H. Brune, J. V. Barth, A. Fricke, and K. Kern, *Nucleation kinetics on inhomogeneous substrates: Al/Au(111)*, Phys. Rev. Lett. **82**, 1732 (1999).

[193] C. J. Lu, S. Senz, and D. Hesse, *The impact of YSZ surface steps on structure and morphology of $La_2Zr_2O_7$ islands growing on YSZ(1 0 0) surfaces by vapour-solid reaction*, Surf. Sci. **515**, 507 (2002).

[194] C. J. Lu, S. Senz, and D. Hesse, *Formation and structure of misfit dislocations at the $La_2Zr_2O_7$-$Y_2O_3$-stabilized $ZrO_2$ (001) reaction front during vapour-solid reaction*, Philos. Mag. Lett. **82**, 167 (2002).

[195] S. Chikazumi, *Physics of Magnetism* (John Wiley & Sons, 1964).

[196] A. Haghiri-Gosnet, *Microstructure and magnetic properties of strained $La_{0.7}Sr_{0.3}MnO_3$ thin films*, J. Appl. Phys. **88**, 4257 (2000).

[197] J. Curiale, M. Granada, H. E. Troiani, R. D. Sanchez, A. G. Leyva, P. Levy, and K. Samwer, *Magnetic dead layer in ferromagnetic manganite nanoparticles*, Appl. Phys. Lett. **95**, (2009).

[198] J. Smit and H. G. Beljers, Philips Res. Rep. **10**, 113 (1955).

[199] K. Steenbeck and R. Hiergeist, *Magnetic anisotropy of ferromagnetic $La_{0.7}(Sr, Ca)_{0.3}MnO_3$ epitaxial films*, Appl. Phys. Lett. **75**, 1778 (1999).

[200] P. Abellán, J. Zabaleta, J. Santiso, M. J. Casanove, N. Dix, J. Aguiar, N. D. Browning, N. Mestres, T. Puig, X. Obradors, and F. Sandiumenge, *Interface structure governed by plastic and structural dissimilarity in perovskite $La_{0.7}Sr_{0.3}MnO_3$ nanodots on rock-salt MgO substrates.* (Submitted).

[201] B. Yang, F. Liu, and M. G. Lagally, *Local strain-mediated chemical potential control of quantum dot self-organization in heteroepitaxy*, Phys. Rev. Lett. **92**, (2004).

[202] Y. Du, S. Atha, R. Hull, J. F. Groves, I. Lyubinetsky, and D. R. Baer, *Focused-ion-beam directed self-assembly of $Cu_2O$ islands on $SrTiO_3$ (100)*, Appl. Phys. Lett. **84**, 5213 (2004).

[203] A. Strachan, T. Çagin, and W. A. Goddard III, *Phase diagram of MgO from density-functional theory and molecular-dynamics simulations*, Phys. Rev. B **60**, 15084 (1999).

[204] in *Magnesium oxide (MgO) impurities and defects. Landolt-Börnstein - Group III Condensed Matter Numerical Data and Functional Relationships in Science and Technology*, Vol. 41B, edited by O. Madelung, U. Rössler, and M. Schulz (SpringerMaterials).

[205] A. M. Glass, *Reactions between vacancies and impurities in magnesium oxide. I. $Cr^{3+}$ ion impurities*, J. Chem. Phys. **46**, 2080 (1967).

[206] http://www.2spi.com/catalog/submat/magnesium-oxide.shtml (2011).

[207] Y. S. Kuz'minov, E. E. Lomonova, and V. V. Osiko, *Cubic Zirconia and Skull Melting*, 2nd ed. (Cambridge Int Science Publishing, 2008).

[208] M. Khalid, A. Setzer, M. Ziese, P. Esquinazi, D. Spemann, A. Pöppl, and E. Goering, *Ubiquity of ferromagnetic signals in common diamagnetic oxide crystals*, Phys. Rev. B **81**, 214414 (2010).

[209] M. J. Hÿtch, E. Snoeck, and R. Kilaas, *Quantitative measurement of displacement and strain fields from HREM micrographs*, Ultramicroscopy **74**, 131 (1998).

[210] R. M. Bozorth and H. J. Williams, Rev. Mod. Phys **17**, 72 (1945).

[211] S. Xie, J. Cheng, B. W. Wessels, and V. P. Dravid, *Interfacial structure and chemistry of epitaxial $CoFe_2O_4$ thin films on $SrTiO_3$ and MgO substrates*, Appl. Phys. Lett. **93**, 181901 (2008).

[212] T. W. Darling, A. Migliori, E. G. Moshopoulou, S. A. Trugman, J. J. Neumeier, J. L. Sarrao, A. R. Bishop, and J. D. Thompson, *Measurement of the elastic tensor of a single crystal of $La_{0.83}Sr_{0.17}MnO_3$ and its response to magnetic fields*, Phys. Rev. B **57**, 5093 (1998).

[213] R. V. Demin, L. I. Koroleva, and A. M. Balbashov, *Anomalies of magnetostriction and thermal expansion in $La_{0.7}Sr_{0.3}MnO_3$ perovskite*, J. Magn. Magn. Mater. **177-181**, 871 (1998).

[214] K. Nakamura, X. Liu, T. Hatano, Z. Jiao, K. Shang, and A. Ishii, *Mn and Mg interdiffusion and magnetotransport properties of $La_{0.7}Sr_{0.3}MnO_3$ films on MgO (100) substrate*, Jpn. J. Appl. Phys **39**, 1721 (2000).

[215] J. E. Huheey, E. A. Keiter, and R. L. Keiter, *Inorganic Chemistry: Principles of Structure and Reactivity*, 4th ed. (Prentice Hall, 1997).

[216] M. Winter, http://www.webelements.com (2011).

[217] C.-C. T. Yang, W.-C. J. Wei, and A. Roosen, *Reaction kinetics and mechanisms between $La_{0.65}Sr_{0.3}MnO_3$ and 8 mol% Yttria-Stabilized Zirconia*, J. Am. Ceram. Soc. **87**, 1110 (2004).

[218] M. Palcut, K. Wiik, and T. Grande, *Cation self-diffusion and nonstoichiometry of lanthanum manganite studied by diffusion couple measurements*, J. Phys. Chem. C **111**, 813 (2006).

[219] Y. Martin and H. K. Wickramasinghe, *Magnetic imaging by force microscopy with 1000-Å resolution*, Appl. Phys. Lett. **50**, 1455 (1987).

[220] J. J. Saenz, N. Garcia, P. Grutter, E. Meyer, H. Heinzelmann, R. Wiesendanger, L. Rosenthaler, H. R. Hidber, and H. J. Guntherodt, *Observation of magnetic forces by the atomic force microscope*, J. Appl. Phys. **62**, 4293 (1987).

[221] B. L. Ramakrishna and E. W. Ong, *Surface evaluation by atomic force microscopy*, Encyclopedia of Materials: Science and Technology, Elsevier Science Ltd. , 9030 (2001).

[222] R. García and R. Pérez, *Dynamic atomic force microscopy methods*, Surf. Sci. Rep. **47**, 197 (2002).

[223] A. Asenjo, J. M. Garcia, and M. Vazquez, *Magnetic force microscopy: an advanced technique for the observation of magnetic domain and walls*, in *Research Developments in Magnetics*, Vol. 2, edited by S. Pandalai (Transworld Res. Network, 2001) pp. 25–34.

[224] U. Hartmann, *Magnetic force microscopy - some remarks from the micromagnetic point of view*, J. Appl. Phys. **64**, 1561 (1988).

[225] J. J. Saenz, N. Garcia, and J. C. Slonczewski, *Theory of magnetic imaging by force microscopy*, Appl. Phys. Lett. **53**, 1449 (1988).

[226] H. J. Mamin, D. Rugar, J. E. Stern, B. D. Terris, and S. E. Lambert, *Force microscopy of magnetization patterns in longitudinal recording media*, Appl. Phys. Lett. **53**, 1563 (1988).

[227] U. Hartmann, *The point dipole approximation in magnetic force microscopy*, Phys. Lett. A **137**, 475 (1989).

[228] J. M. Garcia, A. Thiaville, J. Miltat, K. J. Kirk, J. N. Chapman, and F. Alouges, *Quantitative interpretation of magnetic force microscopy images from soft patterned elements*, Appl. Phys. Lett. **79**, 656 (2001).

[229] R. Engel-Herbert, D. M. Schaadt, and T. Hesjedal, *Analytical and numerical calculations of the magnetic force microscopy response: A comparison*, J. Appl. Phys. **99**, 113905 (2006).

[230] W. G. Morris, *Atomic force microscopy*, Encyclopedia of Materials: Science and Technology, Elsevier Science , 365 (2001).

[231] M. Jaafar, *Procesos de imanación en la nanoescala mediante microscopía de fuerzas magnéticas*, Ph.D. thesis, Universidad Autónoma de Madrid (2009).

[232] M. Jaafar, J. Gomez-Herrero, A. Gil, P. Ares, M. Vazquez, and A. Asenjo, *Variable-field magnetic force microscopy*, Ultramicroscopy **109**, 693 (2009).

[233] http://www.nanosensors.com/, .

[234] R. M. Bozorth and J. G. Walker, *Effect of ordering on the magnetic anisotropy of iron nickel alloys*, Phys. Rev. **83**, 871 (1951).

[235] M. M. Yang, S. E. Lambert, J. K. Howard, and C. Hwang, *Laminated CoPtCr/Cr films for low noise longitudinal recording*, IEEE Trans. Magn. **27**, 5052 (1991).

[236] C. D. Fuerst and E. G. Brewer, *High-remanence rapidly solidified Nd-Fe-B: Die-upset magnets*, J. Appl. Phys. **73**, 5751 (1993).

[237] J. W. F. Brown, *The fundamental theorem of fine-ferromagnetic-particle theory*, J. Appl. Phys. **39**, 993 (1968).

[238] K. L. Metlov and K. Y. Guslienko, *Stability of magnetic vortex in soft magnetic nano-sized circular cylinder*, J. Magn. Magn. Mater. **242**, 1015 (2002).

[239] E. Y. Tsymbal, *Theory of magnetostatic coupling in thin-film rectangular magnetic elements*, Appl. Phys. Lett. **77**, 2740 (2000).

[240] J. Mejia-Lopez, D. Altbir, A. H. Romero, X. Batlle, I. V. Roshchin, C. P. Li, and I. K. Schuller, *Vortex state and effect of anisotropy in sub-100-nm magnetic nanodots*, J. Appl. Phys. **100**, (2006).

[241] http://math.nist.gov/oommf/, .

[242] R. Akiyama, H. Tanaka, T. Matsumoto, and T. Kawai, *Spin-polarized scanning tunneling microscopy on half-metallic manganite thin film with half-metallic manganite tip*, Appl. Phys. Lett. **79**, 4378 (2001).

[243] S. Y. Chou, *Patterned magnetic nanostructures and quantized magnetic disks*, Proceedings of the Ieee **85**, 652 (1997).

[244] L. S. Kong, L. Zhuang, and S. Y. Chou, *Writing and reading 7.5 Gbits/in$^2$ longitudinal quantized magnetic disk using magnetic force microscope tips*, IEEE Trans. Magn. **33**, 3019 (1997).

[245] M. Todorovic, S. Schultz, J. Wong, and A. Scherer, *Writing and reading of single magnetic domain per bit perpendicular patterned media*, Appl. Phys. Lett. **74**, 2516 (1999).

[246] B. Van Waeyenberge, A. Puzic, H. Stoll, K. W. Chou, T. Tyliszczak, R. Hertel, M. Fahnle, H. Bruckl, K. Rott, G. Reiss, I. Neudecker, D. Weiss, C. H. Back, and G. Schutz, *Magnetic vortex core reversal by excitation with short bursts of an alternating field*, Nature **444**, 461 (2006).

[247] R. Hertel, S. Gliga, auml, M. hnle, and C. M. Schneider, *Ultrafast nanomagnetic toggle switching of vortex cores*, Phys. Rev. Lett. **98**, 117201 (2007).

[248] M. Jaafar, R. Yanes, D. P. de Lara, O. Chubykalo-Fesenko, A. Asenjo, E. M. Gonzalez, J. V. Anguita, M. Vazquez, and J. L. Vicent, *Control of the chirality and polarity of magnetic vortices in triangular nanodots*, Phys. Rev. B **81**, (2010).

[249] J. Raabe, R. Pulwey, R. Sattler, T. Schweinbock, J. Zweck, and D. Weiss, *Magnetization pattern of ferromagnetic nanodisks*, J. Appl. Phys. **88**, 4437 (2000).

[250] J. M. Garcia-Martin, A. Thiaville, J. Miltat, T. Okuno, L. Vila, and L. Piraux, *Imaging magnetic vortices by magnetic force microscopy: experiments and modelling*, J. Phys. D: Appl. Phys. **37**, 965 (2004).

[251] L. D. Buda, I. L. Prejbeanu, U. Ebels, and K. Ounadjela, *Micromagnetic simulations of magnetisation in circular cobalt dots*, Comp. Mater. Sci. **24**, 181 (2002).

[252] A. Schwarz, M. Liebmann, U. Kaiser, R. Wiesendanger, T. W. Noh, and D. W. Kim, *Visualization of the Barkhausen effect by magnetic force microscopy*, Phys. Rev. Lett. **92**, (2004).

[253] J. Mejia-Lopez, D. Altbir, P. Landeros, J. Escrig, A. H. Romero, I. V. Roshchin, C. P. Li, M. R. Fitzsimmons, X. Batlle, and I. K. Schuller, *Development of vortex state in circular magnetic nanodots: Theory and experiment*, Phys. Rev. B **81**, (2010).

[254] R. Hertel and C. M. Schneider, *Exchange explosions: Magnetization dynamics during vortex-antivortex annihilation*, Phys. Rev. Lett. **97**, (2006).

[255] M. Konoto, T. Kohashi, K. Koikie, T. Arima, Y. Kaneko, Y. Tomioka, and Y. Tokura, *Magnetic domain structure of a $La_{0.7}Sr_{0.3}MnO_3$ (001) surface observed by a spin-polarized scanning electron microscope*, Appl. Phys. Lett. **84**, 2361 (2004).

[256] T. Pokhil, D. A. Song, and J. Nowak, *Spin vortex states and hysteretic properties of submicron size NiFe elements*, J. Appl. Phys. **87**, 6319 (2000).

[257] L. D. Buda, I. L. Prejbeanu, I. L. Demand, M. Demand, U. Ebels, and K. Ounadjela, *Vortex states stability in circular Co(0001) dots*, IEEE Trans. Magn. **37**, 2061 (2001).

[258] N. Martin, N. C. Bigall, I. Monch, T. Gemming, A. Eychmuller, R. Mattheis, R. Schafer, L. Schultz, and J. McCord, *Enhanced nucleation of vortices in soft magnetic materials prepared by silica nanosphere lithography*, Adv. Funct. Mater. **21**, 891 (2011).

[259] T. Okuno, K. Shigeto, T. Ono, K. Mibu, and T. Shinjo, *MFM study of magnetic vortex cores in circular permalloy dots: behavior in external field*, J. Magn. Magn. Mater. **240**, 1 (2002).

[260] K. Y. Guslienko, V. Novosad, Y. Otani, H. Shima, and K. Fukamichi, *Magnetization reversal due to vortex nucleation, displacement, and annihilation in submicron ferromagnetic dot arrays*, Phys. Rev. B **65**, 024414 (2001).

[261] L. Kelvin, *Contact electricity of metals*, Philos. Mag. **46**, 82 (1898).

[262] G. H. Enevoldsen, T. Glatzel, M. C. Christensen, J. V. Lauritsen, and F. Besenbacher, *Atomic scale Kelvin Probe Force Microscopy studies of the surface potential variations on the $TiO_2$(110) surface*, Phys. Rev. Lett. **100**, 236104 (2008).

[263] S. Sadewasser, P. Jelinek, C.-K. Fang, O. Custance, Y. Yamada, Y. Sugimoto, M. Abe, and S. Morita, *New insights on atomic-resolution frequency-modulation Kelvin-Probe Force-Microscopy imaging of semiconductors*, Phys. Rev. Lett. **103**, 266103 (2009).

[264] W. Wan, J. Feng, H. A. Padmore, and D. S. Robin, *Simulation of a mirror corrector for PEEM3*, Nucl. Instrum. Methods Phys. Res., Sect. A **519**, 222 (2004).

[265] M. Schneider, Claus and G. Schönhense, *Investigating surface magnetism by means of photoexcitation electron emission microscopy*, Reports on Progress in Physics **65**, 1785 (2002).

[266] J. Feng and A. Scholl, *Photoemission electron microscopy (PEEM)*, in *Science of Microscopy*, edited by P. W. Hawkes and J. C. H. Spence (Springer New York, 2007) pp. 657–695.

[267] B. T. Thole, G. van der Laan, J. C. Fuggle, G. A. Sawatzky, R. C. Karnatak, and J. M. Esteva, *3d X-ray-absorption lines and the $3d^9 4f^{n+1}$ multiplets of the lanthanides*, Phys. Rev. B **32**, 5107 (1985).

[268] Y. Ufuktepe, G. Akgül, and J. Lüning, *X-ray photoabsorption and total electron yield of Fe thin films at the $L_{2,3}$ edge*, J. Alloys Compd. **401**, 193 (2005).

[269] R. Nakajima, J. Stöhr, and Y. U. Idzerda, *Electron-yield saturation effects in L-edge x-ray magnetic circular dichroism spectra of Fe, Co, and Ni*, Phys. Rev. B **59**, 6421 (1999).

[270] M. C. Richter, P. De Padova, C. Quaresima, P. Perfetti, R. Brochier, V. Ilakovac, O. Heckmann, L. Lechevallier, M. Zerrouki, C. Teodorescu, C. S. Fadley, N. Hamdan, and K. Hricovini, *Resonant photoemission and XMCD on Mn-based systems*, J. Alloys Compd. **362**, 41 (2004).

[271] B. T. Thole, P. Carra, F. Sette, and G. van der Laan, *X-ray circular dichroism as a probe of orbital magnetization*, Phys. Rev. Lett. **68**, 1943 (1992).

[272] C. T. Chen, Y. U. Idzerda, H. J. Lin, N. V. Smith, G. Meigs, E. Chaban, G. H. Ho, E. Pellegrin, and F. Sette, *Experimental confirmation of the X-ray magnetic circular dichroism sum rules for iron and cobalt*, Phys. Rev. Lett. **75**, 152 (1995).

[273] A. Scholl, J. Stöhr, J. Lüning, J. W. Seo, J. Fompeyrine, H. Siegwart, J. P. Locquet, F. Nolting, S. Anders, E. E. Fullerton, M. R. Scheinfein, and H. A. Padmore, *Observation of antiferromagnetic domains in epitaxial thin films*, Science **287**, 1014 (2000).

[274] B. Henke, E. Gullikson, and J. Davis, *X-ray interactions: photoabsorption, scattering, transmission, and reflection at E=50-30000 eV, Z=1-92*, Atomic Data and Nuclear Data Tables **54**, 181 (1993).

[275] C. J. Powell and A. Jablonski, *Surface sensitivity of X-ray photoelectron spectroscopy*, Nucl. Instrum. Methods Phys. Res., Sect. A **601**, 54 (2009).

[276] C. J. Powell and A. Jablonski, *NIST Electron Effective-Attenuation-Length Database Version 1.3* (National Institute of Standards and Technology, Gaithersburg, MD, 2011).

[277] S. Stadler, Y. U. Idzerda, Z. Chen, S. B. Ogale, and T. Venkatesan, *The magnetism of a buried $La_{0.7}Sr_{0.3}MnO_3$ interface*, Appl. Phys. Lett. **75**, 3384 (1999).

[278] M. P. de Jong, I. Bergenti, V. A. Dediu, M. Fahlman, M. Marsi, and C. Taliani, *Evidence for $Mn^{2+}$ ions at surfaces of $La_{0.7}Sr_{0.3}MnO_3$ thin films*, Phys. Rev. B **71**, 014434 (2005).

[279] S. Valencia, A. Gaupp, W. Gudat, L. Abad, L. Balcells, A. Cavallaro, B. Martínez, and F. J. Palomares, *Mn valence instability in $La_{2/3}Ca_{1/3}MnO_3$ thin films*, Phys. Rev. B **73**, 104402 (2006).

[280] M. P. de Jong, I. Bergenti, W. Osikowicz, R. Friedlein, V. A. Dediu, C. Taliani, and W. R. Salaneck, *Valence electronic states related to $Mn^{2+}$ at $La_{0.7}Sr_{0.3}MnO_3$ surfaces characterized by resonant photoemission*, Phys. Rev. B **73**, 052403 (2006).

[281] S. Valencia, A. Gaupp, W. Gudat, L. Abad, L. Balcells, and B. Martínez, *Impact of microstructure on the Mn valence of $La_{2/3}Ca_{1/3}MnO_3$ thin films*, Phys. Rev. B **75**, 184431 (2007).

[282] C. Mitra, Z. Hu, P. Raychaudhuri, S. Wirth, S. I. Csiszar, H. H. Hsieh, H. J. Lin, C. T. Chen, and L. H. Tjeng, *Direct observation of electron doping in $La_{0.7}Ce_{0.3}MnO_3$ using X-ray absorption spectroscopy*, Phys. Rev. B **67**, 092404 (2003).

[283] F. M. F. de Groot, J. C. Fuggle, B. T. Thole, and G. A. Sawatzky, *2p x-ray absorption of 3d transition-metal compounds: An atomic multiplet description including the crystal field*, Phys. Rev. B **42**, 5459 (1990).

[284] S. Heun, Y. Watanabe, B. Ressel, D. Bottomley, T. Schmidt, and K. C. Prince, *Core-level photoelectron spectroscopy from individual heteroepitaxial nanocrystals on GaAs(001)*, Phys. Rev. B **63**, 125335 (2001).

[285] F. Ratto, A. Locatelli, S. Fontana, S. Kharrazi, S. Ashtaputre, S. K. Kulkarni, S. Heun, and F. Rosei, *Chemical mapping of individual semiconductor nanostructures*, Small **2**, 401 (2006).

[286] W. Yang, M. Zeman, and R. J. Nemanich, *Coarsening dynamics of nanoscale Ti-silicide islands on Si surfaces*, J. Korean Phys. Soc. **50**, 575 (2007).

[287] A. Moewes, S. Stadler, R. P. Winarski, D. L. Ederer, M. M. Grush, and T. A. Callcott, *Core-hole induced charge transfer and Coster-Kronig enhanced fluorescence at the 3d threshold of lanthanum studied by resonant inelastic scattering*, Phys. Rev. B **58**, R15951 (1998).

[288] www.efunda.com/materials/elements/TC_Table.cfm?Element_ID=pt (2011).

[289] J. L. Cohn, J. J. Neumeier, C. P. Popoviciu, K. J. McClellan, and T. Leventouri, *Local lattice distortions and thermal transport in perovskite manganites*, Phys. Rev. B **56**, R8495 (1997).

[290] D. D. Hass, *Directed Vapor Deposition of Thermal Barrier Coatings*, Ph.D. thesis, University of Virginia (2000).

[291] M. Nonnenmacher, M. P. O. Boyle, and H. K. Wickramasinghe, *Kelvin Probe Force Microscopy*, Appl. Phys. Lett. **58**, 2921 (1991).

[292] C. Sommerhalter, *High-sensitivity quantitative kelvin probe microscopy by noncontact ultra-high-vacuum atomic force microscopy*, Appl. Phys. Lett. **75**, 286 (1999).

[293] T. Glatzel, M. C. Lux-Steiner, E. Strasbourg, A. Boag, and Y. Rosenwaks, *Principles of Kelvin Probe Force Microscopy*, in *Scanning Probe Microscopy: Electrical and Electromechanical Phenomena at the Nanoscale*, Vol. 2, edited by S. V. Kalinin and A. Gruverman (Springer, New York, 2007) pp. 113–131.

[294] O. Douhéret, S. Anand, T. Glatzel, K. Maknys, and S. Sadewasser, *Characterization of quantum wells by cross-sectional Kelvin probe force microscopy*, Appl. Phys. Lett. **85**, 5245 (2004).

[295] A. Schwarzman, *Nanoscale potential distribution across multi-quantum well structures: Kelvin probe force microscopy and secondary electron imaging*, J. Appl. Phys. **98**, 084310 (2005).

[296] S. Shusterman, A. Raizman, A. Sher, Y. Paltiel, A. Schwarzman, E. Lepkifker, and Y. Rosenwaks, *Nanoscale mapping of strain and composition in quantum dots using Kelvin probe force microscopy*, Nano Letters **7**, 2089 (2007).

[297] G. N. Luo, K. Yamaguchi, T. Terai, and M. Yamawaki, *Charging effect on work function measurements of lithium ceramics under irradiation*, J. Alloys Compd. **349**, 211 (2003).

[298] C. Barth and C. R. Henry, *Gold nanoclusters on alkali halide surfaces: Charging and tunneling*, Appl. Phys. Lett. **89**, 252119 (2006).

[299] C. Barth and C. R. Henry, *Kelvin probe force microscopy on surfaces of UHV cleaved ionic crystals*, Nanotechnology **17**, S155 (2006).

[300] C. Barth and C. R. Henry, *Surface double layer on (001) surfaces of alkali halide crystals: A scanning force microscopy study*, Phys. Rev. Lett. **98**, 136804 (2007).

[301] S. Gómez-Moñivas, L. Froufe-Pérez, A. Caamaño, and J. Sáenz, *Electrostatic forces between sharp tips and metallic and dielectric samples*, Appl. Phys. Lett. **79**, 4048 (2001).

[302] J. Zuñiga-Pérez, E. Palacios-Lidón, V. Muñoz-Sanjosé, and J. Colchero, *Nanoscale determination of surface orientation and electrostatic properties of ZnO thin films*, Appl. Phys. A **88**, 77 (2007).

[303] M. Fujihira, *Kelvin Probe Force Microscopy of molecular surfaces*, Annual Review of Materials Science **29**, 353 (1999).

[304] W. A. Zisman, *A new method of measuring contact potential differences in metals*, Rev. Sci. Instrum. **3**, 367 (1932).

[305] D. W. Abraham, C. Williams, J. Slinkman, and H. K. Wickramasinghe, *Lateral dopant profiling in semiconductors by force microscopy using capacitive detection*, J. Vac. Sci. Technol. B **9**, 703 (1991).

[306] S. V. Kalinin and A. Gruverman, *Scanning Probe Microscopy* (Springer, New York, 2007).

[307] A. Sasahara, C. L. Pang, and H. Onishi, *Probe microscope observation of platinum atoms deposited on the $TiO_2$(110)-(1×1) surface*, J. Phys. Chem. B **110**, 13453 (2006).

[308] L. Nony, A. S. Foster, F. Bocquet, and C. Loppacher, *Understanding the atomic-scale contrast in Kelvin Probe Force Microscopy*, Phys. Rev. Lett. **103**, 036802 (2009).

[309] S. Lee, A. Shinde, and R. Ragan, *Morphological work function dependence of rare-earth disilicide metal nanostructures*, Nanotechnology **20**, 035701 (2009).

[310] T. Glatzel, S. Sadewasser, and M. C. Lux-Steiner, *Amplitude or frequency modulation-detection in Kelvin Probe Force Microscopy*, Appl. Surf. Sci. **210**, 84 (2003).

[311] A. Kikukawa, S. Hosaka, and R. Imura, *Vacuum compatible high-sensitive Kelvin Probe Force Microscopy*, Rev. Sci. Instrum. **67**, 1463 (1996).

[312] Y. Rosenwaks, R. Shikler, T. Glatzel, and S. Sadewasser, *Kelvin Probe Force Microscopy of semiconductor surface defects*, Phys. Rev. B **70**, 085320 (2004).

[313] T. R. Albrecht, P. Grütter, D. Horne, and D. Rugar, *Frequency modulation detection using high-Q cantilevers for enhanced force microscope sensitivity*, J. Appl. Phys. **69**, 668 (1991).

[314] http://www.budgetsensors.com.

[315] T. Ngai, W. J. Qi, R. Sharma, J. Fretwell, X. Chen, J. C. Lee, and S. Banerjee, *Electrical properties of $ZrO_2$ gate dielectric on SiGe*, Appl. Phys. Lett. **76**, 502 (2000).

[316] G. A. Samara, *Low temperature dielectric properties of candidate substrates for high-temperature superconductors: $LaAlO_3$ and $ZrO_2$: 9.5 mol% $Y_2O_3$*, J. Appl. Phys **68**, 4214 (1990).

[317] M. Weinert and R. E. Watson, *Contributions to the work function of crystals*, Phys. Rev. B **29**, 3001 (1984).

[318] S. Duhm, G. Heimel, I. Salzmann, H. Glowatzki, R. L. Johnson, A. Vollmer, J. P. Rabe, and N. Koch, *Orientation-dependent ionization energies and interface dipoles in ordered molecular assemblies*, Nat. Mater. **7**, 326 (2008).

[319] K. Okamoto, Y. Sugawara, and S. Morita, *The elimination of the artifact in the electrostatic force measurement using a novel noncontact atomic force microscope/electrostatic force microscope*, Appl. Surf. Sci. **188**, 381 (2002).

[320] M. Lee, W. Lee, and F. B. Prinz, *Geometric artefact suppressed surface potential measurements*, Nanotechnology **17**, 3728 (2006).

[321] N. W. Ashcroft and N. D. Mermin, *Solid State Physics* (Brooks/Cole Thomson Learning, 1976).

[322] D. Cahen and A. Kahn, *Electron energetics at surfaces and interfaces: Concepts and experiments*, Adv. Mater. **15**, 271 (2003).

[323] H. Ishii, K. Sugiyama, E. Ito, and K. Seki, *Energy level alignment and interfacial electronic structures at organic/metal and organic/organic interfaces*, Adv. Mater. **11**, 605 (1999).

[324] N. D. Lang and W. Kohn, *Theory of metal surfaces: Work function*, Phys. Rev. B **3**, 1215 (1971).

[325] C. Fall, *Ab-initio study of the work functions of elemental metal crystals*, Ph.D. thesis, EPFL (1999).

[326] K. Wandelt, *The local work function: Concept and implications*, Appl. Surf. Sci. **111**, 1 (1997).

[327] R. Smoluchowski, *Anisotropy of the electronic work function of metals*, Phys. Rev. **60**, 661 (1941).

[328] H. B. Michaelson, *The work function of the elements and its periodicity*, J. Appl. Phys. **48**, 4729 (1977).

[329] G. Binnig, C. F. Quate, and C. Gerber, *Atomic force microscope*, Phys. Rev. Lett. **56**, 930 (1986).

[330] G. Binnig, H. Rohrer, C. Gerber, and E. Weibel, *Surface studies by scanning tunneling microscopy*, Phys. Rev. Lett. **49**, 57 (1982).

[331] H. Fuchs, H. Hölscher, and A. Schirmeisen, *Scanning probe microscopy*, Encyclopedia of Materials: Science and Technology, Elsevier Ltd. , 12 (2005).

[332] http://knol.google.com/k/atomic-force-microscopy-afm (2011).

[333] E. Meyer, H. J. Hug, and R. Bennewitz, *Scanning Probe Microscopy The Lab on a Tip*, Advanced Texts in Physics (Springer, 2004).

[334] S. V. Kalinin, R. Shao, and D. A. Bonnell, *Local phenomena in oxides by advanced scanning probe microscopy*, J. Am. Ceram. Soc. **88**, 1077 (2005).

[335] www.nanosensors.com (2011).

[336] I. Horcas, R. Fernandez, J. M. Gomez-Rodriguez, J. Colchero, J. Gomez-Herrero, and A. M. Baro, *WSXM: A software for scanning probe microscopy and a tool for nanotechnology*, Rev. Sci. Instrum. **78**, (2007).

[337] B. B. He, *Two-Dimensional X-ray diffraction* (Wiley, 2009).

[338] D. B. Williams and C. B. Carter, *Transmission Electron Microscopy. A textbook for materials science* (Springer, New York, 1996,2009).

[339] P. D. Nellist and S. J. Pennycook, *Incoherent imaging using dynamically scattered coherent electrons*, Ultramicroscopy **78**, 111 (1999).


ICMAB
UAB
CSIC